

UC Irvine

UC Irvine Electronic Theses and Dissertations

Title

The First-moment Integral Equations for Boundary Layer Flows and Their Application

Permalink

<https://escholarship.org/uc/item/4rp5p6st>

Author

Kianfar, Armin

Publication Date

2024

Peer reviewed|Thesis/dissertation

UNIVERSITY OF CALIFORNIA,
IRVINE

The First-moment Integral Equations for Boundary Layer Flows and Their Application

DISSERTATION

submitted in partial satisfaction of the requirements
for the degree of

DOCTOR OF PHILOSOPHY

in Mechanical and Aerospace Engineering

by

Armin Kianfar

Dissertation Committee:
Assistant Professor Perry L. Johnson, Chair
Professor Dimitri Papamoschou and
Professor Feng Liu

March 11, 2024

DEDICATION

I am so grateful to my father who waited hours when I was a teenager going to different maths and physics classes so he could pick me up and drive me home safely. We would listen to sports radio together on the way. To my mother, who was the symbol of resilience; she taught me to resist unfairness, and always seek to be a better person. I thank them for never suppressing my dreams and always being open-minded. I must thank my best friend, my older brother, who despite his innumerable distractions, is always there for me, showing me new ideas with his un-pausable and creative brain!

Most importantly, I would like to thank my beloved wife, em irvin, who has been the column of our life in the past years with their patience and trust. I am grateful for the times you listened to my ideas and never really said no! Without their emotional support and unconditional belief in me, I would not have been able to reach this milestone.

TABLE OF CONTENTS

	Page
LIST OF FIGURES	v
LIST OF TABLES	x
ACKNOWLEDGMENTS	xi
VITA	xii
ABSTRACT OF THE DISSERTATION	xiv
NOMENCLATURE	1
1 Introduction and Background	4
1.1 Introduction	4
1.1.1 Motivation	4
1.2 Background	8
1.2.1 Transitional Flow	9
1.2.2 Turbulent Flow	12
1.2.3 Integral Equations	22
1.3 Research goal	32
1.3.1 Thesis Outline	34
2 Governing Equations	35
2.1 Equation of Motion – Fluid Flow	35
2.1.1 Averaged Equations	38
3 Computational Methods	42
3.1 Incompressible Flow Field	42
3.2 Boundary Layers Post-processing	47
4 First-moment Integral Equations for Low-speed Boundary Layers with Heat Transfer	54
4.1 Derivation and Interpretation	55
4.1.1 Angular Momentum Integral Equation	55
4.1.2 Moment of Enthalpy Integral Equation	60
4.2 Results and Analysis	67
4.2.1 Transitional and Turbulent Regimes	67

4.3	Conclusion	77
5	First-moment Integral Equations for Boundary Layers with Pressure Gradient	80
5.1	Derivation and Interpretation	81
5.2	Dataset and Numerical Techniques	87
5.2.1	Wing dataset	88
5.2.2	Bump dataset	90
5.2.3	Flat-plate dataset	92
5.2.4	Numerical techniques for AMI analysis	93
5.3	Results and Analysis	95
5.3.1	Flow over airfoil	95
5.3.2	Flow over Gaussian bump	98
5.3.3	Adverse pressure gradient & history effects	105
5.3.4	AMI analysis - Falkner-Skan solution	118
5.4	Conclusion	123
6	First-moment Integral Equations for High-speed Boundary Layers	126
6.1	Derivation and Interpretation	128
6.1.1	Compressible Angular Momentum Integral Equation	128
6.1.2	Moment of Total Enthalpy Integral Equation	137
6.2	Results and Analysis	146
6.2.1	Laminar Regime	146
6.2.2	Turbulent Regime	152
6.3	Conclusion	173
7	Application of the First-moment Integral Equations	177
7.1	Flow Control in Wall-bounded Flows	177
7.1.1	Surface suction and blowing	179
7.2	Wall-normal Integral-based Turbulent Modelling	183
8	Conclusion and Future Works	186
8.1	Summary of Completed Works	186
8.2	Future Research Ideas	189
	Bibliography	192
	Appendix A Full budget of the AMI Equation for flows with Pressure Gradient	205
	Appendix B Step-by-step Full Derivation of Angular Momentum Integral Equation	208
	Appendix C Full Budget of the First-moment Integral Equations for High-speed Flows	213
C.1	Angular Momentum Integral Equation	213
C.2	Moment of Total Enthalpy Integral Equation	213

LIST OF FIGURES

	Page
1.1 Skin friction coefficient for the incompressible boundary layer during the transition to turbulence.	6
1.2 High-speed boundary layer flow over a flat plate; transition to turbulence increases the skin-friction coefficient (a) and the Stanton number (b). Results from Ref. [43]	7
1.3 Local Stanton number predicted by Reynolds analogy on an adiabatic flat plate for laminar and turbulent regimes. Results from Ref. [171].	8
1.4 The “roadmap” from receptivity to transition [140]	10
1.5 Natural transition to turbulence in incompressible BLs. DNS instantaneous wall-normal velocity in $x - z$ plane at some distance away from the wall from [38].	11
1.6 (Very) Large-scale turbulent motions within the outer region; blue and red contours, respectively, represent low- and high-speed motions. Figure from Ref. [94]	14
1.7 Schematic of applying torque with respect to axis $y = \ell$ (black solid line) to the blue velocity profile: (a) applying a counterclockwise torque, and (b) applying a clockwise torque.	31
3.1 Two-dimensional staggered grid system; pressure is located at the center of a cell, and velocities are at the faces.	44
3.2 Normalized total pressure (a), and velocity profiles (mean and inviscid) in the wall-normal direction for flow over NACA-4412 airfoil. Symbols “o” and “*” denote two streamwise stations with moderate and strong pressure gradients, respectively. The red dotted line in (b) represents δ_{99} . c here is the chord length.	50
3.3 Normalized total enthalpy (a), and velocity profiles (mean and inviscid) in the wall-normal direction for high-speed turbulent flow over a flat plate. The red dotted line in (b) represents δ_{99} . L denotes the length of the flat plate.	51
3.4 Normalized spanwise vorticity contour for incompressible H-type transitional BL saturated to $0.01 \left \text{Max} [\omega_z] \right $. Solid and dashed red lines represent $1.5\delta_{99}$ and δ_{99} , respectively.	53
4.1 The balance of the right-hand side of the AMI equation compared with C_f . The labeled dashed curves are laminar (Blasius) friction and turbulent correlation of skin-friction coefficient [171].	68

4.2	The AMI budget for the four significant flow phenomena with respect to Re_{δ_2} : (a) the contribution of each term to $C_f/2$, and (b) the contribution of each term normalized by $C_f/2$	70
4.3	The balance of the right-hand side of the MEI equation compared with St . The labeled dashed curves are laminar Stanton number and turbulent power-law prediction of the Stanton number [171].	71
4.4	The MEI budget for the four significant flow phenomena with respect to Re_{δ_2} : (a) the contribution of each term to St , and (b) the contribution of each term normalized by St	72
4.5	Integrands of the explicit turbulence enhancement on the (a) Stanton number by $\overline{T'v'}/\ell U_\infty(T_w - T_\infty)$, and (b) skin-friction coefficient by $-\overline{u'v'}/\ell U_\infty^2$	74
4.6	Impact of the <i>mean wall-normal</i> flux to the AMI and MEI analysis. (a) Contour plot of wall-normal velocity in the $x - y$ plane, and (b) the direct contribution of the <i>mean wall-normal</i> flux to St and $C_f/2$	75
4.7	(a) Contour plot of the mean wall-normal velocity acceleration in y , and (b) profiles of the streamwise velocity and (spatial) streamwise acceleration ($\partial\bar{u}/\partial x$) within transitional BL.	76
4.8	Contour plots of the integrands of the <i>streamwise growth</i> : (a) in the MEI equation for St , (b) in the AMI equation for $C_f/2$	77
5.1	The suction side of NACA-4412; the region of interest in this study spans from $\xi/c = 0.2$ to $\xi/c = 0.9$. The solid and dashed blue lines denote the displacement and momentum thicknesses, respectively. The red arrows represent the (local) tangent-normal coordination system represented by $x - y$	89
5.2	Wing dataset; the BL shape factor with respect to ξ (a), and the Clasuer parameter with respect to friction Reynolds number Re_τ (b).	90
5.3	Boundary layer shape factor, δ_1/δ_2 , in the bump flow with respect to ξ . Flow separation causes a substantial increase in the shape factor about $\xi/L = 0.25$	91
5.4	Flat-plate dataset; plots of the skin friction coefficient with respect to x (a), and the Clauser parameter with respect to Re_τ (b).	93
5.5	Calculation of the locally reconstructed inviscid velocity, U_i , along the wall-normal direction for (a) Wing and (b) Bump datasets. The solid and dashed lines represent the mean streamwise and inviscid velocity profiles normalized by the free-stream velocity, U_∞ . The solid black lines denote the location of δ_{99} computed by the local reconstruction method.	94
5.6	The AMI budget with respect to the chord length, ξ/c , for the Wing case (table 5.1); (a) the absolute budget, and (b) the relative budget normalized by $C_f/2$	97
5.7	The AMI budget (middle) for BL over a Gaussian bump with respect to the normalized streamwise location, ξ/L ; dotted and solid black lines in the bottom panel represent the AMI length scale ℓ and BL thickness δ_{99} , respectively. The top panel exhibits <i>turbulent torque</i> within the different regions of BL; $y^* = y/\delta_{99}$ and y^+ denote the wall-normal position normalized by outer and inner scales, respectively. Symbol * represents three streamwise locations where the turbulent statistics are compared in figure 5.8.	100

5.8	Reynolds shear stress and turbulent kinetic energy profiles in the bump flow with respect to y^+ : absolute (a, c) and outer-scaled (normalized by U_{io}^2) (b, d). In (c, d), shaded dashed and dotted lines are associated with $\overline{u'u'}$ and $\overline{v'v'} + \overline{w'w'}$, respectively.	102
5.9	The AMI budget within the APG region with respect to Re_{δ_1} ; contribution of the substantial flow phenomena impacting $C_f/2$: (a) laminar friction, (b) turbulent torque, (c) torque due to pressure gradient, and (d) torque due to total mean flux. (e) exhibits the contribution to $C_f/2$ by the sum of (c) and (d).	108
5.10	Contribution of the <i>turbulent torque</i> to $C_f/2$ within the (a) inner layer (from $y = 0$ to $y^* = 0.1$), (b) log-law region (from $y^+ = 30$ to $y^* = 0.3$), and outer layer (from $y^+ = 50$ to $y^* = 1$). Panel (d) shows the ratio of the <i>turbulent torque</i> within the outer layer and its total value. $y^* = y/\delta_{99}$ and $y^+ = y/\delta_\nu$ denote the normalized wall-normal distance by the BL thickness, δ_{99} , and viscous length scale, δ_ν , respectively. Shaded lines represent the total <i>turbulent torque</i> in the AMI budget Fig. 5.9 (b).	111
5.11	The Clauser parameter with respect to Re_{δ_1} ; (a) based on δ_1 (the classic definition), and (b) based on δ_1^ℓ obtained from the AMI analysis. V, X, and XI ₆ mark the streamwise matching locations at which turbulent statistics are compared (shown in Fig. 5.12) based on table 5.2.	112
5.12	History effects; the inner-scaled mean velocity and Reynolds stress components with respect to y/ℓ at matching $Re_{\delta_1} - \beta_\ell$ ($Re_{\delta_1} - \beta$ shaded lines) for V, X, XI ₆ (shown in Figs. 5.11); the solid, dashed, dashed-dotted, and dotted lines represent $\overline{u'u'}^+$, $\overline{v'v'}^+$, $\overline{w'w'}^+$, and $-\overline{u'v'}^+$, respectively. The insets exhibit the same profiles Vs. y^+ . Symbol \diamond denotes the wall-normal position of δ_{99} .	114
5.13	The correlation between C_f and β_ℓ (or β). Skin friction coefficient at the streamwise location of matching $Re_{\delta_1} - \beta_\ell$ (and $Re_{\delta_1} - \beta$ shaded color) according to table 5.2; a comparison between (a) Wing and flat-plates, and (b) Bump and flat-plates.	116
5.14	The correlation between C_f and β_ℓ (or β) for the Wing and Bump datasets. Skin friction coefficient at the streamwise location of matching $Re_{\delta_1} - \beta_\ell$ ($Re_{\delta_1} - \beta$ shaded color).	118
5.15	Self-similar Falkner-Skan solution and the Clauser parameter; relationships between β and m (a), and α_{FS} and β (b).	120
5.16	<i>Turbulent torque</i> with respect to Re_{δ_1} when ℓ is obtained from the Falkner-Skan solution; (a) the absolute contribution to $C_f/2$, (b) the relative contribution (normalized by $C_f/2$).	121
5.17	The Clauser parameter with respect to Re_{δ_1} based on δ_1^ℓ obtained from the AMI analysis using Falkner-Skan laminar solution. The shaded lines denote β as in Fig. 5.11 (a).	122
6.1	The budget of the laminar AMI equation, Eq. (6.40), based on $\mu_{\text{Ref}} = \mu_w$: laminar skin friction (a), the viscous deviation (b), the streamwise growth of the angular momentum thickness (c), and the torque due to wall-normal velocity (d). Each term is shown as a function of $Re_{\delta_2} = U_e \rho_e \delta_2 / \mu_w$. In (a), C-2 is shown with dashed lines.	150
6.2	The budget of the laminar AMI equation, Eq. (6.40), based on $\mu_{\text{Ref}} = \mu_2$: laminar skin friction (a), the viscous deviation (b), the streamwise growth of the angular momentum thickness (c), and the torque due to wall-normal velocity (d).	151

6.3	The budget of the laminar MTEI equation, Eq. (6.42), based on $\mu_{\text{Ref}} = \mu_w$: laminar Stanton number (a), the viscous deviation (b), the streamwise growth (c), and the flux due to wall-normal velocity (d).	153
6.4	The budget of the laminar MTEI equation, Eq. (6.42), based on $\mu_{\text{Ref}} = \mu_H$: laminar Stanton number (a), the viscous deviation (b), the streamwise growth (c), and the flux due to wall-normal velocity (d).	154
6.5	Normalized Favre averaged (a) velocity by the edge velocity and (b) Reynolds shear stress by the wall shear stress. The profiles are plotted at Re_2 shown with “*” in Figure 6.9(a)	156
6.6	Normalized Favre averaged (a) total enthalpy by the edge total enthalpy, and (b) wall-normal velocity and total enthalpy turbulent covariance by the wall heat flux (for study cases of MTEI equation). In (b) the dashed-, dashed-dotted-, and dotted-lines represent $c_p \overline{\rho T'' v''}$, $\overline{\rho u u'' v''}$, and $\frac{1}{2} \overline{\rho u'' u'' v''}$, respectively. The profiles are plotted at Pe_H shown with “*” in Figure 6.13(a)	157
6.7	Normalized (a) average density by the edge density, and (b) Favre average viscosity by the edge viscosity. The dashed lines in (a) show ρ_2 , Eq. (6.16). Also, the dashed and dotted lines in (b) represent the value of μ_2 , Eq. (6.11), and μ_H , Eq. (6.28), respectively. The profiles are plotted at Re_2 shown with “*” in Figure 6.9(a), except for μ_H that is plotted at Pe_H shown with “*” in Figure 6.13(a)	158
6.8	Evaluation of non-negligible terms in the AMI equation, Eq. (6.7), based on $\ell = \ell_{2,C}$ and $\mu_{\text{Ref}} = \mu_2$ for the cases in Table 6.1 within the fully turbulent regime: (a) baseline laminar skin friction, (b) the integral torque of the Reynolds shear stress –the dashed lines exhibit $C_f/2$ –, (c) the streamwise growth of the angular momentum thickness, and (d) the torque due to mean wall-normal velocity. Each term is shown as a function of Re_2 , Eq. (6.14). A part of the upstream data is truncated because of the effect of the turbulent recycling.	160
6.9	Contribution of the <i>turbulent torque</i> to $C_f/2$ and the profile of its integrand at “*”: (a) turbulent torque by choosing ℓ based on self-similar laminar compressible BLs, $\ell = \ell_{2,C}$, and (b) profile of the integrand of turbulent torque with respect to wall-normal distance normalized by $\ell_{2,C}$. In (a), the thinner dashed- and dotted lines show the $C_f/2$ and the right-hand side of the AMI equation. The Inset of (b) exhibits the integrand of turbulent torque by removing the effect of density variation within the BL. (c) The <i>turbulent torque</i> by choosing ℓ based on Blasius solution for IC BLs, $\ell = \ell_{1C}$, and (d) profile of the integrand of the <i>turbulent torque</i> with respect to the wall-normal distance normalized by ℓ_{1C} . Inset of (d) presents the integrand of the <i>turbulent torque</i> multiplied by the ratio of compressible and incompressible length scales, $\ell_{2,C} = \ell_{1C}$, with respect to $y/\ell_{2,C}$	164
6.10	Normalized contribution of <i>turbulent torque</i> (white background), <i>laminar friction</i> (light gray background), and <i>streamwise growth</i> (dark gray background) by $C_f/2$: when the reference viscosity (a) $\mu_{\text{Ref}} = \mu_2$, and (b) $\mu_{\text{Ref}} = \mu_w$	166
6.11	(a) Skin friction coefficients without transformation, (b) integral transformation based on stress-weighted density, and (c) integral transformation based on the ratio of the compressible and incompressible AMI length scales.	167

6.12	Budget of MTEI based on $\ell = \ell_{H,C}$ and $\mu_{\text{Ref}} = \mu_H$ within the fully turbulent regime: (a) laminar Stanton number, (b) contribution of turbulent flux to Stanton number, (c) streamwise growth of the first moment of total enthalpy thickness, and (d) contribution of mean wall-normal flux. The incompressible (IC) data is shown in black. A part of the upstream data is truncated because of the effect of the turbulent recycling.	170
6.13	Contribution of <i>turbulent flux</i> to St and the profile of its integrand at “*”: (a) turbulent flux of total enthalpy based on $\ell = \ell_{H,C}$, and (b) profile of its integrand with respect to the wall-normal distance normalized by $\ell_{H,C}$. In (a), the dim, thin dashed- and dotted lines show the St and the right-hand side of the MTEI equation. The inset of (b) shows the integrand of <i>turbulent flux</i> by pulling out the influence of density variation within the BL.	171
6.14	Decomposition of the <i>turbulent flux</i> of total enthalpy and the profile of its integrand at “*”: (a) direct contribution of turbulent transport of mean kinetic energy (dashed-dotted line) and turbulent enthalpy (heat) flux (dashed lines) to St with respect to the streamwise location, Pe_H , and (b) profile of their integrands with respect to wall-normal distance normalized by $\ell_{H,C}$. In (a,b), the dim, thin solid lines represent the net contribution of the turbulent flux of total enthalpy. Insets of (b) show the integrands by pulling out the effect of density variation within the BL.	171
7.1	The AMI budget of the reference wing compared with the suction and blowing cases with respect to ξ/c for: (a) <i>turbulent torque</i> , (b) <i>pressure gradient</i> , (c) <i>mean flux</i> , and (d) <i>wall BC</i> . The shaded gray region denotes the streamwise position under suction (or blowing). In (a) shaded black lines exhibit $C_f/2$	180
7.2	Comparison of the inner-scaled instantaneous streamwise velocity in $x - z$ plane: (a) at wall-normal distance $y/\delta = 0.2$, and (b) after applying the wall-normal integral operator. Results from Ragan & Johnson [134].	184

LIST OF TABLES

	Page
5.1 Turbulent BL datasets. Three types of BLs are examined: flow over an airfoil, a Gaussian bump, and a flat-plate. For flat-plates, including ZPG, the reference Reynolds number is computed based on the displacement thickness at the inlet, δ_1^o . The reported values of β are associated with the APG region $Re_{\delta_1} \leq 6500$	88
5.2 Matching positions between $Re_{\delta_1} - \beta_e$ and $Re_{\delta_1} - \beta$ for the dataset in table 5.1. . .	113
6.1 DNS inputs and some fundamental flow outputs; $Re_{\delta_{in}} = \rho_e U_e \delta_{in} / \mu_e$ is the Reynolds number based on the inflow BL thickness (δ_{in}); Prandtl number $Pr = 0.72$, (non-dimensional) specific heat $c_p = 3.5$, and heat capacity ratio $\gamma = 1.4$ are set as constants and the same for all cases.	155

ACKNOWLEDGMENTS

First and foremost, I express my sincere gratitude to my advisor, Professor Perry Johnson, whose unwavering support and trust have been the spine of my graduate studies. His guidance, professionalism, and profound expertise across various fields of fluid dynamics have been invaluable in shaping my research journey. His insightful feedback and mentorship have enabled the development of innovative ideas and the exploration of intricate flow physics problems. I am deeply grateful for his encouragement, patience, and wisdom, without which this thesis would not have come to fruition.

I am grateful for the fruitful discussions with Ahmed Elnahas toward developing the first-moment integral equations and providing the preliminary dataset for incompressible boundary layers in Chapter 4. I also appreciate the vast contribution of Professor Mario Di Renzo, Christopher Williams, and the Center for Turbulence Research at Stanford University for providing the required dataset and the opportunity to study compressible flows in Chapter 6.

I appreciate Professors Ricardo Vinuesa and Kenneth Jansen for providing their non-zero pressure gradients turbulent datasets, which were invaluable toward completing Chapter 5.

I also thank Tanner Ragan for his guidance and contribution to Chapter 7 regarding developing integral-based turbulent models.

VITA

Armin Kianfar

EDUCATION

Master of Science in Aerospace Engineering Sciences University of Colorado, Boulder	2020 <i>Boulder, Colorado</i>
Master of Science in Mechanical Engineering University of Tehran	2018 <i>Tehran, Iran</i>
Bachelor of Science in Mechanical Engineering Iran University of Science and Technology	2015 <i>Tehran, Iran</i>

RESEARCH EXPERIENCE

Graduate Student Researcher University of California, Irvine	2023–2024 <i>Irvine, California</i>
Graduate Research Assistant University of Colorado, Boulder	2021–2023 <i>Boulder, Colorado</i>

TEACHING EXPERIENCE

Graduate Teaching Assistant University of Colorado, Boulder	2018–2020 <i>Boulder, Colorado</i>
---	--

Rocket Propulsion, ASEN-5053
Aircraft Propulsion, ASEN-5063
Structures Aerospace, ASEN-3112
Material Science Aerospace, ASEN-1022

REFEREED JOURNAL PUBLICATIONS

Angular momentum and moment of total enthalpy integral equations for high-speed boundary layers 2023
Physical Review Fluids

Quantifying how turbulence enhances boundary layer skin friction and surface heat transfer 2023
AIAA Journal

REFEREED IN PREPARATION JOURNAL PUBLICATIONS

Angular momentum integral equation for boundary layer flows with pressure gradient 2024
in preparation for publication

REFEREED CONFERENCE PUBLICATIONS

Angular momentum integral equation on turbulent boundary layers with pressure gradient November 2023
Bulletin of the American Physical Society

An angular momentum integral equation for high-speed boundary layers October 2022
Proceedings of the Summer Program, Center for Turbulence Research

The influence of turbulence on surface heat transfer in boundary layers using a moment of temperature integral equation November 2021
Bulletin of the American Physical Society

ABSTRACT OF THE DISSERTATION

The First-moment Integral Equations for Boundary Layer Flows and Their Application

By

Armin Kianfar

Doctor of Philosophy in Mechanical and Aerospace Engineering

University of California, Irvine, March 11, 2024

Assistant Professor Perry L. Johnson, Chair

The enhancement of skin friction drag and surface heat flux by the transition to turbulence is a crucial physical phenomenon in wall-bounded flows. An interpretable mapping of how various flow phenomena such as turbulence and pressure gradient influence these key surface quantities is desirable for advancing our understanding of fundamental flow physics, as well as informing engineering design analysis and developing efficient flow control techniques. To accomplish such a mapping, in this study, integral forms based on the first-moment of conservation equations are developed. The angular momentum integral (AMI) equation, obtained from the first moment of the momentum equation, yields an identity for the skin friction coefficient (friction drag). Furthermore, the moment of (total) enthalpy integral (MTEI) equation, derived from the first moment of the energy equation, provides a mapping for the Stanton number (surface heat flux). This first-moment approach uniquely isolates the skin friction (or surface heat flux) of a laminar BL in a single term that depends only on the Reynolds number (or Peclet number) most relevant to the flow's engineering context, hence other terms are interpreted as augmentations or reductions relative to the laminar case having the same Reynolds number (or Peclet number).

In the case of zero-pressure-gradient incompressible transitional BLs, the AMI and MTEI equations examine the peak friction drag and surface heat flux during the transition. These tools demonstrate and quantify how the streamwise growth of the BL and the mean wall-normal flux resist the extreme

growth of turbulent enhancement via Reynolds shear stress. This rapid growth of turbulence during transition imposes near-wall streamwise acceleration that results in a negative wall-normal velocity very close to the wall. For a fully turbulent regime, the explicit turbulent enhancement is the primary process of near-wall momentum (or heat) flux, not molecular transport. Consequently, the other flow phenomena weakly impact the skin friction (or surface heat flux).

The AMI analysis of turbulent flows subjected to strong favorable pressure gradients presents a substantial reduction of the turbulent enhancement due to a phenomenon referred to as reversion. The AMI analysis captures this complex phenomenon caused by flow acceleration and exhibits re-laminarization which deactivates the turbulence. Conversely, adverse pressure gradients cause marginal alteration in turbulent enhancement downstream, suggesting a weak correlation between the total Reynolds shear stress and the strength of the pressure gradient. Additionally, the AMI equation introduces a pressure gradient parameter, which compared to the classic Clauser parameter, offers a more robust similarity in turbulent statistics between two flows with a distinct upstream history.

In high-speed boundary layers, e.g., supersonic vehicles, due to severe heating, surface heat flux is more critical than friction drag. To analyze the surface heat flux and friction drag the first-moment integral approach is extended to compressible flows, considering the variation of density, viscosity, and thermal conductivity across the boundary layer. The AMI results quantify how the variation of mean density inside a high-speed turbulent boundary layer impacts the momentum transport and reduces the friction drag. From an alternative viewpoint, the results demonstrate how the effect of compressibility on laminar boundary layers can be utilized to develop a mapping between the skin friction coefficient of the incompressible and compressible turbulent flows. The MTEI analysis similarly demonstrates how the mean density alters the impact of turbulence on the transport of total enthalpy and Stanton number. In doing so, the MTEI results highlight the relative role of turbulent fluxes of enthalpy and mean kinetic energy on the Stanton number.

These results suggest that the first-moment integral equations could be a valuable tool for evalu-

ating flow control schemes. In the case of turbulent boundary layers over an airfoil with surface suction or blowing, only minor variations occurred in the turbulent enhancement. The AMI equation is also applicable to evaluate more complex control methods such as using porous mediums. Beyond its role as an analysis tool, the concept of first-moment integral equations holds promise for the development of computationally efficient turbulent models. The AMI analysis quantifies approximately 80% of the turbulent enhancement in wall-bounded flows originates from the outer layer of the flow. Therefore, solving the integral form of the Navier-Stokes equation, focusing on resolving the outer layer, could provide a promising platform for turbulent modeling.

NOMENCLATURE

Latin Symbols

\mathbf{u}	Velocity vector
\mathbf{x}	Position vector
c	Airfoil chord length
C_f	Skin friction coefficient
c_p	Specific heat capacity
f	Force
H	Total enthalpy
h	Enthalpy
i	Inviscid flow solution
io	Inviscid flow solution at the surface
k	thermal conductivity
l	Length scale
M	Mach number
P	Base (mean) pressure
p	Pressure
Pe	Peclet number
Re	Reynolds number
St	Stanton number
T	Temperature
U	Velocity scale
u	Streamwise velocity
v	Wall-normal velocity
x	Streamwise position
y	Wall-normal position

Greek Symbols

α	Thermal diffusivity
β	Cluser parameter
β_ℓ	First-moment-based Cluser parameter
δ	Boundary layer thickness or channel flow half height
δ_1	Displacement thickness
δ_2	Momentum thickness
δ_H	Total ethalpy thickness
δ_h	Etnhalpy thickness

ℓ	First-moment integral length scale
μ	Dynamic viscosity
ν	Kinematic viscosity
ρ	Density
τ	Shear stress
K	Kinetic energy
t	Time

Subscripts

∞	Free-stream quantity
e	Edge quantity
H	Total enthalpy
h	Enthalpy
M	Momentum
o	Stagnation quantity
Ref	Reference quantity
w	Wall quantity
B	Bulck quantity
b	Base flow quantity
C	Compressible
FS	Falkner-Skan solution
IC	Incompressible

Superscripts

$*$	Dimensional quantity
$+$	Viscous scale (wall units)
ℓ	First-moment with respect to length scale ℓ
$//$	Density-averaged turbulent fluctuation
$'$	RANS turbulent fluctuation
sl	Semi-local viscous scale

Acronyms

AMI	Angular momentum integral
APG	Adverse pressure gradient
BL	Boundary layer
FIK	Fukagata-Iwamoto-Kasagi
FPG	Favorable pressure gradient
MEI	Moment of enthalpy integral
MTEI	Moment of total enthalpy integral
NS	Navier-Stokes
RANS	Reynolds-averaged Navier-Stokes
RD	Renard-Deck
TS	Tollmien-Schlichting
ZPG	Zero-pressure-gradient

Other Symbols

$ \cdot $	Absolute value
$\bar{\cdot}$	Mean quantity
$\tilde{\cdot}$	Density weighted average quantity

Chapter 1

Introduction and Background

1.1 Introduction

1.1.1 Motivation

Wall-bounded flows find widespread applications in both engineering and scientific contexts, spanning a broad range of Reynolds numbers. A fundamental application of boundary-layer theory lies in the computation of friction drag for objects immersed in fluid flow. This includes scenarios such as the drag experienced by a flat plate at zero incidence, the frictional resistance of ships, airfoils, airplane fuselages, and turbine blades. One noteworthy characteristic of the boundary layer is its potential to exhibit reverse flow conditions directly at the solid surface under certain circumstances. This can lead to the detachment of the boundary layer from the object and the generation of either large or small eddies at the object's downstream side. Such behavior can significantly alter the pressure distribution at the object's rear, contributing to what is known as form or pressure drag. The boundary-layer theory addresses a vital question: how can the shape of an object be designed to prevent this undesirable separation phenomenon? Separation is not limited to objects in free flow;

it also occurs in confined passages like ducts.

Consequently, boundary-layer theory plays a crucial role in describing the flow behavior in blade cascades within compressors and turbines, as well as in diffusers and nozzles. Moreover, boundary-layer theory is indispensable for comprehending the processes governing maximum lift in airfoil designs, where separation phenomena hold paramount significance. Beyond drag and lift considerations, the boundary layer plays a pivotal role in analyzing heat transfer between an object and the surrounding fluid.

Transition to turbulence is a natural phenomenon that occurs in wall-bounded flows due to the growth of flow disturbances. Transition to turbulence is mainly predicted by the Reynolds number depending on flow conditions, e.g., wall roughness and geometry. When compared to its laminar counterpart, a boundary layer undergoing the transition to turbulence exhibits rapid growth and significantly higher wall shear stress and surface heat flux. Fig 1.1 exhibits the skin friction coefficient of natural and bypass transitional incompressible BLs with respect to Reynolds number based on the momentum thickness; for both cases, the skin friction peaks during the transition, and its value is higher than the laminar regime. This enhancement in wall shear stress plays a pivotal role in determining the drag experienced by streamlined objects, contributing to roughly 50% and 90% of the drag for commercial aircraft and underwater vehicles, respectively [48]. For high-speed vehicles, however, drag is often less crucial than tremendous surface heat flux. In Figure 1.2 (a,b), the non-dimensional wall-shear stress (skin friction coefficient) and surface heat flux (the Stanton number) with respect to the streamwise distance of a high-speed boundary layer at free-stream Mach number six are plotted (Results from [43]); these quantities are higher during the transition and turbulence relative to the laminar flow. Supersonic and hypersonic flows are energetic and create high-temperature regions that directly diminish the aerodynamic performance and make the flow control schemes less efficient [17]. Compressibility adds more complexity to the flow field as the density variation across the BL impacts the mass, momentum, and energy transport, and hence the skin friction and surface heat flux. Figure 1.3 exhibits the computed local wall heat flux coeffi-

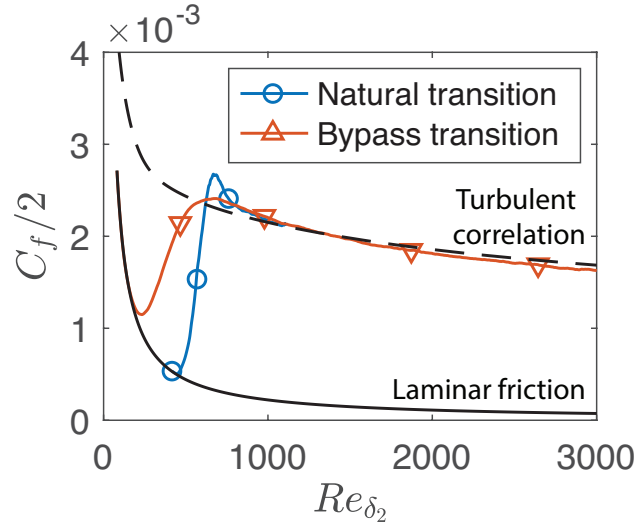


Figure 1.1: Skin friction coefficient for the incompressible boundary layer during the transition to turbulence.

cient, the so-called Stanton number, using the Reynolds analogy on an adiabatic flat plate; for both laminar and turbulent regimes compressibility –Mach number– decreases the surface heat flux.

The practical importance of transitional and turbulent boundary layers serves as a driving force for gaining a deeper understanding of the flow physics responsible for this heightened wall shear stress and surface heat flux. For engineering applications, this understanding is crucial in developing and optimizing flow control schemes to efficiently manipulate the flow field to either stabilize, e.g., friction drag reduction in stream-lined bodies, or destabilize, e.g., separation delay in turbomachinery or heat transfer enhancement in combustion. In order to comprehensively unravel the mechanisms behind these alterations, it is imperative to provide a meticulous examination of the influence of turbulence on wall shear stress and surface heat flux. One approach to examining the role of turbulence on friction drag and surface heat flux is using the integral methods.

Integral methods find wide-ranging applications in the study and analysis of wall-bounded flows, offering valuable insights and practical solutions for engineering and scientific disciplines. These methods serve as indispensable tools in understanding the behavior of fluid flow near solid surfaces. In aerodynamics, integral methods enable the calculation of skin friction and drag on aircraft wings,

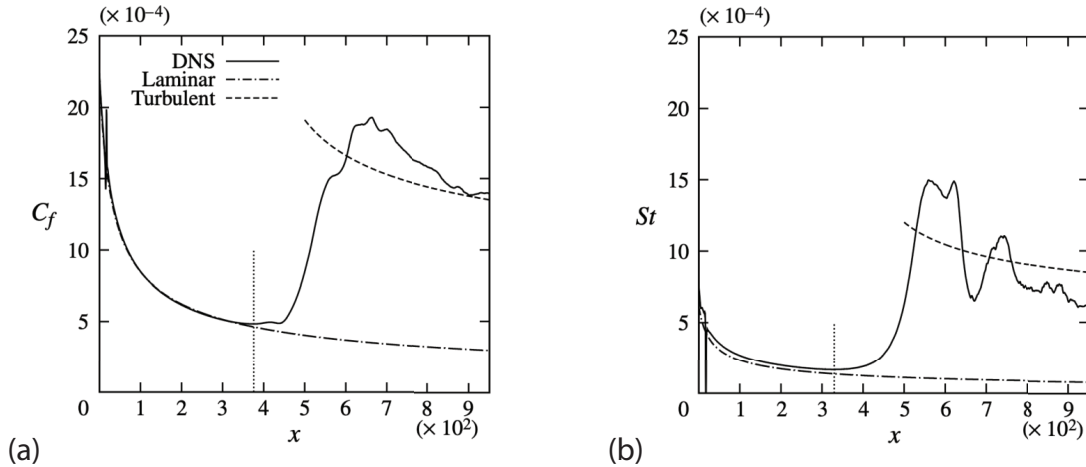


Figure 1.2: High-speed boundary layer flow over a flat plate; transition to turbulence increases the skin-friction coefficient (a) and the Stanton number (b). Results from Ref. [43]

aiding in the design of more efficient and fuel-effective airfoils. They are crucial in heat transfer studies, facilitating the prediction of temperature gradients and cooling requirements for engineering applications like gas turbine design and electronic component cooling systems. In marine engineering, integral methods help assess the hydrodynamic resistance of ships and submarines, optimizing their hull designs for reduced fuel consumption. Additionally, these techniques are employed in the environmental sciences to model pollutant dispersion near the Earth's surface. Integral methods continue to contribute significantly to various fields by providing practical solutions and a deeper understanding of boundary layer phenomena. The history of these methods goes back to the early 20th century when Prandtl established the concept of the boundary layer. Prandtl's pioneering work laid the foundation for integral techniques by emphasizing the importance of integrating the governing equations across the boundary layer to obtain simplified yet insightful solutions. Over the decades, researchers and engineers have refined and expanded these integral methods to tackle various aspects of wall-bounded flows, from laminar to turbulent regimes. These methods have been invaluable for estimating essential parameters such as skin friction, boundary layer thickness, and heat transfer rates, making them indispensable tools in the study of fluid dynamics and the design of aerodynamic and hydrodynamic systems.

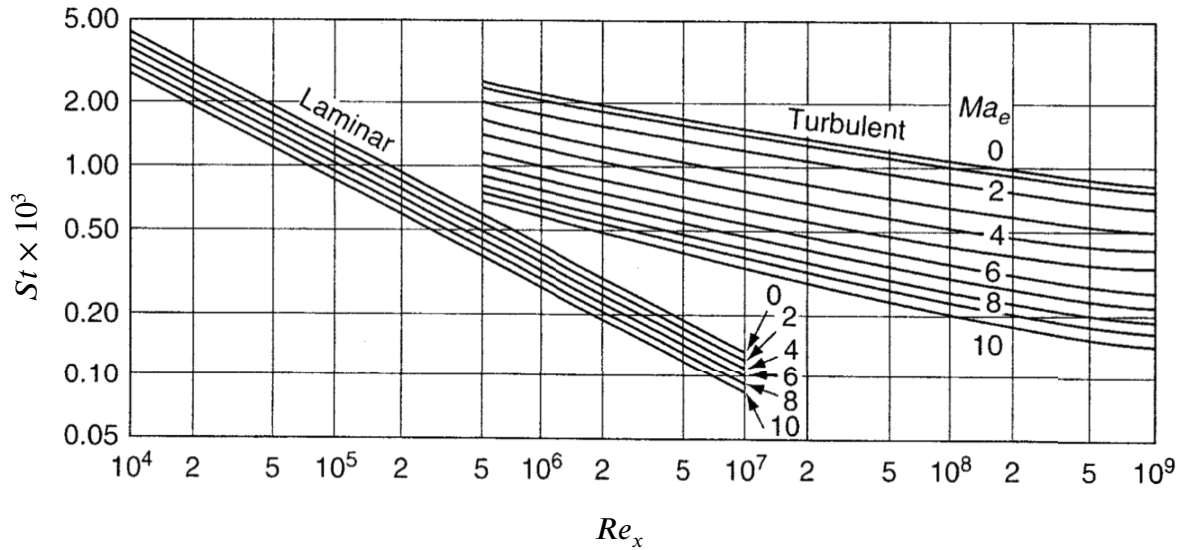


Figure 1.3: Local Stanton number predicted by Reynolds analogy on an adiabatic flat plate for laminar and turbulent regimes. Results from Ref. [171].

1.2 Background

Initially, boundary-layer theory was primarily developed for laminar flows of incompressible fluids, where Stokes' law of friction served as a foundational framework for understanding viscous forces. Over time, extensive research efforts delved into this area, resulting in a comprehensive understanding of these flows. Subsequently, the theory was expanded to encompass the practical and significant realm of transitional and turbulent, incompressible boundary layer flows [139].

With the rapid increase in velocities in the field of aviation technology, the study of boundary layers in compressible flows gained significant attention. In addition to the velocity field of the boundary layer, a thermal boundary layer also forms, which holds immense importance in understanding heat transfer between the flow and the solid body. The elevated surface temperatures resulting from internal friction (dissipation) at high Mach numbers have posed substantial challenges, particularly in aviation and satellite missions, often referred to as the “thermal barrier” problem.

1.2.1 Transitional Flow

The transition process from laminar to turbulent within wall-bounded flows holds immense significance in fluid dynamics, particularly in the context of flow control and drag reduction. Currently, there is no mathematical model available that can precisely forecast the exact moment of transition, even on a flat plate. This challenge arises due to the myriad of factors at play, including the influence of free-stream turbulence, surface irregularities, sound waves, and entrainment effects. Disturbances, whether steady or unsteady, in the free-stream, such as sound or vorticity, act as the triggers for transition. Their impact on the fundamental state of the boundary layer is referred to as "receptivity" [114], where these disturbances provide the initial conditions in terms of disturbance amplitude, frequency, and phase that ultimately lead to the transition from laminar to turbulent flow [140]. Natural receptivity, occurring with the free-stream, consists of two different mechanisms: the irrotational acoustic disturbances that travel with the phase speed equal to sound speed in the medium (infinity for incompressible fluid) and rotational vortical parts convected with speed relative to the free-stream velocity. The former is observed to generate the initial amplitude of the TS waves [90]. The latter contributes to the three-dimensional aspects of the breakdown process [77, 78]. Bypass transition occurs when finite-amplitude perturbations bypass the early stages of natural transition. Turbulent spots appear as the perturbations break down. Subsequently, the turbulent spots merge to form a fully turbulent flow. Although the finite-amplitude perturbations can come from any source, the common understanding of bypass transition is centered around the receptivity of boundary layers to free-stream instabilities (or turbulence) [182]. In other words, if the free-stream disturbances are substantial, the growth of linear disturbances is bypassed [114, 115]. Consequently, turbulent spots or subcritical instabilities emerge, and flow becomes turbulent. This process corresponds to path E in Fig. 1.4. In the case of bypass transition, due to the importance of the nonlinear effects, the linear theory utterly fails. Although the bypass transition is not completely comprehended mathematically, it has been documented in cases of roughness and high free-stream turbulence [136, 137, 138], and has been commonly implemented to trigger the transition to turbu-

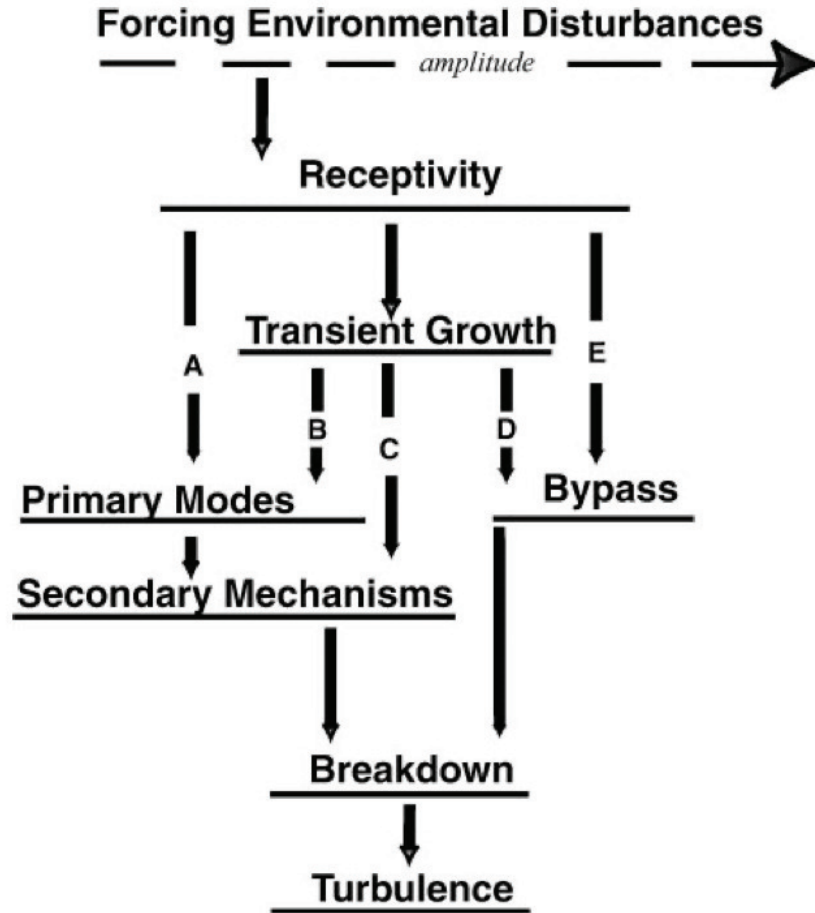


Figure 1.4: The “roadmap” from receptivity to transition [140]

lence [176].

In cases where the amplitude of free-stream disturbances is small, path A in Fig. 1.4, the nonlinear components within the boundary layer disturbance equations can be disregarded, allowing for the prediction of disturbance growth or decay using linear theory [171]. These disturbances, characterized by weak growth or decay in space and time, exhibit a primarily two-dimensional nature and are commonly referred to as Tollmien-Schlichting (TS) waves [87, 120]. Due to the linearity of the problem, these primary modes, which are common in cruise flight conditions, are well-understood mathematically. Predicting TS waves involves decomposing the flow field variables into a base component (\mathbf{u}_b) and a perturbation component (\hat{u}) such that $\mathbf{u} = \mathbf{u}_b + \hat{u}$. Inserting this definition to the Navier-Stokes equation, Eq. (2.2), assuming small disturbances ($\hat{u} \ll \mathbf{u}_b$), then linearizing the

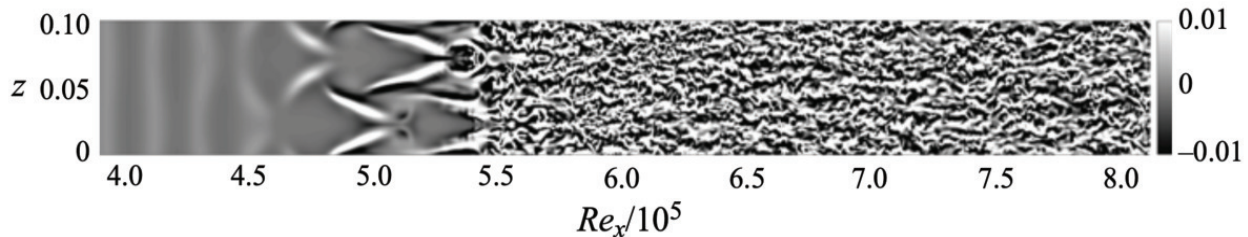


Figure 1.5: Natural transition to turbulence in incompressible BLs. DNS instantaneous wall-normal velocity in $x - z$ plane at some distance away from the wall from [38].

equation yields the Orr-Sommerfeld equation as

$$(u_b - c_{\text{TS}}) (\hat{v}'' - \alpha_{\text{TS}}^2 \hat{v}) - u_b'' \hat{v} + \frac{i}{\alpha_{\text{TS}} Re} (\hat{v}'''' - 2\alpha^2 \hat{v}'' + \alpha_{\text{TS}}^4 \hat{v}) = 0, \quad (1.1)$$

where the superscript prime denotes differentiation in the wall-normal direction, and Re is the Reynolds number. In Eq. (1.1), $c_{\text{TS}} = -\tilde{\omega}_{\text{TS}}/\alpha_{\text{TS}}$ is the complex TS wave-speed, and α_{TS} and $\tilde{\omega}_{\text{TS}}$ are the wavenumber and non-dimensional wave frequency, respectively. Note, $\sqrt{i} = -1$ hence for temporal instability $c_{\text{TS}i} > 0$, whereas for spatially growing TS waves $\alpha_{\text{TS}i} < 0$ [171]. Assuming wave solution for \hat{v} with homogenous boundary conditions at the wall and the free-stream, Eq. (1.1) becomes an eigenvalue problem.

As these initially two-dimensional TS waves propagate and grow downstream, their amplitudes eventually reach finite values, leading to the initiation of substantial nonlinear effects. Consequently, the disturbances become three-dimensional [60]. This three-dimensionality is manifested in the shape of Λ vortices, which can take on either staggered (H-type) or aligned (K-type) configurations, contingent on the initial amplitude of the two-dimensional wave. During this stage, the rapid growth of three-dimensional modes occurs over relatively short distances, leading to the formation of hairpin vortices and eventually culminating in the transition to turbulence [87]. The process of the natural transition to turbulence in an incompressible BL is exhibited in Figure 1.5; the transition process initiates by two-dimensional TS waves at $\sim Re_x = 4 \times 10^5$, then H-type Λ vortices appear at roughly $Re_x = 5 \times 10^5$, and shortly after flow becomes chaotic and fully turbulent.

1.2.2 Turbulent Flow

The transition process, described in the previous section, leads the flow field to a complex regime known as turbulence. Turbulence is described by its chaotic and irregular nature, with the fluid exhibiting rapid and unpredictable changes in velocity, pressure, and temperature. In a fully turbulent flow, the chaotic and irregular motions are dominant throughout the entire volume of the fluid, and there is a lack of any smooth flow patterns. As clarified by Tennekes & Lumely [152], a turbulent regime is characterized by its irregularity (or randomness), strong diffusivity, Large Reynolds number, three-dimensional vorticity fluctuations, and dissipation. The concept of turbulent flows that go under the realm of continuum mechanics is a fundamental phenomenon in science and technology. For instance, The substantial diffusivity of turbulence due to the motion of turbulent eddies and structures, which causes rapid mixing and increased rates of momentum, heat, and mass transfer, delays boundary layer separation on airplane wings. However, it also significantly increases the friction drag. This example signifies the requirement of comprehending the turbulent structures and motions prior to engineering designs.

Incompressible turbulent structures

A fully turbulent flow is characterized by turbulent eddies; all scales of fluid motion, from the largest down to the smallest fluctuations, are chaotic by the nature of turbulence. Besides that, a wall-bounded, fully turbulent flow exhibits a classical division into inner, outer, and overlap layers. These layers delineate distinct regions within the boundary layer, each characterized by specific flow phenomena and scaling laws. The persistence of viscosity mostly marks the inner layer that is closer to the solid surface. Within this region, the flow is dominated by streamwise streaks, first observed by Ref. [89]. These low-speed streamwise streaks were observed to play a substantial role in the process of turbulent production; they coincide with the wall-normal location where the maximum turbulent kinetic energy production rate occurs –within the buffer region. The relation

between the streamwise streaks and turbulent production rate was further investigated by studying BLs with pressure gradient. In the case of adverse pressure gradient BLs, the streaks tend to be shorter and wave more rapidly, causing a stronger turbulent production rate. On the other hand, in favorable pressure gradient flows that are characterized by a less turbulent production rate, these structures tend to be drawn longer and more quiescent. In fact, in the case of a relatively strong favorable pressure gradient, re-laminarization might occur due to the suppression of the streamwise streak and, hence, turbulent production rate. Additionally, streamwise-oriented vortices, as postulated by Ref. [85], are a defining feature of this inner layer. These streaks and vortices interact in a self-sustaining cycle, a concept elucidated by Ref. [57]. These temporal regeneration cycles consist of three steps: streak formation, streak breakdown, and vortex regeneration. Streak formation arises from the momentum advection by streamwise vortices, while streak breakdown results from inherent instabilities within the streaks themselves. This cycle operates with scaling laws specific to the inner layer and can persist independently of the presence of large eddies in the outer flow. This intriguing independence was demonstrated through numerical experiments conducted by Refs. [72, 71].

The outer layer of wall-bounded flows that extends from the logarithmic region onwards contains the large-scale and very large-scale turbulent motions, so-called LSM and VLSM, respectively [56, 31, 96]. The LSMs are characterized by the streamwise wavelength to the order of 2δ - 3δ , where δ denotes the outer region length scale, e.g., the pipe radius or the boundary layer thickness, and span the entire outer region. The VLSMs, also known as superstructures in BLs, are significantly energetic and account for more than 40% of the total Reynolds shear stress and have a statistical streamwise coherence of the order of $\sim 10\delta$ for both internal and external wall-bounded flows (as shown in figure 1.6 [94]). These motions are correlated with the wall and, thus, influencing the inner region of the flow field, and in fact, (V)LSMs extend to the wall [31, 63, 64]. Although, according to the classical description, the near-wall turbulent structures are assumed to be independent of the outer region with distinct physical characteristics, especially in the limit of high Reynolds numbers, recent studies revealed dynamic interactions between the inner and outer

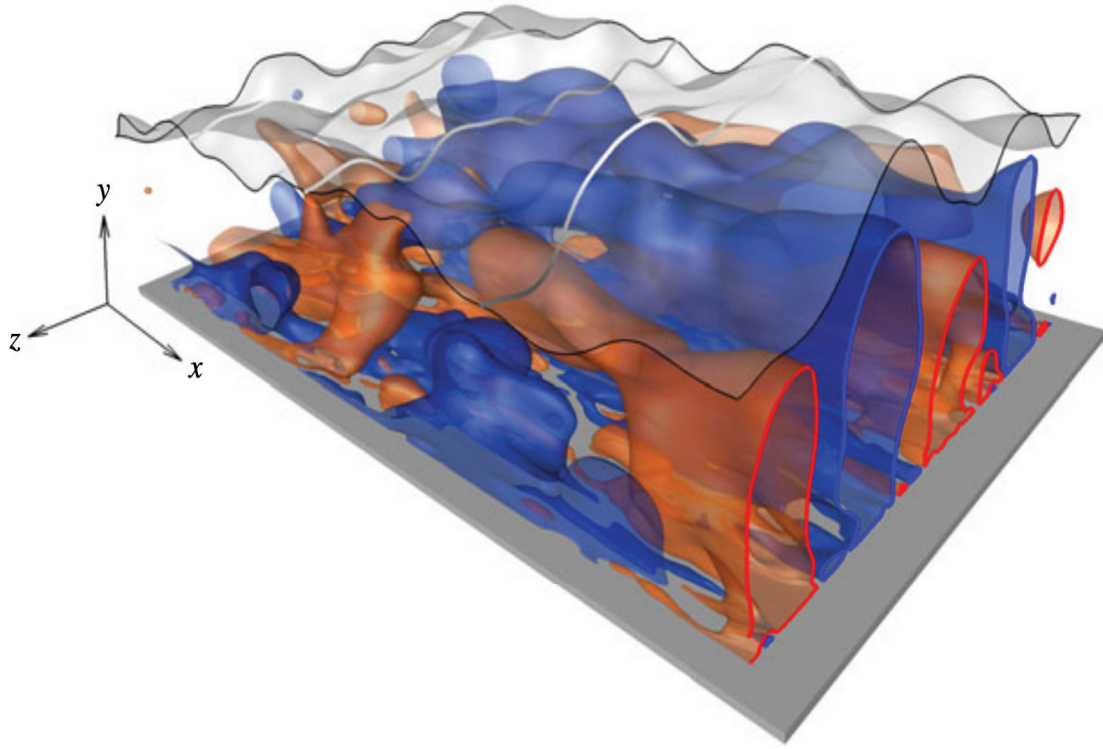


Figure 1.6: (Very) Large-scale turbulent motions within the outer region; blue and red contours, respectively, represent low- and high-speed motions. Figure from Ref. [94]

regions [110, 29, 61]. In experimental studies, it was observed the inner peak of streamwise turbulent intensity does not conform solely to inner scaling laws, suggesting the influence of outer flow dynamics [29, 103]. Later on, Hutchins & Maursic experimentally observed the VLSMs actively modulate the generation of near-wall turbulence, and this impact becomes more significant with Reynolds number [64]. This growing influence of (very) large-scale motions suggests that the small-scale turbulent fluctuations are becoming further inhomogeneous as the Reynolds number increases. This hierarchical structure, where the size of eddies scales proportionally with their distance from the wall, constitutes the dominant eddy framework that occupies the overlap or logarithmic layer in high Reynolds number flows. It forms the foundation of the attached-eddy hypothesis initially proposed by Townsend [155], with subsequent extensions outlined in Ref. [104]. Recent findings indicate that these self-similar eddies also undergo regeneration through a self-sustaining process that mirrors the dynamics occurring near the wall [66].

The dynamic interaction between inner and outer regions suggests their direct influence on the wall shear stress enhancement mechanisms and, hence, the total mean wall shear stress exerted on the wall. This enhancement is not merely limited to the wall shear stress but also to surface heat flux. Numerical studies by Hwang [65] revealed that by excluding the impact of the outer region motions, as the Reynolds number increases, the near-wall structures gradually contribute less to the overall mean wall shear stress. Later, Deck et al. [30] and De Giovanetti et al. [28] implemented spectral decomposition to determine the direct impact of LSMs, VLSMs, and the hierarchy of attached eddies on the wall shear stress. Their numerical investigation yields the increasing enhancement of wall shear stress generation by the motions as mentioned earlier at higher Reynolds numbers.

Non-zero pressure gradient flows

Turbulent boundary layers (BLs) experiencing streamwise pressure gradients are widespread in various engineering applications. Despite their significance, the impact of pressure gradients on the characteristics of wall-bounded turbulence remains unclear. One reason for this lack of detailed understanding is the absence of a systematic approach to characterizing pressure gradients and detecting the edge of the BL, where beyond that, the flow is assumed irrotational. In general, the effect of pressure gradient on turbulent BLs closely relates to their streamwise development, so it is crucial to establish and examine the concept of equilibrium.

According to Townsend's idealized definition [154], equilibrium is attained when all flow properties achieve self-similarity based on a consistent set of scaling variables, rendering the normalized flow independent of streamwise position. Self-similarity implies that profiles of a specific flow parameter measured at different locations exhibit identical shapes and can be collapsed onto a single form through appropriate normalization. The requirement for absolute equilibrium can be relaxed by semi-equilibrium (or approximate equilibrium [32]), which denotes a condition where the normalized flow changes gradually with streamwise position over distances much greater than the boundary layer thickness, often due to Reynolds number dependence.

In the context of two-dimensional turbulent BL with a non-zero pressure gradient, the state of equilibrium can be expressed by a parameter

$$\beta = \frac{\delta_1}{\tau_w} \frac{dP_e}{dx}, \quad (1.2)$$

referred to as the non-equilibrium Clauser parameter [24]. Here, δ_1 is the displacement thickness, and τ_w is the wall shear stress. Also, P_e denotes the edge pressure. The constraint of constant β is assumed to be necessary to approach (approximate) equilibrium in BL flows [32]. The Clauser parameter (β) can also be interpreted through the von Kármán momentum integral equation by looking into the streamwise change in the momentum defect

$$\frac{d}{dx} (\rho U_e^2 \delta_2) = \tau_w + \delta_1 \frac{dP_e}{dx}; \quad (1.3)$$

This parameter represents the ratio between the excess pressure force applied on the BL ($\delta_1 \frac{dP_e}{dx}$) (relative to potential flow solution) and wall shear stress (τ_w). In the above equation, U_e is the edge velocity in the streamwise flow direction, and δ_2 is the momentum thickness. It is important to note that while a constant β is a prerequisite for equilibrium behavior, turbulent BLs, even in zero-pressure-gradient scenarios, are not completely similar due to the inherent independence of the inner and outer flow scales. The potential for an equilibrium state in turbulent BLs under pressure gradients can be illustrated through similarity analyses outlined by several researchers, including Refs. [32, 20].

The presence of pressure gradients, whether adverse or favorable, serves as a source of non-equilibrium, thereby influencing the dynamics and behavior of turbulent boundary layers (BLs). The large-scale motions in the outer region have been observed to be sensitive to pressure gradient effects. For instance, Harun et. al using spectral and scale decomposition analysis noted that the turbulent large structures are more energetic under the APG effects [59]. Despite being more energized, they observed a similar spectral distribution of energy within the wake region of the flow, indicating that

the geometrical structure of the outer layer remains universal.

In BLs subjected to imposed APGs, deviations of the mean velocity profile within the logarithmic region were observed for both approximate equilibrium (constant β) and non-equilibrium flows [112, 14]. Additionally, the impact of APG on the stronger wake region has been documented [36]. Bobke et al. [14] further analyzed the effect of APG on Reynolds stress components through a series of high-fidelity numerical experiments on flat plates and the suction side of an airfoil. They observed that inner-scaled Reynolds stress components increase with higher levels of β . Specifically, the streamwise normal Reynolds stress develops a secondary peak within the outer layer; a peak that amplifies at higher β . On the other hand, the strength and location of the inner peak remain unchanged. Moreover, APG leads to a significant enhancement of the Reynolds shear stress within the outer layer, resulting in an increase in correlation between streamwise and wall-normal velocities and indicating a shift in the location and mechanism of turbulent production of kinetic energy [145]. APGs have been observed to induce changes in the dynamic of turbulent structures. Specifically, they lead to a reduction in the number and an increase in the distance of low-speed streaks within the viscous sublayer [95]. In addition, compared to ZPG BLs, the frequency of bursts in the inner region is reduced, whereas the frequency of sweeps events is increased [93]. As discussed above, the impact of APG on the outer region of the BL is more substantial; within the outer region, the presence of trains of the hairpin vertical structures and elongated low-momentum regions becomes more prominent compared with ZPG BLs [95].

While APGs have received considerable attention in research, there is a notable scarcity of experimental and simulation studies focusing on BL flows with favorable pressure gradients (FPG). FPGs entail flow acceleration in the flow's principal direction, resulting in a thinning of the BL thickness. When imposed on turbulent BLs, strong FPG also leads to a phenomenon known as the reversion process to a laminar state, as described by Narasimha et al. [117]. The first evidence of flow relaminarization under acceleration goes back to high-speed BLs experiments by Sternberg [149] on a cone. However, here, I limit our focus on flow acceleration in low-speed BLs, i.e., incompress-

ible regime. As elucidated by Narasimha et al. [117], the re-laminarization process entails the suppression of turbulence to such an extent that Reynolds stresses exert minimal influence on the mean flow. Consequently, the mean velocity profile deviates from the law of the wall, ultimately resulting in a drop in the skin friction coefficient. During the re-laminarization process, turbulent intensity may not necessarily decrease; the production rate of turbulent kinetic energy can remain higher than its dissipation. However, the dominance of pressure forces due to flow acceleration leads the Reynolds stress components to become frozen, rendering them irrelevant to the flow dynamics. Hence, the term “quasi-laminar” is taken by Ref. [117] to characterize this flow state. Several parameters have been proposed to quantify and predict re-laminarization under favorable pressure gradients (FPG). Patel [125] initially observed deviations in the streamwise velocity profile beyond the logarithmic region, a finding subsequently corroborated by other studies [177, 106]. Patel introduced a parameter to define the threshold for the breakdown of the logarithmic law as

$$\Delta p = \frac{\nu}{\rho u_\tau^3} \frac{\partial P_e}{\partial x}, \quad (1.4)$$

where ν is the fluid’s kinematic viscosity and u_τ represents the friction velocity. Patel proposed a limit of $\Delta p = -0.018$ for predicting re-laminarization. However, this value was later revised; Patel et al. [126] suggested that the non-dimensional shear stress gradient can offer a more universal criterion

$$\Delta \tau = \frac{\nu}{u_\tau^3} \frac{\partial \tau}{\partial y}. \quad (1.5)$$

They identified a critical value of -0.009 for the departure from the logarithmic law, indicating the onset of re-laminarization. Bradshaw [15] later revised the proposed value to $\Delta \tau = -0.013$, suggesting that it signifies the beginning of the logarithmic law overshoot rather than the initiation of the re-laminarization process. It is important to note that computing the wall-normal shear stress gradient $\partial \tau / \partial y$ presents challenges in the above equation. According to the literature, the examination of FPG and re-laminarization was primarily focused on flows over flat plates and overlooked

the influence of upstream APG on FPG effects. Initially, these effects were experimentally investigated in turbulent BLs over bumps and hills [157, 9, 10, 168], followed by numerical analyses on bump flows [177, 106]. Uzun & Malik [158] simulated the NASA wall-mounted hump using the wall-resolved large eddy simulation (LES) and observed the trend in the skin friction matches the empirical outputs of Greenblatt et al. [52]. Additionally, they examined re-laminarization under FPGs using the so-called re-laminarization parameter

$$K_{Lam} = \frac{\nu}{U_e^2} \frac{\partial U_e}{\partial x}, \quad (1.6)$$

and concluded this process was incomplete. Balin & Jansen [7] conducted a direct numerical simulation (DNS) of low-speed flow over a two-dimensional Gaussian bump with Reynolds number $Re_L = 1,000,000$ to examine the effects of alternating adverse and favorable pressure gradients. Consistent with prior studies, they observed deviations from the logarithmic law due to FPG effects and identified critical values of $\Delta p = -0.025$ and $K_{Lam} = 3 \times 10^{-6}$ to characterize the re-laminarization process, despite the flow remaining in the fully turbulent regime. Additionally, they observed the emergence of two internal layers resulting from the curvature changes on the bump surface, similar to the observation of Ref. [9]. The formation of distinct internal layers within the boundary layer suggests a decoupling between the inner and outer regions of the flow. This phenomenon was further evidenced by recent numerical experiments conducted by Uzun and Malik [160] on a Gaussian bump at Reynolds number $Re_L = 2,000,000$, where they observed an internal layer created in the FPG region behaving similarly to free shear layer. The internal flow near the wall behaves as a regular BL and is responsible for generating wall shear stress. Yet, far from the wall, flow behaves similarly to a free-shear flow (as described by Ref. [9]) influenced by local pressure gradients and surface curvature [7].

As discussed above, the generation of internal layers due to alternating favorable and adverse pressure gradients pertains to the flow history effects, which describe how upstream pressure gradients alter the turbulent statistics downstream. These history effects are known to make achieving simi-

larity between the inner-scaled statistics more difficult. This is one of the major challenges in developing robust turbulent models for non-equilibrium BLs. Bobke et al. [14] examined the history effects for APG BLs by comparing the inner-scaled mean velocity and Reynolds stress components of two distinct BLs with matching β and Reynolds number based on the friction velocity (Re_τ). Their findings indicated the large structures within the outer layer are less energetic under APG if the upstream pressure gradients throughout their streamwise development is weaker, i.e., weaker history effect. Additionally, their study suggested that Re_τ appears to inadequately capture the non-equilibrium effects, thus making it less feasible to observe similarity; however, the choice of Re_{δ_1} yields more robust similarity for two distinct BL, primarily because of its direct correlation with the definition of β .

Compressible flows and transformation

For the turbulent structures in compressible BLs, at least in the scope of this study, central to our present understanding is the hypothesis of Morkovin [113]. He postulated that density and enthalpy fluctuations do not significantly impact the turbulent time and length scales. This is often true for BLs below the hypersonic regime in which the turbulent Mach number is much lower than unity. Later, Spina and Smits [148] experimentally showed evidence that the influence of compressibility on turbulent large-scale organized structures is relatively minor for (relatively low Mach number) supersonic BLs. As such, our understanding of turbulence in compressible BLs often borrows heavily from our (comparatively more mature) understanding of incompressible turbulent BLs. This analogy between compressible and incompressible turbulent structures is the basis for developing mapping between compressible and incompressible boundary layers, e.g., predicting the mean velocity profile for compressible wall-bounded flows. Van Driest [161] introduced the very first successful transformation for adiabatic compressible wall-bounded flows. He postulated that the compressible turbulence obeys Prandtl's incompressible mixing length assumption. Hence the non-dimensional mean shear stress is independent of the Mach number. The concept

of Mach-number-independency signifies that one can integrate the non-dimensional mean shear stress to obtain the law of the wall. Van Driest transformation, however, is inaccurate for diabetics (with heat transfer) wall-bounded flows. To address this issue, more general mappings were proposed by asserting equilibrium in the inner layer energy cascade [184, 62]. Using this assumption, a Mach-independent non-dimensional mean shear stress as a function of semi-local wall-normal coordinate, y^{sl} was obtained, where the semi-local velocity scale $u^{sl} = \sqrt{\tau_w/\bar{\rho}(y)}$ and length scale $l^{sl} = \bar{v}(y)/u^{sl}$ are shown to yield more accurate transformation for the wall-normal distribution of turbulence. These so-called (quasi-) equilibrium transformations demonstrate a robust collapse of compressible datasets to the incompressible reference within the log layer, whereas its accuracy fails within the viscous sub-layer. To achieve an accurate mapping within the viscous sub-layer where the equilibrium assumption is not valid, Trettel & Larson [156] proposed a mean velocity profile scaling by neglecting the Reynolds shear stress and assuming that the total shear stress does not change with wall-normal distance in the wall units, y^+ . They asserted that the non-dimensional viscous stress –by friction velocity and wall units– is merely a function of the semi-local wall-normal coordinate, y^{sl} . Although mapping proposed by Ref. [156] demonstrated a robust method for wall-bounded flows in the viscous sub-layer, it over-predicts the compressible mean velocity profile within the logarithmic region, specifically in boundary layers in which the viscous shear stress is relatively low. Recently, Griffin et al. [54] proposed a mapping on the basis of equilibrium and viscous stress transformations. This mapping, referred to as total-stress-based transformation, decomposes the non-dimensional total mean shear stress as $\tau^+ = \tau_v^+ + \tau_t^+$, where the terms on the right-hand side denote the non-dimensional viscous and Reynolds shear stresses, respectively. Consequently, the total shear stress can be written as

$$\tau^+ = S^+ \left(\frac{\tau_v^+}{S_{TL}^+} + \frac{\tau_t^+}{S_{eq}^+} \right), \quad (1.7)$$

where S^+ is the generalized non-dimensional mean shear. This quantity demonstrates a robust Mach-independency across the whole inner layer for internal and external flows [54]. It is also

only a function of the semi-local wall-normal distance, y^{sl} . In Eq. (1.7), S_{TL}^+ and S_{eq}^+ are the non-dimensional mean shear stress proposed by Refs. [156] and [62], respectively. Note, Eq. (1.7) asymptotes to the Trettel & Larson transformation [156] close to the wall where $\tau^+ \rightarrow \tau_v^+$. However, within the log layer, where the equilibrium assumption is approximately valid and $\tau^+ \approx \tau_t^+$, $S^+ \sim S_{eq}^+$. This approach exhibits a general applicability to different types of wall-bounded turbulence. Using the transformation proposed by Ref. [54], it was observed that compressible velocity profiles collapsed to the high Reynolds number incompressible BL even if the wall is diabatic. All of the above methods accounted for distinct effects of compressibility on the viscous and Reynolds shear stresses to develop mappings. Another approach is to obtain a transformation from the similarities in integral methods. In this study, the author seeks mapping between the compressible and incompressible boundary layers on the basis of wall-normal integral methods.

1.2.3 Integral Equations

The previous sections reviewed the dynamics and motion of turbulent wall-bounded flows and discussed the turbulent structures in different regions of the flow. In addition, we discussed the influence of non-equilibrium effects like pressure gradient and compressibility on different turbulent scales. This section discusses the implementation of the integral methods to further study turbulence and its impact on the major engineering quantities such as skin friction.

The characterization of contributions from different scales required spectral decomposition in addition to a relationship that distinguishes the mean turbulent enhancement of the wall shear stress from the other flow phenomena. Such a relationship can be obtained using the wall-normal integral form of the Navier-Stokes equation (integral methods). The so-called FIK relationship, introduced by Fukagata, Iwamoto & Kasagi [46], was applied by Refs. [30, 28] to characterize the high-Reynolds-number turbulent wall-shear stress.

Integral methods in boundary layer flows are a fundamental and powerful approach used in fluid

mechanics and aerodynamics to analyze and understand the behavior of viscous fluids near solid surfaces. These methods employ integral equations derived from the fundamental equations of fluid dynamics, such as the Navier-Stokes equations. By integrating these equations at any station in the flow direction, from the solid surface into the outer flow, integral methods provide insights into crucial boundary layer parameters like skin friction, pressure distribution, and boundary layer thickness. Integral methods are precious when analytical or closed-form solutions are sought for practical engineering problems. They have been instrumental in the design of aerodynamic shapes, optimization of boundary layer control, and the development of high-performance aircraft and vehicles. Additionally, they serve as a bridge between theoretical analysis and experimental results, aiding in the validation and verification of numerical simulations and wind tunnel experiments in the study of boundary layer flows. For the wall-bounded flows, the integral methods are constructed based on integration in the wall-normal direction; hence, the complexity of transitional perturbations or turbulent fluctuations within the flow field is filtered over. However, their impact on surface friction or heat flux might be determined.

von Kármán equation

In boundary layers, the classic form of integral relation is the zeroth-order moment integral equation that is obtained by wall-normal integration of momentum deficit equation. This equation, referred to as von Kármán equation [165], reads

$$\frac{\tau_w}{\rho} = U_e^2 \frac{d\delta_2}{dx} + (\delta_1 + 2\delta_2) U_e \frac{dU_e}{dx}, \quad (1.8)$$

for incompressible BLs, where δ_1 and δ_2 are the displacement and momentum thicknesses, subscript e denotes the BL edge. The zeroth order moment integral equation for internal wall-bounded flows, e.g., channel or pipe flows, yields an explicit relationship between the wall-shear stress and the streamwise mean pressure gradient. Kármán-type integral equations also exist in compressible

BLs for the wall shear stress and surface heat flux. Eq. (1.8) is valid for laminar, transitional, and turbulent regimes. However, the information embedded within the Kármán type equations does not explicitly yield the mean turbulent enhancement of the wall shear stress.

Fukagata, Iwamoto & Kasagi equation

Fukagata, Iwamoto, and Kasagi [46] introduced an integral equation (original for internal flows), known as the FIK identity, that provides a relationship between the mean skin friction coefficient and distinct flow phenomena, namely the laminar, turbulent, and streamwise inhomogeneous contributions. Later on Peet & Sagaut [128] extended and generalized the FIK equation for three-dimensional complex wall shapes. The FIK identity is a result of three-fold integration, with the third integration carried across the half-height of the channel (δ), i.e., $\int_0^\delta dy \int_0^y dy \int_0^y dy$, of the streamwise momentum equation. The three-fold integration of the streamwise momentum equation is, in fact, equivalent to the second moment of the momentum equation through the Cauchy's formula of repeated integration

$$\int_a^b dx_n \int_a^{x_n} dx_{n-1} \dots \int_a^{x_3} \int_a^{x_2} dx_1 f(x_1) = \frac{1}{(n-1)!} \int_a^b dx (b-x)^{n-1} f(x). \quad (1.9)$$

By applying the three-fold integration or its alternative, the second moment of momentum, the viscous term in the Navier-Stokes equation is transformed from a second derivative of the mean velocity into the bulk velocity (flow rate), i.e., $U_b = 1/\delta \int_0^\delta \bar{u}(y) dy$. This is the primary outcome of triple integration, as the bulk velocity is a particular engineering quantity in internal flows through the definition of skin-friction coefficient $C_f = 2\tau_w/\rho U_b^2$. The FIK equation for fully-developed channel flow reads

$$C_f = \frac{12}{Re_b} + 12 \int_0^1 2(1-y) \left(-\overline{u'v'} \right) dy - 12 \int_0^1 (1-y)^2 (I_x) dy, \quad (1.10)$$

where Re_b is the Reynolds number based on the bulk velocity and half height of the channel. The first two terms on the right-hand side of Eq. (1.10) represent the laminar friction and turbulent enhancement. In contrast, the third term contains the inhomogeneous and transient contributions that are negligible in homogenous and statistically stationary flows, respectively. This way, the FIK identity represents a comparison between the skin friction coefficient in a turbulent channel flow to a laminar one at the same Re_b —the same flow rate in both regimes; the integral of the Reynolds shear stress quantifies the difference between two regimes.

Notably, the turbulence enhancement in the FIK equation is weighted linearly with the distance from the wall, a direct consequence of triple integration. This monotonically decreasing weight away from the wall qualitatively supports the previous observations about the impact of the turbulence structures at different distances from the wall on the wall-shear stress [46]. In principle, an integral form of the conservation equations can be constructed for any order [8]. Furthermore, the first-order moment yields

$$\frac{C_f}{4} = \frac{1}{Re_c} + \int_0^1 \frac{-\overline{u'v'}}{U_c^2} d\left(\frac{y}{h}\right), \quad (1.11)$$

where $C_f = 2\tau_w/\rho U_c^2$ and $Re_c = U_c h/\nu$, and U_c representing the centerline velocity. In Eq. (1.11), the turbulence enhancement (unweighted) represents the difference between the skin friction of turbulent and laminar regimes at the same Re_c . Therefore, the order of moment in the integral equation (alternatively, the sequence of successive integrations) determines the velocity scale that appears in the dimensionless equations. For internal flows, the original FIK identity is preferred since it yields the bulk velocity (flow rate). Fukagata et al. [46] further applied the three-fold integration to the mean equations governing the ZPG external flows and proposed an identity for BL flows

$$C_f = \frac{4(1 - \delta_1/\delta_{99})}{Re_{\delta_{99}}} + 4 \int_0^1 \frac{-\overline{u'v'}}{U_\infty^2} \left(1 - \frac{y}{\delta_{99}}\right) d\left(\frac{y}{\delta_{99}}\right) - 2 \int_0^1 \left(1 - \frac{y}{\delta_{99}}\right)^2 \frac{I_x \delta_{99}}{U_\infty^2} d\left(\frac{y}{\delta_{99}}\right), \quad (1.12)$$

where δ_{99} denotes the 99% BL thickness definition and $Re_{\delta_{99}} = U_{\infty}\delta_{99}/\nu$. Also, the boundary layer skin-friction coefficient C_f depends on the free-stream velocity

$$C_f \equiv \frac{\tau_w}{\frac{1}{2}\rho U_{\infty}^2}. \quad (1.13)$$

It is noticeable that there is no single term on the right-hand side of Eq. (1.12) that represents the true laminar friction in the same Reynolds number; the first term depends on the ratio of δ_1/δ_{99} , which is implicitly affected by turbulence. Thus, a critical shortcoming of the BL version of the FIK relation is its failure to isolate the laminar skin friction.

Later on, several derivations of the FIK equation were developed based on the triple integration for turbulent BLs [109, 108], even for non-equilibrium flows encountering pressure gradient [5]. The definition of C_f in BLs is based on the free-stream velocity, not the flow rate (U_b). This choice of velocity scale shows the inherent difference between BLs and channel flows; internal flows are characterized based on the pressure difference and flow rate. However, in BLs, the friction drag depends on the momentum deficit with respect to the free-stream velocity. Therefore, we must reflect engineering context in the analysis of friction or heat transfer. This difference was illustrated by Xia et al. [178], where they developed a twofold repeated integration for incompressible BLs inspired by FIK identity that yields

$$\begin{aligned} C_f = & \underbrace{\frac{2}{Re_{\delta_{99}}}}_{C_v} + 2 \underbrace{\int_0^1 (-\overline{u'v'}) dy}_{C_R} \\ & + 2 \underbrace{\int_0^1 (1-y) \left(-\frac{\partial \bar{u}\bar{u}}{\partial x} - \frac{\partial \bar{u}\bar{v}}{\partial y} - \frac{\partial \bar{p}}{\partial x} \right) dy}_{C_c} \\ & + 2 \underbrace{\int_0^1 (1-y) \left(\frac{1}{Re_{\delta_{99}}} \frac{\partial^2 \bar{u}}{\partial x^2} - \frac{\partial \overline{u'u'}}{\partial x} \right) dy}_{C_D}, \end{aligned} \quad (1.14)$$

where C_v and C_R denote the contributions of the viscous and Reynolds shear stresses, respectively, whereas C_C is the contribution of the mean convection term and C_D is the contribution from the mean streamwise derivatives. The twofold repeated integration technique, based on the FIK identity, was recently implemented to decompose the wall shear stress and surface heat flux in compressible BLs [170, 180]. The FIK identity for BLs is not constrained to ZPG BLs; Atzori et al. [5] developed a FIK formulation from the convective form of the governing equation to examine incompressible BLs undergoing adverse pressure gradient.

There are two major concerns regarding the FIK identity and its derivations. The first one is the linear weight of the turbulent enhancement based on the distance from the wall. The second concern is the mandate of truncating the wall-normal integral at $y/\delta_{99} = 1$, while there still could be fluctuation beyond that. The latter is especially critical at higher Reynolds numbers, for which the turbulence-induced excess friction is mainly generated within the logarithmic region, while the influence of buffer and wake regions gradually diminishes. Besides that, to the knowledge of the author, there is no clear physical explanation regarding the linear weighting.

Renard & Deck equation

Taking into account the above concerns regarding the FIK identity, Renard & Deck [135] proposed an integral equation based on the mean streamwise kinetic energy budget, $\bar{u}^2/2$, to decompose the skin friction coefficient of the wall-bounded flows. In order to preserve the power generated by the wall shear stress, they used the absolute frame of reference; the wall is moving at $-U_\infty$ and the undisturbed fluid outside of the BL has zero streamwise velocity. Note, the absolute frame for ZPG BLs over a flat plate is inertial since U_∞ is constant. The caveat, however, is this choice of reference frame. In contrast to flat plates, for complex geometries and non-equilibrium flows, such a frame of reference is not trivial. The mean streamwise kinetic-energy budget-based integral equation,

referred to as the RD relation, reads

$$\begin{aligned}
C_f = & \underbrace{\frac{2}{U_\infty^3} \int_0^\infty v \left(\frac{\partial \bar{u}}{\partial y} \right)^2 dy}_{C_{f,a}} + \underbrace{\frac{2}{U_\infty^3} \int_0^\infty -\overline{u'v'} \frac{\partial \bar{u}}{\partial y} dy}_{C_{f,b}} \\
& + \underbrace{\frac{2}{U_\infty^3} \int_0^\infty (\bar{u} - U_\infty) \frac{\partial}{\partial y} \left(\frac{\bar{\tau}}{\rho} \right) dy}_{C_{f,c}}.
\end{aligned} \tag{1.15}$$

In Eq. (1.15), the skin friction coefficient C_f denotes the mean power generated by the wall towards the fluid –in the absolute frame of reference. This power is diffused through the BL due to (molecular) viscosity, $C_{f,a}$. Note this term is not the skin friction that would be seen in a laminar flow at a matching Reynolds number. In other words, the RD decomposition cannot isolate the laminar friction as we saw in the FIK relation for internal flows. A portion of the mean power generated by the wall towards the fluid in the absolute frame is taken by turbulence through the production of turbulent kinetic energy, $C_{f,b}$. This term represents the local source of the excess turbulent friction that is dominated within the logarithmic region at higher Reynolds numbers. In other words, unlike the FIK identity that is claimed not to be able to predict the importance of the logarithmic region at higher Reynolds numbers, the RD relation addresses this matter via $C_{f,b}$ [135]. This term is expected to be the dominant contributor to the skin friction coefficient in high-Reynolds-number flows. In Eq. (1.15), $C_{f,c}$, originally, denotes the increase rate of absolute-frame mean streamwise kinetic energy. In other words, this is part of the skin friction power that does not dissipate or convert to turbulent kinetic energy. $C_{f,c}$, however, is written in terms of the wall-normal gradient of the mean total shear stress in Eq. (1.15). This form of $C_{f,c}$ simplifies the application of the RD relation on standard experimental and numerical datasets as it avoids the requirement of knowing the streamwise dependent information, e.g., streamwise derivatives.

The application of the RD equation is not limited to ZPG BLs. Fan et al. [41] applied the RD identity to incompressible turbulent BLs experiencing adverse pressure gradients. They observed as the Clauser parameter increases –a stronger adverse pressure gradient– the outer region dynamics

contribute more to the skin friction, whereas the inner region becomes less prominent. The RD decomposition has also been extended to compressible BLs [97] and hypersonic flows, including high-enthalpy effects [124]. Passiatore et al. [124] confirmed the validity of the compressible RD identity at relatively low Reynolds numbers and showed the contribution of $C_{f,a}$ is more substantial than $C_{f,b}$. Moreover, they exhibited that the presence of chemical reactions does not deteriorate the budget of the RD decomposition. The RD decomposition was also applied to interpret the higher wall-shear stress during the transition to turbulence rather than fully turbulent flow [105]; $C_{f,b}$ contribution to the skin friction is higher than fully turbulent flow because the production rate enhances within the transition zone populated by turbulent spots. This interpretation, however, depends on choosing the RD identity as the platform of the analysis. For example, selecting the FIK equation instead presumably leads to a different explanation. In other words, the interpretations based on different decompositions depend on the reference state that skin friction enhancement or reduction is compared with. Zhang et al. [183] pointed out this concept by examining the turbulent friction drag reduction in the numerical study of viscoelastic incompressible channel flows. They showed that implementing either the FIK or RD decompositions emphasizes different physical interpretations. Consequently, there are several different ways to decompose the skin friction coefficient or other engineering quantities, and the purpose of application must impose the identity to be used beforehand.

Angular momentum integral equation

Recall that in the FIK equation for BLs, the first (viscous) term no longer represents the skin friction of laminar flow. In other words, the FIK identity could not isolate the laminar friction at a matching Reynolds number. To resolve this matter, Elnahas & Johnson [38] introduced the angular momentum integral (AMI) equation that is built on the first-moment of momentum equation and applied it to numerical datasets of an H-type natural transition to turbulence and two bypass transitions by Refs. [176] and [129, 182]. This so-called AMI equation isolates the skin friction of

a ZPG laminar BL –similar to the first term in the right-hand side of the FIK identity of the internal flows. Therefore, a single viscous term gives the skin friction coefficient that would be seen in the ZPG laminar BL at a matching Reynolds number, e.g., Re_x , Re_{δ_1} , or Re_{δ_2} . Such a choice makes the other terms to be interpreted as enhancements or reductions with respect to the reference laminar case. This AMI’s property is non-trivial and depends on taking the first moment with respect to an axis located in an appropriate wall-normal distance, ℓ that is the center of action of the viscous force, i.e., the viscous torque about ℓ is zero. This concept mathematically reads

$$T_{v,\ell} = \int_0^\infty \nu(y - \ell) \frac{\partial^2 \bar{u}}{\partial y^2} dy = \frac{\ell \tau_w}{\rho} - \nu U_\infty = U_\infty^2 \ell \left(\frac{C_f}{2} - \frac{1}{Re_\ell} \right), \quad (1.16)$$

where $T_{v,\ell}$ denotes the viscous “torque” and Re_ℓ is the Reynolds number based on the length scale ℓ . For instance, by setting the viscous torque zero, $T_{v,\ell} = 0$, in incompressible laminar BLs, i.e., Blasius solution [12]

$$\frac{C_f}{2} \equiv \frac{1}{Re_\ell} = \frac{0.332}{\sqrt{Re_x}} = \frac{0.221}{Re_{\delta_2}} = \frac{0.571}{Re_{\delta_1}} = \frac{1.63}{Re_{\delta_{99}}} \quad (1.17)$$

that is varying with respect to the streamwise direction. Subsequently, the length scale ℓ is obtained as

$$\ell = 3.01 \sqrt{\frac{\nu x}{U_\infty}} = 4.54 \delta_2 = 1.75 \delta_1 = 0.613 \delta_{99}. \quad (1.18)$$

The AMI equation is derived by multiplying the streamwise momentum deficit equation by $(y - \ell)$ –the first moment– then integrating with respect to the wall-normal direction from $y = 0$ to $y \rightarrow \infty$. Thus, the AMI derivation of the AMI equation is somewhat similar to the Kármán-type equations; if $\ell \rightarrow \infty$, the AMI equation asymptotes to the well-known von Kármán momentum equation. With such a choice for ℓ , Elnahas & Johnson proposed a decomposition for skin friction coefficient,

known as the AMI equation that reads

$$\frac{C_f}{2} = \frac{1}{Re_\ell} + \int_0^\infty \frac{-\overline{u'v'}}{U_\infty^2 \ell} dy + \left\{ \frac{\partial \delta_2^\ell}{\partial x} - \frac{\delta_2 - \delta_2^\ell}{\ell} \frac{d\ell}{dx} \right\} + \frac{\delta_{2,v}}{\ell} + \frac{\delta_1^\ell + 2\delta_2^\ell}{U_\infty} \frac{\partial U_\infty}{\partial x} + \mathcal{I}_{x,\ell}, \quad (1.19)$$

where δ_2^ℓ and δ_1^ℓ are, respectively, the first-moment (or generalized form) of the momentum and displacement thicknesses [38]. The first term in the right-hand side of Eq. (1.19) represents the (equivalent) laminar skin friction at the matching Reynolds number. The other terms represent the contribution of different flow phenomena to the skin friction as torques about distance $y = \ell$ from the surface. For instance, the second term on the right-hand side of the AMI equation denotes the explicit turbulence enhancement, i.e., the contribution of Reynolds shear stress to the skin friction coefficient. This flow phenomenon acts as a counterclockwise torque about axis $y = \ell$ and reshapes the velocity profile in a way that increases the skin friction coefficient (Fig. 1.7 (a)). Conversely, another flow phenomenon –represented by the AMI equation– might act as a clockwise torque that reduces skin friction. For example, adverse pressure gradient is an example of clockwise torque as shown in Fig. 1.7 (b). The third term in the AMI equation is introduced as the rate of streamwise

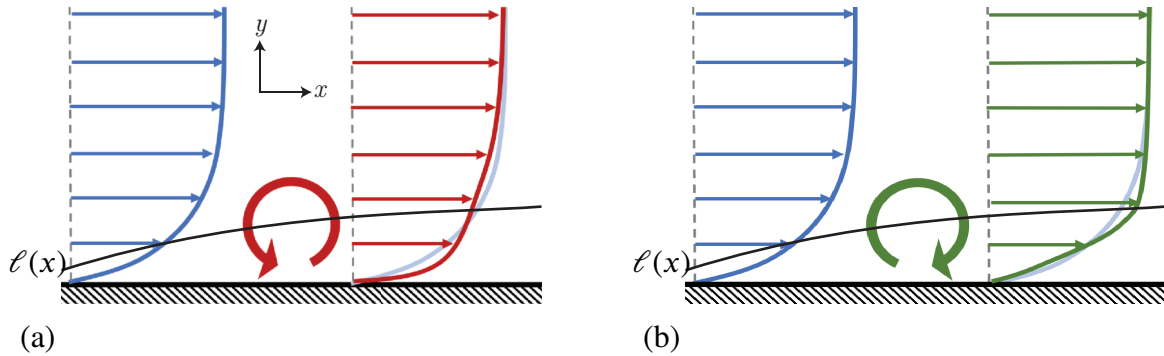


Figure 1.7: Schematic of applying torque with respect to axis $y = \ell$ (black solid line) to the blue velocity profile: (a) applying a counterclockwise torque, and (b) applying a clockwise torque.

growth of δ_2^ℓ relative to ℓ . The fourth term directly depends on the mean wall-normal flux of momentum thickness, $\delta_{2,v}$. It represents the redistribution of angular momentum through the mean flow away from the wall. Finally, the last term, $\mathcal{I}_{x,\ell}$, denotes the flow features often neglected in statistically stationary boundary layers [38].

It is worth mentioning that the AMI equation, Eq. (1.19) has responded to the concerns regarding the FIK identity for BL flows. Namely, with an appropriate choice of the length scale ℓ , one can isolate the laminar friction at a matching Reynolds number. Moreover, the concept of the first-moment integration with respect to axis $y = \ell$ is physically justified –imposing zero viscous torque– to avoid the not-physically-justified implementation of three-fold (or two-fold) integration in the FIK method. Also, the ambiguity of the linear weight of turbulence enhancement that was discussed by Ref. [135] is resolved in the AMI equation. Additionally, the AMI equation is built on the momentum deficit, so the wall-normal integration does not need to be truncated mathematically. This gives an advantage over the FIK identity for BLs in which the integration must be truncated at δ_{99} . Furthermore, the AMI equation provides a clear interpretation of other flow phenomena, including the effect of pressure gradient.

1.3 Research goal

The AMI equation is derived from the Navier-Stokes equation without any approximation or assumption. Thus, it can be applied to all boundary layer flows, even with complex configurations and geometries, e.g., non-equilibrium flows. The AMI equation provides a physical interpretation of flow phenomena above the wall and how they impact the skin friction coefficient relative to a based laminar flow. In this study, we seek to develop the first-moment integral equations, on the basis of the AMI equation, for boundary layer flows to decompose the skin friction coefficient and surface heat flux, subsequently to study the influence of different flow phenomena on these engineering quantities. One engineering application of first-moment integral equations is evaluating the flow control schemes. The integral equations have been extensively used to examine the effectiveness of control schemes on skin friction coefficient and surface heat flux [67, 121, 75, 150] and to explore the theoretical limit for friction drag reduction [83]. Since the first-moment integral equations based on the AMI approach provide an interpretation of different flow phenomena,

such as the explicit contribution of turbulence relative to a base laminar flow, it can be used as a tool to examine several active or passive control schemes on turbulent fluctuation (or transitional perturbations). The major research goals that are completed in this writing are the following:

1. Developing the first-moment integral equations for incompressible zero-pressure-gradient boundary layers with heat transfer to study the skin friction coefficient and Stanton number in transitional and turbulent regimes; investigating the peak surface friction and heat flux during the transition,
2. Applying the first-moment integral equation to non-equilibrium boundary layers, experiencing pressure gradient –adverse or favorable– to investigate the complexity between the effect of pressure gradient and turbulence on the skin friction coefficient. Developing a quantity to represent the pressure gradient strength based on the AMI equation, similar to the Clauser parameter. Investigating history effects in BLs encountering pressure gradient and how it impacts the turbulent structures,
3. Extending the first-moment integral equations to high-speed boundary layers and investigating the impact of compressibility, turbulence, and other flow phenomena on the skin friction coefficient and Stanton number. Exploring the skin friction coefficient and Stanton number mapping between compressible and incompressible BLs using the first-moment integral equation,
4. Developing a basis for the other applications of the first-moment integral equations beyond a post-processing tool. This includes modifying the AMI equation to examine flow control schemes.

1.3.1 Thesis Outline

The thesis is organized as follows. Chapter 1 developed the motivation of the topic and, later on, provided the related previous studies and discussed what needs to be done in the future. In Chapter 2, the governing equations to model the physics of flow fields are stated. This is followed by the numerical schemes implemented to discretize and solve the given governing equations, as well as post-processing methods for the first-moment integral analysis in Chapter 3. Chapter 4 extends the first-moment integral equation to incompressible boundary layers with heat transfer and discusses how different flow phenomena impact the friction drag and surface heat flux during the transition and in early turbulence. Chapter 5 extends the angular momentum integral analysis to non-equilibrium turbulent boundary layers with non-zero pressure gradients. This chapter also discusses more complex BLs, such as flows over an airfoil and a two-dimensional bump surface, to examine the mild surface curvature effects on the turbulent enhancement. Chapter 6 introduces the first-moment integral equations to high-speed boundary layers for the skin friction coefficient and Stanton number, considering the variation of fluid density, viscosity, and thermal conductivity. In Chapter 7, we introduce the other applications of the first-moment integral analysis beyond using it as a post-processing analysis tool. In this chapter, the concept of using the AMI analysis to evaluate a flow control scheme is examined. Additionally, using this concept to develop computationally efficient turbulent models will be discussed.

Chapter 2

Governing Equations

This chapter covers the Navier-Stokes (NS) equations governing the physics of the fluid flow based on conservation principles and the integral relations derived from them. The conservation equations for viscous flows are provided in 2.1, in which the physical interpretation of each term is discussed. Taking the NS equations and applying some mathematics works, the integral equations are derived and elaborated.

2.1 Equation of Motion – Fluid Flow

The governing equations for fluid flows expressed in the conservative form within the three-dimensional Cartesian coordination system –using index notation– read

$$\frac{\partial \rho}{\partial t} + \frac{\partial}{\partial x_i}(\rho u_i) = 0 \quad (2.1)$$

for mass (or continuity), and

$$\frac{\partial}{\partial t}(\rho u_i) + \frac{\partial}{\partial x_j}(\rho u_i u_j) = -\frac{\partial p}{\partial x_i} + \frac{\partial \tau_{ij}}{\partial x_j} + \rho f_i^B \quad (2.2)$$

for momentum with body force component f_i^B , where $i = 1, 2$, or 3 . In the above equations, ρ is the fluid density. u_i represents a component of the velocity vector, $\mathbf{u} = (u, v, w)$. p is the thermodynamic pressure causing fluid-static stress on the fluid element, whereas τ_{ij} is the deviatoric stress tensor representing the fluid-dynamic contributions –an approximate since p is only well-defined for equilibrium conditions. For an isotropic flow, the stress-strain rate constitutive relationship is independent of the orientation of the coordinate system. Moreover, τ_{ij} is symmetric, $\tau_{ij} = \tau_{ji}$, hence

$$\tau_{ij} = 2\mu \left(S_{ij} - \frac{1}{3} S_{kk} \delta_{ij} \right) + \mu_v S_{kk} \delta_{ij}, \quad (2.3)$$

where $S_{ij} = \frac{1}{2} \left(\frac{\partial u_i}{\partial x_j} + \frac{\partial u_j}{\partial x_i} \right)$ is the strain rate tensor, also μ and μ_v are the fluid dynamic viscosity and bulk viscosity, respectively; the kinematic viscosity is defined as $\nu = \mu/\rho$. The constitutive relation, (2.3), is valid for Newtonian fluid in which there is a linear relationship between the stress and strain rate tensor components.

The physics of a fluid flow requires a balance of heat transfer and kinetic and internal energy. To complete the governing equations, the differential conservation of energy –in conservative form– reads

$$\frac{\partial}{\partial t} \left(\rho \left[h + \frac{1}{2} u_i u_i \right] \right) + \frac{\partial}{\partial x_j} \left(\rho \left[h + \frac{1}{2} u_i u_i \right] u_j \right) = \frac{\partial p}{\partial t} + \rho f_i^B u_i + \tau_{ij} \frac{\partial u_i}{\partial x_j} + u_i \frac{\partial \tau_{ij}}{\partial x_j} - \frac{\partial q_i}{\partial x_i}, \quad (2.4)$$

where h and $\frac{1}{2} u_i u_i$ represent flow's enthalpy and kinetic energy, respectively; using the definition of total (or stagnation enthalpy) $H = h + \frac{1}{2} u_i u_i$ the above equation might be written in terms of H . The first two terms in the right-hand side of Eq. (2.4) represent work by body force and viscous stress, respectively. q_i is a component of the heat flux vector, including thermal conduction and radiation;

the radiation heat flux is often neglected unless the static temperature is enormous. Neglecting radiation, thus, heat flux is modeled as $q_i = -k \frac{\partial T}{\partial x_i}$ based on Fourier's law for heat conduction, where T is static temperature and k is the fluid's thermal conductivity.

Equation of state for perfect gas

A relation defining one state function, such as pressure or internal energy, in terms of two or more others is called an equation of state. For a compressible fluid flow composed of a single component—the subject of this study—the specification of two independent thermodynamic quantities determines the state of the system. For instance, in such a system, the equation of state for pressure is $p = p(\rho, T)$. The equation of state is simplified to $pV = Nk_B T$ using the perfect (or idea) gas assumption for N identical noninteracting gas molecules confined within a container with volume V , where k_B is the Boltzmann's constant. The perfect gas assumption is valid as long as attractive forces between the molecules are negligible and V/N is much greater than the volume of an individual gas molecule.

Kinetic theory and statistical mechanics analysis justified the assumption that at ordinary temperatures and pressures, most gases can be modeled as perfect gases. This assumption has been prevalently implemented in studying gas dynamic systems unless temperature and pressure are, respectively, extremely low and high. Using the perfect gas assumption, one can relate enthalpy to temperature using the definition of constant specific heat $c_p = (\partial h / \partial T) |_{\text{constant pressure}}$. If the flow is further assumed to be calorically perfect for which c_p does not vary with temperature, enthalpy is simply $h = c_p T$. Note the calorically perfect assumption is limited to perfect gases away from extremely high (the specific heat capacities may change significantly) or low (quantum effects become important) temperatures. In this work, the author models compressible fluids, like air, as thermally and calorically perfect gases using the equation of state $p = \rho RT$ to relate pressure, density, and temperature, where R is the gas constant that reads $R = 287 \text{ J/kgK}$ for dry air at ordinary temperatures.

2.1.1 Averaged Equations

For transitional and turbulent flows, the mean (or expected) flow field is of more interest to predicting the flow behavior for engineering and scientific applications. For instance, knowledge of the mean allows one to determine the average lift and drag on an airfoil or the pressure drop in a pipe. Also, friction drag and surface heat flux depend on the mean velocity and temperature gradients, respectively. Therefore, much effort has been directed towards determining the expected values of transitional and turbulent flow fields. In this section, the governing equations provided in Section 2.1 are (time) averaged to obtain a partial differential equation for the mean field, referred to as Reynolds-averaged Navier–Stokes (RANS) equations.

Incompressible Flow

In incompressible flows with constant density, viscosity, and thermal conductivity, one can simplify the governing equation discussed in 2.1; $S_{kk} = \nabla \cdot \mathbf{u} = 0$, and hence the fluid-dynamic stress rate tensor reduces to $\tau_{ij} = 2\mu S_{ij}$.

For transitional and turbulent flows, one can obtain the RANS equations by taking the mean of the NS equations discussed in Section 2.1. To do so, the instantaneous flow quantities must be decomposed into the mean and fluctuation (or perturbation for transitional flows) components. For example, the instantaneous velocity vector is $\mathbf{u} = \bar{\mathbf{u}} + \mathbf{u}'$ in which $(\bar{\cdot})$ and (\cdot') represent the mean and fluctuation components of flow quantities, respectively. Besides that, In incompressible flows, density, viscosity, and thermal conductivity are constant. $S_{kk} = \nabla \cdot \mathbf{u} = 0$ from (2.1), and hence the the fluid-dynamic stress rate tensor reduces to $\tau_{ij} = 2\mu S_{ij}$. Consequently, The RANS equation yield

$$\frac{\partial \bar{u}_i}{\partial x_i} = 0, \tag{2.5}$$

for mass conservation and

$$\frac{\partial \bar{u}_i}{\partial t} + \frac{\partial}{\partial x_j} (\bar{u}_i \bar{u}_j) = -\frac{1}{\rho} \frac{\partial \bar{p}}{\partial x_i} + \nu \frac{\partial^2 \bar{u}_i}{\partial x_j \partial x_j} - \frac{\partial \overline{u'_i u'_j}}{\partial x_j}, \quad (2.6)$$

for momentum conservation (without body force). The averaged energy equation is further simplified for incompressible flows; enthalpy is substantially larger than kinetic energy, $h \gg \frac{1}{2} u_i u_i$, and fluid's density and conductivity are constant. Given the assumption above for incompressible flows, the energy equation is simplified to

$$\frac{\partial \bar{T}}{\partial t} + \frac{\partial (\bar{u}_i \bar{T})}{\partial x_i} = \alpha \frac{\partial^2 \bar{T}}{\partial x_i \partial x_i} - \frac{\partial (\overline{u'_i T'})}{\partial x_i}, \quad (2.7)$$

in terms of the temperature field, where $\alpha = k/c_p \rho$ is the fluid's thermal diffusivity. In incompressible flows (neglecting the Boussinesq Approximation [147]), the energy equation is uncoupled from the momentum equation. In other words, the temperature field does not impact the velocity field.

Note, the RANS Eqs. (2.5), (2.6), and (2.7) appear nearly identical to the NS equations except for the term involving $-\overline{u'_i u'_j}$ in momentum conservation (and $-\overline{u'_i T'}$ in energy equation). In Eq. (2.6) $-\overline{u'_i u'_j}$ is a second-order tensor, referred to as the Reynolds (or turbulent) stress tensor, which represents the explicit contribution of turbulence on momentum transport alongside with viscous effects. Similar to deviatoric stress tensor τ_{ij} , the Reynolds stress is also symmetric. The RANS equation is a manifestation of the closure problem, i.e., there are more unknowns than equations. Hence, the system is unclosed. In general, the set of equations governing the evolution of statistical quantities (obtained from the NS equations) will always be unclosed. As a consequence of the closure problem, modeling of some statistical quantities, e.g., the Reynolds stress, is a subject of major turbulence research studies.

Compressible Flow

For compressible flows, density is not constant. To alleviate the complexity caused by non-constant density in RANS equations, the density-weighted (Favre) averaging, introduced by Favre [42], can be applied. The Favre average of a flow quantity f is defined as

$$\tilde{f} = \frac{\overline{\rho f}}{\bar{\rho}}. \quad (2.8)$$

The fluctuation component is the difference between a Favre average quantity and its instantaneous value, e.g., $f'' = f - \tilde{f}$. Throughout this report, the Favre average flow quantities and their fluctuations are represented by $(\tilde{\cdot})$ and (\cdot'') , respectively to be distinguished from regular (time) average quantities discussed in the previous section. Analogous to the RANS equation, we derive the Favre averaged equations for the mean flow and turbulent quantities. Note that Favre averaging is applied for the velocity and temperature (and enthalpy) fields, whereas density and pressure are not Favre averaged. Thus, we impose the following decomposition on the NS equations to obtain the averaged equations

$$\begin{aligned} u_i &= \tilde{u}_i + u_i'', & \rho &= \bar{\rho} + \rho' \\ p &= \bar{p} + p', & h &= \tilde{h} + h''. \end{aligned}$$

The averaged NS equations without body forces are simplified to

$$\frac{\partial \bar{\rho}}{\partial t} + \frac{\partial}{\partial x_i} \bar{\rho} \tilde{u}_i = 0, \quad (2.9)$$

for continuity,

$$\frac{\partial}{\partial t} \bar{\rho} \tilde{u}_i + \frac{\partial}{\partial x_j} \bar{\rho} \tilde{u}_i \tilde{u}_j = -\frac{\partial \bar{p}}{\partial x_i} + \frac{\partial}{\partial x_j} \left(\bar{\tau}_{ij} - \bar{\rho} \widetilde{u_i'' u_j''} \right) \quad (2.10)$$

momentum, and

$$\frac{\partial}{\partial t} (\bar{\rho} \tilde{H}) + \frac{\partial}{\partial x_j} (\bar{\rho} \tilde{H} \tilde{u}_j) = \frac{\partial \bar{p}}{\partial t} + \overline{\tau_{ij} \frac{\partial u_i}{\partial x_j}} + \overline{u_i \frac{\partial \tau_{ij}}{\partial x_j}} + \frac{\partial}{\partial x_j} \left(\overline{k \frac{\partial T}{\partial x_j}} \right) \quad (2.11)$$

total enthalpy conservation, respectively.

Chapter 3

Computational Methods

In this chapter, the numerical schemes used to develop high-performance computing software to simulate incompressible transitional boundary layers are elaborated. This software was originally developed at Stanford University [100]. The first section discusses the numerical techniques to computationally discretize and integrate incompressible transitional and turbulent wall-bounded flows.

Besides the computational methods to integrate the governing equations, later in this chapter, we introduce the computational schemes applied to post-process the transitional and turbulent boundary layer datasets, namely for the integral equations.

3.1 Incompressible Flow Field

Prior to the numerical scheme, we must introduce a dimensionless form of the governing equations. In computational fluid dynamics (CFD), the Navier-Stokes equations are written and integrated in a dimensionless form using the appropriate characteristic velocity and length scales. These characteristics are problem-dependent, i.e., given the nature of the flow, one can choose a different set of

scales. For incompressible flows, the dimensionless form of the Navier-Stokes equations equation reads

$$\frac{\partial u_i}{\partial x_i} =, \quad (3.1)$$

for continuity, and

$$\frac{\partial u_i}{\partial t} + \frac{\partial u_j u_i}{\partial x_j} = -\frac{\partial p}{\partial x_i} + \frac{1}{Re} \frac{\partial u_i}{\partial x_j x_j}, \quad (3.2)$$

for momentum conservation. Here, Re is the Reynolds number defined by the given velocity and length scales, $Re = UL/\nu$. Also, the base mean pressure is absorbed as a body force in the momentum equation. Note, in incompressible flows, that absolute pressure is indeterminate in incompressible flows, and only its gradients can be computed. We choose the BL free-stream velocity, U_∞ , and the flat plate streamwise length, L , as the velocity and length scales, respectively, hence the reference Reynolds number is $Re = U_\infty L/\nu$.

Numerical scheme

To computationally solve Eq. (3.2) for boundary layer flows developing on a flat-plate, we employ direct numerical simulation (DNS) on a three-dimensional staggered grid system, aiming to enhance coupling between the velocity components and the pressure gradient as proposed by Harlow and Welch [58]. In this approach, considering a three-dimensional cell, the pressure is computed and stored at the center of a cell. Meanwhile, the velocity components are computed at the faces of the cell corresponding to their direction. For instance, the x -velocity component is stored at the vertical faces of a cell as shown in Fig. 3.1 for a two-dimensional staggered system). This arrangement facilitates the evaluation of the pressure gradient with second-order accuracy. It involves using central finite differences for all the spatial discretization, considering two neighboring points for each velocity component. A fully explicit scheme is implemented for all the advection

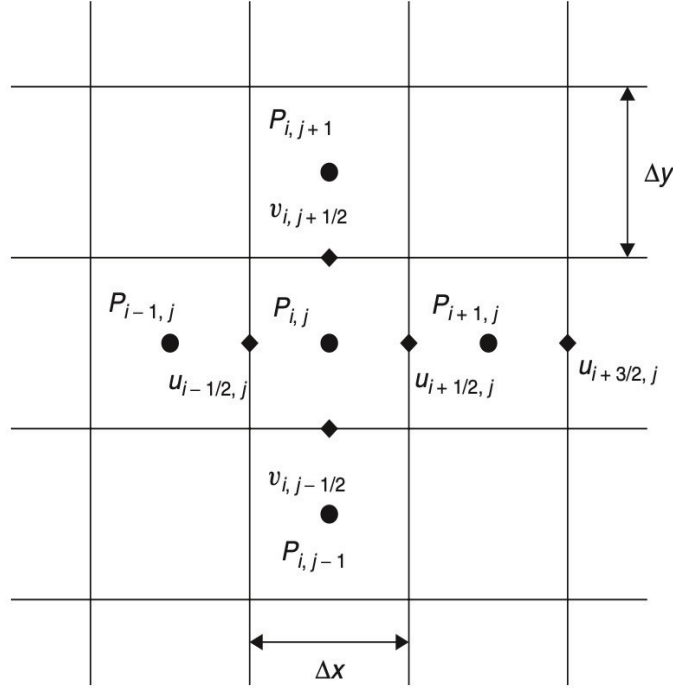


Figure 3.1: Two-dimensional staggered grid system; pressure is located at the center of a cell, and velocities are at the faces.

and diffusion terms in Eq. (3.2) using the fractional-step method [84]. Using the fractional-step method we can interpret the role of pressure in the momentum equations as a projection operator. In other words, exploiting the continuity constraint pressure projects an arbitrary vector into a divergence-free velocity field. Therefore, following Ref. [84], a two-step time integration of Eq. (3.2) can be implemented. In the first step, we omit the pressure gradient and explicitly solve for the predicted velocity (\hat{u}_i),

$$\frac{\hat{u}_i - u_i^n}{\Delta t} = -\frac{\partial u_j^n u_i^n}{\partial x_j} - \frac{1}{Re} \frac{\partial u_i^n}{\partial x_j x_j}, \quad (3.3)$$

where superscript n and Δt denote the index of the time step and time-step size, respectively. The velocity field in the next time step, $n + 1$, is obtained using the corrector step

$$\frac{u_i^{n+1} - \hat{u}_i}{\Delta t} = -\frac{\partial \phi}{\partial x_i}, \quad (3.4)$$

where ϕ here is the pseudo-pressure field. Note, the (corrected) velocity field must satisfy the continuity, $\partial u_i^{n+1} / \partial x_i = 0$. Therefore, pseudo-pressure ϕ can be computed by solving a Poisson equation that is obtained by taking the divergence of the above equation. This Poisson equation for pressure projection reads

$$\frac{\partial^2 \phi}{\partial x_i \partial x_i} = -\frac{1}{\Delta t} \frac{\partial \hat{u}_i}{\partial x_i}, \quad (3.5)$$

where the right-hand side is known at each time step. Knowing the predicted velocity and pseudo-pressure fields, we can substitute them in Eq. (3.4) to compute the velocity field in the advanced time step, $n + 1$. To solve the system of equations in pressure projection, I utilized the Linear Algebra PACKage (LAPACK) library in Fortran. Additionally, Fast Fourier Transform (FFT) was employed in the periodic spanwise direction to enhance computational efficiency and accuracy. These methods collectively provided robust and reliable solutions for the pressure projection equations, ensuring efficient computation of the flow variables in the simulation domain.

It is worth mentioning that since a fully explicit scheme was applied in the software ([100]), the pseudo-pressure, ϕ , and original pressure, p , are equivalent. However, if one uses an implicit (or a semi-implicit) numerical scheme, like the Crank-Nicholson Adam-Bashforth method, the original (or true) pressure must be computed from

$$p = \phi + \frac{\Delta t}{2Re} \frac{\partial^2 \phi}{\partial x_2^2}; \quad (3.6)$$

however, this correction relation is an order of $\mathcal{O}(Re)$, and hence could be assumed negligible for high Reynolds numbers [84].

In this study, time integration for both predictor and corrector steps is performed using an explicit third-order Runge-Kutta (RK3) scheme, as described in Ref. [122]. Assuming numerical time

integration of an equation as

$$\frac{d\psi}{dt} = g(\psi, t), \quad (3.7)$$

where ψ and g are known in time step n , ψ^{n+1} can be computed following these steps

$$\begin{aligned} \psi' &\equiv \psi^n + a\Delta t g^n \\ \psi'' &\equiv \psi' + b\Delta t f(\psi^A, t_n + A\Delta t) \\ \psi^{n+1} &\equiv \psi'' + c\Delta t g(\psi^B, t_n + (a+B)\Delta t). \end{aligned} \quad (3.8)$$

In the above steps $\psi^A \equiv \psi^n + A\Delta t g^n$ and $\psi^B \equiv \psi' + B\Delta t g(\psi^A, t_n + A\Delta t)$, where t_n denotes time in n^{th} step. Also, the RK3 coefficients are

$$a = \frac{1}{4}, \quad A = \frac{8}{15}, \quad B = \frac{5}{12}, \quad c = \frac{3}{4}. \quad (3.9)$$

Boundary Conditions

For an incompressible boundary layer flow, no-slip, no-penetration boundary conditions are imposed at the wall. To initialize the flow within the domain, the laminar Blasius solution, accurately interpolated at the wall-normal grid points using suitable flow scales, is superimposed with H-type temporal instability obtained derived from the parabolized stability equation [100]. This induced instability mode amplifies downstream, facilitating the transition to a fully turbulent regime. The outflow is modeled based on the linearized Navier-Stokes equation with the convective velocity. To ensure a proper outflow condition, the linearized Navier-Stokes equation with the convective velocity is employed. Finally, at the upper boundary of the computational domain, the flow variables gradually approach the scaled laminar Blasius solution, maintaining consistency with the overall flow behavior.

Parallel Architecture

The parallelization of the Fortran DNS BL code is handled by the message passing interface (MPI) merely in the spanwise z -direction where the flow is periodic. Subtracting two from the total number of grid points in the spanwise direction, the resulting must be divisible by the number of the machine's processors. Therefore, the total number of spanwise planes allocated to each processor is $(n_z - 2) / n_p$, where n_z and n_p denote the total number of grid points in z -direction and total number of processors, respectively. To simulate BLs at high Reynolds numbers, the DNS BL code might be further parallelized in the other two directions, namely the wall-normal and streamwise directions, to reduce the computational cost.

3.2 Boundary Layers Post-processing

Identifying the edge of the boundary layer

In the realm of both experimental investigations and simulations involving viscous flows, it is vital to possess the capability to establish and calculate the boundary layer thickness, denoted as δ . This refers to the distance perpendicular to the surface where viscous influences become non-negligible. Furthermore, the definition of δ becomes essential for the calculation of integral quantities characterizing the boundary layer. For instance, it is required for the determination of the displacement thickness δ_1 and momentum thickness δ_2 , respectively, to represent the length scales associated with near-wall mass and momentum deficits. These measurements are the building blocks of integral equations for BLs, e.g., AMI or Karman-type equations. Therefore, using a robust but user-friendly approach to obtain the boundary layer thickness and the edge velocity and pressure is of paramount importance in the accuracy of integral equations.

Although calculating δ is a relatively straightforward task for canonical equilibrium flows, e.g.,

zero-pressure-gradient (ZPG) BLs, no established definitions exist for more complex non-equilibrium ones. Also, even for simple ZPG flows, the nature of the integral methods was observed to be remarkably sensitive to the determination of the BL edge and outer scale velocity. In ZPG BLs, the velocity field approaches the edge velocity as the wall-normal distance $y \rightarrow \infty$. The thickness $\delta_{n\%}$ is defined as the location where $n\%$ of edge velocity is attained, that is

$$\frac{u}{U_e} \Big|_{y=\delta_{n\%}} = \frac{n}{100}, \quad (3.10)$$

where $n = 99\%$ is a common choice. This procedure, however, is not applicable to boundary layers encountering pressure gradients or complex geometries. For example, for flows around an airfoil—a complex geometry—the above definition cannot distinguish the viscous region within the BL from the inviscid flow since it also features a wall-normal velocity gradient. In other words, for non-equilibrium flows, the (mean) flow field does not approach a constant asymptote at the edge. In this section, we discuss the so-called local-reconstruction method introduced by Griffin et al. [53] to predict the BL thickness and obtain the BL edge quantities as well as the counterpart inviscid streamwise velocity field, U_i . This method is established based on the application of the Bernoulli equation in the wall-normal direction. The local-reconstruction method proposed key features despite many other methods such as mean-vorticity based [25, 159, 151] and mean-shear threshold techniques [4], it does not require numerical integration or differential to determine the edge of the boundary layer. Also, the computation of the boundary layer thickness in a non-iterative process reduces the computational cost. Additionally, this method is versatile for a wide range of Reynolds numbers and free-stream flow conditions (with or without free-stream turbulence). Finally, the local reconstruction only requires the mean velocity profiles (\bar{u} and \bar{v}) and the mean pressure profile (\bar{p}) as inputs. Thus, it can be readily applied to both numerical and experimental datasets. In conclusion, this method is robust versatile, and computationally efficient to locate the edge of the BL and to compute the outer scale velocity.

The local-reconstruction method defines the boundary layer thickness as

$$\frac{u}{U_i} \Big|_{y=\delta_n\%} = \frac{n}{100}, \quad (3.11)$$

where $U_i(y)$ is the inviscid mean streamwise velocity profile. Note, for ZPG boundary layers, both (3.10) and (3.11) are equivalent. Generally, the inviscid velocity profile can be determined by solving the Euler equations while imposing no-penetration boundaries, which are shaped according to the local displacement thickness computed through a viscous simulation. However, this approach becomes impractical due to the interdependence between the displacement thickness and the boundary layer thickness. Alternatively, the local reconstruction method introduces a straightforward and computationally efficient technique to construct the inviscid solution. For steady incompressible BLs, the local-reconstruction method starts with the definition of the total (stagnation) pressure

$$P_o = \bar{p} + \frac{1}{2}\rho \left(\bar{u}^2 + \bar{v}^2 \right), \quad (3.12)$$

assuming the mean wall-normal velocity (\bar{v}) and (static) pressure (\bar{p}) are equal to their inviscid solution counterparts; the no-penetration boundary condition is imposed to both inviscid and viscous simulations. However, the no-slip boundary condition is only relevant in the context of viscous flows. Consequently, the reconstructed inviscid streamwise velocity profile, U_i , exhibits deviations in the vicinity of the wall, where viscous effects hold sway. Conversely, the mean wall-normal velocity and pressure profiles exhibit substantially weaker reliance on viscous effects, justifying the above assumption. Taking into account the (presumptive) irrotational inviscid flow with wall-normal velocity and pressure profiles, respectively, equivalent to \bar{v} and \bar{p} —from the viscous flow—the Bernoulli equation might be approximated globally rather than only along the streamlines. Thus, the streamwise inviscid velocity at each streamwise location is reconstructed as

$$U_i = \pm \sqrt{\frac{2}{\rho} [P_{o,\text{Ref}} - \bar{p}] - \bar{v}^2}, \quad (3.13)$$

where the sign of U_i must be compatible with the mean streamwise velocity at the edge of the BL, $\bar{u}(y = \delta)$. One can choose $P_{o,Ref} = \text{Max} [P_o]$; recall, the total pressure is a measurement of the flow's capacity to do work. Naturally, it diminishes closer to the wall due to the viscous effects, hence choosing $P_{o,Ref} = \text{Max} [P_o]$ guarantees the robustness of the method. Also, P_o is expected to remain constant at $y \geq \delta$. This is shown in Figure 3.2 (a) for NACA-4412 airfoil at two different streamwise locations experiencing moderate “o” and strong “*” pressure gradient, respectively. According to Figure 3.2 (b), the reconstructed inviscid velocity profile, U_i , agrees with the mean velocity profile, \bar{u} , outside of the BL, where the flow is approximately irrotational. In Fig. 3.2 (b), the red dotted-line depicts δ_{99} thickness predicted by local-reconstruction method, where $\bar{u}/U_e = 0.99$.

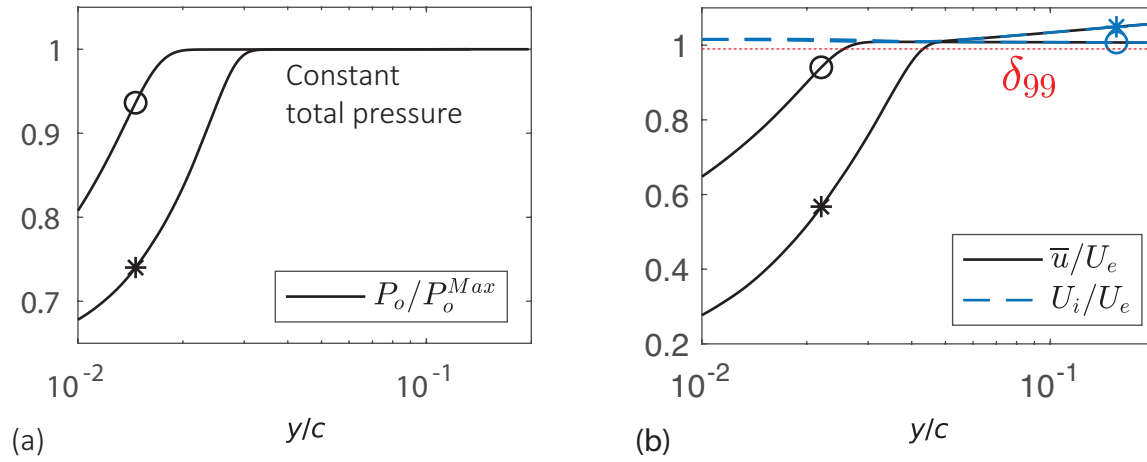


Figure 3.2: Normalized total pressure (a), and velocity profiles (mean and inviscid) in the wall-normal direction for flow over NACA-4412 airfoil. Symbols “o” and “*” denote two streamwise stations with moderate and strong pressure gradients, respectively. The red dotted line in (b) represents δ_{99} . c here is the chord length.

The local-reconstruction method can be extended for compressible boundary layers by using the total (stagnation) enthalpy, H , instead of the P_o . The total enthalpy is constant outside of the BL if the free-stream is irrotational and adiabatic. Similar to Eq. (3.13) for incompressible flows, the inviscid compressible velocity profile is reconstructed as

$$U_i = \pm \sqrt{2 \left[H_{Ref} - \bar{h} \right] - \bar{v}^2}, \quad (3.14)$$

where, similarly, $H_{\text{Ref}} = \text{Max}[H]$ is a unique choice to ensure the validity of the method. From the energy conservation laws, the total enthalpy is constant across shock waves. Hence, the local-reconstruction method is still applicable for the flows experiencing shocks. The normalized distribution of total enthalpy, H , as well as mean and inviscid velocity profiles for a cold-wall, ZPG, Mach five turbulent BL over a flat plate are presented in Figures 3.3 (a,b), respectively. Unsurprisingly, H is maximum and approximately constant outside of the BL. Since the flow does not experience a pressure gradient, the mean velocity profile, \bar{u} , remains constant outside of the BL, matching the locally reconstructed inviscid velocity, U_i .

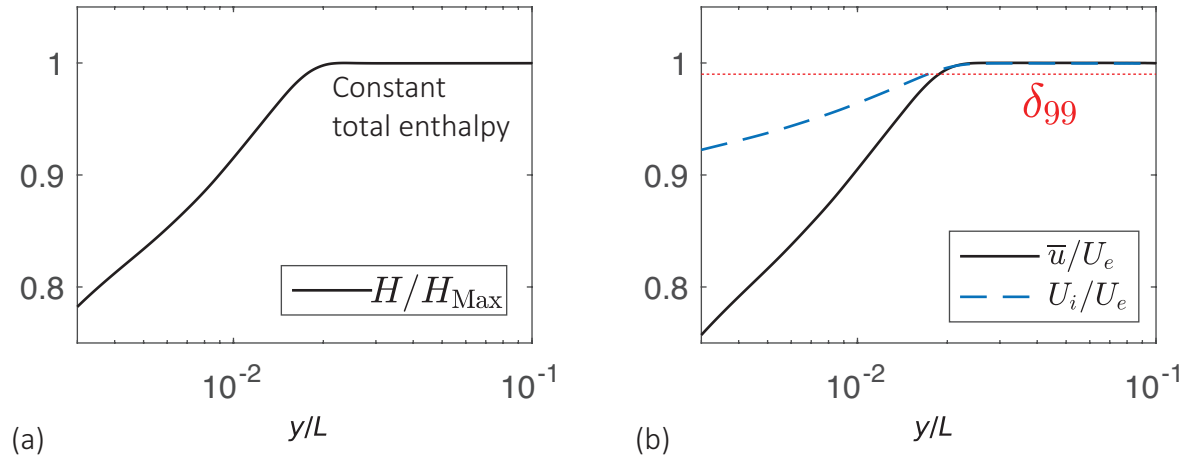


Figure 3.3: Normalized total enthalpy (a), and velocity profiles (mean and inviscid) in the wall-normal direction for high-speed turbulent flow over a flat plate. The red dotted line in (b) represents δ_{99} . L denotes the length of the flat plate.

Wall-normal integration

Calculating the wall-normal integrated quantities, such as displacement and momentum thicknesses, is of paramount importance in the analysis of viscous BLs. In addition, these quantities are the building blocks of the integral methods. Computing these integrals often requires using numerical methods. In this work, we perform the wall-normal integration by applying a commonly

used trapezoidal rule that reads

$$\int_{x_i}^{x_{i+1}} f(x)dx \approx \frac{\Delta x}{2} (f_i + f_{i+1}) \quad (3.15)$$

for one interval $x_i \leq x \leq x_{i+1}$, where Δx is the size of the interval. The accuracy of this scheme can be evaluated by Taylor series expansion; for a single interval, the trapezoidal approximation yields

$$\int_{x_i}^{x_{i+1}} f(x)dx = \Delta x_i \frac{f(x_i) + f(x_{i+1})}{2} - \frac{1}{12} \Delta x_i^3 f''(y_i) + \dots \quad (3.16)$$

that is third-order accurate. For the entire domain, we examine the accuracy by summing over the intervals –assuming uniform spacing $\Delta x = \text{Constant}$ – and using the mean value theorem of integral calculus. Thus for the entire domain from $x_0 \leq x \leq x_n$

$$\int_{x_0}^{x_n} f(x)dx = \sum_{i=0}^{n-1} \int_{x_i}^{x_{i+1}} f(x)dx = \frac{\Delta x}{2} \left(f(x_0) + f(x_n) + 2 \sum_{j=1}^{n-1} f_j \right) + \dots \quad (3.17)$$

where \bar{x} is a point within the interval $[x_0, x_n]$. Consequently, the trapezoidal rule is second-order accurate over the entire domain. Note this second-order accuracy in space is consistent with the numerical schemes we introduced earlier to discretize and solve the NS equation.

Theoretically, in BLs, the wall-normal integrals are taken from $y = 0$ to $y \rightarrow \infty$; however, numerically, the integration must be truncated at some distance away from the wall, outside of the BL. The truncation is essential in most numerical experiments to remove unwanted and unphysical effects from the analysis that are caused by imperfect boundary conditions. For instance, including the free-stream vortical disturbances, the vorticity mixing layer type flow, or the shear layer due to the top boundary condition can deteriorate the statistical convergence. In this work, we choose $1.5\delta_{99}$

as the upper limit of the integration, i.e.

$$\int_{y=0}^{\infty} [\cdot] dy \approx \int_{y=0}^{1.5\delta_{99}} [\cdot] dy, \quad (3.18)$$

where the flow beyond this limit, from $y = 1.5\delta_{99}$ to $y \rightarrow \infty$, is approximately completely irrotational. The contour plot of vorticity for an H-type transitional incompressible BL flow is presented in Figure 3.4. Here $1.5\delta_{99}$ is shown to be away from the region where vorticity, ω_z , is non-negligible.

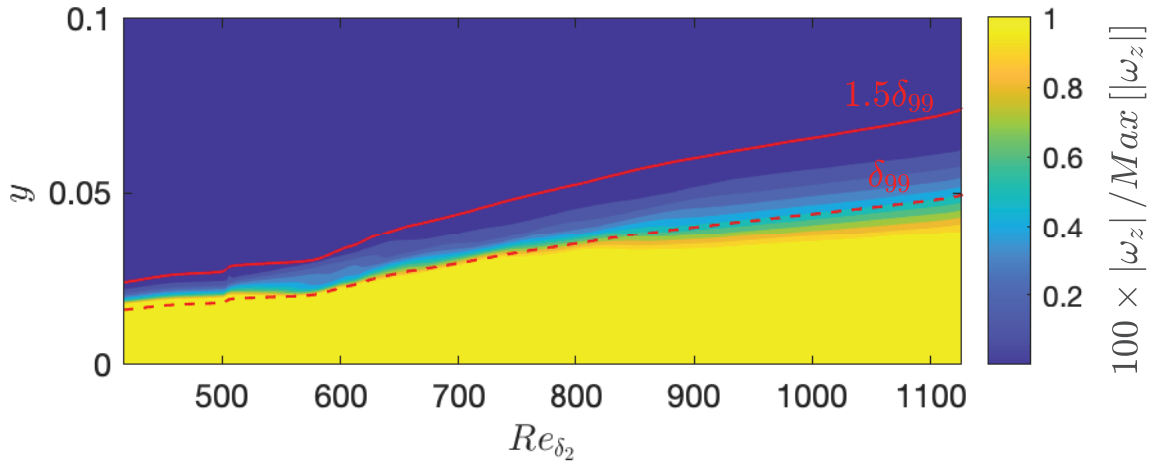


Figure 3.4: Normalized spanwise vorticity contour for incompressible H-type transitional BL saturated to $0.01 \left| \text{Max} [\omega_z] \right|$. Solid and dashed red lines represent $1.5\delta_{99}$ and δ_{99} , respectively.

Chapter 4

First-moment Integral Equations for Low-speed Boundary Layers with Heat Transfer

Transitional and turbulent boundary layer (BL) flows possess dramatically more considerable wall-shear stresses and surface heat fluxes than their laminar counterparts. Locally, this can be explained by appealing to the presence of spatio-temporally coherent velocity and temperature regions, which enhance the momentum and thermal transport across the BL. However, these coherent structures are seldom present alone but are usually influenced by other physical phenomena, such as the stream-wise growth of boundary layers or free-stream pressure gradients.

This chapter first reviews the angular momentum integral (AMI) equation introduced in [38] in incompressible BLs. On the basis of the AMI equation, Section 4.1.2 first provides the derivation of the moment of enthalpy integral (MEI) equation from the conservation equations. This is followed by an interpretation of the terms that appeared on the right-hand side of the MEI equation and explains how turbulence and other flow phenomena enhance surface heat flux. Section 4.2 examines

the application of the AMI and MEI equation by studying the direct numerical simulation dataset of a transitional and turbulent BL obtained by Wu *et al.* [176]. Finally, the conclusion is given in Sec. 4.3.

4.1 Derivation and Interpretation

This section provides the fundamental steps to obtain the first-moment integral equations for ZPG incompressible boundary layers. We first review the angular momentum integral equation introduced in Ref. [38]. We extend the concept of the first-moment integral equations to energy equations based on the enthalpy of the flow field.

4.1.1 Angular Momentum Integral Equation

The derivation of the angular momentum integral (AMI) equation, introduced in Ref. [38], proceeds similarly to von Kármán's momentum integral equation [165]. For the present work, the statistically two-dimensional mean flow in a flat-plate BL is described in Cartesian coordinates. The RANS equations for incompressible BLs read

$$\frac{\partial \bar{u}}{\partial x} + \frac{\partial \bar{v}}{\partial y} = 0, \quad (4.1)$$

for continuity and

$$\frac{\partial \bar{u}}{\partial t} + \frac{\partial (\bar{u}^2)}{\partial x} + \frac{\partial (\bar{u}\bar{v})}{\partial y} = -\frac{1}{\rho} \frac{\partial \bar{p}}{\partial x} + \nu \frac{\partial^2 \bar{u}}{\partial x^2} + \nu \frac{\partial^2 \bar{u}}{\partial y^2} - \frac{\partial \overline{u'u'}}{\partial x} - \frac{\partial \overline{u'v'}}{\partial y}, \quad (4.2)$$

for the x -momentum conservation, respectively. In Eq. (4.2), the fluid's density (ρ) and kinematic viscosity ν remain constant. Also, \bar{p} is the mean pressure. The effect of surface curvature on boundary layers can be neglected in some cases. The generalization of this approach to include

BLs on surfaces with significant curvature effects is a topic for future work.

The BL is subjected from above to a free-stream flow with velocity $U_\infty(x, t)$ and pressure $P_\infty(x, t)$, where x is the streamwise coordinate along the surface; note, for ZPG BLs, the free-stream quantities –subscript ∞ – are the same as the edge ones –subscript U_e . Within the free-stream, the streamwise momentum equation is

$$\frac{\partial U_\infty}{\partial t} + U_\infty \frac{\partial U_\infty}{\partial x} = -\frac{1}{\rho} \frac{\partial P_\infty}{\partial x}. \quad (4.3)$$

It is assumed here that the wall-normal variation of U_∞ on the scale of the boundary layer thickness is insignificant compared to the wall-normal variation of the velocity within the BL. However, this assumption may need to be relaxed in the future to apply this approach to strong adverse pressure gradients and boundary layer separation.

Now, subtracting Eq. (4.2) from Eq. (4.3) yields a transport equation for the streamwise momentum deficit ($U_\infty - \bar{u}$) as

$$\frac{\partial ((U_\infty - \bar{u})\bar{u})}{\partial x} + \frac{\partial ((U_\infty - \bar{u})\bar{v})}{\partial y} + (U_\infty - \bar{u}) \frac{\partial U_\infty}{\partial x} = -\nu \frac{\partial^2 \bar{u}}{\partial y^2} + \frac{\partial \overline{u'v'}}{\partial y} - I_M, \quad (4.4)$$

where all the terms neglected in statistically stationary high Reynolds number BL theory to the skin-friction coefficient are gathered in a single term

$$I_M = \frac{\partial}{\partial t} (U_\infty - \bar{u}) + \frac{\partial}{\partial x} \left(-\overline{u'u'} + \nu \frac{\partial \bar{u}}{\partial x} \right) - \frac{1}{\rho} \left(\frac{dP_\infty}{dx} - \frac{d\bar{p}}{dx} \right). \quad (4.5)$$

Equation (4.4) expresses how the streamwise momentum deficit in BLs changes because of the streamwise and wall-normal fluxes, free-stream acceleration, pressure gradient, viscous transport, and Reynolds stresses. Integration of Eq. (4.4) across the BL from $y = 0$ to $y = \infty$, then normal-

izing by U_∞^2 results in the von Kármán momentum integral equation [165]

$$\frac{C_f}{2} = \frac{d\delta_2}{dx} + \frac{2\delta_2 + \delta_1}{U_\infty} \frac{dU_\infty}{dx} + \mathcal{I}_M, \quad (4.6)$$

where the momentum and displacement thicknesses are defined, respectively, as

$$\delta_2 \equiv \int_0^\infty \left(1 - \frac{\bar{u}}{U_\infty}\right) \frac{\bar{u}}{U_\infty} dy, \quad \delta_1 \equiv \int_0^\infty \left(1 - \frac{\bar{u}}{U_\infty}\right) dy, \quad (4.7)$$

and \mathcal{I}_M represents the contribution of all the negligible terms (inside I_M , Eq. (4.5)) to $C_f/2$. Also, the skin-friction coefficient for BLs is $C_f \equiv 2\tau_w/\rho U_\infty^2$, in which $\tau_w = \mu (\partial\bar{u}/\partial y)_{y=0}$ is the shear stress at the wall and $\mu = \rho\nu$ is the fluid's dynamic viscosity. Note Eq. (4.6) is valid for laminar, transitional, and fully turbulent flows. In other words, the influence of fluctuations, e.g., Reynolds shear stress, momentum flux, and hence skin friction, is implicit. Because turbulence only rearranges momentum in the wall-normal direction, it does not directly provide a source or sink for the integral of momentum (deficit). Instead, the impact of turbulence on Eq. (4.6) is to change the relationship between C_f and δ_2 . To see the effect of turbulence explicitly, one must consider how momentum is distributed in the wall-normal direction, e.g., by considering moments of momentum.

The AMI equation is derived by multiplying Eq. (4.4) by $(y - \ell(x))$ –as the first moment– and integrating in the wall-normal direction from $y = 0$ to $y = \infty$. This may then be stated in terms of the skin-friction coefficient with a subsequent division by ℓU_∞^2 that yields

$$\frac{C_f}{2} = \frac{1}{Re_\ell} + \frac{1}{\ell} \int_0^\infty \frac{-\overline{u'v'}}{U_\infty^2} dy + \left(\frac{d\delta_2^\ell}{dx} - \frac{\delta_2 - \delta_2^\ell}{\ell} \frac{d\ell}{dx} \right) + \frac{\delta_{2,v}}{\ell} + \left(\frac{2\delta_2^\ell + \delta_1^\ell}{U_\infty} \frac{dU_\infty}{dx} \right) + \mathcal{I}_M^\ell, \quad (4.8)$$

where the left-hand side is the skin-friction coefficient, and on the right-hand side, there are several terms related to several physical flow phenomena. In (4.8), $Re_\ell = U_\infty \ell / \nu$ represents the Reynolds number based on the length scale $\ell(x)$, and \mathcal{I}_M^ℓ contains all terms neglected in BL theory (in Eq.

(4.5.) The angular momentum and displacement thicknesses are defined as

$$\delta_2^\ell \equiv \int_0^\infty \left(1 - \frac{y}{\ell}\right) \left(1 - \frac{\bar{u}}{U_\infty}\right) \frac{\bar{u}}{U_\infty} dy, \quad \delta_1^\ell \equiv \int_0^\infty \left(1 - \frac{y}{\ell}\right) \left(1 - \frac{\bar{u}}{U_\infty}\right) dy, \quad (4.9)$$

which collapse to $\delta_2^\ell = \delta_2$ and $\delta_1^\ell = \delta_1$ in the limit of $\ell \rightarrow \infty$. In fact, the AMI equation returns the von Kármán momentum integral equation when $\ell \rightarrow \infty$. The wall-normal momentum thickness is defined as

$$\delta_{2,v} \equiv \int_0^\infty \left(1 - \frac{\bar{u}}{U_\infty}\right) \frac{\bar{v}}{U_\infty} dy, \quad (4.10)$$

representing the integration of the mean wall-normal flux of the streamwise momentum deficit. Equation (4.8) represents the integral budget of mean angular momentum with respect to $y = \ell$, in the BL approximation where x is a time-like variable. It may also be called a first moment of momentum integral equation [73] (for historical context, see also [88]).

According to Ref. [38], the choice of $\ell(x)$ can be made to isolate the ZPG laminar skin friction coefficient in a single term of the AMI equation, $2/Re_\ell$. This choice allows the other terms in the equation to be straightforwardly interpreted as enhancement or attenuation of the skin friction compared to a laminar BL at a matching Reynolds number. The skin-friction coefficient of ZPG laminar BLs from Blasius solution, [12], yields

$$\frac{C_f}{2} = \frac{1}{Re_\ell} \approx \frac{0.332}{\sqrt{Re_x}} \approx \frac{0.221}{Re_{\delta_2}} \approx \frac{0.571}{Re_{\delta_1}}, \quad (4.11)$$

which corresponds to

$$\ell(x) \approx 3.01 \sqrt{\frac{vx}{U_\infty}} \approx 4.54 \delta_2(x) \approx 1.75 \delta_1(x). \quad (4.12)$$

Each of these relations represents a unique choice for the AMI equation. For example, the choice of $\ell \sim \sqrt{x}$ makes the first term equal to the skin friction of the Blasius BL at a given Re_x . In

that case, the AMI equation expresses the BL skin friction relative to the laminar case at the same Re_x . Similarly, the choice $\ell \sim \delta_2$ makes the first term equal to the Blasius friction for a given Re_{δ_2} , and thus the AMI equation quantifies the skin friction relative to a laminar BL as the same Re_{δ_2} . Therefore, the ability to choose $\ell(x)$ provides flexibility for the analysis and clarity of interpretation. Due to the physical basis of the momentum thickness stemming from the von Kármán momentum integral equation (4.6), the results in this chapter will use the AMI equation with the length scale $\ell \sim \delta_2$. Elnahhas & Johnson [38] briefly considered different choices for the length scale, and further insights from other choices are left for future work. Once the choice of ℓ is made, the other terms may now be interpreted as changes to the skin friction relative to a Blasius BL having the same Re_ℓ . The second term in Eq. (4.8) accounts for how turbulent fluctuations (via the Reynolds stress) alter the skin friction coefficient. Unsurprisingly, a negative correlation between streamwise and spanwise fluctuations increases skin friction (Figure 1.7). In the AMI equation, the contribution of the Reynolds shear stress to skin friction is unweighted as a function of wall-normal distance so that the wake region of the BL contains most of this integral.

The third term on the right-hand side of Eq. (4.8) expresses the streamwise growth of the angular momentum thickness, δ_2^ℓ , relative to how quickly ℓ increases. The increase in ℓ is dictated by the choice of length scale to use for Eq. (4.12), e.g., $\ell \sim \sqrt{x}$ or $\ell \sim \delta_2$, where the Blasius solution sets the coefficient. Another way of thinking about the AMI equation is that an increase in angular momentum thickness must be equal to the sum of the skin friction torque along with the other torques represented on the right-hand-side of Eq. (4.8).

The mean wall-normal velocity also redistributes streamwise momentum (deficit), reflected in the fourth term on the right-hand side of Eq. (4.8). In the case of a positive mean wall-normal velocity, momentum deficit is carried away from the wall. This may be thought of as a torque that decelerates the mean flow in the outer BL and speeds up the near-wall flow, increasing the skin friction.

Any free-stream pressure gradient also acts as a torque on the BL velocity profile. As quantified by the fifth term on the right-hand side of Eq. (4.8), an accelerating free-stream (favorable pres-

sure gradient) acts to increase the skin friction coefficient. In contrast, a decelerating free-stream (adverse pressure gradient) does the opposite. Finally, the contribution of the terms neglected by BL approximation is accumulated in the sixth term. A comprehensive interpretation of each flow phenomenon in the AMI equation is provided in Ref. [38].

4.1.2 Moment of Enthalpy Integral Equation

Derivation

The derivation and interpretation of the AMI equation for skin friction was given previously by Elnahas & Johnson [38]. An analogy between skin friction and surface heat transfer has long been a staple of boundary layer theory. In this section, we build on the approach of the AMI equation to introduce an analogous moment of enthalpy integral (MEI) equation for surface heat transfer.

For incompressible flows, the averaged conservation equation for enthalpy provides an expression for how turbulence and other flow phenomena alter the Stanton number, and hence the Reynolds' analogy. For statistically stationary, two-dimensional BLs, without heating source/sink, and with constant fluid properties, the Reynolds-averaged conservation equation for thermal energy –written in terms of temperature, T ,– reads

$$\frac{\partial \bar{T}}{\partial t} + \frac{\partial(\bar{u}\bar{T})}{\partial x} + \frac{\partial(\bar{v}\bar{T})}{\partial y} = \alpha \frac{\partial^2 \bar{T}}{\partial x^2} + \alpha \frac{\partial^2 \bar{T}}{\partial y^2} - \frac{\partial(\overline{u'T'})}{\partial x} - \frac{\partial(\overline{v'T'})}{\partial y}, \quad (4.13)$$

where α is the fluid's thermal diffusivity. Subtracting the adiabatic free-stream (T_∞ is constant) enthalpy, equation,

$$\frac{\partial T_\infty}{\partial t} + U_\infty \frac{\partial T_\infty}{\partial x} = 0, \quad (4.14)$$

from (4.13) yields a transport equation for the mean excess enthalpy equation (often $T_w \geq T_\infty$ in

incompressible BLs) in terms of temperature as

$$\frac{\partial \left((\bar{T} - T_\infty) \bar{u} \right)}{\partial x} + \frac{\partial \left((\bar{T} - T_\infty) \bar{v} \right)}{\partial y} - (U_\infty - \bar{u}) \frac{\partial T_\infty}{\partial x} = \alpha \frac{\partial^2 \bar{T}}{\partial y^2} - \frac{\partial (\overline{v'T'})}{\partial y} + I_h, \quad (4.15)$$

where all the terms neglected in statistically stationary, two-dimensional BL approximations are gathered in a single term

$$I_h = \frac{\partial}{\partial t} (T_\infty - \bar{T}) + \frac{\partial}{\partial x} \left(-(\overline{v'T'}) \right) + \alpha \frac{\partial \bar{T}}{\partial x} \quad (4.16)$$

Integrating Eq. (4.15) in the wall-normal direction from $y = 0$ to $y = \infty$, then normalizing by $U_\infty(T_w - T_\infty)$ results a Kármán integral type relation for the Stanton number [142]

$$St = \frac{d\delta_h}{dx} + \frac{\delta_h}{U_\infty} \frac{dU_\infty}{dx} + \frac{\delta_h}{T_w - T_\infty} \frac{dT_w}{dx} + I_h, \quad (4.17)$$

where δ_h is the enthalpy thickness,

$$\delta_h \equiv \int_0^\infty \frac{\bar{u}}{U_\infty} \left(\frac{\bar{T} - T_\infty}{T_w - T_\infty} \right) dy, \quad (4.18)$$

representing the wall-normal integral of the streamwise flux of the enthalpy excess (or deficit) [171].

Moreover, I_h corresponds to the contributions of the negligible terms (I_h) to the Stanton number.

The Stanton number for incompressible BLs is defined as

$$St \equiv \frac{q_w}{\rho U_\infty c_p (T_w - T_\infty)}, \quad (4.19)$$

representing the non-dimensional form of surface heat flux $\overline{q_w} = -k(\partial \bar{T} / \partial y)_{y=0}$, where $k = \rho c_p \alpha$ and c_p are the fluid's thermal conductivity and constant specific heat capacity, respectively.

Note the influence of turbulence in the Eq. (4.17) is implicit because turbulence rearranges enthalpy (and momentum) in the wall-normal direction; it does not directly provide a source or sink. Instead,

the impact of turbulence in Eq. (4.17) is to change the relationship between St and δ_h . In order to explicitly quantify the impact of turbulence on the surface heat transfer, one must consider how enthalpy is distributed in the wall-normal direction, e.g., by considering the first moment of the enthalpy equation.

Similar to the AMI equation, the moment of enthalpy integral (MEI) equation is obtained by multiplying Eq. (4.15) by $(y - \ell)$ –the first moment– then integrating across the BL, $\int_0^\infty (y - \ell) [\cdot] dy$. Normalizing the resulting by $\ell U_\infty (T_w - T_\infty)$ yields the MEI equation

$$St = \frac{1}{Pe_\ell} + \frac{1}{\ell} \int_0^\infty \frac{\overline{T'v'}}{U_\infty(T_w - T_\infty)} dy + \left(\frac{d\delta_h^\ell}{dx} - \frac{\delta_h - \delta_h^\ell}{\ell} \frac{d\ell}{dx} \right) + \frac{\delta_{h,v}}{\ell} + \frac{\delta_h^\ell}{U_\infty} \frac{dU_\infty}{dx} + \frac{\delta_h^\ell}{T_w - T_\infty} \frac{dT_w}{dx} + \mathcal{I}_h^\ell, \quad (4.20)$$

where $Pe_\ell = 1 / (Pr \cdot Re_\ell)$ is the Péclet number, and $Pr = \nu/\alpha$. δ_h^ℓ and $\delta_{h,v}$ are the first-moment of enthalpy thickness and wall-normal enthalpy thickness, respectively, defined as

$$\delta_h^\ell \equiv \int_0^\infty \left(1 - \frac{y}{\ell}\right) \frac{\bar{u}}{U_\infty} \left(\frac{\bar{T} - T_\infty}{T_w - T_\infty}\right) dy, \quad \delta_{h,v} \equiv \int_0^\infty \frac{\bar{v}}{U_\infty} \left(\frac{\bar{T} - T_\infty}{T_w - T_\infty}\right) dy. \quad (4.21)$$

Note in the limit of $\ell \rightarrow \infty$ the first moment of enthalpy thickness collapses to δ_h , and hence the MEI equation becomes the classic integral Eq. (4.17). In Eq. 4.20, \mathcal{I}_h^ℓ represents the contribution of the neglected terms (I_h) to the Stanton number based on the first moment integral approach. Note a meaningful interpretation of the MEI equation depends on the choice of the length scale ℓ ; an appropriate definition of ℓ is precisely discussed later in this section.

Interpretation

The right-hand side of the MEI equation, Eq. (4.20), consists of different terms mapping different physical flow phenomena and quantifying how they alter the Stanton number. A summary of the physical interpretation of these terms is provided below and supplemented by a brief discussion of

each flow phenomenon in the following paragraphs.

- (I) $\frac{1}{Pe_\ell}$ \rightarrow surface heat flux of an equivalent *laminar* BL at matched Pe_ℓ ,
- (II) $\frac{1}{\ell} \int_0^\infty \frac{\overline{T'v'}}{U_\infty(T_w - T_\infty)} dy$ \rightarrow *turbulent flux* integral, turbulent transport of enthalpy,
- (III) $\frac{d\delta_h^\ell}{dx} - \frac{\delta_h - \delta_h^\ell}{\ell} \frac{d\ell}{dx}$ \rightarrow *streamwise growth* of the first moment of enthalpy thickness,
- (IV) $\frac{\delta_{h,v}}{\ell}$ \rightarrow flux by *mean wall-normal* transport,
- (V) $\frac{\delta_h^\ell}{U_\infty} \frac{dU_\infty}{dx}$ \rightarrow *free-stream pressure gradient* flux,
- (VI) $\frac{\delta_h^\ell}{T_w - T_\infty} \frac{dT_w}{dx}$ \rightarrow flux by *wall temperature-variation*, and
- (VII) \mathcal{I}_h^ℓ \rightarrow heat flux due to *negligible terms*.

Diffusion flux and the laminar Stanton number (I)

In the MEI equation, the Stanton number and the *laminar* surface heat flux are obtained from the wall-normal integration of the first moment of the diffusion flux in Eq. (4.15)

$$\int_0^\infty (y - \ell) \left[\alpha \frac{\partial^2 \overline{T}}{\partial y^2} \right] dy = -\ell(T_w - T_\infty)U_\infty \left(St - \frac{1}{Pr \cdot Re_\ell} \right) \quad (4.22)$$

From Eq. (4.22), if ℓ is chosen such that $St = 1/Pr \cdot Re_\ell$ for a ZPG incompressible laminar BL, then the integral of total diffusion flux about $y = \ell(x)$ vanishes. Therefore, the length scale $\ell(x)$ mathematically connects two BLs, the BL to be analyzed (in this study, transition to turbulent) and the baseline (ZPG) incompressible laminar BL. In other words, the *laminar* Stanton number in the MEI equation is isolated in $1/Pr \cdot Re_\ell$ with such a choice for $\ell(x)$. Because of the physical basis of Eq. (4.17) we tie the definition of the length scale $\ell(x)$ to the enthalpy thickness, $\ell(x) \sim \delta_h(x)$,

hence for an (a ZPG) incompressible laminar BL

$$St = \frac{1}{Pr \cdot Re_\ell} = \frac{\alpha}{U_\infty (c_T \delta_h(x))}, \quad (4.23)$$

where c_T is a constant determined by solving the self-similar laminar incompressible BL equations, e.g., Blasius solution. For incompressible flows, there is a Prandtl number dependency between proposed length scales in the AMI and MEI equations (approximated ratio of the thermal and momentum BL thickness $\delta_h/\delta \approx Pr^{-0.4}$, where δ_h and δ are the thermal and momentum BL thicknesses, respectively [171]). In particular, when $Pr = 1$, the length scale of the MEI equation is equal to the AMI equation's length scale (obtained from Blasius solution) $\ell(x) = 4.54\delta_h = 4.54\delta_2$ ($\delta_h = \delta_2$ in laminar regime), i.e. $c_h = 4.54$. Thus, the Reynolds number used for similarity with the baseline laminar BL is $Re_{\delta_h} = U_\infty \delta_h/\nu = Re_{\delta_2}$. Note this equality is not perfectly valid for the transitional and turbulent flows. In other words, the turbulent transport mechanism is not exactly the same for enthalpy (scalar quantity) and momentum (vector quantity) fluxes.

Turbulent enthalpy flux (II)

The second term on the right-hand side of the MEI equation is the *turbulent flux* by wall-normal velocity temperature covariance, $\overline{v'T'}$. The turbulent heat flux does not appear directly in the Kármán integral type equation, Eq. (4.17), since it vanishes at boundaries (wall and free-stream). However, by integrating the first moment of the velocity-temperature covariance in the enthalpy excess equation,

$$-\int_0^\infty (y - \ell) \frac{\partial (\overline{v'T'})}{\partial y} dy = \int_0^\infty \overline{v'T'} dy, \quad (4.24)$$

the *turbulent flux* is preserved. The *turbulent flux* represents how turbulence carries enthalpy excess away from the wall, generating further heat flux relative to the base *laminar* heat flux.

Streamwise growth of moment-of-enthalpy thickness (III)

Integrating the first moment of the streamwise enthalpy excess yields

$$-\int_0^{\infty} (y - \ell) \frac{\partial}{\partial x} \left(\frac{\bar{u}}{U_{\infty}} \left(\frac{\bar{T} - T_{\infty}}{T_w - T_{\infty}} \right) \right) dy = \ell \frac{d\delta_{\ell}^h}{dx} - (\delta_h - \delta_{\ell}^h) \frac{d\ell}{dx}. \quad (4.25)$$

The enthalpy thickness δ_h from the Kármán integral type equation, Eq. (4.17), represents the net streamwise flux of enthalpy deficit/excess. Equation (4.25) represents the rate at which the first moment of enthalpy thickness grows relative to the growth rate of $\ell(x)$. The first moment of enthalpy thickness, δ_{ℓ}^h , is a signed quantity so that it can be negative or positive depending on the choice of $\ell(x)$. A physical interpretation of Eq. (4.25) is considering it as the resultant term from all of the fluxes impacting the BL as well as the surface heat flux itself in the left-hand side of the MEI equation. In other words, the first moment of enthalpy thickness absorbs any imbalance of enthalpy fluxes at a given streamwise location. For example, it will be shown that this term is often negative (attenuation of surface heat flux). In this case, this streamwise growth term may be interpreted as absorbing the turbulent heat flux, which would otherwise necessitate a more considerable surface heat flux, into a growth of the moment of enthalpy.

Mean wall-normal flux (IV)

The *mean wall-normal* flux in the MEI equation originates from the flux of enthalpy excess carried by the mean wall-normal velocity,

$$-\int_0^{\infty} (y - \ell) \frac{\partial}{\partial y} \left(\frac{\bar{v}}{U_{\infty}} \left(\frac{\bar{T} - T_{\infty}}{T_w - T_{\infty}} \right) \right) dy = \delta_v^h \quad (4.26)$$

This term represents the wall-normal flux of enthalpy. When \bar{v} is positive, as is typically in BLs, this term increases the Stanton number by assisting the wall-normal transport of enthalpy away from the wall. Conversely, if $\bar{v} < 0$, the mean wall-normal velocity transports enthalpy excess toward

the wall, attenuating the Stanton number. This reversal behavior is observed for transitional BLs in the AMI equation for the skin friction coefficient [38].

Flux by free-stream pressure gradient (IV)

A non-zero free-stream pressure gradient due to variable U_∞ with the streamwise direction impacts the surface heat flux. For instance, a favorable free-stream pressure gradient accelerates U_∞ , damping the velocity defect in the BL and contributing to the Stanton number. In contrast, an adverse free-stream pressure gradient decreases the surface heat flux. In this study, only zero free-stream pressure gradient incompressible BL will be considered, so this term is expected to be negligible. MEI-based analysis of pressure gradient effects on surface heat transfer is reserved for future work.

Flux by non-isothermal wall (VI)

According to the MEI equation, wall temperature variation impacts the surface heat flux. Increasing wall temperature in the streamwise direction enhances the surface heat flux, yet diminishing wall temperature causes a negative contribution to the Stanton number. This chapter focuses on isothermal BL. Hence, this term is going to be negligible. Analysis of BLs with wall temperature variation is left to future work.

Departure from the BL approximations (VII)

All terms in the enthalpy excess transport equation that are typically small in statistically stationary and two-dimensional BLs are accumulated in a single term, the \mathcal{I}_h^ℓ . While not the case in this study, these terms could become considerable in the vicinity of flow separation.

4.2 Results and Analysis

4.2.1 Transitional and Turbulent Regimes

The angular momentum integral equation and its extension to heat transfer, the moment of enthalpy integral equation, are generally applicable analysis tools for BL flows, i.e., they are valid for laminar, transitional, and turbulent regimes. One primary application of the first moment integral equations is measuring the explicit turbulence enhancement of the skin friction and surface heat flux in transitional and turbulent BLs. Therefore, in this section, we apply these equations to DNS results to further investigate the role of turbulence on skin friction and surface heat flux.

Dataset

Here, we work with a ZPG incompressible BL dataset obtained from a direct numerical simulation (DNS) by Wu et al. [176]. The simulation inlet is a laminar (Blasius) BL at $Re_{\delta_2} \approx 80$, with turbulence from a precursor simulation of homogeneous isotropic turbulence added to the free-stream to trigger bypass transition. The inlet turbulent intensity in the free-stream is 3%. The simulation domain is long enough in the streamwise direction, allowing the turbulent BL to grow to $Re_{\delta_2} \approx 3000$ and $Re_\tau \approx 1000$ at the outlet. A total of $16384 \times 500 \times 512$ grid points are used. Grid resolutions in wall-parallel planes are $3.5 < \Delta x^+ < 5.5$ and $4.5 < \Delta z^+ < 7$, respectively, where the superscript “+” denotes normalization with viscous scales. The streamwise grid resolution is within the range of $2\eta < \Delta x < 3\eta$ for the inner layer and $0.5\eta < \Delta x < 2\eta$ for the outer region, where η is the local Kolmogorov length scale obtained from the fluid kinematic viscosity, ν and turbulent dissipation, ε , as $\eta = (\nu^3/\varepsilon)^{1/4}$. In the wall-normal direction, the resolution ranges over $0.4\eta < \Delta y < 2\eta$ across the BL thickness. The temperature field (passive scalar) is simulated with $Pr = 1$ and isothermal boundary conditions at the wall. The incompressible Navier–Stokes and energy equations were solved using the fractional step method.

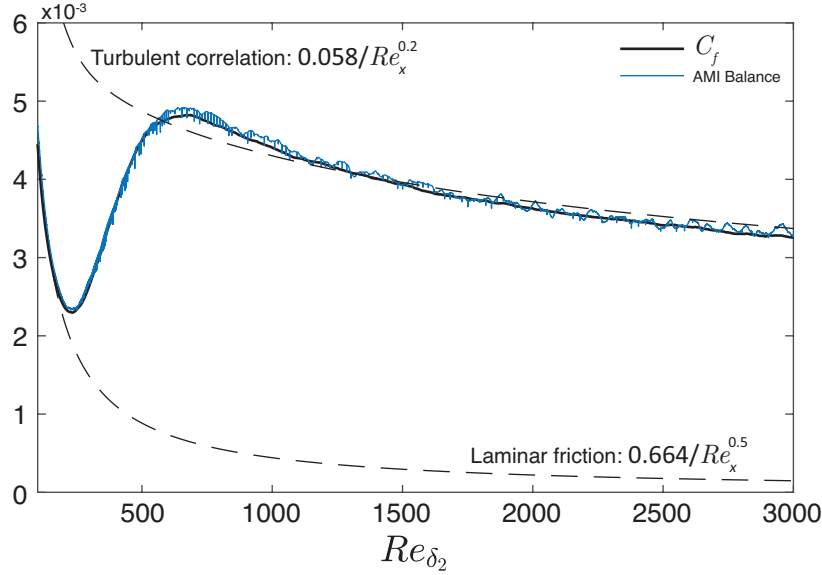


Figure 4.1: The balance of the right-hand side of the AMI equation compared with C_f . The labeled dashed curves are laminar (Blasius) friction and turbulent correlation of skin-friction coefficient [171].

Angular Momentum Integral Equation

Preliminary results for the skin friction and the right-hand side of Eqn. (4.8) are shown in Fig. 4.1. The right-hand side of the AMI equation balances the skin-friction coefficient with approximately 1.4% average error. The major cause of the deviation is the amplification of statistical convergence errors generated by calculating the derivatives in the streamwise direction in the *streamwise growth*. Also plotted are the skin friction formulae from the Blasius solution, $0.442/Re_{\delta_2}$, and a power-law approximation for turbulent BLs, $0.058/Re_x^{0.2}$. According to these results, the skin friction deviates from the laminar solution at approximately $Re_{\delta_2} = 200$, and the flow becomes fully turbulent at roughly $Re_{\delta_2} = 900$.

In Figures 4.2(a,b), the contributions of the four significant terms on the right-hand side of the AMI equation to the skin-friction coefficient are shown with respect to Re_{δ_2} . The AMI equation's length scale $\ell(x) = 4.54\delta_2(x)$ is based on the Blasius solution. Note the DNS simulation has a nominal zero free-stream pressure gradient and is far from BL separation. Therefore, the contribution of these two AMI terms to the skin-friction coefficient is orders of magnitude smaller than the other

four terms. Figure 4.2(a) exhibits the direct impact of the first four terms on $C_f/2$, and Figure 4.2(b) provides their normalized contribution by $C_f/2$.

For $Re_{\delta_2} < 200$, where the flow is mostly laminar, the dominant flow phenomenon in the AMI equation generating friction is the *laminar* term. The *laminar* friction, however, decreases downstream with $\sim 1/\sqrt{x}$ in the streamwise direction. During the initial stages of transition, the fluctuations (or perturbations) are significantly weak. Hence, the enhancement of *turbulent torque* to $C_f/2$ is negligible. In contrast, for the fully turbulent regime ($Re_{\delta_2} > 900$), the contribution of *turbulent torque* to $C_f/2$ is dominant since most of the wall-normal momentum transport is done by Reynolds shear stress that brings high-speed flow towards the wall. According to Figure 4.2(b), the normalized contribution of *turbulent torque* is about one, confirming roughly that all of the wall-normal transport mechanism is done by Reynolds shear stress.

The *streamwise growth* in angular momentum thickness is an overall negative contribution to the skin friction because this represents that the mean velocity profile of the BL absorbs angular momentum as it becomes thicker, offsetting the torques and decreasing the required skin friction needed to balance the integral equation. The mean wall-normal velocity is usually positive as the BL grows so that $\delta_{2,v}$ is positive in the laminar and fully turbulent regimes. Thus, the mean transport of momentum deficit away from the wall provides torque in the direction requiring a larger skin friction coefficient. However, the contribution of *mean-wall normal* is generally weaker than the aforementioned dominant terms in the laminar and turbulent regimes.

Within the laminar regime ($Re_{\delta_2} < 200$), the *mean-wall normal* and *streamwise growth* balance each other so that their sum is zero by design. That is, the choice of ℓ ensures that streamwise growth precisely offsets the wall-normal velocity of the Blasius BL. For fully turbulent BL ($Re_{\delta_2} > 900$), also, the normalized contribution of these two flow phenomena to $C_f/2$ in Fig. 4.2(b) are small and relatively constant. In fact, beyond $Re_{\delta_2} \approx 1200$, none of the terms in the AMI equation vary significantly in relative magnitude. Therefore, from the perspective of the AMI equation, the basic physics of skin friction enhancement by turbulence can be understood at relatively modest

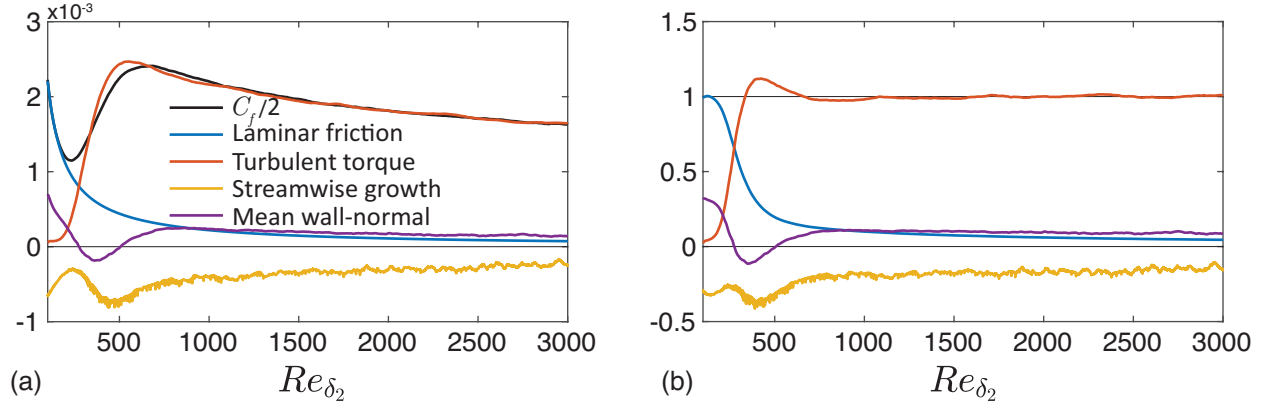


Figure 4.2: The AMI budget for the four significant flow phenomena with respect to Re_{δ_2} : (a) the contribution of each term to $C_f/2$, and (b) the contribution of each term normalized by $C_f/2$.

Reynolds numbers. For the remainder of this chapter, the focus will be on the behavior of the four major flow phenomena in the AMI and MEI equations during the transition to turbulence and early turbulent regime ($Re_{\delta_2} \leq 1200$).

Moment of Enthalpy Integral Equation

In this section, the moment of enthalpy integral (MEI) equation is applied to analyze the mean surface heat flux in the BL database from Ref. [176]. The balance of the right-hand side of the MEI equation is compared with the left-hand side (the Stanton number) in Fig. 4.3 within the transitional and early turbulent regime ($Re_{\delta_2} \leq 1200$). The average error is approximately 1.3%, approximately the same as observed for the AMI equation in Fig. 4.1.

The DNS simulation has an adiabatic free-stream condition with zero pressure gradient, and an isothermal wall boundary condition is imposed. Hence, the contributions of *edge pressure gradient flux* and *wall temperature variation* to the Stanton number are found to be negligible, as expected. In addition, the BL is away from any flow separations, so the BL approximations are valid, resulting in a substantially small effect from the *negligible terms* on surface heat flux. In Figures 4.4(a,b), the four significant flow phenomena in the right-hand side of the MEI equation with respect to $Re_{\delta_h} = U_\infty \delta_h / \nu$ are shown. The MEI equation's length scale, $\ell(x) = 4.54 \delta_h(x)$, is the same as

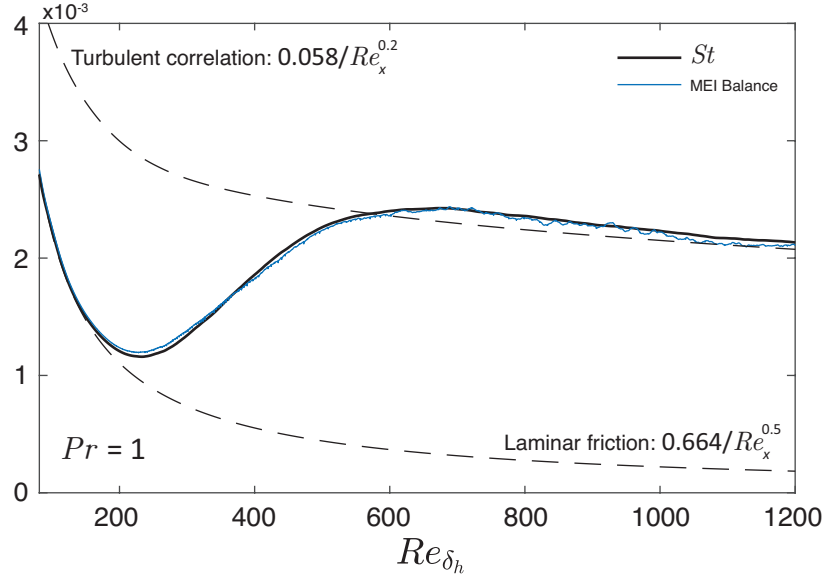


Figure 4.3: The balance of the right-hand side of the MEI equation compared with St . The labeled dashed curves are laminar Stanton number and turbulent power-law prediction of the Stanton number [171].

the AMI equation for $Pr = 1$. Figure 4.4(a) shows the direct contribution of each term to St , and Figure 4.4(b) provides their relative contribution (each term normalized by St). Given the DNS data for $Pr = 1$ (and $Re_{\delta_2} \approx Re_{\delta_h}$), the Reynolds analogy is expected and, qualitatively observed by comparing Figures 4.4(a,b) and Figures 4.2(a,b) for the MEI and AMI equations, respectively. Quantitatively, however, we spot a deviation in Reynolds analogy, especially within the fully turbulent regime; downstream of $Re_{\delta_2} = 900$, the explicit turbulence enhancement to the Stanton number is greater than its counterpart contribution to the skin friction coefficient. This deviation is more clear comparing the value of the normalized contribution of *turbulent flux* to St and *turbulent flux* to $C_f/2$ –Figures 4.2(b) and 4.4(b); for the *turbulent torque* it yields one, whereas for the *turbulent flux* is about 10% higher. The main explanation for this deviation is the slight difference between the turbulent transport mechanism for a scalar quantity (enthalpy/temperature) in comparison with a divergence-free vector quantity (momentum/velocity).

Within the laminar region (early transition), $Re_{\delta_2} < 200$, the fractional contribution of the *laminar* heat flux is about one –verifying that this term properly represents the laminar heat flux– while

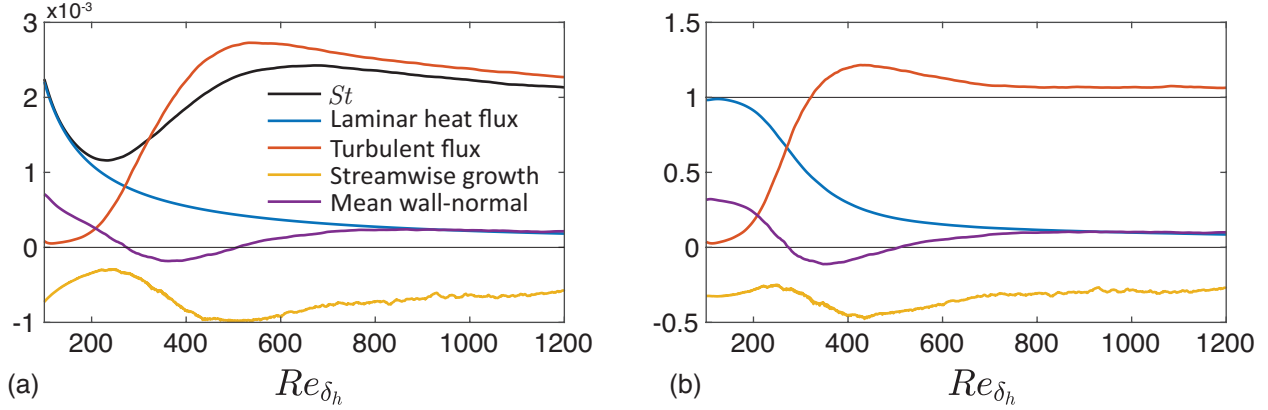


Figure 4.4: The MEI budget for the four significant flow phenomena with respect to Re_{δ_2} : (a) the contribution of each term to St , and (b) the contribution of each term normalized by St .

the *streamwise growth* and *mean wall-normal* flux precisely offset each other by design. For fully turbulent flow, the *laminar* Stanton number is insignificant, and the surface heat flux generated directly by turbulence is slightly higher than the net Stanton number. Therefore, there must be (at least) one term resisting the turbulent heat flux. Similar to the AMI analysis, the *streamwise growth* negatively contributes to St . That is, it absorbs the impact of turbulence into growth in the moment of enthalpy. According to Figure 4.4(b), since the normalized enhancement of *turbulent flux* is somehow converged, the normalized negative contribution of *streamwise growth* does not vary significantly downstream. Moreover, the relatively small positive mean wall-normal velocity assists the wall-normal transport of enthalpy; hence, *mean wall-normal* flux weakly contributes to the enhancement of the mean Stanton number.

Whereas for the laminar and fully turbulent BLs (away from separation), the balance of the MEI and AMI equations follow the fundamental physical expectations, during the transition and early turbulent we observe an unexpected trend by the major flow phenomena resulting in the maximum surface heat flux and skin friction. The transitional BL is explored in more detail in Section 4.2.1 by considering the MEI and AMI equations together.

Peak surface friction and heat flux during the transition to turbulence

In this section, the peak surface heat flux and friction during the transition are examined by applying the physical understanding of the MEI and AMI equations. As the transition initiates ($Re_{\delta_2} > 200$), the *turbulent flux* boosts up and outpaces St beyond $Re_{\delta_2} \approx 380$, Fig. 4.4. A similar trend is observed for the *turbulent torque* in the AMI equation, but the outpacing is temporal, confined between $Re_{\delta_2} \approx 380$ and $Re_{\delta_2} \approx 1000$, Fig. 4.2. The integral of $-\overline{u'v'}$ reaches its peak value roughly at $Re_{\delta_2} \approx 530$. With a slight spatial delay, the maximum St and $C_f/2$ about $Re_{\delta_2} \approx 650$. Surprisingly, in contrast to the laminar regime, during the transition, the *streamwise growth* and *mean wall-normal* cooperate, resisting the severe turbulent enhancement of surface heat flux and friction. To examine the (stronger) negative contribution of these two flow features, we examine the contours of the integrands of *turbulent flux* (and *turbulent torque*), *mean wall-normal*, and *streamwise growth* in the $x - y$ plane in the following paragraphs.

The direct impact of turbulence on St (and $C_f/2$) relative to the laminar effect is through the wall-normal integral of the turbulent covariance. Figures 4.5(a,b) exhibit the contour plots of the turbulent heat flux, $\overline{v'T'}$, and Reynolds shear stress, $-\overline{u'v'}$, normalized by $U_\infty(T_w - T_\infty)$ and U_∞^2 , respectively. These two are the integrands of the associated terms in the AMI and MEI equations. The Reynolds stress and heat flux reaches a maximum during the transition in a region close to the wall, $y < \ell$, approximately from $Re_{\delta_2} = 380$ to $Re_{\delta_2} = 550$ where the turbulent covariance is substantially high and reaches the maximum within a localized region (yellow). This region coincides with the maximum contribution of *turbulent heat flux* (and *turbulent torque*) to St and $C_f/2$, and is slightly higher for the former than the latter, explaining the higher contribution of *turbulent flux* to St compared with the contribution of *turbulent torque* to $C_f/2$ in Figs. 4.2 and 4.4.

For laminar or fully turbulent regimes, the *mean wall-normal* velocity is positive and thus increases St (and $C_f/2$) by assisting in the transport of temperature excess (or velocity deficit) away from the wall. During the transition to turbulence ($230 \leq Re_{\delta_2} \leq 680$), however, the wall-normal velocity

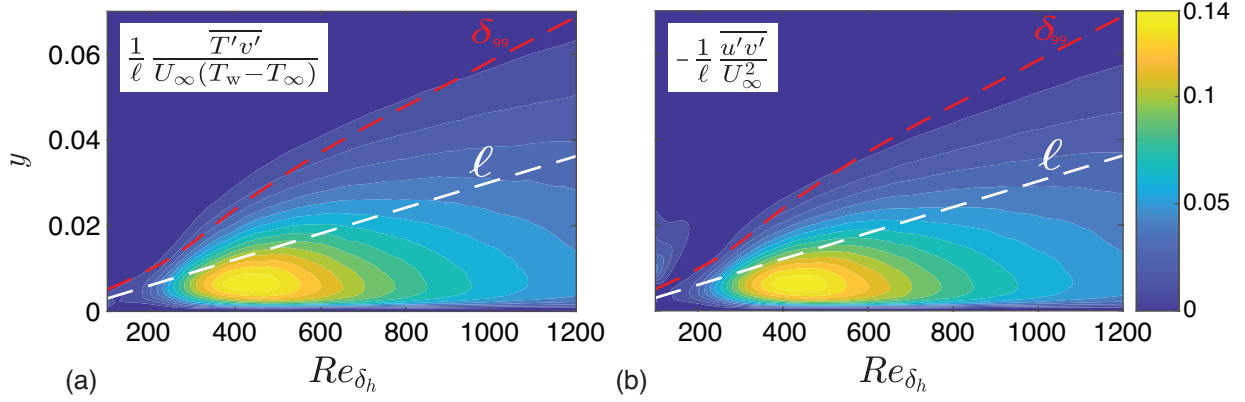


Figure 4.5: Integrands of the explicit turbulence enhancement on the (a) Stanton number by $\overline{T'v'}/\ell U_\infty(T_w - T_\infty)$, and (b) skin-friction coefficient by $-\overline{u'v'}/\ell U_\infty^2$.

\overline{v} switches sign to negative in a region near the wall, as shown in Fig. 4.6(b). When $\overline{v} < 0$, the contribution of the *mean wall-normal* flux to St (and $C_f/2$) is negative. This effect can be observed in Fig. 4.6 (c) within the range of $300 \leq Re_{\delta_2} \leq 500$.

The author is not aware of previous research exploring the observed negative wall-normal velocity during transition, so a short explanation is pursued here. The conservation of mass in an incompressible flow constrains the mean velocity field to be divergence-free, Eq. (4.1). As a laminar or fully turbulent boundary layer grows, the near-wall flow typically decelerates gradually, $\partial \overline{u}/\partial x < 0$. During the transition to turbulence, however, the introduction of coherent transitional structures rapidly mixes higher-speed fluid toward the wall. This accelerates the near-wall flow in the streamwise direction, i.e., $\partial \overline{u}/\partial x \geq 0$, as shown in Fig. 4.7(a). To satisfy the continuity constraint, $\partial \overline{v}/\partial y \leq 0$ in this near-wall region, Fig. 4.7(b). Given the no-penetration boundary condition that $v = 0$ at the wall, the wall-normal velocity must, therefore, be toward the wall to accommodate the localized streamwise acceleration. Thus, the mean wall-normal transport of momentum and heat (temporarily) reverses direction. The impact of this reversal on skin friction and surface heat transfer is quantified in Fig. 4.6(c). In Figure 4.4 (and Figure 4.2), the contribution of the *turbulent flux* (and *turbulent torque*) demonstrates an inflection point (a curvature change) –at about $Re_{\delta_2} = 380$ – during the transition. This curvature change corresponds to the streamwise location where the turbulent enhancement growth weakens that, coincides with the negative contribution

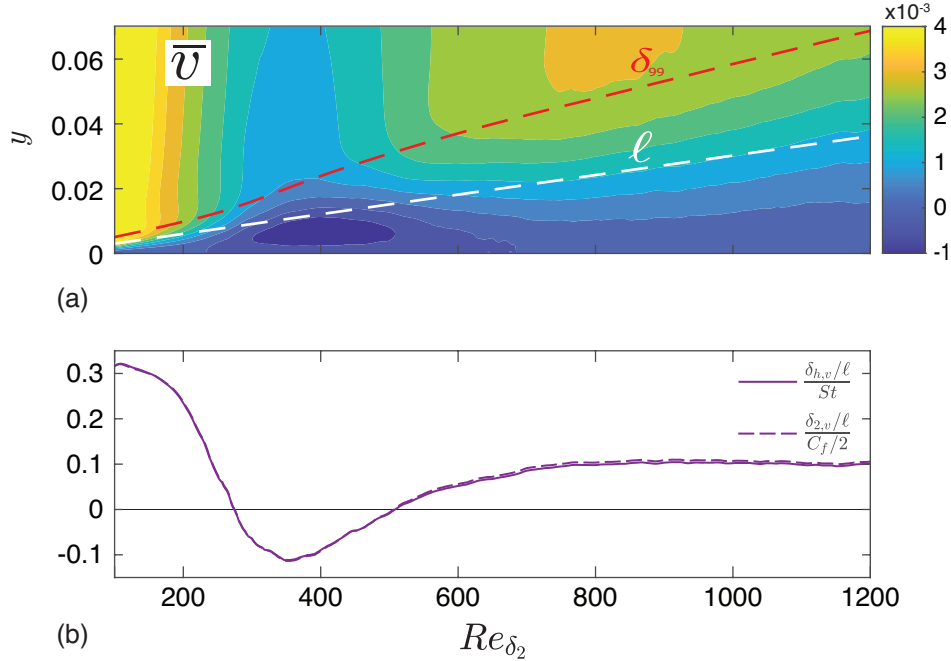


Figure 4.6: Impact of the *mean wall-normal* flux to the AMI and MEI analysis. (a) Contour plot of wall-normal velocity in the $x - y$ plane, and (b) the direct contribution of the *mean wall-normal* flux to St and $C_f/2$.

of *mean wall-normal* during the transition as well as the stronger streamwise growth of the BL thickness.

The other flow feature influencing the turbulence enhancement of surface heat transfer (and skin friction) is the streamwise growth of the first moment of enthalpy thickness (or angular momentum thickness). This flow phenomenon has a negative contribution in incompressible BLs away from flow separation to skin friction, [38], and surface heat flux, see Figs. 4.2 and 4.4. For laminar flows, the streamwise growth term in AMI and MEI is negative with a decaying magnitude. During the transition, the negative contribution of the *streamwise growth* to St (and $C_f/2$) grows in magnitude from $Re_{\delta_2} = 230$ to $Re_{\delta_2} = 500$ (at the peak *turbulent flux*), partially offsetting the sharp increase in the turbulent heat flux. Downstream of $Re_{\delta_2} = 500$, when the near-wall streamwise velocity gradually decelerates in the streamwise direction, the effect of *streamwise growth* slowly drops. In Figures 4.8(a,b), contours of the integrands of the *streamwise growth* for the MEI and AMI equations are shown, corresponding to a quantitative mapping based on its effect on the surface

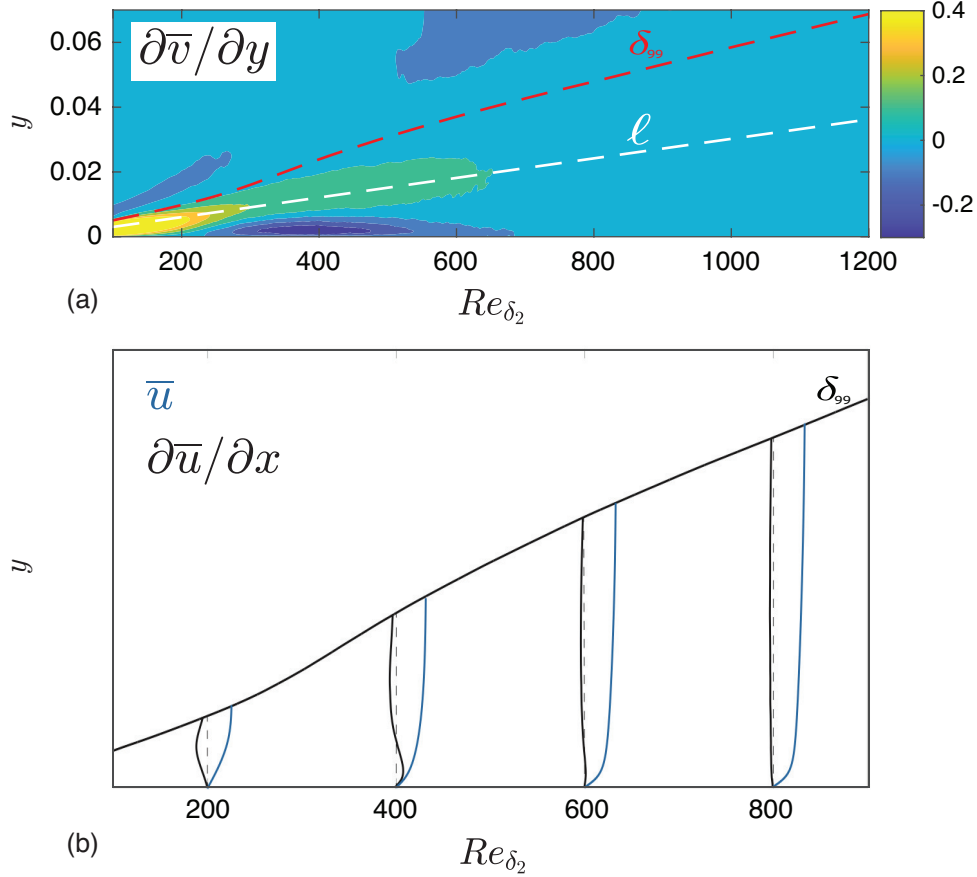


Figure 4.7: (a) Contour plot of the mean wall-normal velocity acceleration in y , and (b) profiles of the streamwise velocity and (spatial) streamwise acceleration ($\partial \bar{u} / \partial x$) within transitional BL.

flux quantities. During the transition (from $Re_{\delta_2} \approx 230$ to $Re_{\delta_2} \approx 680$), a reversed behavior in the integrand of the *streamwise growth* is observable near the wall, corresponding to the region where the near-wall flow accelerates in the streamwise direction, Figure 4.7. Note $\partial \bar{u} / \partial x$ is a crucial term in the integrands. Therefore, the higher the streamwise acceleration, the greater the negative contribution of *streamwise growth* to St (and $C_f/2$).

To summarize, in the transitional region, there are several flow aspects involved in a rapid process to increase the Stanton number (and skin friction coefficient). The dominant effect is simply the significant increase in momentum and enthalpy transport by rapidly growing instabilities. Other phenomena of the flow above the wall tend to partially offset the impact of the enhanced transport on surface flux quantities. Specifically, the *mean wall-normal* flux and *streamwise growth* of BL

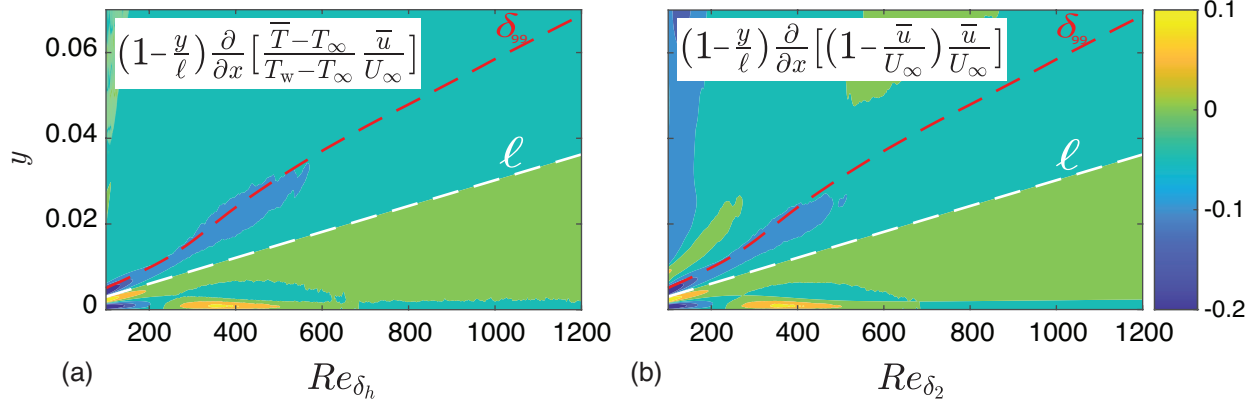


Figure 4.8: Contour plots of the integrands of the *streamwise growth*: (a) in the MEI equation for St , (b) in the AMI equation for $C_f/2$.

thickness act in a manner to attenuate skin friction and surface heat flux, mitigating the turbulence's impact. For the fully turbulent flow, the dominant flow phenomenon generating skin friction and heat transfer at the wall is the turbulent heat flux, while the other terms involved in Eq. (4.20) have a relatively small effect, without significant streamwise variation, merely balancing each other.

4.3 Conclusion

The turbulent enhancement of the surface friction and heat transfer is implicit in the classic Kármán type integral equations for boundary layer (BL) flows. This chapter introduced a new moment of enthalpy integral (MEI) equation to quantify the impact of various flow phenomena on the Stanton number of incompressible boundary layer (BL) flows. Analogous to the angular momentum integral (AMI) equation of Elnahhas & Johnson [38], the MEI equation is developed using the first moment of the excess enthalpy (or temperature) equation and explicitly quantifies the impact of turbulent transport on surface heat transfer as an integral of the turbulent heat flux. More generally, the MEI equation provides a quantifying mapping of the BL flow phenomenon based on how they alter the surface heat flux. The MEI equation represents a comparison of a turbulent BL with an equivalent laminar one, which is represented by the first term on the right-hand side. As such, other terms affecting the surface heat flux are cleanly interpreted as changes relative to the surface heat flux of

the equivalent laminar BL case.

The use of the AMI and MEI equations as incisive analysis tools was demonstrated on a DNS database of a transitional and turbulent boundary layer. Through the transition to turbulence, the rapid growth of the turbulent heat flux is quantitatively mapped to its influence on surface heat flux. At the same time, the MEI equation reveals how mean wall-normal and streamwise growth terms are both resisting the turbulence enhancement of the Stanton number. A closer look at the mean flow reveals how the Reynolds shear stress accelerates the near-wall flow. This phenomenon results in two effects. First, the streamwise positive acceleration near the wall causes the moment of enthalpy thickness to grow faster, absorbing more of the turbulent heat flux into a reshaping of the mean enthalpy (or temperature) profile. Second, the near-wall flow acceleration induces a negative mean wall-normal velocity to satisfy continuity. This negative wall-normal flux, due to the mean velocity, temporarily opposes the action of the turbulent heat flux in rearranging the distribution of the thermal energy in the BL. In a fully turbulent flow, the dominant enhancement of the Stanton number (and skin friction coefficient) is quantified as the integral of the turbulent heat (and momentum) flux. In contrast, the contribution of other flow phenomena in the MEI (and AMI) equation is relatively smaller and asymptote (to our knowledge).

In conclusion, the MEI and AMI equations provide a flexible, intuitive framework for quantitatively connecting flow phenomena throughout the BL to their effect on the surface heat flux and skin friction, respectively. While this analysis tool is demonstrated only for a relatively simple flow in this chapter, it opens up the possibility of using this approach for many other applications and purposes in future work. For example, the AMI and MEI equations are suitable for the analysis of boundary layers subjected to free-stream pressure gradients, and they may be adapted to account for surface curvature effects. The design and optimization of flow control schemes aiming to decrease skin friction, delay transition, or alter surface heat transfer may benefit from the quantitative nature of the insight provided by the AMI and MEI equations. For future studies, this concept can be extended to incorporate how different turbulent length scales are responsible for turbulent

enhancement, connecting turbulence structure with engineering quantities of interest.

Chapter 5

First-moment Integral Equations for Boundary Layers with Pressure Gradient

Turbulent boundary layers (BLs) experiencing pressure gradients and separation have been extensively studied due to their prevalence in science and engineering. A thorough understanding of their intricate physics is crucial for accurately predicting and designing various engineering systems, such as wing design in the aviation industry. These flows exist in a state of non-equilibrium, wherein the mean flow and Reynolds-stress tensor profiles do not guarantee a similar behavior when scaled with the appropriate local velocity and length scales. Under favorable pressure gradients (FPG), where the streamwise flow accelerates, there is a tendency for re-laminarization. This phenomenon entails the persistence of turbulence in the outer region but with a passive downstream influence on the BL development. Conversely, adverse pressure gradients (APG) stimulate turbulent structures in the outer layer, leading to higher turbulent production rates due to increased Reynolds shear stress and dissipation. Generally, the history effects caused by pressure gradients, whether favorable or adverse, alter the turbulent statistics, predominantly within the logarithmic and wake regions.

In turbulent flows, surface curvature and imposed boundary conditions (BCs) can generate pressure gradients. Examples of the former include flow over an airfoil, while the latter involves simulating BLs over a flat plate with imposed suction or blowing. The pressure gradient can either accelerate the flow downstream, known as a favorable pressure gradient (FPG) or decelerate it, termed an adverse pressure gradient (APG). Intense flow acceleration due to FPG can trigger flow re-laminarization, as discussed by [118]. Conversely, studies by [112] and [164] have suggested a more pronounced wake region in turbulent BLs under APG compared to those under zero pressure gradient (ZPG). This observation is linked to the presence of more energetic turbulent structures within the outer layer of the BL. Moreover, severe APG can lead to more complex conditions, specifically flow separation, under which the BL approximations become invalid.

In this chapter, I reformulate the AMI equation based on inviscid flow solutions and apply it to various turbulent BL scenarios, including APGs for flow over flat-plates and airfoils. Also, I will study a more complex flow over a two-dimensional Gaussian bump to examine how the AMI equation tackles flows with an alternating pressure gradient.

5.1 Derivation and Interpretation

The derivation of the AMI equation to tackle boundary layers with pressure gradient follows a similar approach as section 4.1. The major difference, however, is implementing the inviscid streamwise velocity (at the surface) as the outer-scale velocity instead of the edge or free stream velocities. Such a choice is justified due to the ambiguity of the definition of the edge in non-equilibrium BLs with pressure gradient. Similar to section 4.1 the derivation begins with the (statistically) two-dimensional conservation of mass and streamwise momentum equations outside a thin BL. This “outer flow” state is governed by Euler’s equations

$$\frac{\partial U_i}{\partial x} + \frac{\partial V_i}{\partial y} = 0, \tag{5.1}$$

for continuity and

$$\frac{\partial U_i}{\partial t} + U_i \frac{\partial U_i}{\partial x} + V_i \frac{\partial U_i}{\partial y} = -\frac{dP}{dx}, \quad (5.2)$$

for x -momentum. In this study, we adopt a common notation where x and y denote the wall-tangential (or streamwise) and wall-normal directions, respectively, whereas ξ represents the x -axis in the Cartesian coordinate system. Furthermore, U_i and V_i represent the (inviscid) velocities corresponding to the streamwise (x) and wall-normal (y) directions, respectively, and P denotes the outer flow pressure. It's worth noting that, for the sake of simplicity, we neglect the explicit curvature effects within the scope of this study. The outer flow does not see to the no-slip, no-penetration BCs. A zero vorticity BC thus can be applied at the wall for the outer flow, resulting in a more generalized form allowing non-zero vorticity in the free-stream, represented as $\partial U_i / \partial y = \partial V_i / \partial x - \Omega$. However, in many cases of interest, such as inflow, outflow, or far-field conditions, these boundary conditions do not introduce any vorticity, and the flow is fully irrotational, with $\Omega = 0$. Additionally, it is essential to note that in the outer layer, we assume there is no Reynolds stress, implying no turbulence above the boundary layer. Although beyond the scope of this work, this assumption could be relaxed to handle more complex geometries, such as a turbulent shear layer impinging on a boundary layer.

Inside the BL, the Reynolds-Averaged Navier-Stokes (RANS) equations describe the flow. Using lowercase letters, the continuity and x -momentum equations are expressed as

$$\frac{\partial \bar{u}}{\partial x} + \frac{\partial \bar{v}}{\partial y} = 0, \quad (5.3)$$

and

$$\frac{\partial \bar{u}}{\partial t} + \bar{u} \frac{\partial \bar{u}}{\partial x} + \bar{v} \frac{\partial \bar{u}}{\partial y} = -\frac{\partial \bar{p}}{\partial x} + \nu \left(\frac{\partial^2 \bar{u}}{\partial x^2} + \frac{\partial^2 \bar{u}}{\partial y^2} \right) - \frac{\partial \overline{u'u'}}{\partial x} - \frac{\partial \overline{u'v'}}{\partial y}. \quad (5.4)$$

In these equations, ν denotes the fluid kinematic viscosity, \bar{u} and \bar{v} represent the mean streamwise

and wall-normal velocities, respectively, and \bar{p} is the mean pressure.

By subtracting the x -momentum equation inside the BL, Eq. 5.4, from that of the outer flow, Eq. 5.2, and utilizing the continuity equation, we derive a general equation for the streamwise momentum deficit

$$\frac{\partial [(U_i - \bar{u})\bar{u}]}{\partial x} + \frac{\partial [(U_i - \bar{u})\bar{v}]}{\partial y} + (U_i - \bar{u})\frac{\partial U_i}{\partial x} + (V_i - \bar{v})\frac{\partial U_i}{\partial y} + \nu\frac{\partial^2 \bar{u}}{\partial y^2} - \frac{\partial \overline{u'v'}}{\partial y} + I_M = 0, \quad (5.5)$$

where the unsteady acceleration and terms neglected by BL approximation are collected in a single term

$$I_M = \frac{\partial(U_i - \bar{u})}{\partial t} + \frac{\partial(P - \bar{p})}{\partial x} + \nu\frac{\partial^2 \bar{u}}{\partial x^2} - \frac{\partial \overline{u'u'}}{\partial x}. \quad (5.6)$$

Multiplying Eq. 5.5 by $(y - \ell)$ yields the first moment of the momentum deficit, where $\ell(x)$ represents the AMI's length scale, indicating a distance from the wall (shown in Fig. 1.7). Integrating this expression in the wall-normal direction, $\int_0^\infty (\cdot) dy$, and normalizing by ℓU_{io}^2 , we obtain the AMI equation for the skin friction coefficient

$$\frac{C_f}{2} = \frac{1}{Re_\ell} + \frac{1}{\ell} \int_0^\infty \frac{-\overline{u'v'}}{U_{io}^2} dy + \frac{\delta_1^\ell}{U_{io}} \frac{dU_{io}}{dx} + \left(\frac{d\delta_2^\ell}{dx} + \frac{\delta_2^\ell - \delta_2}{\ell} \frac{d\ell}{dx} + \frac{2\delta_2^\ell}{U_{io}} \frac{dU_{io}}{dx} + \frac{\delta_{2,v}}{\ell} \right) + \mathcal{I}^\ell. \quad (5.7)$$

In this form of the AMI equation, we adopt the inviscid velocity at the wall, denoted as U_{io} , as the outer velocity scale for several reasons. Specifically, this choice offers robustness in calculating the AMI equation's budget compared to using the edge velocity, which relies on determining the boundary layer edge in flows with a non-zero pressure gradient. Typically, the inviscid velocity is determined using potential flow solutions. However, in our work, we employ the local reconstruction method described in section 3.2, adapted to our numerical dataset detailed in section 5.2. This technique enables us to reconstruct U_i at each streamwise location from the given turbulent statistics with the assumption that the BL's mean wall-normal velocity and pressure are equivalent to the inviscid solution. Additionally, the local reconstruction method predicts the BL thickness,

δ_{99} , defined as the distance from the wall where $\bar{u}/U_{io} = 0.99$. Due to the sensitivity of the AMI equation, a physical prediction of the BL edge is crucial for numerically computing the wall-normal integrals. Similarly, we can linearly interpolate to compute the edge velocity, U_e , at $y = \delta_{99}$. Now, utilizing the inviscid velocity, we define the skin friction coefficient as

$$C_f \equiv \frac{\tau_w}{\frac{1}{2}\rho U_{io}^2}, \quad (5.8)$$

where τ_w is the wall shear stress, and ρ is the fluid's density. On the right-hand side of Eq. 5.7, $Re_\ell = U_{io}\ell/\nu$ represents the Reynolds number based on the AMI's length scale, ℓ . δ_1^ℓ and δ_2^ℓ denote the angular displacement and momentum thicknesses, respectively, defined as

$$\delta_1^\ell \equiv \int_0^\infty \left(1 - \frac{y}{\ell}\right) \left(\frac{U_i - \bar{u}}{U_{io}}\right) dy, \quad \& \quad \delta_2^\ell \equiv \int_0^\infty \left(1 - \frac{y}{\ell}\right) \frac{\bar{u}}{U_i} \left(\frac{U_i - \bar{u}}{U_{io}}\right) dy, \quad (5.9)$$

using the inviscid velocity, which is slightly different from their definition by [38], but similarly, in the limit of $\ell \rightarrow \infty$ the first-moment forms of displacement and momentum thicknesses asymptote to their classic form δ_1 and δ_2 . Similarly, we define the wall-normal momentum thickness

$$\delta_{2,v} \equiv \int_0^\infty \frac{\bar{v}}{U_i} \left(\frac{U_i - \bar{u}}{U_{io}}\right) dy, \quad (5.10)$$

which represents the wall-normal transport of the streamwise momentum deficit. The last term in Eq. 5.7, \mathcal{I}^ℓ , denotes the integral of the first moment of I_M (Eq. 5.5) corresponding to the sum of the departure from the BL approximations and unsteady acceleration.

As presented in section 1.2.3, the notion of the first moment of momentum can be envisioned as the angular momentum of a flow, where the streamwise coordinate x behaves akin to a time-like variable. The reference point around which the moment is calculated, the AMI's length scale is allowed to vary downstream, i.e., $\ell = \ell(x)$. Therefore, Eq. 5.7 acts as the integral conservation equation for the angular momentum of a BL mean velocity profile, wherein the terms in the right-hand side of the equation are interpreted as torques redistributing momentum in the wall-normal

direction. In the following paragraphs, we provide a summary of flow phenomena that appear in AMI analysis.

The skin friction coefficient and the first term on the right-hand side of Eq. 5.7 stem from the viscous torque, T_v^ℓ , given by

$$T_v^\ell = \int_0^\infty v(y - \ell) \frac{\partial^2 \bar{u}}{\partial y^2} dy = \frac{\ell \tau_w}{\rho} - vUio = U_{io}^2 \ell \left(\frac{C_f}{2} - \frac{1}{Re_\ell} \right). \quad (5.11)$$

Although the selection of ℓ as input of the AMI analysis is arbitrary (e.g., one can choose $\ell \rightarrow \infty$ by which Eq. 5.7 reverts to the well-known von Kármán integral equation [76]), a natural choice is to define ℓ as the center of action of viscous force, i.e., $T_v^\ell = 0$, in a reference laminar flow. Consequently, $1/Re_\ell$ precisely represents the *laminar friction* experienced by a boundary layer at the same Reynolds number. The rationale behind this choice is to compare turbulent boundary layers (with pressure gradient) with a base laminar flow and observe how other flow phenomena, such as turbulence and pressure gradient, modify (or diminish) the reference laminar flow (as illustrated in Fig. 1.7). In the scope of this paper, the base laminar flow can be either Blasius or Falkner-Skan solutions. Such a choice, and setting $T_v^\ell = 0$, result in $\ell = \alpha\delta_1$ (or $\ell = \alpha\delta_2$), where α is a coefficient determined numerically by solving the respective self-similar laminar solutions. For instance, assuming Blasius solution as the base laminar solution

$$\frac{C_f}{2} = \frac{0.571}{Re_{\delta_1}} = \frac{0.221}{Re_{\delta_2}}, \quad (5.12)$$

which leads to $\ell = 1.75\delta_1$ (or $\ell = 4.54\delta_2$). Note that the choice between $\ell \sim \delta_1$ or $\ell \sim \delta_2$ yields an identical interpretation of the AMI budget and *laminar friction*. Therefore, the user must decide which form of ℓ to use in defining the Reynolds number fixed for the sake of comparison. More information regarding the choice of ℓ was detailed in section 1.2.3.

The second term on the right-hand side of Eq. 5.7 represents the explicit enhancement of the skin friction coefficient due to turbulence, i.e., Reynolds shear stress. Note that the integral of the

spatial derivative of Reynolds stress in Eq. 5.5 is naturally zero across the BL, thus not explicitly influencing the von Kármán integral equation. However, in the first-moment-based AMI equation, the contribution of Reynolds shear stress acts as a torque, directly augmenting the wall shear stress. This contribution of Reynolds shear stress in the AMI equation is therefore referred to as *turbulent torque*.

The direct impact of the imposed non-zero pressure gradient on the skin friction coefficient is directly assessed through the AMI analysis by wall-normal integration of the first moment of the edge velocity acceleration that yields

$$\rho \frac{dU_{io}}{dx} \int_0^\infty (1 - y/\ell) (U_i - \bar{u}) dy = \rho U_{io} \frac{dU_{io}}{dx} \delta_1^\ell. \quad (5.13)$$

This term, referred to as *pressure gradient*, in the AMI equation signifies the direct influence of the inviscid flow acceleration (or deceleration) on the wall shear stress. For instance, in the case of an adverse pressure gradient, this flow phenomenon acts as a clockwise torque with respect to ℓ , thereby reducing C_f (Fig. 1.7 (b)). Note the pressure gradient term introduced by [38] is different from the above definition. Specifically, Ref. [38] defined the pressure gradient torque based on the free-stream velocity (U_∞) as

$$T_{\nabla p, \ell} = \ell U_\infty \frac{dU_\infty}{dx} (\delta_1^\ell + 2\delta_2^\ell). \quad (5.14)$$

Also, the extra term with $2\delta_2^\ell$, originates from the first moment of the streamwise flux –will be discussed in the next paragraph– and corresponds to streamwise transport of momentum deficit rather than pressure gradient. Additionally, using our formulation, *pressure gradient* mimics the pressure gradient term in the von Kármán equation. Also, analogous to the classic definition of the non-equilibrium Clauser parameter, β , which measures the relative contribution of a pressure gradient to the transport of the momentum deficit (normalized by the wall shear stress), we define

the AMI-based Clauser parameter as:

$$\beta_\ell = -\rho U_{io} \frac{dU_{io}}{dx} \frac{\delta_1^\ell}{\tau_w}, \quad (5.15)$$

which differs from the definition of β in this work by employing δ_1^ℓ instead of δ_1 . In the next sections, we employ β_ℓ and compare it with β as a measurement of the strength of pressure gradient to study the pressure gradient history effects on turbulent statistics.

The fourth term on the right-hand side of the AMI equation arises from the integration of the first moment of the collective streamwise and mean wall-normal fluxes. This term, known as the *mean flux* (or total mean flux), encompasses two distinct mechanisms: 1) the rate of streamwise growth of the angular momentum thickness relative to the growth rate of ℓ , and 2) the redistribution of angular momentum via mean wall-normal flow. Ref. [82] noted that this flow phenomenon partially counterbalances the substantial growth of *turbulent torque* during the transition to turbulence, serving as a resistance to non-equilibrium.

The last term on the right-hand side of the AMI equation represents the combined effect of unsteady acceleration and terms that are typically neglected by BL approximations. The unsteady acceleration is zero in statistically steady flows, such as the BL around an airplane wing in cruise conditions. In addition, at high Reynolds numbers and away from the separation point, the deviation from the BL approximation is minimal, making these *negligible* terms insignificant for the AMI analysis.

5.2 Dataset and Numerical Techniques

We consider several high-fidelity numerical simulations of incompressible turbulent BLs with non-zero pressure gradients, including BL over flat-plates, wing airfoils, and a two-dimensional Gaussian bump. The flow configuration of each turbulent dataset is detailed in table 5.1. As discussed in section 5.1, we derive the AMI equation, Eq. 5.7, for BLs in tangential-normal coordination









Label ID	Color	Data type	Reynolds number Re	Clauser parameter β
Wing		WRLES	$Re_c = 400,000$	0 – 40.78
Bump		DNS	$Re_L = 1,000,000$	0 – 38.91
$\beta 1$		WRLES	$Re_{\delta_1^o} = 450$	0 – 1.18
m13		WRLES	$Re_{\delta_1^o} = 450$	0 – 1.7
$\beta 2$		WRLES	$Re_{\delta_1^o} = 450$	0 – 2.31
m16		WRLES	$Re_{\delta_1^o} = 450$	0 – 2.95
m18		WRLES	$Re_{\delta_1^o} = 450$	0 – 4.90
ZPG		DNS	$Re_{\delta_1^o} = 454$	~ 0

Table 5.1: Turbulent BL datasets. Three types of BLs are examined: flow over an airfoil, a Gaussian bump, and a flat-plate. For flat-plates, including ZPG, the reference Reynolds number is computed based on the displacement thickness at the inlet, δ_1^o . The reported values of β are associated with the APG region $Re_{\delta_1} \leq 6500$.

system, assuming the explicit curvature effects are insignificant –an assumption that is valid for the Wing and Bump datasets [162, 7, 5]. Therefore, for simplicity, in all cases, including the flat-plates, x and y denote the wall-tangential and wall-normal directions, respectively.

5.2.1 Wing dataset

The datasets for the Wing simulations correspond to the suction side of the NACA-4412 airfoil (Fig. 5.1) at an angle of attack of 5° [5]. Referred to as the Wing case, the Reynolds number based on the chord length (c) is $Re_c = U_\infty c / \nu = 400,000$, where U_∞ denotes the free-stream velocity. The flow experiences deceleration in the streamwise direction (adverse pressure gradient) due to surface curvature, resulting in Clauser parameter values ranging between $0 < \beta < 40$ along the chord length $\xi/c < 0.95$. It is worth noting that the reported values of β slightly differ from Ref. [5] due to the use of inviscid velocity as the velocity scale for defining

$$\beta = -\rho U_{io} \frac{dU_{io}}{dx} \frac{\delta_1}{\tau_w}, \quad (5.16)$$

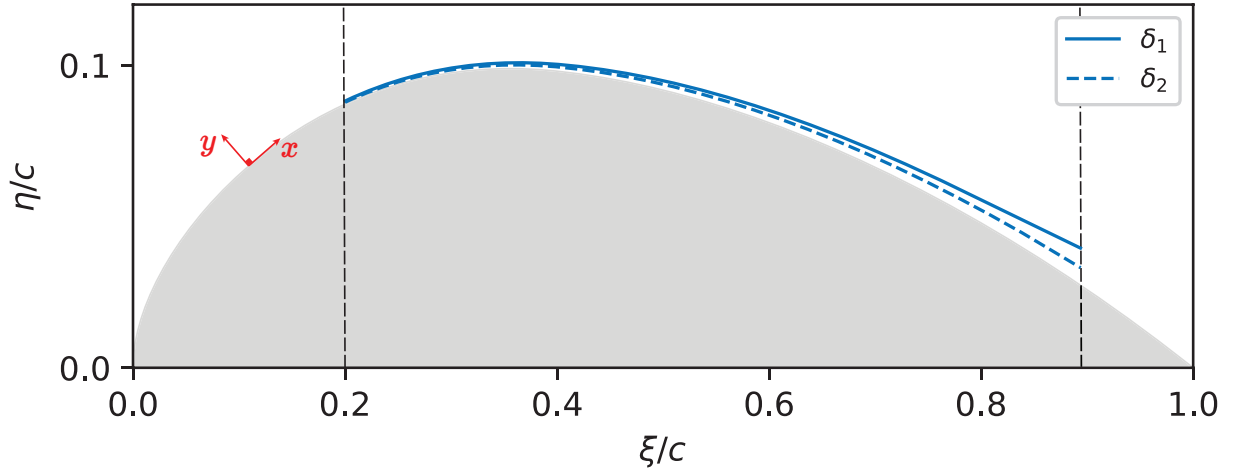


Figure 5.1: The suction side of NACA-4412; the region of interest in this study spans from $\xi/c = 0.2$ to $\xi/c = 0.9$. The solid and dashed blue lines denote the displacement and momentum thicknesses, respectively. The red arrows represent the (local) tangent-normal coordination system represented by $x - y$.

which differs from Eq. 1.2. Figure 5.2 (a) illustrates the shape factor for the Wing data under adverse pressure gradient (APG); as expected, the shape factor increases monotonically due to the APG effect, leading to boundary layer thickening. The Clauser parameter β is depicted with respect to Re_τ in Figure 5.2 (b). It's noteworthy that Re_τ exhibits a reversal trend: typically, Re_τ increases downstream in boundary layers, as in zero pressure gradient (ZPG) boundary layers; however, for the flow over the airfoil, Re_τ shows an increasing trend followed by a decreasing behavior at higher β . This is because the friction Reynolds number Re_τ , which represents the ratio between the outer region length scale, δ (or δ_{99}), and the viscous length scale δ_ν , decreases due to the influence of severe APG.

The Wing dataset was simulated by well-resolved LES on the open-source nek-5000 solver, which operates based on the spectral-element method developed by Ref. [127]. The LES filtering technique follows the approximate deconvolution relaxation-term (ADM-RT) sub-grid model developed by Ref. [141]. A RANS simulation provides boundary conditions at the inlet, upper, and lower sides, while a local-stress outflow condition is utilized for the rear side of the domain (Ref. [35]). The mesh is generated based on the wall-shear stress from RANS simulations to ensure a

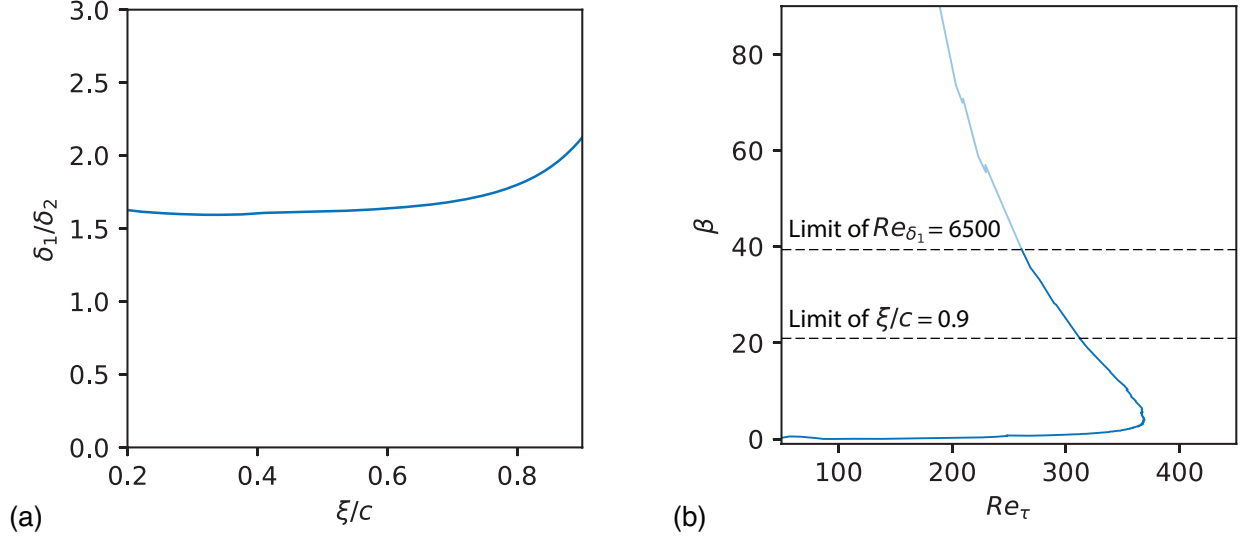


Figure 5.2: Wing dataset; the BL shape factor with respect to ξ (a), and the Clasuer parameter with respect to friction Reynolds number Re_τ (b).

resolution of approximately $(\Delta\xi^+, \Delta\eta^+, \Delta z^+) < (18, 0.64, 11.9)$ in the turbulent region of the domain, where superscript (+) denotes wall-units (normalized by $\delta_v = \nu/u_\tau$, where $u_\tau = \sqrt{\tau_w/\rho}$ is the friction velocity) and z represents the spanwise direction. For further information regarding the numerical setup and its validity, please visit Refs. [163, 6, 5].

5.2.2 Bump dataset

The bump dataset corresponds to a DNS of a turbulent BL over a two-dimensional Gaussian bump, as investigated by Ref. [7]. The surface of the bump is defined by the equation $\eta(\xi) = h \exp(-(\xi/\xi_0)^2)$, where η represents the y -axis in the Cartesian coordinate system. This geometry, illustrated in Fig. 5.7 (bottom), is designed to replicate the three-dimensional Boeing company bump flow (Ref. [146]) experimentally studied by Ref. [175]. In the bump's surface relation, $h = 0.085L$ and $\xi_0 = 0.195L$ are length parameters describing the bump's dimensions, with $L = 0.9144$ m representing the length of the square cross-section of the wind tunnel used in the experimental setup. The flow is characterized by a reference Reynolds number $Re_L = U_\infty L/\nu = 1,000,000$, where the dimensional free-stream velocity $U_\infty = 16.4$ m/s, matching standard sea level conditions, resulting

in an incompressible flow with Mach number $M = 0.045$. This flow experiences an alternating pressure gradient due to surface curvature, resulting in a weak APG region upstream, followed by a strong FPG behind the bump's peak at $\xi/L = 0$. A severe APG causes flow separation downstream of the bump's peak ($\beta \rightarrow \infty$) about $\xi/L = 0.2$, though the BL re-attaches and continues developing at $\xi/L = 0.4$ under a weak FPG. Figure 5.3 exhibits the BL's shape factor, e.g., the ratio of δ_1/δ_2 , with respect to ξ . A natural impact of FPG is reducing the shape factor, as is evident upstream of the bump's peak. A decreasing shape factor indicates a thinner boundary layer with a sharper velocity profile. APG, on the other hand, increases the ratio between the displacement and momentum thicknesses, attributed to BL thickening.

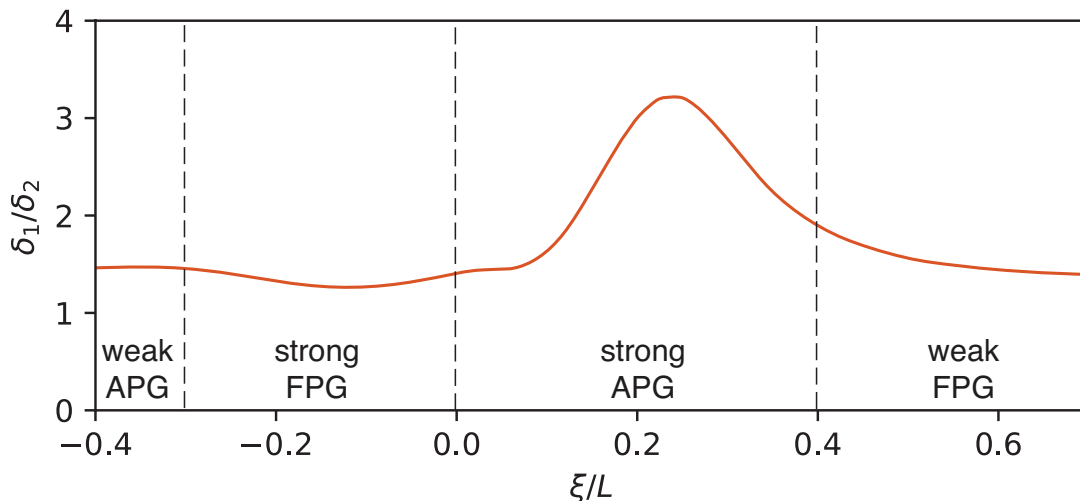


Figure 5.3: Boundary layer shape factor, δ_1/δ_2 , in the bump flow with respect to ξ . Flow separation causes a substantial increase in the shape factor about $\xi/L = 0.25$.

The DNS simulation was performed using the stabilized finite element method by applying trilinear hexahedral elements and second-order accurate, implicit time integration following Refs. [173, 69]. No-slip no-penetration BC is imposed at the bump's surface, while the top BC (at $\eta/L = 0.5$) was modeled as an inviscid wall offset by the RANS predicted displacement thickness described above with zero transpiration (zero velocity component normal to the surface) and zero traction. The inflow is generated by the synthetic turbulence generator (STG) (Ref. [143]). Finally, for the outflow, weak enforcement of zero pressure was applied along with zero traction. The computa-

tional grid used for the DNS was structured with a total of 554 million points, which yields spacing $(\Delta\xi^+, \Delta\eta^+, \Delta z^+) < (15, 10, 8)$ with the minimum $\Delta\eta^+ = 0.1$ near the surface, in wall units. The reader is suggested to visit [7] to obtain more information about the numerical setup and validity of the simulation.

5.2.3 Flat-plate dataset

For comparison purposes, we investigate a series of turbulent BLs developing over a flat-plate. These simulations are conducted using well-resolved LES techniques, employing the ADM-RT sub-grid model, similar to the approach used for the airfoil simulations. The simulations are executed using the SIMSON code, a pseudo-spectral-based solver developed by [22]. Specifically, we examine the ZPG case studied by Ref. [37] and APG cases investigated by Refs. [13, 14], both with similar numerical setup that results in spatial resolution $(\Delta x^+, \Delta y^+, \Delta z^+) = (20, 0.2-30, 10)$ in wall units. However, for the flat-plates with APG, the pressure gradient was imposed through the variation of the free-stream velocity at the top of the numerical domain, following the near-equilibrium definition by Ref. [155] using a power-law function for the edge velocity. It is important to note that in the context of flat-plate simulations, the wall-tangential and wall-normal coordinates are aligned with the Cartesian coordinate system, and hence no mapping is required.

Figures 5.4 (a, b) show the skin friction coefficient with respect to the streamwise position and the Clauser parameter with respect to Re_τ , respectively. For all the APG flat-plates, C_f is always lower than the ZPG case. This is because of the BL thickening caused by flow deceleration. According to Fig. 5.4 (b), in contrast to the trend of Re_τ for the Wing case (shown in Fig. 5.2), for the flat-plates, Re_τ monotonically increases under APG. The plots of β also exhibit that $m18$ yields the strongest APG effect, with the maximum hardly reaching $\beta = 5$, while $\beta1$ is the weakest case. Moreover, despite the region upstream (that is still under the effect of inflow conditions), the $\beta1$ and $\beta2$ cases have approximately constant β values, reading values of one and two, respectively. Therefore,

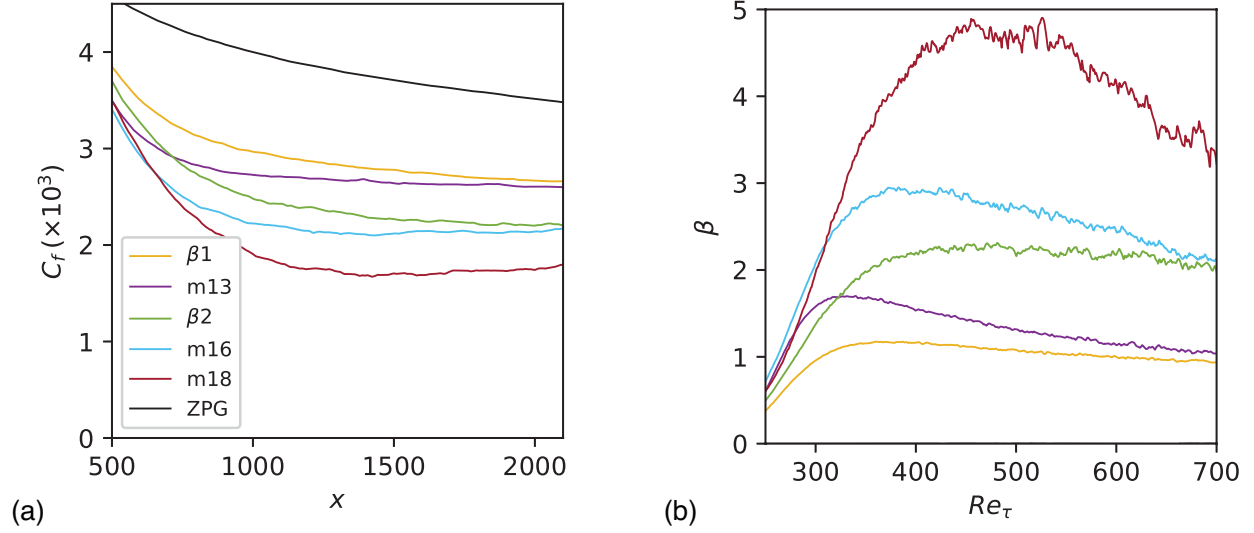


Figure 5.4: Flat-plate dataset; plots of the skin friction coefficient with respect to x (a), and the Clauser parameter with respect to Re_τ (b).

according to the definition of equilibrium discussed in section 1.2.2, they are in semi-equilibrium condition.

5.2.4 Numerical techniques for AMI analysis

Because the AMI analysis is established in curvilinear coordination, for the Wing and Bump flows, an appropriate tensor rotation is employed to map the flow statistics from the Cartesian frame of reference to local orthogonal directions. Additionally, as detailed in Section 5.1, we utilize the methodology developed by Ref. [53] to quantify the locally reconstructed inviscid velocity at each streamwise position and predict the location of the BL edge based on δ_{99} . To check the robustness, especially in the Bump case with the most substantial curvature, we examine the normal rays to the surface (in y -direction) at each streamwise location, confirming they neither intersect within the BL nor near the BL edge. Figures 5.5 (a, b) illustrate U_i by dashed lines, alongside \bar{u} normalized by U_∞ , at three distinct streamwise locations for Wing and Bump, respectively. Notably, there is a remarkable agreement between U_i and \bar{u} profiles within the outer flow, marked beyond the black symbols that indicate the prediction of δ_{99} . For example, the three streamwise locations in the Bump

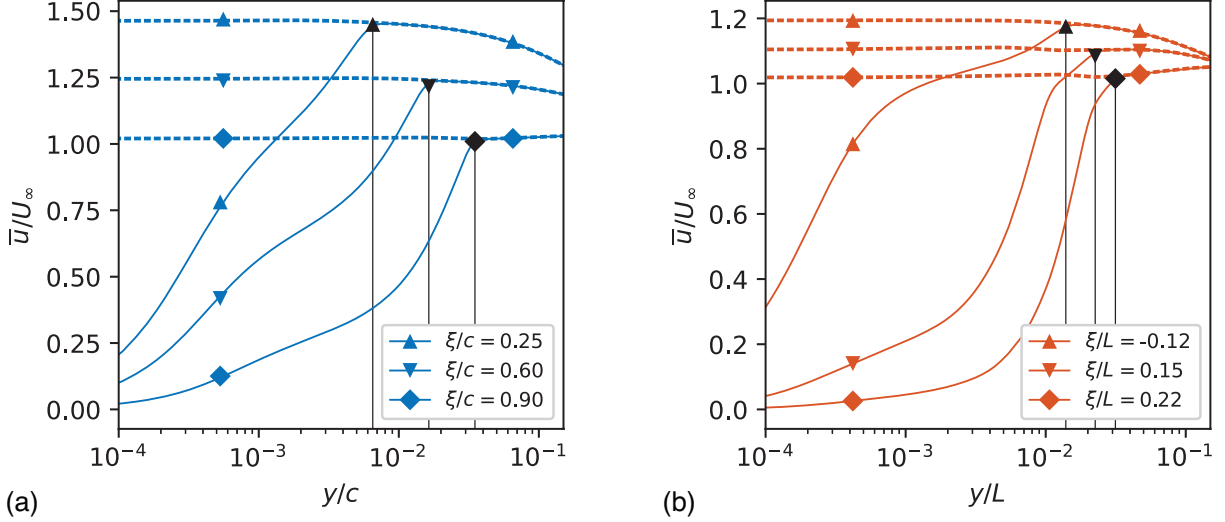


Figure 5.5: Calculation of the locally reconstructed inviscid velocity, U_i , along the wall-normal direction for (a) Wing and (b) Bump datasets. The solid and dashed lines represent the mean streamwise and inviscid velocity profiles normalized by the free-stream velocity, U_∞ . The solid black lines denote the location of δ_{99} computed by the local reconstruction method.

flow are associated with the region under strong FPG $\xi/L = -0.12$, strong APG $\xi/L = 0.15$, and very close to the separation point $\xi/L = 0.22$. These plots confirm that the local reconstruction method is capable of quantifying U_i , δ_{99} , and the edge velocity accurately. It is important to note that the trends observed in the computed U_{io} and predicted U_e are similar (see Fig. A.3 in Appendix A). However, when using U_{io} , we noticed a smaller error in the budget of the AMI equation defined as

$$\epsilon(x) = \frac{|C_f - 2RHS|}{C_f}, \quad (5.17)$$

for both the Wing and Bump cases. Here, RHS represents the sum of all terms on the right-hand side of Eq. 5.7.

To compute the streamwise derivatives of flow statistics required for closing the AMI budget, we utilize the second-order central finite difference scheme, excluding the end grid points. However, it's worth noting that computing these derivatives can amplify natural turbulent noise, which tends to increase ϵ (Refs. [38, 81]). Furthermore, for the numerical wall-normal integration in the AMI

analysis, we employ the trapezoidal scheme introduced in 3.2. It is important to recall that the computation of derivatives and integration is conducted concerning the curvilinear coordinates.

5.3 Results and Analysis

This section applies Eq. 5.7 to the set of turbulent introduced in section 5.2. The aim is to investigate how non-zero pressure gradients –either adverse or favorable– affect the AMI equation’s budget, specifically *turbulent torque*, and consequently, the skin friction coefficient.

Initially, we analyze the AMI equation for the Wing dataset subjected to an adverse pressure gradient. Subsequently, we delve into a more intricate scenario, such as the flow over a Gaussian bump, which encounters alternating adverse-favorable pressure gradients. Finally, we narrow our focus to the region under adverse pressure gradient conditions to explore the upstream history effects on turbulent statistics.

5.3.1 Flow over airfoil

In this section, we apply the AMI analysis to a series of turbulent BLs over the suction side of a NACA-4412 airfoil at an angle of attack of 5° , referred to as the Wing case in table 5.1. The objective is to assess the accuracy of our methodology in handling BLs subjected to curvature-induced pressure gradients.

Figure 5.6 presents the budget of the AMI equation (Eq. 5.7) for turbulent BL developing over the suction side of an airfoil, namely the Wing case described in table 5.1; the top figure shows the absolute contributions of each flow phenomena, and the bottom figure exhibits the relative (normalized by $C_f/2$) contributions. The budget includes the four significant flow phenomena in the AMI equation, namely *laminar friction*, *turbulent torque*, *pressure gradient*, and *mean flux*. The

unsteady effects and terms neglected by the BL approximation, referred to as *negligible terms*, are not included. This omission is justified by their limited contribution to the skin friction coefficient away from separation (see Appendix A. The *negligible terms* are expected to become more significant as the flow approaches the separation point, which does not occur in the Wing case. In this case, we opt for $\ell = 4.54\delta_2$, a value derived from the Blasius solution based on momentum thickness. This selection results in a streamwise-averaged ϵ of less than 6%, underscoring the validity and accuracy of the AMI methodology for BL undergoing weak-to-moderate APG. Similar observations were made in ZPG transitional and turbulent incompressible BLs [38, 82], as well as in high-speed ZPG turbulent BLs [81]. In all these cases, the primary source of error was the computation of streamwise derivatives, $\partial(\cdot)/\partial x$, in the AMI equation. It is worth noting that this error would be further diminished with additional (time) averaging. Compared with ZPG turbulent BLs, APG turbulent BLs exhibit a faster reduction of skin friction coefficient (shown with a black line in Fig. 5.6 (top)) as the flow develops downstream. This trend quantitatively matches with the budget of the right-hand side of the AMI equation, Eq. 5.7 (shown in Fig. A.1).

As depicted in Fig. 5.6, the negative contribution of *pressure gradient* to $C_f/2$ consistently strengthens due to the curvature of the airfoil, especially, its growth ramps up as the flow approaches the trailing edge. The normalized contribution of *pressure gradient* (Fig. 5.6 bottom) exhibits a range from approximately 0% upstream to more than -600% , highlighting the profound impact of pressure gradient on the transport of momentum deficit and, consequently, wall-shear stress. Although *pressure gradient* ramps up rapidly, it does not exert a significant impact on *laminar friction*; this flow phenomenon – with about 4% contribution to $C_f/2$ (Fig. 5.6 (bottom)) – gradually diminishes downstream in fully turbulent BLs, exhibiting behavior similar to ZPG turbulent BLs. Therefore, it is reasonable to argue that *laminar friction* shall be neglected from the AMI budget for turbulent BLs without any flow control scheme.

In contrast to the modest impact of *laminar friction* on wall shear stress, the turbulence-induced enhancement of surface friction through *turbulent torque* in the AMI equation is substantial. Its

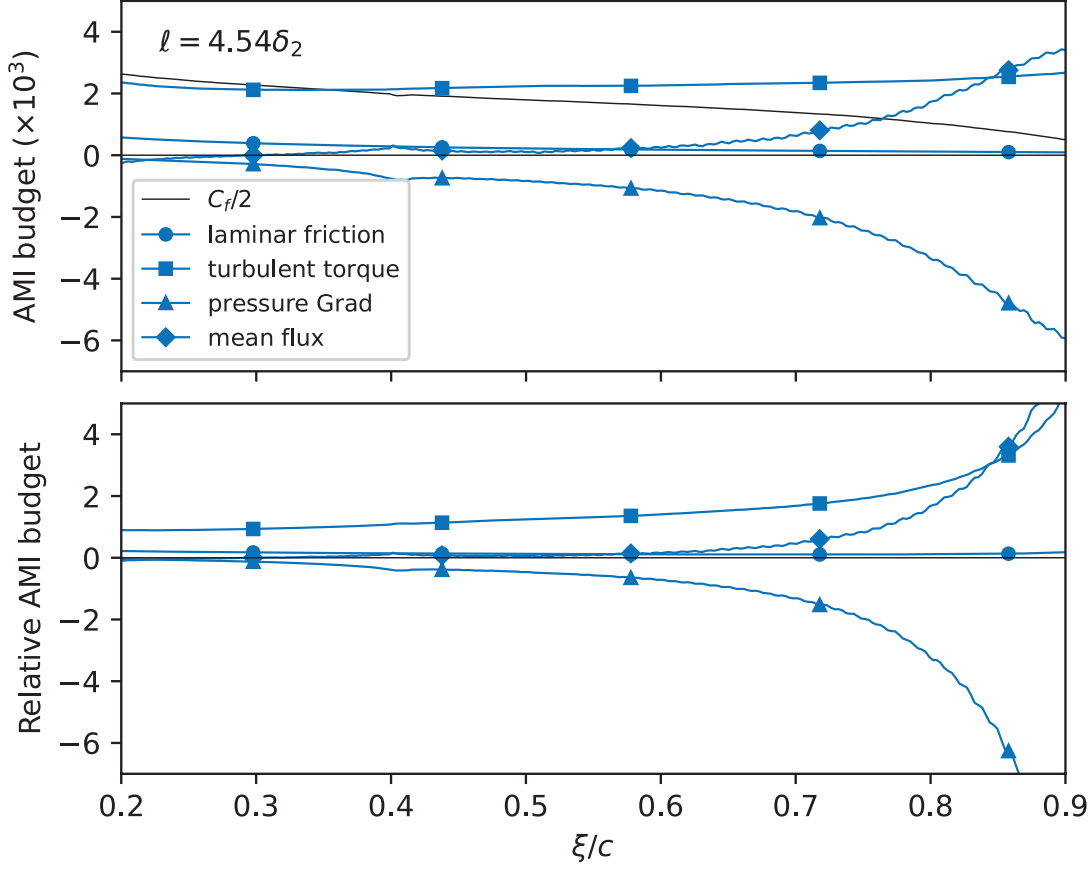


Figure 5.6: The AMI budget with respect to the chord length, ξ/c , for the Wing case (table 5.1); (a) the absolute budget, and (b) the relative budget normalized by $C_f/2$.

relative contribution (normalized by $C_f/2$) is approximately 100% within the range of $0.2 < \xi/c < 0.4$, where $\beta < 2$ (weak-to-moderate pressure gradient); an observation analogous to ZPG turbulent BLs [82]. Generally, the upstream-to-downstream variation of *turbulent torque*, when ℓ is obtained from the Blasius solution, is relatively small. This difference amounts to approximately $\sim 13\%$ from $\xi/c = 0.2$ to $\xi/c = 0.9$, while the change in *pressure gradient* is significant (from $\beta \approx 0$ to $\beta \approx 20$). These observations suggest that *turbulent torque* is not necessarily correlated with the strength of adverse pressure gradient. Instead, the author posits that *turbulent torque* is more closely correlated with the rate at which APG changes. As the rate of change of APG increases, *turbulent torque* becomes more pronounced. A similar observation is documented by [5], where the FIK identity was utilized to establish a connection between the variation of the so-called turbulent contribution, denoted by C_f^T , and the rate of change of β .

Since the non-equilibrium caused by pressure gradient ramps up downstream, *mean flux* is the flow phenomena in the AMI equation resisting it. The friction enhancement by *mean flux*, especially, becomes significant for $\beta > 2$, where the impact of the pressure gradient (on the transport of momentum deficit) is two times greater than wall shear stress. In fully-turbulent ZPG incompressible BLs, *mean flux* negatively contributes to $C_f/2$, while its upstream-to-downstream variation was reported insignificant in Refs. [38, 82], merely because these flows are in the equilibrium state. Conversely, in this case, *mean flux* increases C_f , partially alleviating the enormous negative contribution of *pressure gradient*. In fact, the friction enhancement of *mean flux* exceeds *turbulent torque*'s beyond $\xi/c = 0.85$ ($\beta > 10$), becoming the dominant contributor to C_f .

5.3.2 Flow over Gaussian bump

In this section, we extend the application of the AMI equation to include a DNS dataset of flow over a two-dimensional Gaussian bump, referred to as the Bump case in table 5.1 (Ref. [7]). This presents a more complex scenario due to the alternate adverse and favorable pressure gradients induced by the bump's surface curvature. Specifically, the boundary layer experiences a significant FPG from $\xi/L = -0.29$ to the peak of the bump at $\xi/L = 0$, followed by an extreme APG downstream, leading to boundary layer separation where $\tau_w \leq 0$.

Within the streamwise range of interest in this paper, the averaged error (ϵ) is maintained at $\epsilon < 10\%$. Downstream of the bump's peak, characterized by an adverse pressure gradient ($\xi/L \leq 0.18$), the averaged ϵ further diminishes to approximately 6%, followed by a noticeable escalation approaching the separation region; plot of $C_f/2$ compared with the sum of the right-hand side of the AMI equation is presented in Fig. A.2. The author attributes this increase primarily to inadequate (time) averaging, a consequence of the unstable separation bubble. As discussed in section 5.2.4, calculating the streamwise derivatives for the AMI analysis that amplifies the inherent turbulence noise is another source of error. Therefore, improved (time) averaging techniques are expected to

enhance the accuracy of these derivative computations, ultimately resulting in reduced errors within the AMI budget.

According to Fig. 5.7 (bottom), the bump flow undergoes alternating adverse and favorable pressure gradients due to the geometry of the surface; far upstream, the BL encounters weak APG followed by relatively strong FPG on the left side of the bump's peak. From $0 \leq \xi/c \leq 0.4$ the BL experiences vigorous APG, leading to flow separation at $\sim \xi/c = 0.2$. The AMI budget, with $\ell = 4.54\delta_2$ (derived from the Blasius solution), is illustrated in the middle panel of figure 5.7 for the four primary flow phenomena on the right-hand side of the AMI equation: *laminar friction*, *turbulent torque*, *pressure gradient*, and *mean flux*. Note that in figure 5.7, the unsteady effects and terms neglected by BL approximations, i.e., *negligible terms*, are not included (visit Appendix A for the entire AMI budget). The maximum contribution of these terms is determined to be 8% only within the separation region, while before separation, the contribution is less than 2%.

Within the FPG region, the skin friction coefficient initially increases, reaching a peak at $\xi/L = -0.14$. According to the AMI budget, this enhancement is primarily attributed to the (simultaneous) increase of *turbulent torque* upstream of $\xi/L \approx -0.2$. This increase can be attributed to both the upstream weak APG and the early effects of FPG (before flow undergoes re-laminarization). The *turbulent torque*'s enhancement occurs while the contributions from *pressure gradient* and *mean flux* mostly offset each other. *Pressure gradient* positively influences C_f , aligning with the curvature of the bump. Conversely, *mean flux* opposes the friction enhancement by FPG and turbulence. This negative contribution becomes more significant downstream of $\xi/L = -0.14$, resisting the rise in *laminar friction* because of the phenomenon of so-called re-laminarization caused by the effect of FPG.

Given the moderate Reynolds number of the flow, re-laminarization is anticipated, yet RANS turbulent models have failed to predict it (Ref. [7]); however, the AMI analysis quantitatively captures this phenomenon showing the feasibility of implementing the AMI approach – or integral methods in general – to develop turbulent models to predict re-laminarization. During this so-called re-

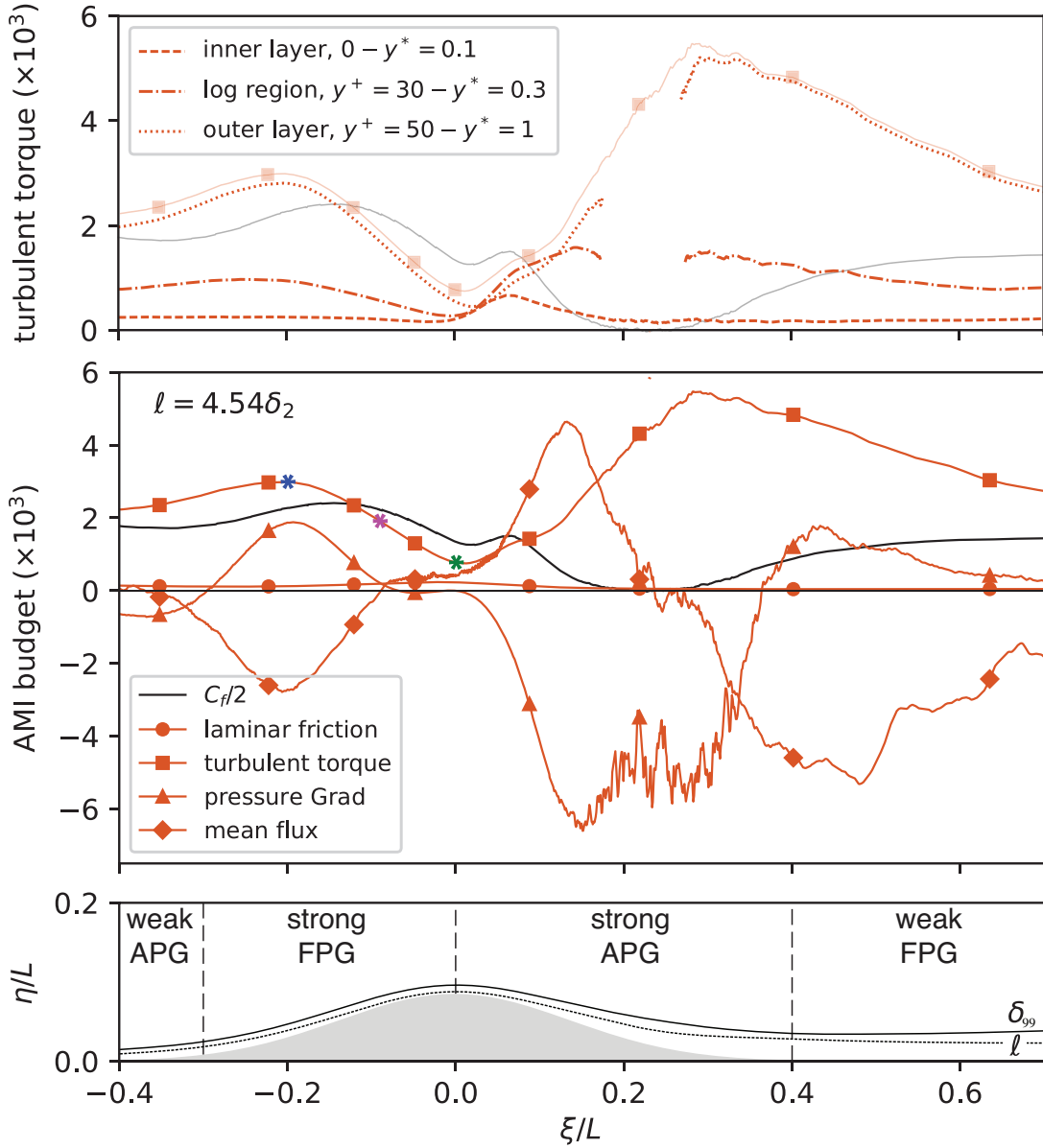


Figure 5.7: The AMI budget (middle) for BL over a Gaussian bump with respect to the normalized streamwise location, ξ/L ; dotted and solid black lines in the bottom panel represent the AMI length scale ℓ and BL thickness δ_{99} , respectively. The top panel exhibits *turbulent torque* within the different regions of BL; $y^* = y/\delta_{99}$ and y^+ denote the wall-normal position normalized by outer and inner scales, respectively. Symbol * represents three streamwise locations where the turbulent statistics are compared in figure 5.8.

laminarization process, *laminar friction* increases from 10% to over 17% of the local skin friction coefficient, concurrently accompanied by a significant decline in *turbulent torque* from approximately 150% to 55% of the skin friction coefficient. Interestingly, downstream of the maximum

wall friction (at $\xi/L \approx -0.1$), the reduction of *turbulent torque* surpasses the decline in $C_f/2$, highlighting the influence of FPG-induced re-laminarization.

To further explore re-laminarization, the absolute and outer-scaled profiles of Reynolds shear stress and turbulent kinetic energy, $k = \frac{1}{2} (\overline{u'u'} + \overline{v'v'} + \overline{w'w'})$, are presented in figure 5.8; these profiles are plotted at three distinct streamwise locations: $\xi/L = -0.2$, $\xi/L = -0.14$, and $\xi/L = -0.01$ (denoted by * in the middle panel of Fig. 5.7). As depicted in Fig. 5.8 (a), $-\overline{u'v'}$ is more pronounced at $\xi/L = -0.2$, where *turbulent torque* peaks. However, as the re-laminarization effect accumulates downstream, the Reynolds shear stress is shifted towards the surface, with its maximum approaching the wall within the buffer region. Additionally, the integral (or total) shear generated by turbulence weakens downstream, where the re-laminarization effect accumulates at $\xi/L = -0.01$. A similar trend is also observed for the outer-scaled profiles of Reynolds shear stress (Fig. 5.8 (b)), showing the increase of denominator, U_{io} , downstream is inadequate to reverse the order of profiles. The author attributes the downstream weakening of Reynolds shear stress caused by re-laminarization to the wall constraint on the turbulent shear. As the turbulent shear moves towards the surface, the wall further suppresses the production of v' , and thus $u'v'$. Therefore, although the reduction of *turbulent torque* partially corresponds to the increase in its denominator U_{io}^2 (explicit effect of FPG), Reynolds shear stress is also weaker and less efficient due to re-laminarization as it is pushed toward the wall.

Surprisingly, according to the absolute profile of turbulent kinetic energy (Fig. 5.8 (c)), k is strongest at $\xi/L = -0.01$, whereas that is the location *turbulent torque* is minimum, and re-laminarization is accumulated. Moreover, re-laminarization does not shift where the maximum turbulent kinetic energy occurs, i.e., within the buffer layer. These findings elucidate that the phenomenon commonly referred to as re-laminarization is more akin to turbulence deactivation, where turbulence becomes one-dimensional, i.e., $\overline{u'u'}$ increases, but streamwise and wall-normal velocities are less correlated. This process is also referred to as “frozen turbulence” since the higher turbulent intensity (k) is frozen and does not contribute to the turbulent transport of momentum via

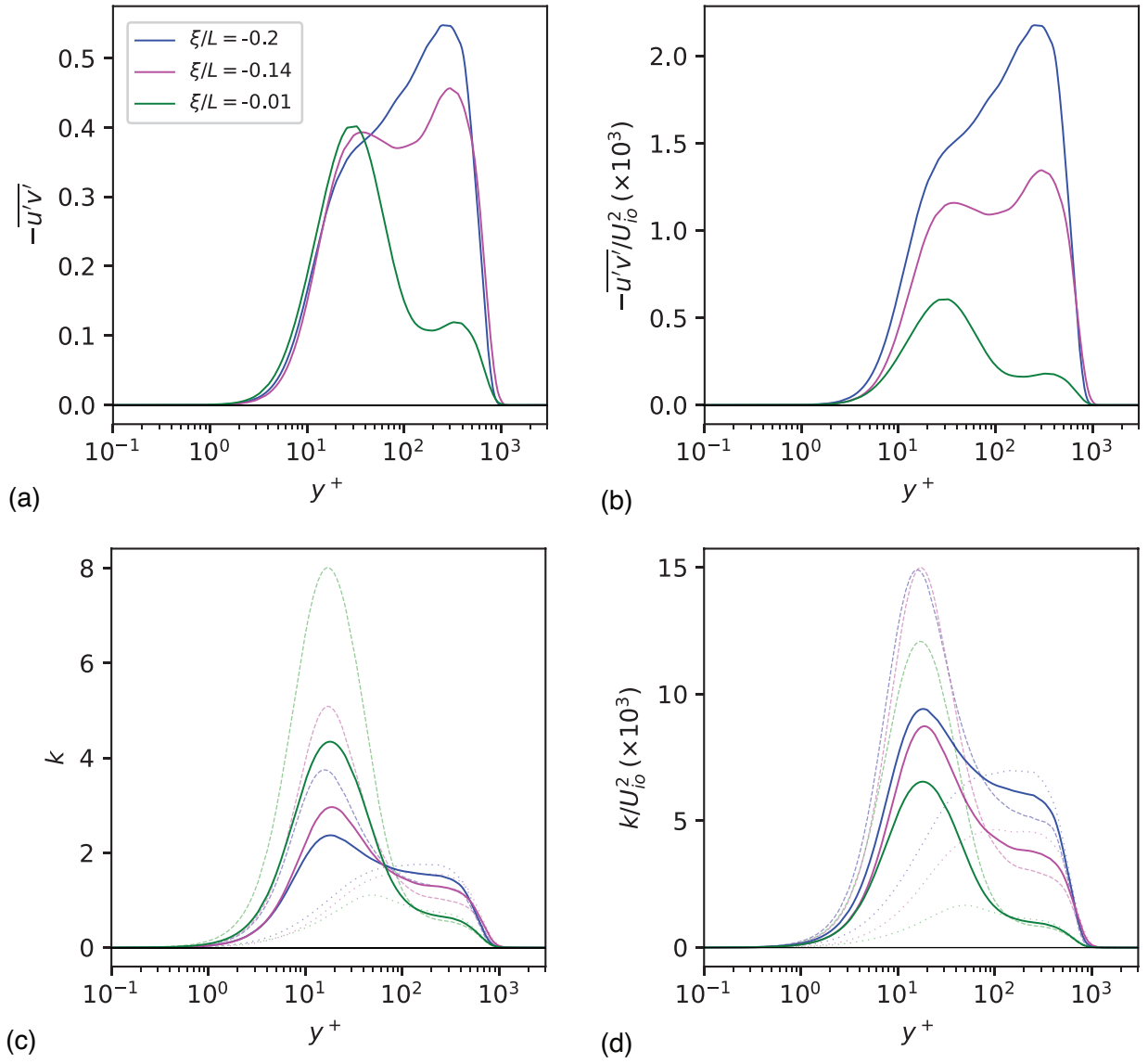


Figure 5.8: Reynolds shear stress and turbulent kinetic energy profiles in the bump flow with respect to y^+ : absolute (a, c) and outer-scaled (normalized by U_{io}^2) (b, d). In (c, d), shaded dashed and dotted lines are associated with $\overline{u'u'}$ and $\overline{v'v'} + \overline{w'w'}$, respectively.

Reynolds shear stress [117, 119]. The one-dimensionalization of turbulence is evident from the substantial enhancement in the profiles of $\overline{u'u'}$ (shaded dashed lines in Fig. 5.8 (c)) from $\xi/L = -0.2$ to $\xi/L = -0.01$, while the sum of $\overline{v'v'}$ and $\overline{w'w'}$ weakens downstream.

The impact of re-laminarization on turbulence is further examined in Fig. 5.7 (top), illustrating the contribution of *turbulent torque* within the inner layer, logarithmic region, and the outer layer of the

BL. The boundaries of these three regions are defined based on the approximation of [133] for wall-bounded flows. Within the range of applied FPG and re-laminarization, *turbulent torque* diminishes in both the logarithmic layer and outer region, with a negligible alteration in the inner layer. The spatial reduction rate in the outer layer mirrors that of the total *turbulent torque*; nevertheless, this rate is comparatively smaller for the logarithmic region and exhibits an inverse correlation with the distance from the wall. Consequently, based on the AMI analysis for moderate to high Reynolds numbers, we deduce that the direct influence of FPG and re-laminarization is more pronounced on the logarithmic region and the outer layer of the BL. Assuming the impact of FPG generated by surface curvature similar to a turbulent control scheme, this observation aligns with findings from flow control studies in Ref. [23] & [21], indicating that as the Reynolds number increases, targeting the near-wall turbulence becomes less crucial for reducing the wall-shear stress since the foot-print of the logarithmic region and the outer layer becomes more profound on the skin friction.

Just upstream of the bump's peak, while the flow is still experiencing FPG and re-laminarization, *pressure gradient* and *mean flux* reach an equilibrium state, exhibiting negligible variations with the streamwise direction. However, this equilibrium is disrupted immediately downstream of the peak, where the flow encounters an intense adverse pressure gradient (APG). Re-laminarization undergoes a reversal, marked by a pseudo-re-transition to turbulence, during which *turbulent torque* increases at a slightly higher rate than the rise of $C_f/2$ (see Fig. 5.7 middle). This phenomenon is reminiscent of observations in prior studies such as [38] and [82] for transitional ZPG BLs. Examining the top panel of Figure 5.7, it is evident that the boost in *turbulent torque* is not confined solely to the logarithmic region and the outer layer; the inner layer's Reynolds shear stress also experiences a significant increase. Notably, during the re-transition, the contribution of the logarithmic region to *turbulent torque* surpasses that of the outer layer, becoming the dominant region. The author attributes this observation to the previously discussed stronger weakening effect of FPG on the outer layer.

A noteworthy difference between transitional ZPG BLs and APG re-transition lies in the role of

mean flux. Under the influence of APG, this flow phenomenon does not resist the *turbulent torque*. On the other hand, it significantly contributes to C_f to counteract the substantial negative contribution of *pressure gradient*. Despite the friction enhancements by both *turbulent torque* and *mean flux*, they prove insufficient, as APG forces the flow to separate at approximately $\xi/L = 0.2$. In the separated flow region, where $C_f \leq 0$, statistics are noisy due to an unstable separation bubble—characterized by several frequencies according to Refs. [144, 116]—, and the BL approximations are naturally invalidated. It is essential to note that the AMI equation, obtained solely from conservation equations, does not depend on the validity of the boundary layer approximation. Therefore, accurate results from AMI can be expected with sufficient (time) averaging, even for separated flows. In the top panel of Figure 5.7, the plots of *turbulent torque* within the logarithmic region and the outer layer are omitted. This exclusion is due to the undetermined nature of y^+ as $\tau_w \rightarrow 0$ in the separated flow region. However, within the inner layer, the contribution of *turbulent torque* remains unchanged where the flow is (weakly) detached (or separated). This observation suggests that the primary impact of separation is limited in the logarithmic region and the outer layer, while the inner layer is weakly impacted by APG and separation; Finally, further downstream of the bump surface ($\xi/L \geq 0.4$), weak FPG causes the flow to reattach. Although the flow is significantly influenced by the upstream alternating pressure gradient, as the *pressure gradient* approaches zero downstream, the boundary layer behavior resembles that of fully turbulent ZPGBL. *Turbulent torque* begins reducing downstream, and *mean flux* roughly converges to a negative value.

This section presented the application of the AMI analysis for investigating a complex non-equilibrium BL over a two-dimensional Gaussian bump. The flow undergoes alternating adverse and favorable pressure gradients, influencing the turbulence structures. Notably, the strong FPG upstream of the bump’s peak induces re-laminarization, a phenomenon effectively captured and quantified by the AMI analysis. The AMI analysis in this section revealed the enhancement of *laminar friction* occurring simultaneously with a significant reduction in *turbulent torque*. In the subsequent sections of this paper, our attention is limited to the region featuring moderate-to-strong APG, $\beta \leq 40$.

5.3.3 Adverse pressure gradient & history effects

In the preceding sections, we delved into the application of the AMI equation, Eq. 5.7, for turbulent BLs over an airfoil (Wing case) and a two-dimensional Gaussian bump (Bump case). Both scenarios involve a non-zero pressure gradient due to surface curvature. In this section, we limit our focus to BLs encountering APG. We undertake a comparative analysis, contrasting the AMI budget and statistics of the Wing and Bump cases with a set of flat-plates that experience weak-to-moderate APG, as detailed in the dataset provided in table 5.1. For our analysis, we opt for an AMI length scale, ℓ , determined by the displacement thickness derived from the laminar Blasius solution, i.e., $\ell = 1.75\delta_1$. This selection is justified by considering the influence of pressure gradient and adhering to the classical definition of the non-equilibrium Clauser parameter, both of which are functions of δ_1 . Additionally, we constrain our investigation to the streamwise positions corresponding to $1400 \leq Re_{\delta_1} \leq 6500$, where $Re_{\delta_1} = U_{io}\delta_1/\nu$. Within this refined range, $0 \leq \beta < 40$ and $0 \leq \beta_\ell < 20$, as illustrated in Figs. 5.11 (a, b). For the Bump case, specifically, due to the alternating adverse and favorable pressure gradients, we limit our analysis to the right-hand side of the bump's peak from $\xi/L \approx 0$ to $\xi/L \approx 0.15$, upstream of the separation bubble.

The primary components of the AMI equation are illustrated in figures 5.9 within the specified range of $1400 \leq Re_{\delta_1} \leq 6500$. To facilitate comparison, a ZPG dataset is represented in black. Notably, *laminar friction* exhibits consistent behavior across all cases due to the uniform determination of ℓ based on the Blasius solution, resulting in a constant AMI coefficient for all instances. In addition, the variation of δ_1 with respect to Re_{δ_1} is also not significantly influenced by the strength of APG, leading to a close alignment of *laminar friction* with the ZPG BL.

Despite the relatively modest contribution of *laminar friction*, it's noteworthy that *turbulent torque* emerges as the predominant flow phenomenon in the AMI budget for all turbulent BLs. Figure 5.9 (b) exhibits the explicit turbulence enhancement of skin friction. Across all flat-plates, as detailed in table 5.1, the incremental change in *turbulent torque* from upstream to downstream remains

modest, with the highest variation at only 8%, associated with case *m18*. Notably, for flat-plates sharing similar base flow and configuration parameters, such as inlet Reynolds number, the trend and magnitude of *turbulent torque* exhibit close similarity. For instance, the difference between cases *$\beta 1$* and *m18* never exceeds 7%. These observations indicate that the variation in *turbulent torque* primarily depends on flow configurations and Reynolds number, while weak-to-moderate APG has an insignificant effect on the wall-normal integral of (or total) Reynolds shear stress. This conclusion gains further support from the Wing case, where there is a substantial change in *pressure gradient* (as depicted in Fig. 5.9 (c)), ranging from $\beta \approx 0$ to $\beta \approx 40$. Despite this significant variation in *pressure gradient*, the trend of *turbulent torque* results in an upstream-to-downstream variation of only 13%.

Additionally, for the Wing case, when *turbulent torque* is plotted against Re_{δ_1} and with $\ell = 1.75\delta_1$, a weak increasing trend is observed within the range $1400 \leq Re_{\delta_1} < 2800$. This trend, however, reverses downstream of $Re_{\delta_1} = 2800$ and exhibits a monotonically decreasing behavior. Interestingly, According to Fig. 5.6 in which $\ell = 4.54\delta_2$, *turbulent torque* increases downstream of $\xi/c = 0.4$, showing an opposite trend from figure 5.9 (b). This opposite trend is attributed to the choice of ℓ and if it is defined based on δ_1 or δ_2 , and thus how the displacement or momentum thickness responds to APG. Nevertheless, both figures indicate that the trend of *turbulent torque* appears to correlate with the curvature of *pressure gradient* or the rate of change of β_ℓ not the strength of APG (absolute value of β). For example, as illustrated in Figure 5.9 (c), within the range $1400 \leq Re_{\delta_1} < 2800$, the curvature of *pressure gradient* is concave, indicating a faster rate of change in the strength of *pressure gradient*. However, downstream of $Re_{\delta_1} = 2800$, the curvature of *pressure gradient* becomes convex, aligning with the streamwise positions where the trend of *turbulent torque* reverses.

In the Bump case, downstream of its peak where the surface curvature imposes APG, the trend of *turbulent torque* is intricate due to the upstream re-laminarization (or turbulence deactivation). Within the range $1400 \leq Re_{\delta_1} < 2000$, *turbulent torque* experiences a substantial increase of about

63%. This augmentation primarily results from the so-called re-transition (turbulence re-activation) process occurring after applying APG. APG thickens the BL and pushes the Reynolds shear stress away from the surface, a process in contrast to what FPG does during re-laminarization. The enhancement of *turbulent torque* due to the re-transition process is quite similar to what was noted in Ref. [82] for incompressible ZPG transitional BLs. Furthermore, from $Re_{\delta_1} = 2000$ to $Re_{\delta_1} = 6500$, *turbulent torque* continues to increase monotonically by approximately 20%. This enhancement predominantly corresponds to the FPG history effects carried over into the APG region and it seems to gradually diminishes downstream as the history effects fade. The plots of *pressure gradient* in Fig. 5.9 (c) clearly demonstrate the carried-over effect of FPG into the APG region. Notably, *pressure gradient's* contribution to $C_f/2$ is positive within the range $1400 \leq Re_{\delta_1} < 2500$, despite this region belonging to the right-hand side of the bump's peak where $\beta > 0$. These findings suggest that the AMI equation, specifically the choice of ℓ , partially captures the FPG history effects, mostly mirrored in *pressure gradient* and *mean flux*. As discussed previously, *mean flux* is the term that resists non-equilibrium physics, such as transition and imposed pressure gradient. In ZPG turbulent boundary layers, this flow phenomenon roughly converges and contributes negatively to C_f . However, in the bump case, *mean flux* generates an increasingly negative contribution from $Re_{\delta_1} = 1400$ to $Re_{\delta_1} = 2000$ to resist the pseudo-re-transition to turbulence (re-activation of turbulence), a parallel observation to [38, 82] for ZPG transitional boundary layers. Beyond $Re_{\delta_1} = 2400$, where the re-transition process has weakened, and the carried-over FPG history has partially faded, *mean flux* begins to mostly compensate the severe negative contribution of *pressure gradient*; as APG strengthens, the *mean flux's* contribution approaches a positive value, eventually becomes the dominant contributor to C_f . A similar phenomenon occurs for the Wing case, where *mean flux* initiates from a negative value upstream, matching ZPG BL, yet increases and approaches a positive value as *pressure gradient* becomes stronger. For the flat-plates, however, since the growth of β is much smaller than Wing and Bump, *mean flux* remains a negative quantity and changes marginally in response to the variation of *pressure gradient*, similar to ZPG BLs. Note that the approximate convergence of *mean flux* is aligned with the definition of semi-equilibrium BLs

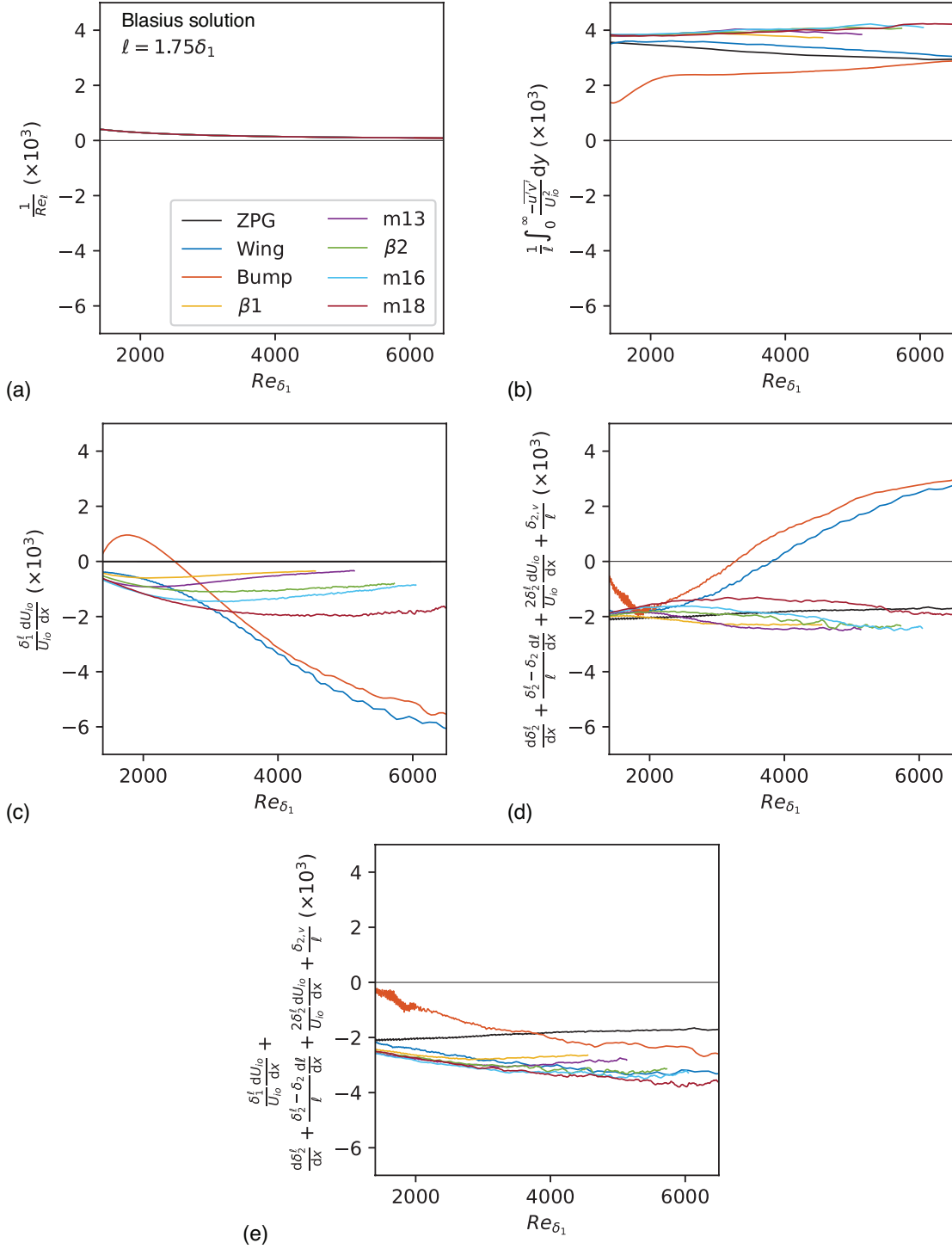


Figure 5.9: The AMI budget within the APG region with respect to Re_{δ_1} ; contribution of the substantial flow phenomena impacting $C_f/2$: (a) laminar friction, (b) turbulent torque, (c) torque due to pressure gradient, and (d) torque due to total mean flux. (e) exhibits the contribution to $C_f/2$ by the sum of (c) and (d).

($\beta = \text{constant}$). Another noteworthy observation in the AMI budget pertains to the summation of *pressure gradient* and *mean flux*. As illustrated in Figure 5.9 (e), for all cases, this combined effect appears to approach convergence downstream when $\ell \sim \delta_1$ based on the Blasius solution. Note the convergence depicted in Fig. 5.9 (e) directly follows from the earlier discussion indicating that the turbulence enhancement of the skin friction coefficient weakly depends on the strength of APG. For instance, in all flat-plates, this term converges beyond $Re_{\delta_1} = 3000$ –less than 3% variation from $Re_{\delta_1} = 3000$ to the far downstream. A similar convergence pattern is observed in the Wing dataset downstream of $Re_{\delta_1} = 4000$. However, for Bump, the FPG history effect delays reaching equilibrium, and the approximate convergence occurs beyond $Re_{\delta_1} > 5000$, where the FPG history effect is faded.

To further explore how APG alters the turbulence enhancement, specifically the integral of Reynolds shear stress, we analyze the *turbulent torque* within different layers of the BL, namely the inner layer, logarithmic region, and outer layer. Figure 5.10 (a) illustrates that under weak-to-moderate APG, like in flat-plates and Wing dataset, the contribution of the inner layer to *turbulent torque* remains small. In the Wing case, for example, the relative contribution of the inner layer is only around 5%, remaining approximately constant across the flow. This ratio is lower than in a ZPG BL, which typically reads 14%, suggesting that the inner layer plays a less crucial role in BLs subjected to APG. A similar trend is observed in Fig. 5.10 (b) for the logarithmic region, where the contribution is weaker for flat-plates and Wing datasets.

For the Bump dataset, the contribution of the inner layer is more significant. Due to the re-laminarization process occurring upstream of the bump’s peak, the role of the inner layer and viscous effects become more substantial, increasing monotonically downstream until $Re_{\delta_1} = 2000$. Within this region, turbulence (i.e., Reynolds shear stress) is pushed towards the wall, as shown in Fig. 5.8 (a), causing an increase in the inner layer. This increase coincides with a reduction of *turbulent torque* within the outer layer, where its relative contribution drops to about 55%, whereas this number for the flat-plates and Wing case read more than 80% as shown in Figure 5.10 (d).

In the logarithmic region that overlaps with both the inner and outer layers, we observe an augmentation downstream until $Re_{\delta_1} = 2400$. To further investigate this increase, we decompose the logarithmic region; from $Re_{\delta_1} = 1400$ to $Re_{\delta_1} = 1800$, this increase occurs from $y^+ = 30$ to $y^* = 0.1$ (the overlap between the inner layer and logarithmic region), whereas above $y^* = 0.1$, the contribution drops. However, in the range of $1800 \leq Re_{\delta_1} \leq 2400$, the enhancement within the logarithmic region is attributed to its overlap with the outer layer. Additionally, for flows similar to the Bump case, which undergoes strong alternative APG and FPG, the logarithmic region might capture more of the total Reynolds shear stress than the outer layer. For instance, within $1600 \leq Re_{\delta_1} \leq 4600$, the relative contribution of the logarithmic region is higher than the outer layer, peaking about 85% of the total *turbulent torque*. These findings emphasize the importance of resolving the logarithmic region or developing LES models to capture its role in such complex flows accurately.

For the Wing and flat-plates that are only under APGs, the majority of Reynolds shear stress is concentrated in the outer region of the BL. The relative contribution of the outer layer to *turbulent torque* increases downstream with Reynolds number, starting from approximately 80% at $Re_{\delta_1} = 1400$ and reaching 97% at $Re_{\delta_1} = 6500$ (in flat-plates). In the Wing case, however, the outer layer responds to the rate of change of APG, i.e., the curvature of *pressure gradient*, reflecting the reduction in total *turbulent torque* due to the growth rate of *pressure gradient*. In other words, the rate of change of APG primarily interacts with the outer layer, aligning with observations in Ref. [14]. Nevertheless, even under substantial variation in APG, as seen in the Wing case, the relative contribution of the outer layer to *turbulent torque* does not go below 80%. Also, for the Bump case, beyond $Re_{\delta_1} = 4600$, where the influence of FPG and re-laminarization diminish, the outer layer is still responsible for more than 75% of the total *turbulent torque*. The importance of the outer layer and the fact that *turbulent torque* captures a substantial amount of the total Reynolds stress can be the backbone of developing integral-based turbulent models (see chapter 7).

In this section, we underscored our adoption of $\ell = 1.75\delta_1$ from the Blasius solution, a choice

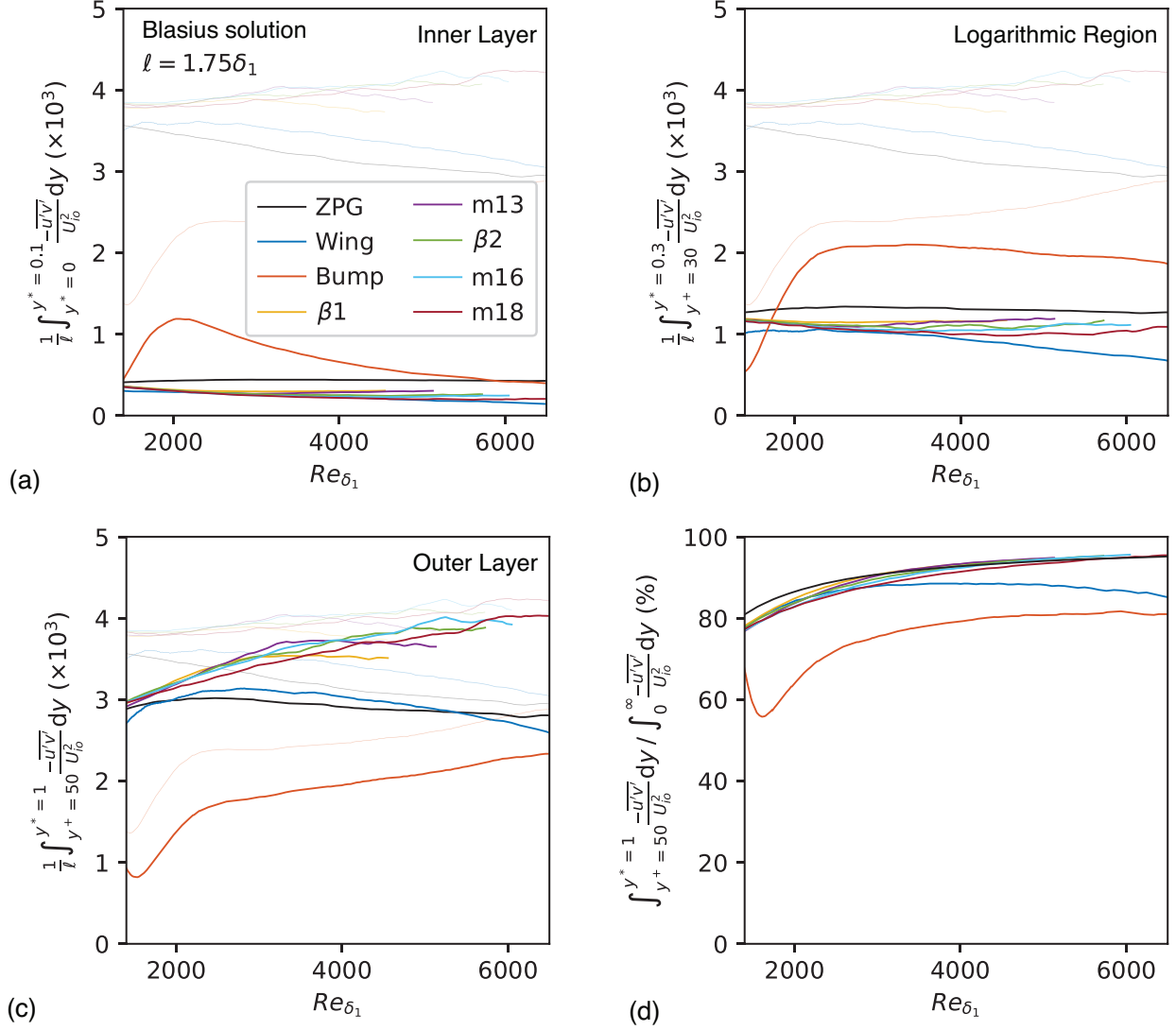


Figure 5.10: Contribution of the *turbulent torque* to $C_f/2$ within the (a) inner layer (from $y = 0$ to $y^* = 0.1$), (b) log-law region (from $y^+ = 30$ to $y^* = 0.3$), and outer layer (from $y^+ = 50$ to $y^* = 1$). Panel (d) shows the ratio of the *turbulent torque* within the outer layer and its total value. $y^* = y/\delta_{99}$ and $y^+ = y/\delta_\nu$ denote the normalized wall-normal distance by the BL thickness, δ_{99} , and viscous length scale, δ_ν , respectively. Shaded lines represent the total *turbulent torque* in the AMI budget Fig. 5.9 (b).

justified by the classical definition of the Clauser parameter as a function of displacement thickness. We aim to establish the AMI's length scale based on the displacement thickness, leading to the derivation of an AMI-based Clauser parameter denoted as β_ℓ . This parameter is formulated as a function of δ_1^ℓ instead of δ_1 , where $\ell \sim \delta_1$. Figures 5.11 (a, b) illustrate the trends of β and β_ℓ , respectively, with respect to Re_{δ_1} . The overall trends of β and β_ℓ are similar; however, β spans

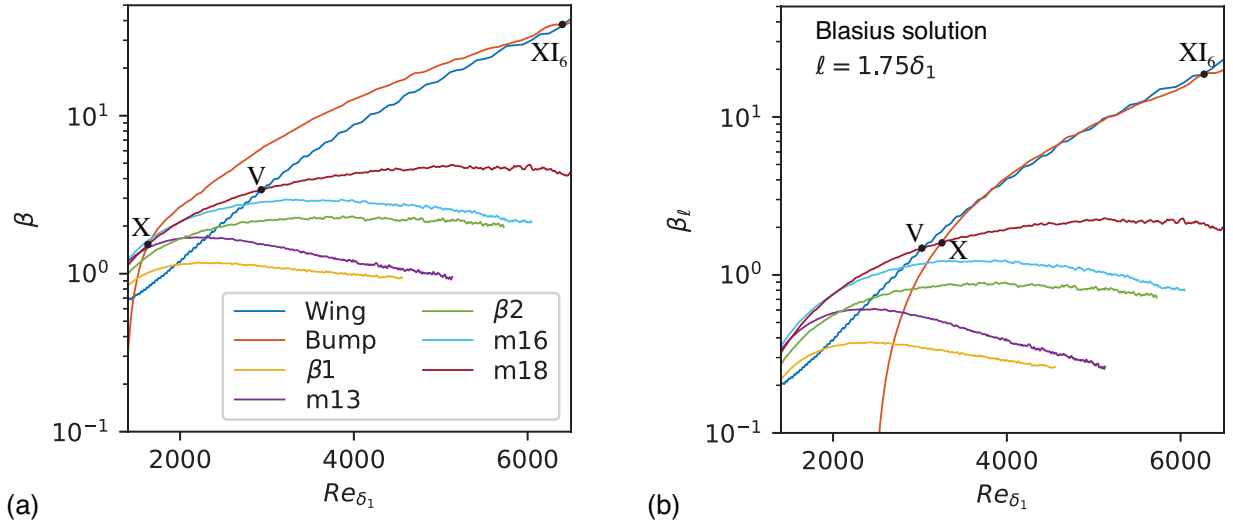


Figure 5.11: The Clauser parameter with respect to Re_{δ_1} ; (a) based on δ_1 (the classic definition), and (b) based on δ_1^ℓ obtained from the AMI analysis. V, X, and XI_6 mark the streamwise matching locations at which turbulent statistics are compared (shown in Fig. 5.12) based on table 5.2.

from 0 to 40, and β_ℓ yields smaller values in the range $0 < \beta_\ell < 20$. Additionally, the growth rates of β and β_ℓ differ, leading to different intersection (or matching) locations between the datasets. The most significant difference in behavior between β and β_ℓ corresponds to the Bump dataset. As previously discussed, the AMI budget, particularly *pressure gradient*, captures the carried-over FPG effect within the APG region, $\xi/L > 0$. This history effect is reflected in Fig. 5.11 (b), where the plot of β_ℓ vs. Re_{δ_1} shifts to the right compared to the plot of β . This shift aligns with the streamwise range where the contribution of *pressure gradient* is positive in figure 5.9 (c). Consequently, the matching locations between the Bump and other cases shift to the right accordingly.

The matching location has been the subject of several studies examining the pressure gradient history effects on turbulent statistics. Specifically, Ref. [14] chose the matching $Re_\tau - \beta$ to examine the upstream pressure gradient history effect. However, they did not identify a systematic similarity in turbulent statistics when comparing BLs undergoing different upstream pressure gradients at matching $Re_\tau - \beta$. These findings suggest that Re_τ may inadequately capture non-equilibrium effects in flows experiencing APG. Moreover, using Re_τ for statistical comparisons becomes problematic for BLs near separation as the wall-shear stress approaches zero. Therefore, for the sake of

ID	Symbol	Data label	$Re_{\delta_1} - \beta_\ell$	$Re_{\delta_1} - \beta$
I	×	Wing- β 1	1886 – 0.34	1958 – 1.14
II	○	Wing-m13	2341 – 0.61	2296 – 1.69
III	▽	Wing- β 2	2455 – 0.72	2421 – 1.96
IV	□	Wing-m16	2811 – 1.13	2732 – 2.71
V	◇	Wing-m18	3044 – 1.48	2965 – 3.45
VI	×	Bump- β 1	2691 – 0.37	1508 – 0.93
VII	○	Bump-m13	2803 – 0.58	1612 – 1.44
VIII	▽	Bump- β 2	2915 – 0.82	1558 – 1.2
IX	□	Bump-m16	3073 – 1.18	1674 – 1.68
X	◇	Bump-m18	3232 – 1.57	1638 – 1.55
XI ₁	⊙	Wing-Bump	3712 – 3.05	–
XI ₂	⊙	Wing-Bump	4193 – 4.83	–
XI ₃	⊙	Wing-Bump	5063 – 9.25	–
XI ₄	⊙	Wing-Bump	5258 – 10.24	–
XI ₅	⊙	Wing-Bump	5585 – 12.48	–
XI ₆	⊙	Wing-Bump	6246 – 18.39	6404 – 37.54

Table 5.2: Matching positions between $Re_{\delta_1} - \beta_\ell$ and $Re_{\delta_1} - \beta$ for the dataset in table 5.1.

identifying similarities in turbulent statistics, including the mean streamwise velocity and Reynolds stress components, we utilize Re_{δ_1} and compare matching locations for $Re_{\delta_1} - \beta$ and $Re_{\delta_1} - \beta_\ell$ (all matching locations in the dataset are recorded in table 5.2).

Furthermore, figure 5.12 illustrates profiles of the inner-scaled mean streamwise velocity, \bar{u} , and Reynolds stress components, $\overline{u'_i u'_j}$, for V (Wing-m18), X (Bump-m18), and XI6 (Wing-Bump) at the matching $Re_{\delta_1} - \beta_\ell$ and $Re_{\delta_1} - \beta$. These corresponding locations are indicated in Fig. 5.11. In all these plots, the x -axis represents the wall-normal position normalized by the AMI's length scale, while the insets present the profiles with respect to y^+ . Please note that the solid lines depict the matching $Re_{\delta_1} - \beta_\ell$, and shaded colors represent the profiles at the matching $Re_{\delta_1} - \beta$ for comparison. As depicted in Fig. 5.12 (a, b) for case V, involving the Wing and m18 datasets, the normalized wall-normal distance, y/ℓ , accurately captures the width of both datasets. When employing $Re_{\delta_1} - \beta_\ell$, the mean velocity profiles exhibit a stronger similarity compared to the matching $Re_{\delta_1} - \beta$ (shaded lines), particularly near the boundary layer's edge. This more robust similarity using β_ℓ instead of β is also shown in Fig. 5.12 (b) for the higher-order statistics, e.g., the Reynolds stress components.

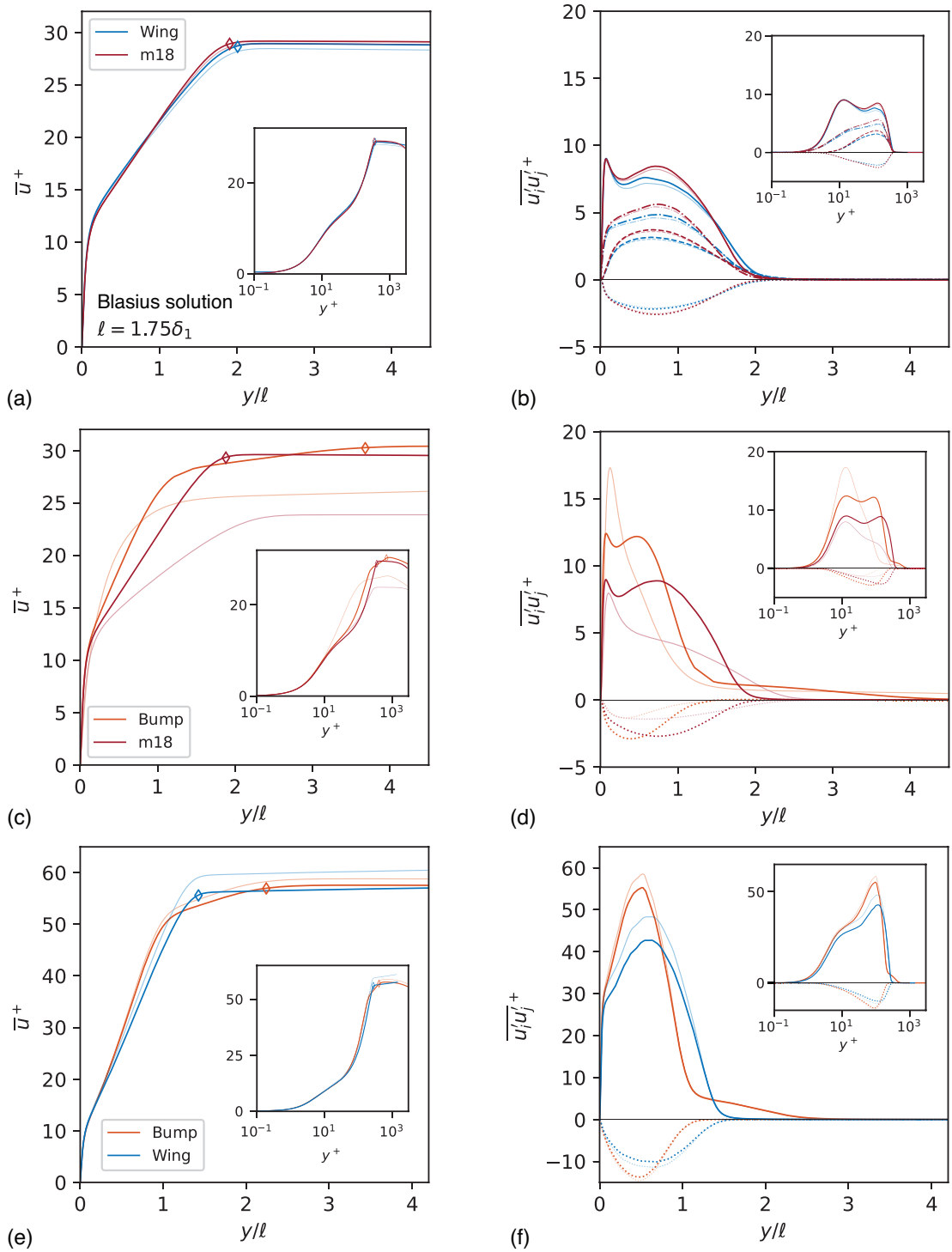


Figure 5.12: History effects; the inner-scaled mean velocity and Reynolds stress components with respect to y/ℓ at matching $Re_{\delta_1} - \beta_\ell$ ($Re_{\delta_1} - \beta$ shaded lines) for V, X, XI₆ (shown in Figs. 5.11); the solid, dashed, dashed-dotted, and dotted lines represent $\overline{u'u'}^+$, $\overline{v'v'}^+$, $\overline{w'w'}^+$, and $-\overline{u'v'}^+$, respectively. The insets exhibit the same profiles Vs. y^+ . Symbol \diamond denotes the wall-normal position of δ_{99} .

According to Fig. 5.12 (b), although using β_ℓ the profiles are not self-similar, especially in the outer layer, their trends are more comparable rather than what β predicts (shown shaded lines). Consistent with [14], we identify a secondary peak in the profile of $\overline{u'u'}^+$ occurring in the range $0.4 < y/\ell < 1$ ($50 < y^+ < 200$) within the outer layer, while the first peak, similar to ZPG BLs, is confined below $y/\ell = 0.1$ ($y^+ < 20$). Therefore, the secondary peak is the outcome of the pressure gradient stimulating the outer region of the BL. Also, the exact location of this secondary peak appears to vary depending on the upstream pressure gradient history. It is noteworthy that $Re_{\delta_1} - \beta_\ell$ yields an even more robust similarity –compared to β – when we analyze the statistics of the Wing and less extreme flat-plate cases, such as $\beta 1$ or $m16$ (not shown in this study). However, for BL flows undergoing a more complex pressure gradient history, the profiles of turbulent statistics are expected to be less similar.

Examining Fig. 5.12 (d) for case X, involving the Bump and m18 datasets, reveals that the width of the profiles, based on y/ℓ , is less alike; specifically the secondary peak for Bump is shifted toward the surface. This shows that the secondary peaks of $\overline{u'u'}^+$ do not necessarily occur at the same y/ℓ , especially if the flow experiences alternating pressure gradients. The author attributes the difference in the width of the profiles to the carried-over FPG, similar to our previous observation in section 5.3.2, where the imposed FPG upstream of the bump’s peak shifts turbulence towards the wall. Despite the lack of an absolute similarity using $Re_{\delta_1} - \beta_\ell$, the statistics appear considerably more similar than those predicted by $Re_{\delta_1} - \beta$ (plotted with shaded lines). The significant discrepancy between the profiles of the statistics when using $Re_{\delta_1} - \beta$ is primarily due to predicting intersections too early upstream since β fails to capture the FPG history effects.

Comparing the matching location of the Wing and Bump datasets, XI6, (Figs. 5.12 (e, f)) which occurs far downstream at $Re_{\delta_1} = 6242$ for β_ℓ (or $Re_{\delta_1} = 6404$ for β), we identify a single peak in both profiles of $\overline{u'u'}^+$ occurring between $0.5 < y/\ell < 0.65$ ($90 < y^+ < 125$) within the outer layer, approximately analogous to the wall-normal positions of the secondary peaks in Figs. 5.12 (b, d). This matching location suggests that a stronger APG does not significantly change the wall-normal

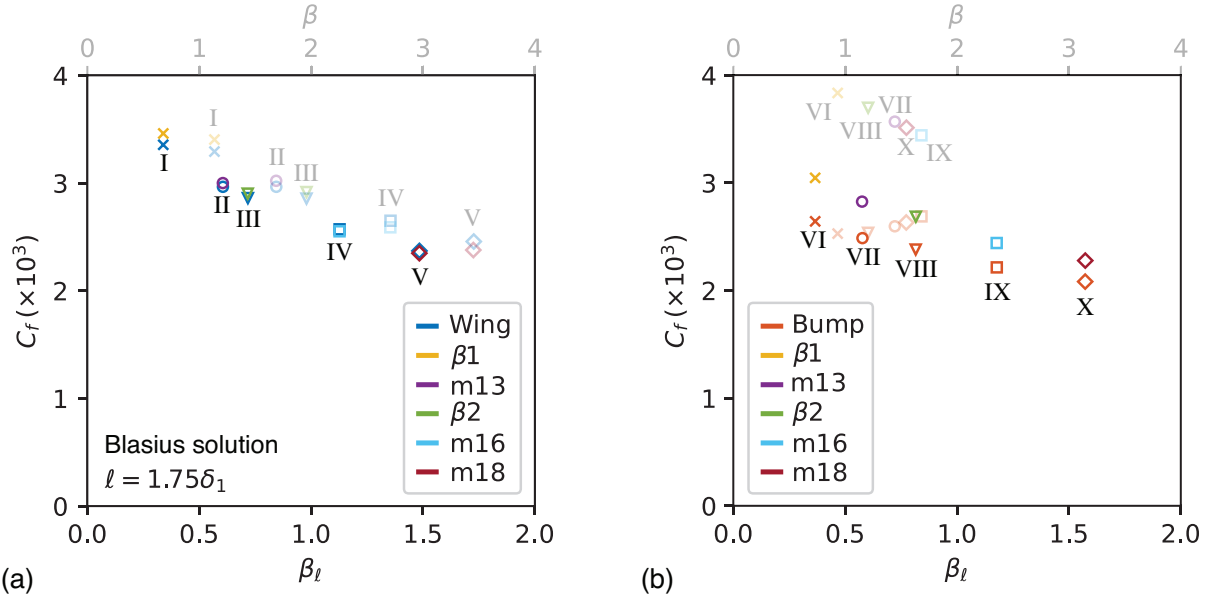


Figure 5.13: The correlation between C_f and β_ℓ (or β). Skin friction coefficient at the streamwise location of matching $Re_{\delta_1} - \beta_\ell$ (and $Re_{\delta_1} - \beta$ shaded color) according to table 5.2; a comparison between (a) Wing and flat-plates, and (b) Bump and flat-plates.

position of the secondary peak, yet it impacts the strength of the secondary peak. Besides that, using β_ℓ (or β shown with shaded color) to compare the Reynolds stress components of Wing and Bump, we conclude it is extremely difficult to obtain a systematic similarity between two distinct BLs undergoing severe alternating pressure gradient history. Nevertheless, for such complex flows, statistics behave substantially more similarly using the matching $Re_{\delta_1} - \beta_\ell$ rather than $Re_{\delta_1} - \beta$. Specifically for the mean velocity profiles, β_ℓ yields a systematic similarity for \bar{u}^+ at the edge of the BL, where $y^+ \rightarrow \infty$. The systematic collapse of inner-scaled mean velocity profiles at the edge of the BL using matching $Re_{\delta_1} - \beta_\ell$ suggests a strong correlation between C_f and β_ℓ . This correlation can be understood from $\bar{u}^+(y^+ \rightarrow \infty) = U_e/u_\tau$, where $U_e \sim U_{io}$; hence, $\bar{u}^+(y^+ \rightarrow \infty) \sim \sqrt{1/C_f}$. To further support this correlation, Figure 5.13 displays the skin friction coefficient at matching $Re_{\delta_1} - \beta_\ell$ (and $Re_{\delta_1} - \beta$ with shaded color) for the intersections between the Wing and flat-plates (a) and Bump and flat-plates (b).

As shown in Fig. 5.13 (a), when using matching $Re_{\delta_1} - \beta$, the values of skin friction coefficients do not coincide and diverge for more extreme cases, indicating a weak correlation between β and C_f .

Conversely, when employing β_ℓ , the skin friction coefficients demonstrate a systematic collapse, suggesting a strong correlation between C_f and β_ℓ . This systematic correlation holds to a weaker degree for more complex flows, such as the Bump case, and the matching locations between this flow and the flat-plates. According to Fig. 5.13 (b), there is no discernible correlation between β and C_f . This is because, as shown in figure 5.11 (a), within the APG region, β values in the Bump dataset cannot capture the FPG history effect, yielding the intersection with the flat-plate way far upstream. On the other hand, since β_ℓ (partially) captures the FPG history effects, C_f and β_ℓ remain (strongly) correlated with a marginal difference between the skin friction coefficients of less than 7%. A difference that is attributed to the partial absorption of Bump’s complex upstream history effect. A different choice of the AMI’s length scale (ℓ) (not based on the Blasius solution) could potentially alleviate the partial absorption of upstream history effects, and hence lead to a stronger correlation between C_f and β_ℓ even for complex flows such as the Bump case. For instance, although not covered in this study, implementing the Falkner-Skan solution by matching the power-law acceleration parameter between turbulent and laminar regimes –as the base of the AMI analysis– might lead to a more robust absorption of the upstream history effects.

To further investigate the $\beta_\ell - C_f$ correlation, we examine the most extreme case by comparing the intersection between the Bump and Wing datasets. In Fig. 5.11 (a, b), for β , there is a single matching location at $Re_{\delta_1} = 6404$ ($\beta = 37.54$). Whereas, in plots of β_ℓ , the Wing and Bump lines follow close to each other starting at $Re_{\delta_1} = 3712$ ($\beta_\ell = 3.05$) until, at $Re_{\delta_1} = 6245$ ($\beta_\ell = 18.51$), where they cross for the last time and eventually diverge. Figure 5.14 illustrates the correlation between C_f and β_ℓ at the crossing points of $Re_{\delta_1} - \beta_\ell$. As β_ℓ of Wing and Bump grow downstream, on top of each other, C_f and β_ℓ become more correlated. At $Re_{\delta_1} = 6245$, corresponding to XI6, the $\beta_\ell - C_f$ correlation is almost perfect, whereas there is a discrepancy between the values of C_f extracted from matching β (shown with shaded colors). It is important to highlight that the $\beta_\ell - C_f$ correlation for Wing and Bump (XI6) (occurs at $Re_{\delta_1} = 6245$) is stronger than Bump and m18 (X) (occurs at ($Re_{\delta_1} = 3232$)). This is reasonable since XI6 is further downstream and the FPG history effect gradually fades at higher Reynolds numbers.

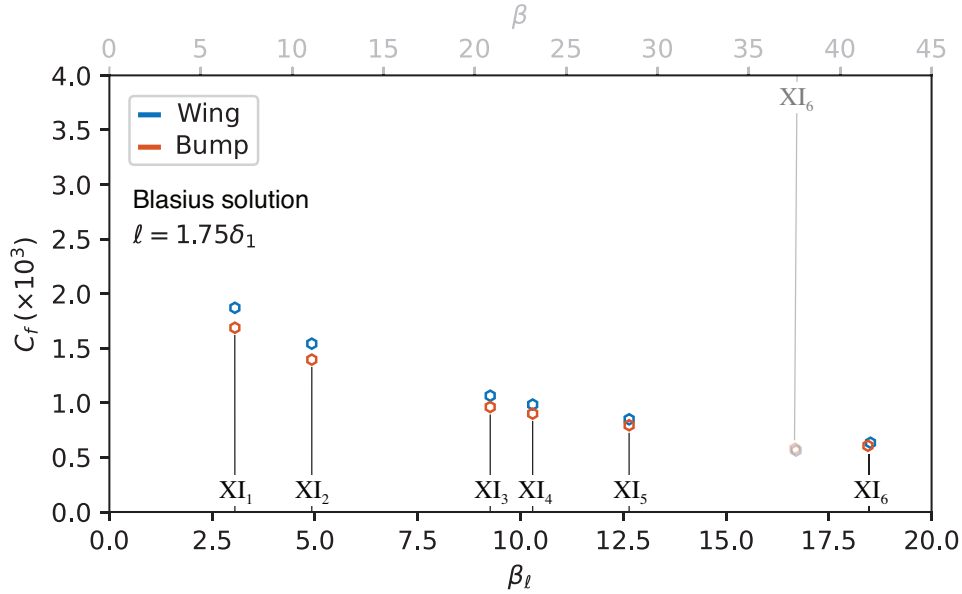


Figure 5.14: The correlation between C_f and β_ℓ (or β) for the Wing and Bump datasets. Skin friction coefficient at the streamwise location of matching $Re_{\delta_1} - \beta_\ell$ ($Re_{\delta_1} - \beta$ shaded color).

5.3.4 AMI analysis - Falkner-Skan solution

In the preceding section, we primarily focused on the BL regions experiencing moderate APG, where we investigated the impact of APG on the Reynolds shear stress enhancement of skin friction coefficient using the AMI analysis. Additionally, we introduced an AMI-based non-equilibrium Clauser parameter, denoted as β_ℓ , to delve into the influence of pressure gradient history effects on turbulent statistics. However, thus far, our approach has relied on an AMI length scale derived from the Blasius solution that yields a straightforward interpretation of the AMI budget, primarily for *pressure gradient* as a torque with respect to a base zero-pressure-gradient BL. In this upcoming section, we explore an alternative approach by employing the Falkner-Skan laminar solution to determine ℓ .

Our objective here is to establish a relationship for ℓ within the APG region, specifically within the range of $1400 \leq Re_{\delta_1} \leq 6500$, by aligning the Clauser parameter between the turbulent datasets listed in table 5.1 and the laminar Falkner-Skan solution. In essence, we determine the coefficient α_{FS} (introduced in section 5.1) by utilizing the Falkner-Skan solution with the precise value of β

at each streamwise location.

To obtain the coefficient α_{FS} based on the Falkner-Skan solution, we developed an ordinary differential equation (ODE) solver using the shooting method to solve the self-similar Falkner-Skan momentum equation. The similarity form, introduced in Ref. [40], is defined by $\eta = C y x^a$, where η represents the self-similar variable, consistent with a power-law edge velocity distribution given by $U_e(x) = K x^m$, where C and K are constants to make η dimensionless and $m = 2a + 1$. The ODE solver selects $\eta = y \sqrt{(m+1)U_e(x)/\nu x}$, and imposes appropriate BCs, similar to Blasius solution for a flat-plate (refer to chapter four in [171]). Using the similarity solution, the skin friction coefficient and displacement thickness, respectively, are expressed as

$$\frac{C_f}{2} \equiv \frac{2\tau_w}{\rho U_e^2} = \sqrt{(m+1)} \frac{\nu}{U_e x} f''(0), \quad (5.18)$$

and

$$\delta_1 \equiv \int_0^\infty \left(1 - \frac{u}{U_e}\right) dy = \sqrt{\frac{1}{m+1} \frac{\nu x}{U_e}} \lim_{\eta \rightarrow \infty} (\eta - f), \quad (5.19)$$

where f represents the similarity function, and the prime superscript indicates differentiation with respect to η . Similarly, we can derive a relationship for the Clauser parameter that reads

$$\beta \equiv -\frac{1}{U_e} \frac{dU_e}{dx} \frac{2\delta_1}{C_f} = -\frac{m}{m+1} \left[\frac{\lim_{\eta \rightarrow \infty} (\eta - f)}{f''(0)} \right], \quad (5.20)$$

where the term enclosed by brackets is self-similar. We further relate β to the AMI's length scale coefficient, α_{FS} , as

$$\beta = \frac{-m}{m+1} \left[\lim_{\eta \rightarrow \infty} (\eta - f) \right]^2 \alpha_{FS}. \quad (5.21)$$

Figure 5.15 (a) illustrates the plot of β with respect to m within the APG region ($m \geq 0$). Interestingly, the plot of α_{FS} with respect to β demonstrates a linear relationship (Fig. 5.15 (b)). Therefore,

one can determine the appropriate α_{FS} at each streamwise position by knowing the Clauser parameter. The linear function $\alpha_{FS}(x) = 1.75 + 0.822\beta(x)$ is fitted to compute α_{FS} from β values.

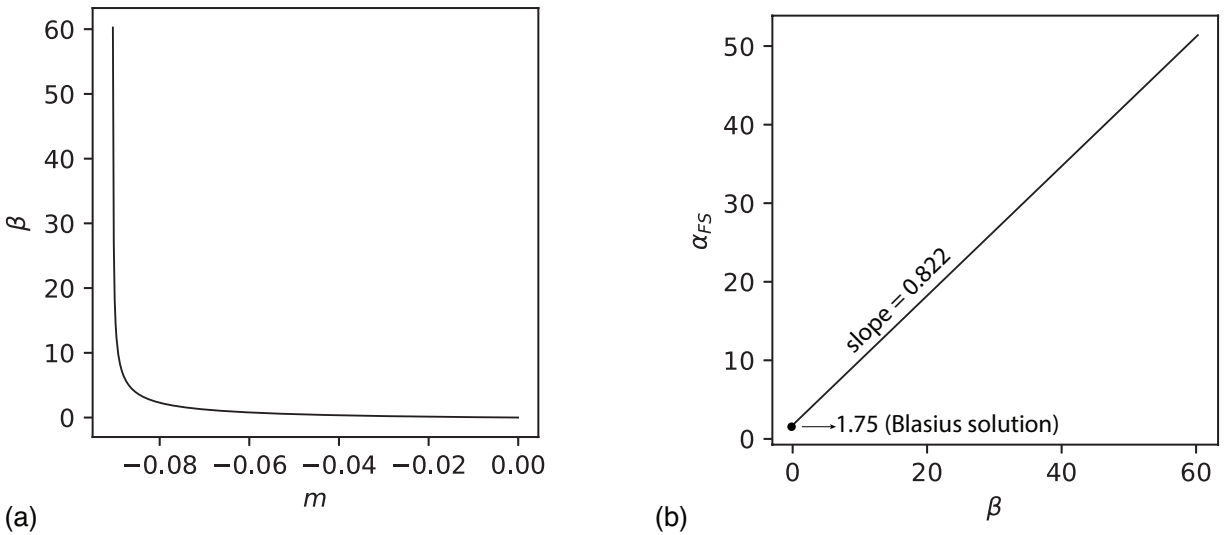


Figure 5.15: Self-similar Falkner-Skan solution and the Clauser parameter; relationships between β and m (a), and α_{FS} and β (b).

Now that we have established a relationship between β and ℓ , we can determine $\ell = \alpha_{FS}\delta_1$ by knowing the β values in the turbulent dataset, table 5.1. As a result, when we apply this ℓ to the AMI analysis, the first term on the right-hand side of the AMI equation, representing *laminar friction* ($1/Re_\ell$), precisely yields half of the skin friction coefficient that would be expected if the flow were laminar (with the same Reynolds number) under the same β . This choice of ℓ , however, makes the interpretation of *pressure gradient* somewhat ambiguous because now a portion of the pressure gradient effect is absorbed by *laminar friction*. One can assume *pressure gradient* as the pressure gradient effects relative to the base Falkner-Skan flow. This term, although for the turbulent dataset is more distinct from each other than in Figure 5.9 (a), weakly contributes to the skin friction coefficient. The explicit turbulent enhancement in the AMI equation based on the Falkner-Skan solution, however, remains the primary contributor to C_f .

In Figure 5.16 (a), we observe a distinct trend in the behavior of *turbulent torque* compared to Figure 5.9 (b), where the analysis was based on the Blasius solution. Specifically, the behavior of

turbulent torque shows an inverse relationship with the strength of the pressure gradient, i.e., β . For flat-plates characterized by weak-to-moderate pressure gradients, there is a minimal variation in *turbulent torque* from upstream to downstream, especially beyond $Re_{\delta_1} = 3500$, where their β is flattened. In contrast, for cases exhibiting rapid growth in β , such as Wing and Bump, the variation in *turbulent torque* from upstream to downstream is more pronounced. This behavior can be attributed to the fact that the total Reynolds shear stress remains constant downstream, as discussed in Section 5.3.3. Consequently, as ℓ increases with β , *turbulent torque* decreases downstream at an inverse rate. Despite the significant changes in *turbulent torque* with β in the Wing and Bump cases,

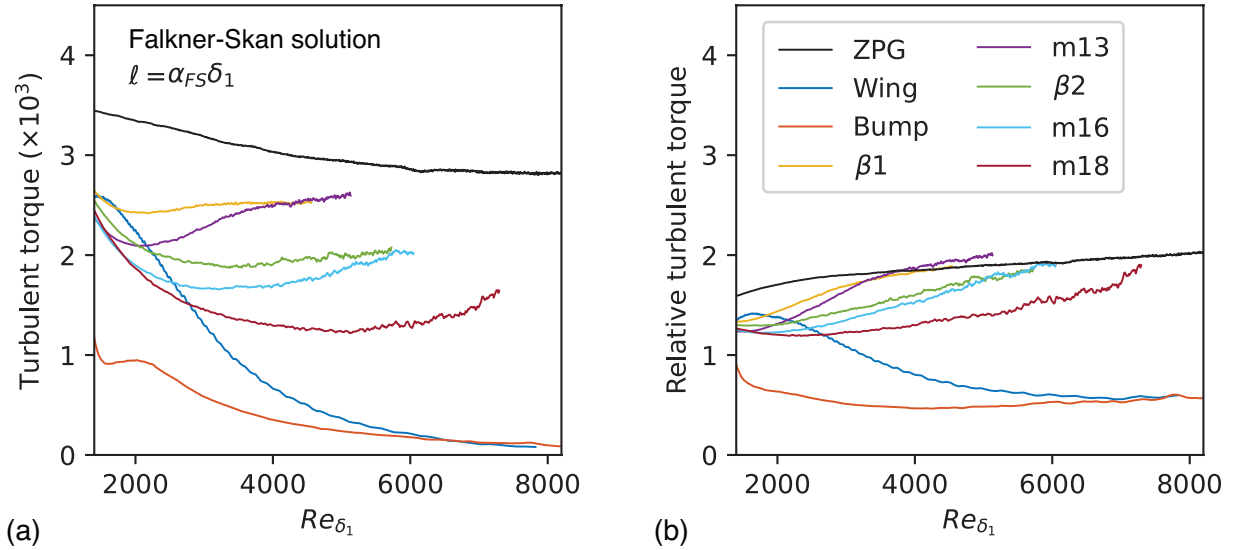


Figure 5.16: *Turbulent torque* with respect to Re_{δ_1} when ℓ is obtained from the Falkner-Skan solution; (a) the absolute contribution to $C_f/2$, (b) the relative contribution (normalized by $C_f/2$).

it is noteworthy that the relative contribution (normalized by $C_f/2$) of *turbulent torque* (shown in Fig. 5.16 (b)) tends to flatten downstream of $Re_{\delta_1} = 6000$. This suggests for relatively strong APG, e.g., $\beta \geq 10$, the spatial rate of change of this flow phenomenon mirrors that of the skin friction coefficient.

Using the Falkner-Skan solution as the reference flow for the AMI equation allows us to derive the AMI's Clauser parameter, β_ℓ , where ℓ varies downstream as a function of β . Figure 5.17 illustrates this β_ℓ with respect to Re_{δ_1} , compared with β (shown with shaded lines). According to the plots of

the Wing and Bump cases in Figure 5.17, far downstream where the pressure gradient is relatively strong ($\beta \geq 40$), β_ℓ and β converge to each other. To understand this phenomenon, consider an asymptotic condition where $\beta \rightarrow \infty$: the AMI's length scale, $\ell \rightarrow \infty$. Consequently, as mentioned in section 5.1, if $\ell \rightarrow \infty$, the AMI equation will recover the von-Kármán integral equation, i.e., $\beta_\ell \rightarrow \beta$. On the other hand, for $\beta \rightarrow 0$ ($\beta < 1$), the Falkner-Skan-based AMI yields analogous results as shown in Figure 5.11 (b) for β_ℓ based on the Blasius solution. Additionally, in the Bump

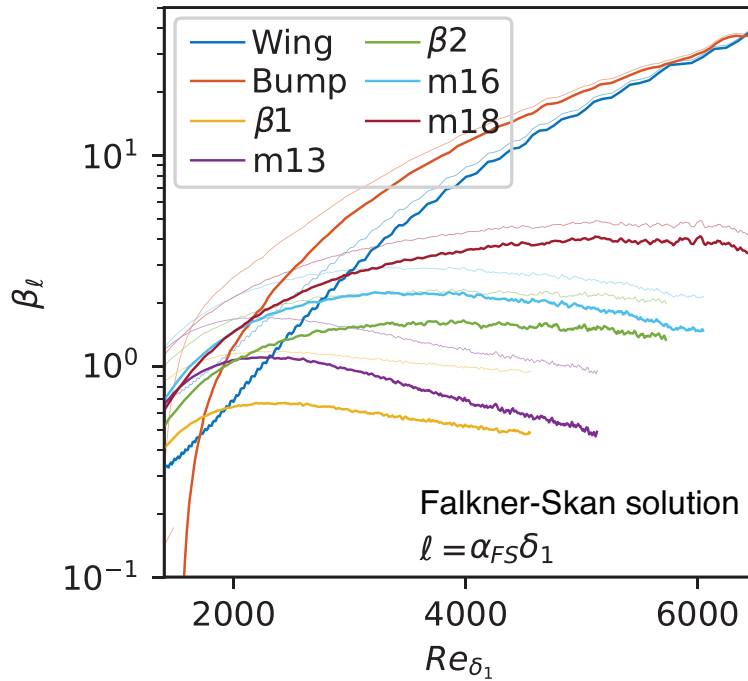


Figure 5.17: The Clauser parameter with respect to Re_{δ_1} based on δ_1^ℓ obtained from the AMI analysis using Falkner-Skan laminar solution. The shaded lines denote β as in Fig. 5.11 (a).

case, Figure 5.17 indicates that β_ℓ has marginally captured the upstream FPG effect. Therefore, compared with β , the plot of β_ℓ is slightly shifted to the right. This absorption of the FPG history effect, however, is not sufficient; also, it is weaker than what we observed in figure 5.11 (b) for β_ℓ based on the Blasius solution. As a result, the matching location between Bump and flat-plates occurs too early upstream when β_ℓ is based on the Flakner-Skan solution. Consequently, the turbulent statistics at these matching locations yield less similarity compared to what we observed earlier for β_ℓ obtained from the Blasius solution, like in figures 5.12 (c, d). This weaker similarity also manifests in the correlation between C_f and β_ℓ , where we compute a weaker correlation when β_ℓ is

based on the Falkner-Skan solution rather than figure 5.13 (b). In conclusion, these findings based on the Falkner-Skan solution clarified that although there might be other options than choosing ℓ from the Blasius solution, this choice yields a more straightforward interpretation and more robust similarity behavior in turbulent statistics of two different BLs.

5.4 Conclusion

This chapter extends the application of the angular momentum integral (AMI) equation, first introduced by [38] for ZPG incompressible boundary layers (BLs), as an analysis tool to study turbulent BLs undergoing non-zero pressure gradient. The AMI analysis measures the explicit turbulent enhancement by Reynolds shear stress relative to a base laminar, referred to as turbulent torque, flow while the BL undergoes a pressure gradient. Additionally, it yields a single term corresponding to the flow acceleration (or deceleration) measuring the direct impact of non-zero pressure gradients. From this term, we derived an AMI-based non-equilibrium Clauser parameter, β_ℓ as a counterpart of the classic Clauser parameter, β , that measures the relative role of pressure gradient on the transport of momentum deficit through the von Kármán integral equation.

We applied the AMI equation, expressed in wall-tangential and wall-normal coordinate system, to a set of high-fidelity numerical turbulent BL simulations, comprising flows over the suction side of NACA-4412 airfoil and a two-dimensional Gaussian bump both under moderate pressure gradients. The AMI analysis with Blasius solution as the base laminar flow for BL over the airfoil quantified a marginal variation of turbulent torque. At the same time, the adverse pressure gradient changes substantially downstream. In the bump flow, the strong favorable pressure gradient resulted in a substantial reduction of turbulent torque, co-occurring with the enhancement of laminar friction in the AMI equation. These results revealed signs of re-laminarization in a way that turbulent energy is deactivated and turbulence becomes one-dimensional, i.e., the streamwise and wall-normal velocities are less correlated. Downstream of the bump's peak, flow experiences a

severe adverse pressure gradient that leads to flow separation at which the error of the AMI budget increases primarily due to the lack of sufficient averaging. Within this region, turbulent torque gradually increases downstream, recovering from the upstream favorable pressure gradient. This increase occurs within the outer layer of the BL, while the inner layer remains unchanged, parallel to observations by [14].

To examine the pressure gradient history effects on turbulent statistics we compared the profiles of the inner-scaled streamwise mean velocity and Reynolds stress components of the airfoil and bump flows with flat-plates under adverse pressure gradients. The profiles were plotted at the matching Reynolds numbers (based on displacement thickness), Re_{δ_1} , and β_ℓ compared with the classic approach of using β . We noticed not perfect but more robust similarity in turbulent statistics using β_ℓ over β . Especially, using matching $Re_{\delta_1} - \beta_\ell$, the mean velocity profiles of two distinct flows are converged at the edge of the BL, revealing a strong correlation between the skin friction coefficient and β_ℓ .

An alternative approach for the AMI analysis involves using the Falkner-Skan laminar solution with a matched β value (at any streamwise position) as the base laminar flow. In this method, ℓ is implicitly calculated from the β values of the turbulent dataset. This approach provides a different interpretation of the AMI's pressure gradient term. For flows with a weak pressure gradient, the Falkner-Skan-based pressure gradient is similar to the one based on the Blasius solution. However, for flows with $\beta > 20$, the Falkner-Skan-based pressure gradient asymptotically approaches the one in the von Kármán integral equation. With this approach, the spatial rate of change of turbulent torque mirrors that of the skin friction coefficient for $\beta > 20$.

In conclusion, the AMI equation provides a flexible and intuitive framework for understanding the impact of flow phenomena within the boundary layer on the skin friction coefficient, especially in the presence of pressure gradients. Future research could explore applying the AMI analysis to boundary layers with significant direct curvature effects to investigate how curvature alters turbulent enhancement. Studying bump flows at high Reynolds numbers, where re-laminarization does not

occur, could be intriguing to examine pressure gradient history effects. Additionally, exploring the AMI equation in separated flows with adequately averaged statistics could give valuable insights into the physics of such a complex phenomenon.

Chapter 6

First-moment Integral Equations for High-speed Boundary Layers

The enhancement of skin-friction drag and surface heat flux by the transition to turbulence is a crucial physical phenomenon for the design of high-speed vehicles. Recently, Elnahhas & Johnson [38] developed the angular momentum integral (AMI) equation by integrating the first moment of momentum deficit equation for incompressible BLs. The AMI equation accomplishes for BLs what the FIK equation does for internal flows (pipes, channels). Specifically, it relates the skin-friction coefficient of any (e.g., turbulent) BL to the sum of an equivalent laminar skin-friction coefficient (as a function of a user-defined Reynolds number) plus an (unweighted) integral of the Reynolds shear stress, along with other terms (e.g., free-stream pressure gradients). In addition to the clear mathematical interpretation as enhancement or attenuation relative to an equivalent laminar BL, the AMI equation also has an intuitive physical explanation in terms of torques that reshape the mean velocity profile, changing its angular momentum (moment of momentum) and affecting the slope at the wall. Analogously, a first-moment integral method for energy (enthalpy) equation was developed to obtain the moment of temperature integral (MEI) equation for transitional and turbulent incompressible BLs with heat transfer in Chapter 4. MEI provides a quantifying mapping

between different flow phenomena, including turbulent contribution, and how they alter the Stanton number. The existing development of the AMI and MEI equations has previously focused solely on incompressible BLs, so the application of this approach for compressible BLs is not yet clear.

The purpose of this chapter is to derive and demonstrate how the AMI equation can be applied to compressible BLs of a calorically perfect gas. In addition, a moment of total enthalpy integral (MTEI) equation is introduced as an extension to the MEI equation previously developed for incompressible BLs. The MTEI equation provides an interpretable relationship for the Stanton number in compressible BLs in terms of key flow physics, analogous to what AMI accomplishes for the skin friction coefficient. This integral-based approach provides another perspective for examining the effect of Mach number and wall cooling on turbulence in high-speed BLs with a particular focus on engineering-relevant surface quantities related to drag and heat transfer. The chapter is organized as follows. Section 6.1 first derives the AMI equation for compressible BL flow of calorically perfect gas and provides an intuitive interpretation for each term related to the skin-friction coefficient. That is followed by the derivation of the MTEI equation for the Stanton number in a similar manner and a comprehensive interpretation of each flow phenomenon in the equation. Section 6.2 covers the application of the AMI and MTEI equations; laminar self-similar compressible datasets are examined first in Section 6.2.1. This is followed by the analysis of the fully turbulent DNS dataset in Section 6.2.2. This section briefly summarizes the DNS data set and the numerical methods to solve turbulent compressible BLs and demonstrates the use of the AMI and MTEI equations. In Sections 6.2.2 and 6.2.2 the AMI and MTEI equations, respectively, are applied to analyze the DNS data for a range of edge Mach numbers and wall-temperature boundary conditions. Finally, conclusions are given in Sec. 6.3.

6.1 Derivation and Interpretation

The derivation of the first-moment integral equations is based on section 4.1 for ZPG incompressible BLs. However, here, due to the compressibility effects the flow quantities such as density and viscosity are not necessarily constants. In this section, a more general form of the first moment integral equations for skin friction and surface heat flux are introduced, taking into account density and viscosity variation. The result provides a direct relationship that quantitatively maps flow physics throughout the boundary layer based on their enhancement or attenuation of the skin friction coefficient and Stanton number relative to a baseline laminar BL.

6.1.1 Compressible Angular Momentum Integral Equation

Derivation

The derivation of the AMI equation for compressible flows is outlined in this subsection. The Reynolds averaged conservation of mass and streamwise momentum for a statistically steady 2D flow, respectively, yield

$$\frac{\partial(\overline{\rho\tilde{u}})}{\partial x} + \frac{\partial(\overline{\rho\tilde{v}})}{\partial y} = 0 \quad \text{and} \quad (6.1)$$

$$\frac{\partial(\overline{\rho u u})}{\partial x} + \frac{\partial(\overline{\rho u v})}{\partial y} = -\frac{\partial \bar{p}}{\partial x} + \frac{\partial}{\partial y} \left(\overline{\mu \frac{\partial u}{\partial y}} - \overline{\rho u'' v''} \right) + I_M, \quad (6.2)$$

where $(\bar{\cdot})$ stands for the Reynolds averaging. Also, $(\tilde{\cdot})$ and $(\cdot)''$ represent a density-weighted (Favre) averaged quantity and fluctuations with respect to the Favre averaging, respectively. In Eq. (6.2), u , v , and p are the streamwise (x) velocity, wall-normal (y) velocity, and pressure, respectively. Also, ρ and μ are the density and dynamic viscosity, respectively. Note that I_M represents the streamwise

derivative terms neglected by the BL approximations. At the edge of the BL, assuming there is no wall-normal gradient and viscous effect, the streamwise momentum equation yields

$$\rho_e U_e \frac{dU_e}{dx} = -\frac{dP_e}{dx}, \quad (6.3)$$

where the subscript $(\cdot)_e$ stands for the edge quantities like the edge velocity, U_e , and pressure, P_e . Subtracting Eq. (6.2) from Eq. (6.3), and adding U_e multiplied by Eq. (6.1), gives a transport equation for the mean streamwise velocity defect

$$\frac{\partial (\bar{\rho}\tilde{u}(U_e - \tilde{u}))}{\partial x} + \frac{\partial (\bar{\rho}\tilde{v}(U_e - \tilde{u}))}{\partial y} = -(\rho_e U_e - \bar{\rho}\tilde{u}) \frac{dU_e}{dx} + \frac{\partial}{\partial y} \left(\overline{\rho u'' v''} - \mu \frac{\partial u}{\partial y} \right) - I_M, \quad (6.4)$$

where the terms neglected by the statistically stationary BL approximations (including the streamwise gradient of the edge and mean pressure difference) are gathered in I_M . Integration of Eq. (6.4) across the BL, $\int_0^\infty [\cdot] dy$ yields the von-Kármán momentum integral equation,

$$\frac{C_f}{2} = \frac{d\delta_2}{dx} + \left(2 + \frac{\delta_1}{\delta_2} + \frac{U_e}{\rho_e} \frac{d\rho_e}{dU_e} \right) \frac{\delta_2}{U_e} \frac{dU_e}{dx} + I_M, \quad (6.5)$$

where the skin-friction coefficient, $C_f = 2\tau_w/\rho_e U_e^2$, is the non-dimensional mean wall shear stress, $\tau_w = \mu_w (\partial u/\partial y)_w$. For isentropic edge flow, $(U_e/\rho_e)\partial\rho_e/\partial U_e = -M_e^2$. Moreover, I_M is the outcome of the integration of I_M and can be safely neglected for most thin BL flows. The momentum and displacement thicknesses for compressible BLs are, respectively,

$$\delta_2 \equiv \int_0^\infty \frac{\bar{\rho}}{\rho_e} \frac{\tilde{u}}{U_e} \left(1 - \frac{\tilde{u}}{U_e} \right) dy \quad \text{and} \quad \delta_1 \equiv \int_0^\infty \left(1 - \frac{\bar{\rho}}{\rho_e} \frac{\tilde{u}}{U_e} \right) dy. \quad (6.6)$$

Eq. (6.5) is valid for both laminar and turbulent regimes; however, the contribution of turbulence is implicit. In other words, Eq. (6.5) does not provide any explicit representation of how turbulence impacts the skin friction coefficient.

The AMI equation is derived by multiplying Eq. (6.4) by $(y - \ell(x))$ –the first moment– and in-

tegrating across the BL, $\int_0^\infty \{y - \ell(x)\} [\cdot] dy$. Applying the no-slip and no-penetration boundary conditions at the wall, the AMI relation reads

$$\begin{aligned} \frac{C_f}{2} = & \frac{1}{Re_\ell} + \frac{1}{\ell} \int_0^\infty \frac{-\overline{\rho u'' v''}}{\rho_e U_e^2} dy + \left\{ \frac{d\delta_2^\ell}{dx} - \frac{\delta_2 - \delta_2^\ell}{\ell} \frac{d\ell}{dx} \right\} + \frac{\delta_{2,v}}{\ell} + \frac{1}{\ell} \int_0^\infty \frac{(\overline{\mu - \mu_{\text{Ref}}}) \frac{\partial u}{\partial y}}{\rho_e U_e^2} dy \\ & + \left(2 + \frac{\delta_1^\ell}{\delta_2^\ell} + \frac{U_e}{\rho_e} \frac{d\rho_e}{dU_e} \right) \frac{\delta_2^\ell}{U_e} \frac{dU_e}{dx} + \mathcal{I}_M^\ell, \end{aligned} \quad (6.7)$$

where μ_{Ref} is a reference viscosity to define the Reynolds number of a compressible BL, $Re_\ell = U_e \rho_e \ell / \mu_{\text{Ref}}$, and \mathcal{I}_M^ℓ is generated by the integration of the first moment of I_M . An appropriate definition of the length scale ℓ to isolate the laminar friction is given in Eq. (6.13), followed by other alternative options in Section 6.1.1. Also, the complete derivation of the AMI equation, Eq. (6.7), is provided in Appendix B. The AMI equation for compressible BLs, Eq. (6.7), was independently introduced by Kianfar et al. [80, 79] and Xu et al. [179]. Note that Ref. [179] used a slightly different treatment of the mean viscosity variation, basing their treatment on the Reynolds number using the edge viscosity.

The angular momentum and displacement thicknesses introduced in Eq. (6.7) are, respectively,

$$\delta_2^\ell \equiv \int_0^\infty \left(1 - \frac{y}{\ell}\right) \frac{\bar{\rho}}{\rho_e} \frac{\tilde{u}}{U_e} \left(1 - \frac{\tilde{u}}{U_e}\right) dy \quad \text{and} \quad \delta_1^\ell \equiv \int_0^\infty \left(1 - \frac{y}{\ell}\right) \left(1 - \frac{\bar{\rho}}{\rho_e} \frac{\tilde{u}}{U_e}\right) dy. \quad (6.8)$$

Finally, Eq. (6.7) also introduces the wall-normal momentum thickness,

$$\delta_{2,v} \equiv \int_0^\infty \frac{\bar{\rho}}{\rho_e} \frac{\tilde{v}}{U_e} \left(1 - \frac{\tilde{u}}{U_e}\right) dy. \quad (6.9)$$

Following the BL theory, the streamwise direction, x , may be interpreted as a time-like variable. In this perspective, Eq. (6.7) may be seen as an integral conservation principle for angular momentum about $y = \ell(x)$. As such, the AMI equation represents the sum of torques equal to the growth of the BL's angular momentum integral, $d\delta_2^\ell/dx$.

Interpretation

The terms appearing on the right-hand side of the AMI equation, Eq. (6.7), represent various physical flow phenomena influencing the skin friction coefficient. A succinct physical description of each term is given in the following paragraph.

- (I) $\frac{1}{Re_\ell}$ \rightarrow skin friction coefficient of an equivalent *laminar* BL at matched Re_ℓ ,
- (II) $\frac{1}{\ell} \int_0^\infty \frac{-\overline{\rho u'' v''}}{\rho_e U_e^2} dy$ \rightarrow *turbulent torque* by Reynolds shear stress,
- (III) $\frac{d\delta_2^\ell}{dx} - \frac{\delta_2 - \delta_2^\ell}{\ell} \frac{d\ell}{dx}$ \rightarrow *streamwise growth* of angular momentum thickness,
- (IV) $\frac{\delta_{2,v}}{\ell}$ \rightarrow torque by *mean wall-normal* transport,
- (V) $\frac{1}{\ell} \int_0^\infty \frac{(\mu - \mu_{Ref}) \frac{\partial u}{\partial y}}{\rho_e U_e^2} dy$ \rightarrow *deviation* from reference viscosity,
- (VI) $\frac{1}{U_e} \frac{dU_e}{dx} (\delta_1^\ell + 2\delta_2^\ell) + \frac{1}{\rho_e} \frac{d\rho_e}{dx} \delta_2^\ell$ \rightarrow *edge pressure gradient torque*,
- (VII) \mathcal{I}_M^ℓ \rightarrow *negligible terms*, departure from BL assumptions.

A more detailed discussion of the terms is given in each of the following paragraphs below. Since the AMI equation arises from the first moment of the velocity defect transport equation, the flow phenomena on the right-hand side of Eq. (6.7) may be interpreted as torques. Figure 1.7 presents a schematic of how these flow phenomena may be seen as torques that redistribute momentum relative to $y = \ell(x)$, reshaping the mean velocity profile. For example, the Reynolds shear stress acts as a counterclockwise torque with respect to $y = \ell(x)$, which redistributes momentum toward the wall (more precisely, velocity defect away from the wall), causing an enhancement in skin friction. As a different example, an adverse pressure gradient acts as a clockwise torque, redistributing momentum away from the wall (velocity defect toward the wall) and decreasing skin friction.

Viscous force and laminar friction coefficient (I) & (VI)

In the AMI equation, the skin-friction coefficient, C_f , the *laminar* friction, and viscous *deviation* terms originate from the first-order moment of viscous force (viscous torque) about $y = \ell(x)$

$$T_{v,\ell} = \int_0^\infty (y - \ell) \left[\frac{\partial}{\partial y} \left(\overline{\mu \frac{\partial u}{\partial y}} \right) \right] dy = \ell \tau_w - \mu_{\text{Ref}} U_e - \int_0^\infty \overline{(\mu - \mu_{\text{Ref}}) \frac{\partial u}{\partial y}} dy. \quad (6.10)$$

If we choose the reference viscosity to be the shear stress weighted viscosity, $\mu_{\text{Ref}} = \mu_2$, defined as

$$\mu_2 = \frac{\int_0^\infty \overline{\mu \frac{\partial u}{\partial y}} dy}{\int_0^\infty \overline{\frac{\partial u}{\partial y}} dy} = \frac{1}{U_e} \int_0^\infty \overline{\mu \frac{\partial u}{\partial y}} dy, \quad (6.11)$$

the *deviation* term (V) will vanish. In that particular case, the viscous torque becomes

$$T_{v,\ell} = \rho_e U_e^2 \ell \left(\frac{C_f}{2} - \frac{1}{Re_\ell} \right). \quad (6.12)$$

From Eq. (6.12), if ℓ is chosen such that $C_f/2 = 1/Re_\ell = \mu_2/(\rho_e U_e \ell)$ for a ZPG laminar BL solution, then the viscous torque about that ℓ vanishes, $T_{v,\ell} = 0$. The length scale ℓ mathematically connects two BLs, the BL to be analyzed and the baseline ZPG laminar BL it is compared against. The interpretation of the laminar term becomes particularly profitable when the length scale ℓ is tied to a thickness measurement of the BL, e.g., δ_2 , δ_1 , or $\sqrt{\nu x/U_e}$. Given the physical significance of the momentum thickness stemming from the momentum integral equation, Eq. (6.5), $\ell \sim \delta_2$ is a natural choice that has provided insight for incompressible BLs [38]. With this choice,

$$\frac{C_f}{2} = \frac{1}{Re_\ell} = \frac{c_2 \mu_{\text{Ref}}}{U_e \rho_e \delta_2}, \quad \text{and} \quad \ell = \delta_2 / c_2, \quad (6.13)$$

where c_2 is a constant determined by solving self-similar laminar compressible (or incompressible) BL equations. From Eq. (6.13) one can extract the appropriate length scale ℓ , representing the center of action of the viscous force for an equivalent laminar BL with the same $Re_{\delta_2} = \rho_e u_e \delta_2 / \mu_{\text{Ref}}$.

Choices are possible, such as tying the length scale to $\ell \sim \delta_1$ or $\ell \sim \sqrt{vx/U_e}$, which would correspond to the center of action for the viscous force in a laminar BL at the same Re_{δ_1} or Re_x , respectively [38, 179]. Therefore, $\ell = \delta_2/c_2$ isolates in a single term of the AMI equation the equivalent skin friction coefficient of a laminar BL having the same $Re_{\delta_2} = \rho_e u_e \delta_2 / \mu_{\text{Ref}}$. In other words, $2/Re_\ell$ represents the skin-friction coefficient if the flow was a ZPG laminar BL at the same momentum thickness Reynolds number. As a result, all other terms in the AMI equation can be interpreted as augmentations or attenuations of the skin friction coefficient compared to the laminar case.

Note that the laminar solution of the skin friction coefficient to determine c_2 may come from an incompressible (e.g., Blasius) or fully compressible formulation. If a solution to the Blasius equation is used ($c_2 \approx 0.22$), then the AMI equation represents the comparison of a general turbulent compressible BL with an incompressible laminar one. Suppose a more general compressible formulation of the self-similar BL equations is used [171]. In that case, the AMI equation can be interpreted as a comparison with a baseline ZPG laminar BL at the same edge Mach number, M_e , and wall-edge temperature ratio T_w/T_e – provided the self-similar solution for c_2 matches those quantities, i.e., $c_2 = c_2(M_e, T_w/T_e)$.

In addition to choosing the reference length scale (e.g., $\ell \sim \delta_2$ or $\ell \sim \delta_1$) and the reference BL formulation (incompressible or compressible), the use of the AMI equation also allows for choosing different reference viscosities. As noted above, there is one particularly advantageous choice for the AMI equation, $\mu_{\text{Ref}} = \mu_2$, because it causes the *deviation* term to vanish. With the choice of μ_2 , the Reynolds number used for similarity with the baseline laminar BL is,

$$Re_2 = \frac{U_e \rho_e \delta_2}{\mu_2} = \frac{\int_0^\infty \overline{\rho u} (U_e - \tilde{u}) dy}{\int_0^\infty \overline{\mu \frac{\partial u}{\partial y}} dy} = \frac{\int_0^x \overline{\tau_w}(\xi) d\xi}{\int_0^\infty \overline{\mu \frac{\partial u}{\partial y}} dy}, \quad (6.14)$$

where $x = 0$ is the start of the boundary layer. The numerator of Re_2 is the net streamwise flux of velocity defect in the boundary layer. Using the momentum integral equation, Eq. (6.5), this is equal

to the upstream-integrated mean wall shear stress (in the absence of an edge pressure gradient). The denominator is the wall-normal integral of the viscous stress across the boundary layer.

One alternative to μ_2 would be the wall viscosity, μ_w . These two probably do not differ much for adiabatic walls but can vary significantly for strong wall cooling. In principle, the edge viscosity, μ_e , could also be chosen. In the end, the choices of length scale and reference viscosity combine to determine the particular interpretation of the AMI equation as a comparison of skin friction coefficient with an equivalent laminar BL with matched $Re_\ell = \rho_e U_e \ell / \mu_{\text{Ref}}$.

Reynolds shear stress and turbulent torque (II)

The second term on the right-hand side of the AMI equation is the torque due to the Reynolds shear stress, $-\overline{\rho u'' v''}$. The Reynolds stress does not appear explicitly in the momentum integral equation, Eq. (6.5), because it evaluates to zero at both boundaries (wall and edge). In contrast, by integrating the first moment of the velocity defect transport equation, the integral of the Reynolds shear stress appears as an effective torque redistributing velocity defect in the wall-normal direction,

$$\int_0^\infty (y - \ell) \frac{\partial (\overline{\rho u'' v''})}{\partial y} dy = - \int_0^\infty \overline{\rho u'' v''} dy. \quad (6.15)$$

This *turbulent torque* explicitly quantifies how turbulence enhances the BL's friction relative to the baseline laminar BL by bringing higher momentum fluid toward the wall. It is worth mentioning that, in the AMI equation, in contrast to the FIK relation for internal flows [46], the contribution of Reynolds shear stress to the skin-friction coefficient is unweighted. The physical interpretation of the weighting (or lack thereof) in the Reynolds shear stress integral is discussed in detail in Ref. [38].

For compressible flows, the velocity covariance is weighted by the mean density, signifying the role of density in the turbulent transport of momentum. The impact of density variation on the wall-

normal turbulent flux is not specific to the definition of Favre averaging. In general, the momentum (and hence momentum flux) is proportional to the local density, regardless of the averaging method. The difference between $\overline{u'v'}$ and $\widetilde{u''v''}$ was not found to be significant in the present work. A stress-weighted density may encapsulate the role of density variation in altering the turbulence stresses,

$$\rho_2 = \frac{\int_0^\infty \overline{\rho u'' v''} dy}{\int_0^\infty \overline{u'' v''} dy}, \quad (6.16)$$

such that, by definition, the turbulent torque may be written as $-\rho_2 \int_0^\infty \widetilde{u'' v''} dy$. For most BL flows, $-\widetilde{u'' v''} > 0$, so the turbulent torque defined here is typically positive (enhancement of wall shear stress).

Streamwise growth of momentum thickness (III)

Integrating the first moment of the streamwise momentum deficit yields

$$-\int_0^\infty (y - \ell) \frac{\partial}{\partial x} \left(\frac{\bar{\rho}}{\rho_e} \frac{\tilde{u}}{U_e} \left(1 - \frac{\tilde{u}}{U_e} \right) \right) dy = \ell \frac{d\delta_2^\ell}{dx} - (\delta_2 - \delta_2^\ell) \frac{d\ell}{dx}. \quad (6.17)$$

The momentum thickness δ_2 from the classical momentum integral equation, Eq. (6.5), represents the net streamwise flux of streamwise velocity defect. Likewise, δ_2^ℓ , the angular momentum thickness, represents the first moment about $y = \ell(x)$ of the streamwise velocity defect flux. Equation (6.17) represents the rate at which the angular momentum thickness grows relative to the growth rate of ℓ . The choice of length scale, ℓ , plays an important quantitative role in this term. The angular momentum thickness, δ_2^ℓ , is a signed quantity and can be negative or positive depending on the choice of ℓ . One way to interpret Eq. (6.17) is to think of it as representing the rate of change of the angular momentum, with the streamwise coordinate as a time-like variable. As such, it is the resultant term from all of the torques acting on the BL profile as well as the wall shear stress itself from the left-hand side of the AMI equation, Eq. (6.7). Thus, the angular momentum thickness can

be thought of as absorbing any imbalance of torques at a given streamwise location.

Mean wall-normal torque (IV)

The *mean wall-normal* torque in the AMI equation originates from the flux of velocity defect carried by the mean wall-normal flow,

$$- \int_0^{\infty} (y - \ell) \frac{\partial}{\partial y} \left(\frac{\bar{\rho}}{\rho_e} \frac{\tilde{v}}{U_e} \left(1 - \frac{\tilde{u}}{U_e} \right) \right) dy = \delta_{2,v}. \quad (6.18)$$

This term represents the wall-normal flux of streamwise velocity defect, typically positive in most BL conditions. When \tilde{v} is positive, as is typical in BLs, this acts to increase the skin friction because the effect is to transport velocity defect away from the wall, increasing the near-wall velocity. Hence, it looks like a counter clock-wise torque in the AMI equation. In special cases, when $\tilde{v} \leq 0$, the mean wall-normal velocity transports velocity defect toward the wall to attenuate the skin friction. For example, a reversal of mean wall-normal flux has been observed for transitional BLs in the incompressible regime [38].

Non-zero edge pressure gradient (VI)

The torque due to edge pressure gradient originates from a non-zero streamwise derivation of edge velocity, U_e , and density, ρ_e . A favorable edge pressure gradient accelerates the edge velocity, damping the velocity defect in the BL and acting as a counterclockwise torque, which tends to increase the skin friction, Figure 1.7(a). In contrast, an adverse pressure gradient reduces the wall shear stress by acting as a clockwise torque with respect to $y = \ell(x)$, Figure 1.7(b). In this study, only zero pressure gradient BLs will be considered, so this term is negligible for all cases shown here. Future work will examine the effect of edge pressure gradients using the AMI equation.

Departure from BL approximations (VII)

Torque caused by the terms corresponding to derivatives with respect to streamwise direction and variation of mean pressure across the BL is included in I_M^ℓ . For most BLs, the contribution of these terms is expected to be negligible. The *negligible terms*, however, might need to be accounted for in some critical scenarios, such as transitional flows and flows in the vicinity of the BL separation or shock-BL interactions.

6.1.2 Moment of Total Enthalpy Integral Equation

In a previous study, the concept of the AMI equation has been extended to study heat transfer in incompressible BLs [82], analogous to the AMI equation for the skin friction coefficient. The resulting Moment of Temperature Integral (MTI) equation relates the surface heat flux to various flow physics through the BL. In this section, this approach is generalized to form the moment of total enthalpy integral (MTEI) equation for compressible BLs, taking into account variations in density, viscosity, and thermal conductivity.

Derivation

Taking a similar approach as in section 6.1.1 yields the MTEI equation from the total enthalpy equation. The Reynolds averaged total enthalpy equation for a statistically stationary 2D BL reads

$$\frac{\partial}{\partial x} \left(\overline{\rho u \tilde{H}} \right) + \frac{\partial}{\partial y} \left(\overline{\rho v \tilde{H}} \right) = \frac{\partial}{\partial y} \left(\overline{k \frac{\partial T}{\partial y}} + \overline{\mu u \frac{\partial u}{\partial y}} - \overline{\rho v'' H''} \right) + I_H, \quad (6.19)$$

in which the Favre averaging is implemented. In Eq. (6.19), $H = c_p T_o = c_p T + u^2/2$ is total enthalpy (by neglecting contributions of wall-normal and spanwise velocities by invoking standard BL arguments), and T is temperature. While the (dynamic) viscosity (μ) and thermal conductivity

(k) are assumed to vary with temperature, Prandtl number, $Pr = \mu c_p/k$, and specific heat capacity, c_p , are approximated as constants in this work. However, this assumption can be straightforwardly relaxed to address more general scenarios. In Eq. (6.19), the terms that are neglected in BL approximation are collected in I_H . Subtracting Eq. (6.19) from H_e times the continuity equation, Eq. (6.1), a transport equation for the total enthalpy defect is achieved,

$$\frac{\partial}{\partial x} \left(\bar{\rho} \tilde{u} (H_e - \tilde{H}) \right) + \frac{\partial}{\partial y} \left(\bar{\rho} \tilde{v} (H_e - \tilde{H}) \right) = -\frac{\partial}{\partial y} \left(k \frac{\partial T}{\partial y} + \overline{\mu u \frac{\partial u}{\partial y}} - \overline{\rho v'' H''} \right) - I_H. \quad (6.20)$$

The total enthalpy at the BL edge, H_e , is assumed constant in the streamwise direction (i.e., assuming adiabatic flow outside the BL). Integrating Eq. (6.20) across the BL yields the (classic) integral equation for the Stanton number

$$St = \frac{d\delta_H}{dx} + \left(1 + \frac{U_e}{\rho_e} \frac{\partial \rho_e}{\partial U_e} \right) \frac{\delta_H}{U_e} \frac{dU_e}{dx} + \frac{\delta_H}{H_{\text{Ref}} - H_w} \frac{d(H_{\text{Ref}} - H_w)}{dx} + \mathcal{I}_H, \quad (6.21)$$

where the Stanton number (St) and total enthalpy thickness (δ_H) are defined as follows,

$$St \equiv \frac{\bar{q}_w}{\rho_e U_e (H_{\text{Ref}} - H_w)}, \quad \delta_H \equiv \int_0^\infty \frac{\bar{\rho}}{\rho_e} \frac{\tilde{u}}{U_e} \left(\frac{H_e - \tilde{H}}{H_{\text{Ref}} - H_w} \right) dy. \quad (6.22)$$

In the above, $q_w = -k_w (\partial T / \partial y)_w$ is the wall heat flux. Typically negligible for BLs, \mathcal{I}_H is the result of integration of I_H . Equation (6.21) is valid for laminar, transitional, and turbulent flow, yet one cannot determine the explicit contribution of fluctuations (or perturbations) on surface heat flux. In contrast, taking a similar approach as the AMI equation, we multiply Eq. (6.20) by a length scale, $(y - \ell)$, (as the first moment), then integrate the whole equation across the BL. Imposing the wall and edge boundary conditions, we obtain the MTEI equation for high-speed compressible BLs

$$\begin{aligned}
St = & \frac{1}{Pr_{\text{Ref}} \cdot Re_\ell} + \frac{1}{\ell} \int_0^\infty \frac{-\bar{\rho} \widetilde{v''} \widetilde{H''}}{\rho_e U_e (H_{\text{Ref}} - H_w)} dy + \left\{ \frac{d\delta_H^\ell}{dx} - \frac{\delta_H - \delta_H^\ell}{\ell} \frac{d\ell}{dx} \right\} + \frac{\delta_{H,v}}{\ell} \\
& + \frac{1}{\ell} \int_0^\infty \frac{(k - k_{\text{Ref}}) \frac{\partial T}{\partial y} + (\mu - \mu_{\text{Ref}}) u \frac{\partial u}{\partial y}}{\rho_e U_e (H_{\text{Ref}} - H_w)} dy + \left(1 + \frac{U_e}{\rho_e} \frac{\partial \rho_e}{\partial U_e} \right) \frac{\delta_H^\ell}{U_e} \frac{dU_e}{dx} \\
& + \frac{\delta_H^\ell}{H_{\text{Ref}} - H_w} \frac{d(H_{\text{Ref}} - H_w)}{dx} + \mathcal{I}_H^\ell.
\end{aligned} \tag{6.23}$$

where the left-hand side is the Stanton number defined in Eq. (6.22). The basis of choosing an appropriate length scale ℓ for the MTEI equation is discussed in Section 6.1.2. In particular, to isolate the laminar Stanton number (like in this report), ℓ is defined in Eq. (6.30). The MTEI equation, Eq. (6.23), introduces the moment of total enthalpy thickness and mean wall-normal enthalpy thickness as

$$\delta_H^\ell \equiv \int_0^\infty \left(1 - \frac{y}{\ell} \right) \frac{\bar{\rho}}{\rho_e} \frac{\tilde{u}}{U_e} \left(\frac{H_e - \tilde{H}}{H_{\text{Ref}} - H_w} \right) dy, \quad \delta_{H,v} \equiv \int_0^\infty \frac{\bar{\rho}}{\rho_e} \frac{\tilde{v}}{U_e} \left(\frac{H_e - \tilde{H}}{H_{\text{Ref}} - H_w} \right) dy, \tag{6.24}$$

respectively. The total enthalpy thickness, δ_H , is recovered in the limit of $\ell \rightarrow \infty$. Finally, \mathcal{I}_H^ℓ in Eq. (6.23), arises from the integration of the first moment of I_H .

In Eq. (6.23), k_{Ref} and μ_{Ref} are the reference conductivity and viscosity, respectively. The reference conductivity and viscosity are related via a reference Prandtl number, $Pr_{\text{Ref}} = c_p \mu_{\text{Ref}} / k_{\text{Ref}}$. It is not necessary to choose $Pr_{\text{Ref}} = Pr$, even for constant Pr flow. Instead, the reference Prandtl number should be chosen based on the desired reference enthalpy,

$$H_{\text{Ref}} = c_p (T_e - T_w) + Pr_{\text{Ref}} \frac{U_e^2}{2}. \tag{6.25}$$

Thus, the reference Prandtl number acts as a sort of reference recovery factor for defining the Stanton number.

A common definition of the Stanton number is based on the difference between the adiabatic wall

temperature, T_{aw} , and wall temperature, T_w , that is, $St = \overline{q_w} / \rho_e U_e (H_{aw} - H_w)$. Such a definition can be facilitated with the choice of $Pr_{Ref} = r_{Ref}$, the reference recovery factor for defining an adiabatic wall temperature. However, it is well known that the recovery factor for laminar and turbulent BLs can be quite different, e.g., $Pr^{1/2}$ for laminar BLs and approximately $Pr^{1/3}$ for turbulent BLs [171]. This complicates the interpretation of the MTEI equation, in particular, the first term, which should represent the Stanton number of an equivalent laminar BL that serves as a reference for the transitional or turbulent BL under consideration. Thus, it is not clear how to choose the reference recovery factor. (Often for BLs in the hypersonic regime with chemical and thermal non-equilibrium, the heat flux coefficient is defined based on the edge kinetic energy, $C_q = \overline{q_w} / \rho_e U_e^3$ [34].)

Instead, the author believes that the interpretation of the MTEI equation is more straightforward if the edge stagnation enthalpy is used in the denominator of the Stanton number, corresponding to the choice of $Pr_{Ref} = 1$. With this choice, the denominator includes the maximum total enthalpy difference, $H_e - H_w$, available to supply energy to the wall (in the form of surface heat flux). This definition does allow for negative Stanton numbers in the case of non-unity recovery factors. Still, such negative Stanton numbers are interpretable as net energy flux opposite the global driving energy difference. The effect of turbulence to increase the recovery factor (adiabatic wall temperature) can thus be included within the broader analysis without causing interpretive difficulties. Thus, the Stanton number definition used in this chapter is given by Eq. (6.22), equivalent to the choice of $Pr_{Ref} = 1$. Other choices are possible and may be the subject of future research.

Interpretation

The right-hand side of the MTEI equation, Eq. (6.23), consists of several terms representing a mapping of flow phenomena based on how they alter the Stanton number. A physical description

of each flow feature in the MTEI equation is summarized as

- (I) $\frac{1}{Pr_{\text{Ref}} \cdot Re_\ell} \rightarrow$ the Stanton number of an equivalent *laminar* BL at matched Re_ℓ ,
- (II) $\frac{1}{\ell} \int_0^\infty \frac{-\overline{\rho v'' H''}}{\rho_e U_e (H_{\text{Ref}} - H_w)} dy \rightarrow$ *turbulent flux* integral, turbulent transport of total enthalpy,
- (III) $\frac{d\delta_H^\ell}{dx} - \frac{\delta_H - \delta_H^\ell}{\ell} \frac{d\ell}{dx} \rightarrow$ *streamwise growth* of the first moment of total enthalpy thickness,
- (IV) $\frac{\delta_{H,v}}{\ell} \rightarrow$ flux by *mean wall-normal* transport,
- (V) $\frac{1}{\ell} \int_0^\infty \frac{\overline{(k - k_{\text{Ref}}) \frac{\partial T}{\partial y} + (\mu - \mu_{\text{Ref}}) u \frac{\partial u}{\partial y}}}{\rho_e U_e (H_{\text{Ref}} - H_w)} dy \rightarrow$ *deviation* from reference viscous transport,
- (VI) $\left(1 + \frac{U_e}{\rho_e} \frac{\partial \rho_e}{\partial U_e}\right) \frac{\delta_H^\ell}{U_e} \frac{dU_e}{dx} \rightarrow$ *edge pressure gradient flux*,
- (VII) $\frac{\delta_H^\ell}{H_{\text{Ref}} - H_w} \frac{d(H_{\text{Ref}} - H_w)}{dx} \rightarrow$ flux by *wall-temperature variation*,
- (VIII) $\mathcal{I}_H^\ell \rightarrow$ *negligible terms*.

A detailed discussion of these flow phenomena is given in the proceeding paragraphs. The MTEI equation is derived from the first moment of the total enthalpy deficit transport equation that involves both internal and kinetic energy transport mechanisms. Thus, we interpret the flow phenomena on the right-hand side of Eq. (6.23) as fluxes of total enthalpy, or redistribution of the total enthalpy profile.

Viscous flux and the laminar Stanton number (I) & (V)

In the MTEI equation, the Stanton number, *laminar* flux, and *deviation* originate from

$$\int_0^\infty (y - \ell) \left[\frac{\partial}{\partial y} \left(\overline{k \frac{\partial T}{\partial y}} + \overline{\mu u \frac{\partial u}{\partial y}} \right) \right] dy = \ell q_w - \frac{k_{\text{Ref}}}{c_p} (H_{\text{Ref}} - H_w) - \int_0^\infty \left(\overline{(k - k_{\text{Ref}}) \frac{\partial T}{\partial y} + (\mu - \mu_{\text{Ref}}) u \frac{\partial u}{\partial y}} \right) dy. \quad (6.26)$$

One can merge all the viscous (laminar) effects in a single term, $1/Pr_{\text{Ref}} \cdot Re_\ell$, by choosing the reference conductivity as $k_{\text{Ref}} = k_H$ (i.e., reference viscosity as $\mu_{\text{Ref}} = \mu_H$), where

$$k_H = \frac{\int_0^\infty \overline{k \left(c_p \frac{\partial T}{\partial y} + Pr u \frac{\partial u}{\partial y} \right) dy}}{\int_0^\infty \overline{\left(c_p \frac{\partial T}{\partial y} + Pr_{\text{Ref}} u \frac{\partial u}{\partial y} \right) dy}} = \frac{\int_0^\infty \overline{\left(k \frac{\partial T}{\partial y} + \mu u \frac{\partial u}{\partial y} \right) dy}}{T_{\text{Ref}} - T_w}, \quad (6.27)$$

$$\mu_H = \frac{\int_0^\infty \overline{\mu \left(\frac{c_p}{Pr} \frac{\partial T}{\partial y} + u \frac{\partial u}{\partial y} \right) dy}}{\int_0^\infty \overline{\left(\frac{c_p}{Pr_{\text{Ref}}} \frac{\partial T}{\partial y} + u \frac{\partial u}{\partial y} \right) dy}} = \frac{Pr_{\text{Ref}} \int_0^\infty \overline{\left(k \frac{\partial T}{\partial y} + \mu u \frac{\partial u}{\partial y} \right) dy}}{c_p (T_{\text{Ref}} - T_w)} = \frac{Pr_{\text{Ref}}}{c_p} k_H, \quad (6.28)$$

where $T_{\text{Ref}} = H_{\text{Ref}}/c_p$ is the adiabatic wall temperature, $T_{\text{Ref}} = T_{\text{aw}}$, for $Pr_{\text{Ref}} = r_{\text{Ref}}$ or the edge stagnation temperature, $T_{\text{Ref}} = T_{o,e}$, for the choice $Pr_{\text{Ref}} = 1$. With such reference values, the *deviation* term (V) will vanish. μ_H can be interpreted as a viscosity balancing between molecular conduction and viscous dissipation of kinetic energy. Hence,

$$\rho_e U_e (H_e - H_w) \ell \left(St - \frac{1}{Pr_{\text{Ref}} Re_\ell} \right) = 0. \quad (6.29)$$

For ZPG compressible BLs,

$$St = \frac{1}{Pr_{\text{Ref}} Re_\ell} = \frac{c_H k_H}{\rho_e c_p U_e \delta_H}, \quad \text{and} \quad \ell = \delta_H / c_H, \quad (6.30)$$

where c_H is a constant calculated by solving self-similar ZPG laminar compressible (or incompressible) momentum and energy equations. Implementing the definition of ℓ according to Eq. (6.30) the laminar St is precisely equal to $1/Pr_{\text{Ref}} Re_\ell$ at specific $\delta_H(x)$. Together, the choice of δ_H and k_H as the reference length and reference transport coefficient, respectively, the Peclet number used

for similarity with the baseline laminar BL is,

$$Pe_H = \frac{U_e \rho_e c_p \delta_H}{k_H} = \frac{\int_0^\infty \bar{\rho} \tilde{u} (H_e - \tilde{H}) dy}{\int_0^\infty \left(k \frac{\partial T}{\partial y} + \mu u \frac{\partial u}{\partial y} \right) dy} = \frac{\int_0^x \bar{q}_w(\xi) d\xi}{\int_0^\infty \left(k \frac{\partial T}{\partial y} + \mu u \frac{\partial u}{\partial y} \right) dy}. \quad (6.31)$$

The numerator is the streamwise flux of the total enthalpy defect. Using the total enthalpy integral equation, Eq. (6.21), this is equal to the upstream-integrated wall heat flux. The denominator is the net wall-normal flux of total enthalpy due to viscous and conductive transport.

Turbulent total enthalpy flux (II)

The second term on the right-hand side of the MTEI equation is the flux due to covariance of wall-normal velocity and total enthalpy, $-\overline{\rho H'' v''}$. By integrating the first moment of the wall-normal derivative of the turbulence covariance,

$$\int_0^\infty (y - \ell) \frac{\partial \left(\overline{\rho H'' v''} \right)}{\partial y} dy = - \int_0^\infty \overline{\rho H'' v''} dy, \quad (6.32)$$

we obtain the explicit contribution of the turbulent flux of total enthalpy (*turbulent flux*) to the surface heat flux. Naturally, the internal and kinetic energies are embedded into total enthalpy. Therefore, the covariance of wall-normal velocity and total enthalpy can be further decomposed to quantify the role of enthalpy and kinetic energies on *turbulent flux*. Eq. 6.32 is rewritten as

$$\int_0^\infty \overline{\rho H'' v''} dy = \int_0^\infty \bar{\rho} \left(c_p \overline{T'' v''} + \overline{u u'' v''} + \frac{1}{2} \overline{u'' u'' v''} \right) dy, \quad (6.33)$$

where $c_p \overline{\rho T'' v''}$, $\overline{\rho u u'' v''}$, and $\overline{\rho u'' u'' v''} / 2$ are wall-normal turbulent fluxes of enthalpy, mean kinetic energy, turbulent kinetic energy, respectively. For high Mach number (supersonic and hypersonic) BLs, the turbulent transport of the mean kinetic energy, $\overline{\rho u u'' v''}$, is expected to be the primary contributor enhancing the surface heat flux, whereas the turbulent flux of enthalpy, $c_p \overline{\rho T'' v''}$, naturally

reduces the surface heat flux toward the wall because $T_w \geq T_e$, as is the case for most high-speed aerodynamic heating applications.

Streamwise growth of enthalpy thickness (III)

The contribution of the *streamwise growth* of the total enthalpy thickness to the surface heat flux originates from

$$\int_0^\infty (y - \ell) \frac{\partial}{\partial x} \left(\frac{\bar{\rho}}{\rho_e} \frac{\tilde{u}}{U_e} \left(\frac{H_e - \tilde{H}}{H_{\text{Ref}} - H_w} \right) \right) dy = -\ell \frac{d\delta_H^\ell}{dx} + (\delta_H - \delta_H^\ell) \frac{d\ell}{dx}. \quad (6.34)$$

The total enthalpy thickness, δ_H , from Eq. (6.21), represents the net streamwise flux of total enthalpy defect in the BL. The first moment of the total enthalpy defect flux is captured by δ_H^ℓ , the moment of total enthalpy thickness. Equation (6.23) can be thought of as an equation for the growth rate of the moment of total enthalpy thickness, $d\delta_H^\ell/dx$, with all other terms being analogous to “torques”, redistributing the total enthalpy in the wall-normal direction to alter its moment about $y = \ell(x)$. Like the angular momentum thickness, the moment of total enthalpy thickness is a signed quantity; its rate of change with x can be positive or negative, depending on how it absorbs total enthalpy fluxes from the other terms. Moreover, the growth rate of the moment of total enthalpy and angular momentum thicknesses are not necessarily the same due to the effect of Prandtl number and complex energy transfer mechanisms.

Mean wall-normal flux (IV)

The *mean wall-normal* flux of total enthalpy is due to the wall-normal advection of total enthalpy deficit,

$$\int_0^\infty (y - \ell) \frac{\partial}{\partial y} \left(\frac{\bar{\rho}}{\rho_e} \frac{\tilde{v}}{U_e} \left(\frac{H_e - \tilde{H}}{H_{\text{Ref}} - H_w} \right) \right) dy = -\delta_{H,v}. \quad (6.35)$$

This term represents how mean wall-normal velocity transports total enthalpy across the BL and affects the surface heat flux. It is analogous to the *mean wall-normal* torque in the AMI equation and will generally have the same behavior. A recent investigation of incompressible BLs revealed a negative contribution of *mean wall-normal* to the Stanton number because of the negative wall-normal velocity region in the vicinity of the surface during the transition to turbulence [82]. However, for a fully turbulent regime, the *mean wall-normal* flux is generally positive and weakly augments the surface heat flux.

Non-zero edge pressure gradient and wall temperature variation (VI) & (VII)

Just as an adverse or favorable pressure gradient may act as torque to alter the mean velocity defect profile, the moment of total enthalpy thickness is also subject to edge pressure gradient effects. Additionally, any variation of the wall temperature also impacts the evolution of the moment of total enthalpy thickness. In this chapter, zero pressure gradient BLs over isothermal walls are considered, so the exploration of these terms is left to future work.

Departure from BL approximations (VIII)

All terms in the total enthalpy conservation equation that are typically small in thin BLs are gathered in a single term, negligible fluxes. For high-speed BLs (with no BL separation), the *negligible terms* originated from the streamwise derivative of the streamwise heat flux, $-\overline{k\partial T/\partial x}$, and the streamwise velocity and total enthalpy covariance, $\overline{\rho v'' H''}$. While not relevant to the present work, these terms could become significant and warrant more attention to flows such as incipient BL separation or shock-BL interactions.

6.2 Results and Analysis

Now that the first-moment integral equations, namely AMI and MTEI equations, are extended to high-speed BLs, The author applies these techniques to laminar and turbulent compressible BL datasets. The BL dataset has a wide range of edge Mach numbers from subsonic to supersonic. Also, a variety of wall-temperature boundary conditions, including adiabatic wall and cold wall, have been applied. This section studies the AMI and MTEI equations within the laminar regime. Subsequently, we focus on fully turbulent BLs to investigate the effect of turbulence on the skin friction coefficient and Stanton number.

6.2.1 Laminar Regime

Before turning our attention to turbulent boundary layers, here, the impact of compressibility on skin friction and surface heat flux is explored. For now, we limit our analysis to ZPG laminar compressible BLs over a flat plate. Similar to incompressible laminar BLs, self-similarity can be achieved in compressible BLs using unique transformations. Taking into account the Illingworth transformation for steady laminar BLs with constant edge conditions, the similarity variables read

$$\xi(x) = \rho_e \mu_e U_e x \quad \text{and} \quad \eta(x, y) = \frac{U_e}{\sqrt{2\xi}} \int_0^y \rho dy. \quad (6.36)$$

A streamfunction $\psi = f(\eta)\sqrt{2\xi}$ satisfies the (steady) continuity equation, Eq. (2.1), in a way that $u = U_e f'$ and $\rho v = -\rho_e \mu_e U_e f / \sqrt{2\xi} - \eta_x f' \sqrt{2\xi}$. Applying the above transformation to the steady BLs momentum equation, the following ordinary differential equation (ODE) for f is achieved

$$(C f'')' + f f'' = 0, \quad (6.37)$$

where $C = \rho\mu/\rho_e\mu_e$ is the Chapman-Rubensin parameter. Note only in this case the superscript \prime denotes differentiation with respect to the similarity variable η . The boundary conditions for Eq. (6.37) are the same as Blasius solution, namely $f(0) = 0$, $f'(0) = 0$, and $f'(\eta \rightarrow \infty) = 1$. The BLs energy equation also takes a self-similar ODE form –under some assumptions [171]– if the enthalpy field is separated into a magnitude, $h_e(\xi)$, multiplied by a shape function, $g(\eta)$, as

$$h(x, y) = h_e(\xi)g(\eta). \quad (6.38)$$

The self-similar energy equation for calorically perfect gas with constant Pr reads

$$(Cg')' + Prfg' + Pr(\gamma - 1)M_e^2Cf''^2 = 0, \quad (6.39)$$

where it's coupled with the momentum equation, Eq. (6.37). The boundary conditions for g , depending on the wall condition, yield

$$\text{Adiabatic wall: } g(0) = g_w, \quad g'(0) = 0, \quad g(\infty) = 1$$

$$\text{Non-adiabatic wall: } g(0) = g_w, \quad g'(0) \neq 0, \quad g(\infty) = 1.$$

The self-similar momentum and energy equations, Eqs. (6.37) and (6.39), are solved numerically by applying second-order finite differences and a Newton-Raphson method with a line-search algorithm, based on Ref. [174]. The inputs for the self-similar BL solver are the edge Mach number and the wall-edge temperature ratio. The C++ solver outputs the self-similar functions f , f' , f'' , and g from which I construct the streamwise and wall-normal velocity profiles as well as the temperature and density fields.

Angular momentum integral equation

For the laminar regime, naturally, the Reynolds stress components are zero, i.e., the *turbulent torque* disappears. Moreover, the *negligible terms* vanish to comply with the BL approximations. In our analysis, although not necessary, I further assumed the BL edge quantities remain constant in the streamwise direction; thus, the *edge pressure gradient* is also zero. Note these conditions are already imposed on the self-similar equation, Eq. (6.37). Consequently, the AMI equation is simplified to

$$\frac{C_f}{2} = \frac{1}{Re_\ell} + \left\{ \frac{d\delta_2^\ell}{dx} - \frac{\delta_2 - \delta_2^\ell}{\ell} \frac{d\ell}{dx} \right\} + \frac{\delta_{2,v}}{\ell} + \frac{1}{\ell} \int_0^\infty \frac{(\mu - \mu_{\text{Ref}}) \frac{\partial u}{\partial y}}{\rho_e U_e^2} dy \quad (6.40)$$

for ZPG laminar compressible BL. If we choose $\ell \sim \delta_2$, and constraint $C_f/2 \equiv 1/Re_\ell$, coefficient c_2 in Eq. (6.13) can be determined from the self-similar solution as

$$c_2 = \left[\frac{\mu_w}{\mu_{\text{Ref}}} \right] \frac{f''(0) \int_0^\infty f'(1-f') d\eta}{g(0)}. \quad (6.41)$$

Having the appropriate AMI's length scale, ℓ , we can proceed with the AMI analysis and apply it to the self-similar laminar solution. Here, I consider the cases in Table 6.1, and input feed M_e and T_w/T_e as inputs to the laminar solver. Figure 6.1 shows the four non-zero flow phenomena that appear in the right-hand side of Eq. (6.40); Fig. 6.1 (a) is the *laminar* term that is equivalent to the skin-friction coefficient. Therefore, the sum of the other three flow phenomena must cancel each other out. Consistent with previous observations, [171], C_f decreases at higher M_e . We observe this is primarily due to the effect of lower near-wall density and how it impacts the momentum transport mechanism; this phenomenon will be further studied in the next section for fully turbulent flows. Moreover, the effect of wall cooling on friction is evident; the stronger the wall cooling, the higher the skin friction coefficient. This effect is significant comparing D-5 and E-5, both with $M_e = 5$, yet E-5 is strongly cooled. The contribution of deviation from the reference viscosity is non-zero as $\mu_{\text{Ref}} = \mu_w$, Figure 6.1 (b). This contribution is directly impacted by the temperature profile within the BL and the imposed wall condition, e.g., adiabatic or non-adiabatic. The *deviation*

negatively contributes to C_f for the adiabatic wall cases for which the peak temperature occurs at the surface, and the reference viscosity is smaller than the wall viscosity. Colder T_w increases the *deviation* until it becomes positive for strongly cold wall cases, such as E-5. The trend of the *streamwise growth* and (*mean*) *wall-normal* torque are similar to what was observed in laminar and early transitional incompressible BLs, Chapter 4. The (*mean*) *wall-normal* torque increases the skin-friction coefficient, whereas the *streamwise growth* approximately balances this enhancement. Their strengths depend on the wall-cooling and edge Mach number and how these confine the BL thickness growth; the thicker the viscous region –higher wall-normal velocity–, the stronger the effect of the (*mean*) *wall-normal* torque, and hence the *streamwise growth*.

A similar laminar AMI analysis is presented in Figs. 6.2 but for the reference viscosity $\mu_{\text{Ref}} = \mu_2$, obtained from Eq. (6.11). Therefore, the *viscous deviation* naturally vanishes, Fig. 6.2 (b). Since $C_f/2 = 1/Re_\ell$, the *streamwise growth* and *wall-normal torque* perfectly balance each other. Interestingly, choosing $\mu_{\text{Ref}} = \mu_2$ absorbs a considerable amount of the wall-cooling effect on the *streamwise growth* and *wall-normal torque*, i.e. these flow phenomena primarily vary with respect to M_e .

Moment of total enthalpy integral equation

The MTEI equation is significantly simplified for the laminar regime as the *turbulent flux* and *negligible terms* naturally disappear. Furthermore, we focus on ZPG BLs over a flat plate with constant wall temperature in the streamwise direction; hence, fluxes by the *edge pressure gradient* and *wall-temperature variation* vanish too. Consequently, the MTEI equation reads

$$St = \frac{1}{Pr_{\text{Ref}} \cdot Re_\ell} + \left\{ \frac{d\delta_H^\ell}{dx} - \frac{\delta_H - \delta_H^\ell}{\ell} \frac{d\ell}{dx} \right\} + \frac{\delta_{H,v}}{\ell} + \frac{1}{\ell} \int_0^\infty \frac{(k - k_{\text{Ref}}) \frac{\partial T}{\partial y} + (\mu - \mu_{\text{Ref}}) u \frac{\partial u}{\partial y}}{\rho_e U_e (H_{\text{Ref}} - H_w)} dy. \quad (6.42)$$

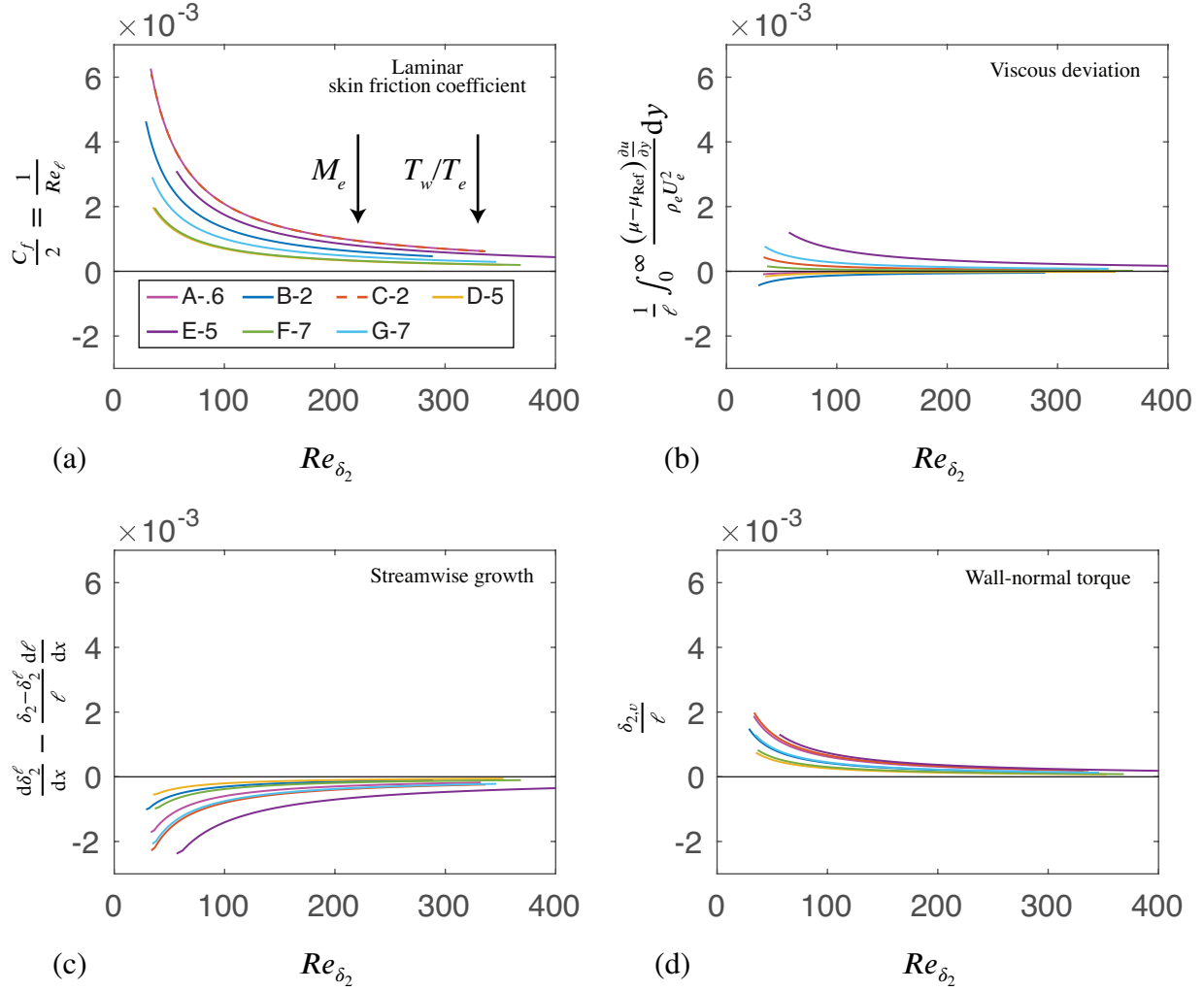


Figure 6.1: The budget of the laminar AMI equation, Eq. (6.40), based on $\mu_{\text{Ref}} = \mu_w$: laminar skin friction (a), the viscous deviation (b), the streamwise growth of the angular momentum thickness (c), and the torque due to wall-normal velocity (d). Each term is shown as a function of $Re_{\delta_2} = U_e \rho_e \delta_2 / \mu_w$. In (a), C-2 is shown with dashed lines.

By assuming $\ell \sim \delta_H$, and isolating the laminar Stanton number to $1/Pr_{\text{Ref}} Re_{\ell}$, we determine coefficient c_H in Eq. (6.30) as

$$c_H = \left[\frac{k_w}{k_{\text{Ref}}} \right] \left[\frac{T_{\text{Ref}} - T_w}{T_e} \right] \frac{g'(0) \int_0^{\infty} f'(1-G) d\eta}{g(0)(1-G(0))}, \quad (6.43)$$

where $G = T_o/T_{o,e}$ is the ratio of the stagnation temperature. Note, the second term within the brackets on the right-hand side of Eq. (6.43) emerges from the definition of the Stanton number,

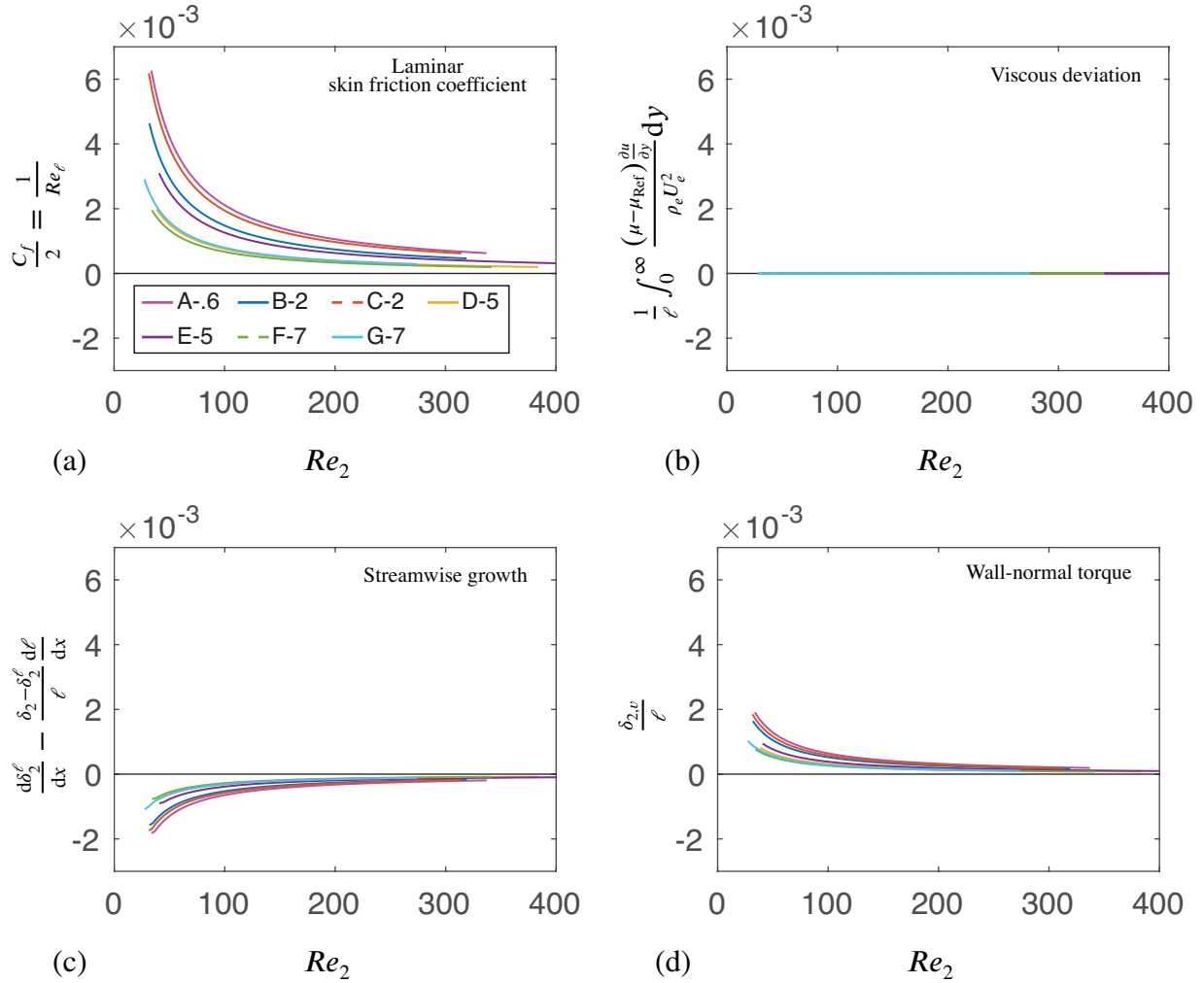


Figure 6.2: The budget of the laminar AMI equation, Eq. (6.40), based on $\mu_{Ref} = \mu_2$: laminar skin friction (a), the viscous deviation (b), the streamwise growth of the angular momentum thickness (c), and the torque due to wall-normal velocity (d).

Eq. (6.22), and hence the choice of the reference total enthalpy; this is discussed in details in Section 6.1.2.

Figures 6.3 present the four non-zero flow phenomena that appeared on the right-hand side of the laminar MTEI equation, Eq. 6.42. The laminar solution is obtained for the non-adiabatic wall cases in Table 6.1 by inputting M_e and T_w/T_e . The influence of the edge Mach number and wall-cooling on the Stanton number are qualitatively similar to what we observed in laminar skin friction coefficient; the higher the edge Mach number or, the weaker the wall cooling, the lower the Stanton

number at the wall, Fig. 6.3 (a). In addition, the *wall-normal flux* in the MTEI analysis behaves analogous to its counterpart in the AMI equation. With the choice of $\mu_{\text{Ref}} = \mu_w$ (and $Pr = 0.72$), the *viscous deviation* term has stronger negative contributions to the Stanton number rather than the *viscous deviation* term in the AMI analysis, Fig. 6.3 (b). Interestingly, wall-cooling forces the deviation term to approach zero; we observe in D-5 that this term approximately vanishes. To alleviate this stronger negative contribution and to satisfy the balance of the MTEI budget, the flux caused by the *streamwise growth* becomes more positive than its counterpart in the AMI equation, Fig. 6.3 (b). Surprisingly, for the cases with weak wall-cooling (D-5), this flow phenomenon, that is often contributes negatively to the Stanton number, flips the sign and becomes positive.

In Figs. 6.4 the laminar MTEI analysis is conducted using the reference viscosity $\mu_{\text{Ref}} = \mu_H$ based on Eq. (6.28). Here, the flow phenomena on the right-hand side of the MTEI equation are plotted with respect to the Peclet number, Pe_H , in the x -axis. Note the choice of the reference viscosity yields zero *viscous deviation*. In analogous to the laminar AMI analysis, by making the *viscous deviation* zero, the *streamwise growth* and *wall-normal flux* perfectly cancel each other. Also, These two flow phenomena are now mainly sorted based on the edge Mach number, i.e., their dependency on wall-cooling have been reduced.

6.2.2 Turbulent Regime

As discussed before, the first moment integral equations are valid for laminar, transitional, or turbulent regimes. In Section 6.2.1, we applied the AMI and MTEI decomposition on laminar compressible BLs with a variety of edge and wall temperature conditions. These equations provide a physical understanding of how and why the skin friction and surface heat flux vary in laminar high-speed BLs. Besides that, the laminar solutions –with matching wall-edge conditions as the turbulent counterpart– are required to determine coefficients c_2 and c_H in the AMI and MTEI equations length scale ℓ , respectively. Having the required coefficients in hand, we can proceed to study

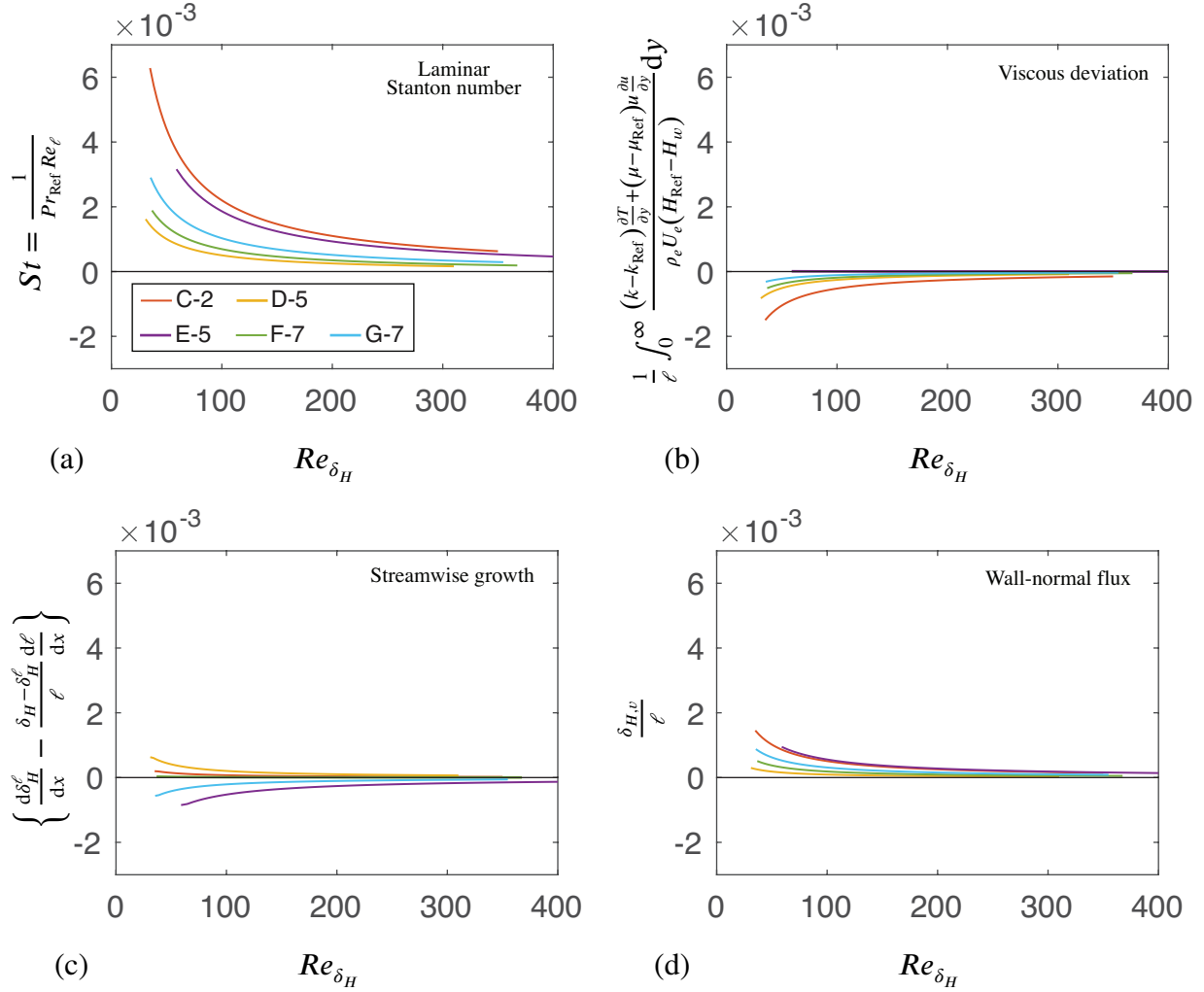


Figure 6.3: The budget of the laminar MTEI equation, Eq. (6.42), based on $\mu_{\text{Ref}} = \mu_w$: laminar Stanton number (a), the viscous deviation (b), the streamwise growth (c), and the flux due to wall-normal velocity (d).

turbulent high-speed BLs.

Dataset

This section discusses the compressible turbulent BL data used to evaluate the AMI and MTEI equations, Eqs. (6.7) and (6.23), respectively. The data are obtained from DNS of compressible BLs using a turbulent recycling method with zero edge pressure gradient [33]. A sixth-order hybrid scheme was utilized in the numerical simulations to ensure very low numerical dissipation.

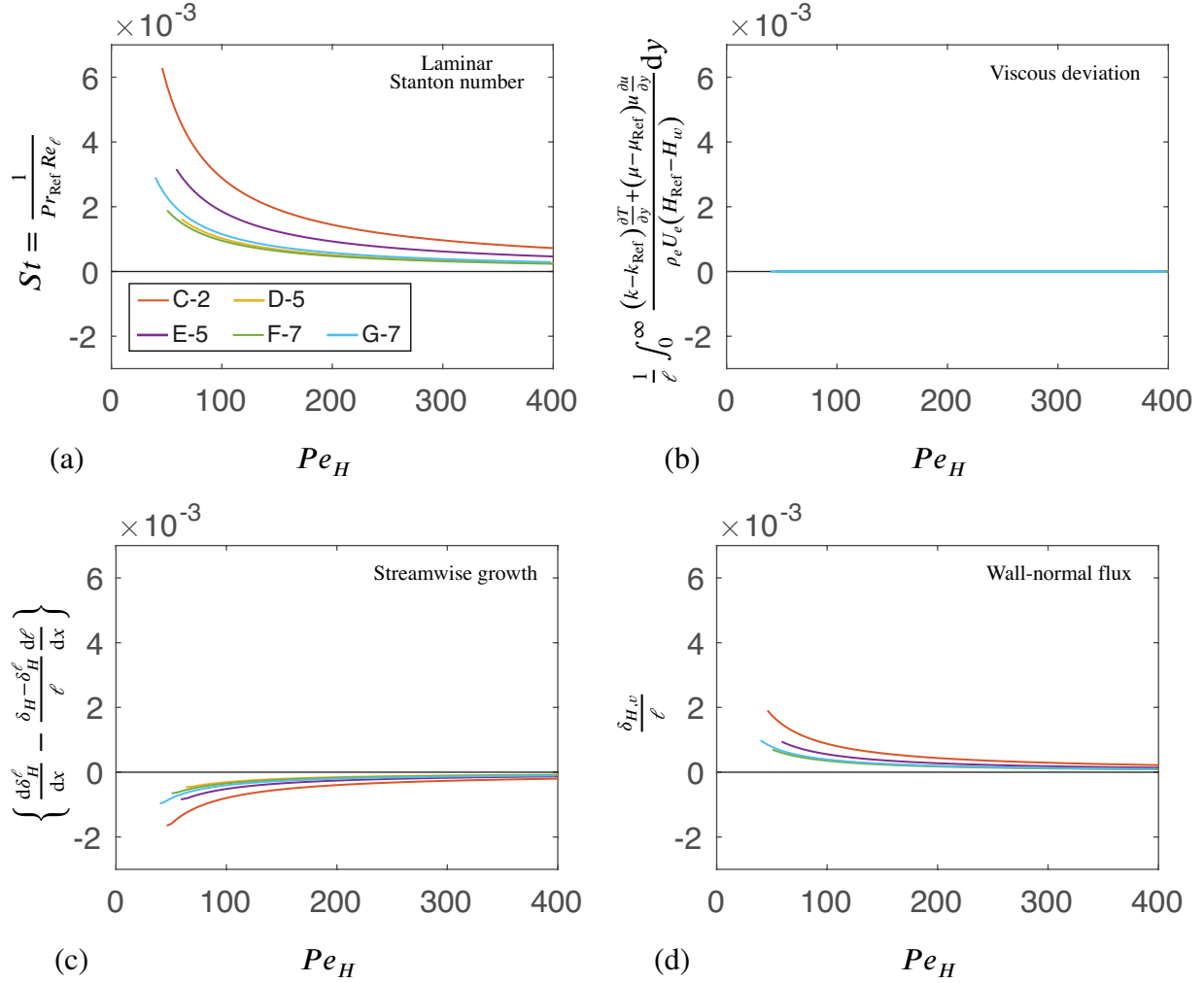


Figure 6.4: The budget of the laminar MTEI equation, Eq. (6.42), based on $\mu_{\text{Ref}} = \mu_H$: laminar Stanton number (a), the viscous deviation (b), the streamwise growth (c), and the flux due to wall-normal velocity (d).

This scheme uses a skew-symmetric formulation [130] in smooth regions of the flow and a sixth-order targeted essentially non-oscillatory (TENO) scheme across discontinuities [45]. In low-Mach-number calculations, the TENO scheme is never utilized, and the calculation is entirely carried out using the skew-symmetric method. At higher Mach numbers, the TENO scheme is triggered only on a small fraction of the computational grid points. Since the Reynolds number is relatively high for the simulations, a second-order central finite-difference stencil is applied for the diffusion fluxes. The time integration is conducted using the strong-stability-preserving third-order Runge–Kutta method [50]. The system of equations for DNS is solved by the hypersonics task-based research








Case		Inputs				Outputs								
ID	Col	M_e	$Re_{\delta_{in}}$	μ_w/μ_e	T_w/T_{aw}	ρ_w/ρ_e	ρ_{min}/ρ_e	ρ_2/ρ_e	ρ_2/ρ_w	μ_2/μ_e	μ_H/μ_e	Re_2	Pe_H	
A-6		0.6	2800	1.05	1	0.94	0.94	0.98	1.04	1.03	-	294-959	-	
B-2		2	4736	1.49	1	0.58	0.58	0.80	1.38	1.34	-	299-928	-	
C-2		2	2800	1.02	0.6	0.96	0.85	0.90	0.93	1.09	-	244-816	-	
D-5		5	20000	2.27	0.6	0.3	0.28	0.52	1.71	2.07	1.54	446-1238	681-1890	
E-5		5	10000	1.07	0.2	0.89	0.48	0.63	0.70	1.49	1.51	361-1104	388-1222	
F-7		7	20000	2.12	0.3	0.33	0.24	0.44	1.31	2.27	2.16	314-901	363-1079	
G-7		7	10000	1.63	0.2	0.49	0.28	0.47	0.95	2.07	-	182-571	-	

Table 6.1: DNS inputs and some fundamental flow outputs; $Re_{\delta_{in}} = \rho_e U_e \delta_{in} / \mu_e$ is the Reynolds number based on the inflow BL thickness (δ_{in}); Prandtl number $Pr = 0.72$, (non-dimensional) specific heat $c_p = 3.5$, and heat capacity ratio $\gamma = 1.4$ are set as constants and the same for all cases.

(HTR) solver [33].

The compressible fluid for DNS is air assumed as a perfect gas. The DNS data covers a range of edge Mach numbers, $0.6 \leq M_e \leq 7$, with different wall temperature boundary conditions, including both cold walls and adiabatic walls. Table 6.1 lists the dimensionless input parameters in addition to parameters summarizing the variation of mean density and viscosity in the simulation results. The (Favre) average normalized velocity and Reynolds shear stress as a function of the wall-normal direction normalized by the semi-local length scale (y^{sl}), [99], are shown in Figure 6.5(a,b), respectively. The average velocity profiles in Figure 6.5(a) are normalized by U_e , reflecting their contributions to the integrands in the AMI equation. Figure 6.5(b) confirms that Reynolds shear stress profiles are similar near the wall when normalized by τ_w . The peak of Reynolds shear stress does depend on the friction Reynolds number, which is not matched between each of the cases because of practical constraints.

Similar plots for the profiles of the (Favre) average total enthalpy and the total enthalpy and wall-normal velocity covariance are provided in Figure 6.6(a,b). A subset of the simulations listed in Table 6.1 is included here to focus on the higher Mach number cases. Figure 6.6(a) exhibits the significance of Mach number and wall cooling on total enthalpy; stronger wall-cooling generates higher edge-wall total enthalpy difference, which is the primary potential of energy transfer within

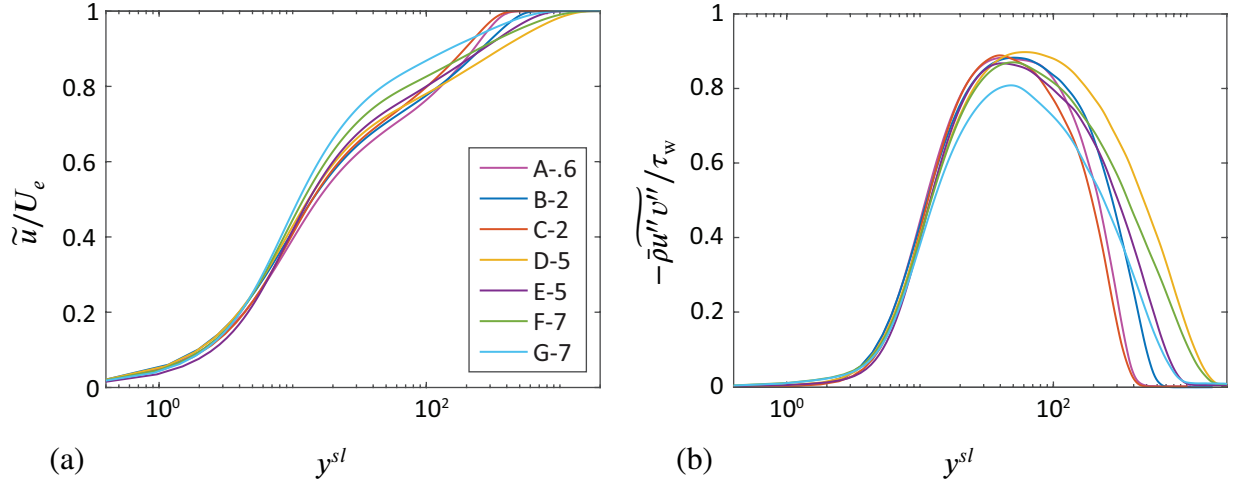


Figure 6.5: Normalized Favre averaged (a) velocity by the edge velocity and (b) Reynolds shear stress by the wall shear stress. The profiles are plotted at Re_2 shown with "*" in Figure 6.9(a)

the BL. Figure 6.6(b) shows the turbulence covariance behaves similar to Reynolds shear stress profiles in Figure 6.5(b), especially close to the wall, when they are normalized by the surface heat flux, q_w . In addition, we decompose $\overline{\tilde{\rho}v''H''}$ to its major contributors according to Eq. (6.33), Figure 6.6(b); the dashed lines represent the wall-normal turbulent flux of enthalpy ($c_p \overline{\tilde{\rho}T''v''}$), with negative impact on the net turbulent flux of total enthalpy, $T_w \geq T_e$, helping wall cooling. The dashed-dotted lines show the wall-normal turbulent transport of the mean kinetic energy, $\overline{\tilde{\rho}uu''v''}$; this transport mechanism enhances the net turbulent flux of total enthalpy by bringing the high energy eddies toward the wall where they stagnate, subsequently generate significant heating at the wall. Finally, the dotted lines represent the turbulent flux of turbulent kinetic energy, $\frac{1}{2}\overline{\tilde{\rho}u''u''v''}$, with relatively negative weak influence.

The effect of compressibility on momentum and energy transport is due to the variation of density and viscosity within the BL. Density and viscosity are explicitly related to temperature; assuming perfect gas, since the pressure variation within the BL is slight, density has a direct inverse relation with temperature. Moreover, viscosity is a function of temperature using Sutherlands' law (with constants $T_0 = 273.15$ K and $S_0 = 110.4$ K) for air. In Figure 6.7(a,b), the profiles of the average density and (Favre) average viscosity, respectively, are presented with respect to y^{sl} . For cold-

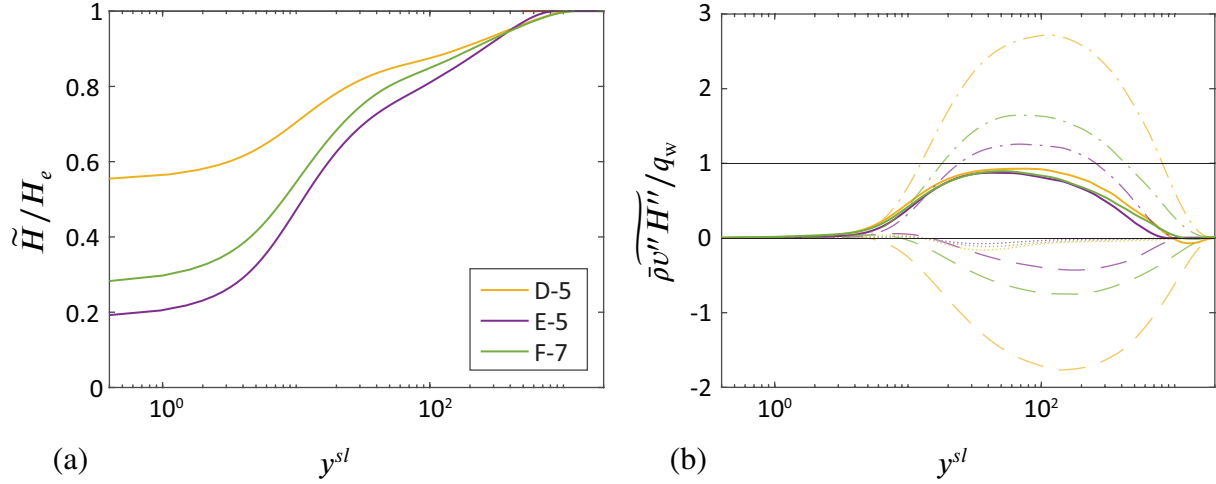


Figure 6.6: Normalized Favre averaged (a) total enthalpy by the edge total enthalpy, and (b) wall-normal velocity and total enthalpy turbulent covariance by the wall heat flux (for study cases of MTEI equation). In (b) the dashed-, dashed-dotted-, and dotted-lines represent $c_p \tilde{\rho T'' v''}$, $\tilde{\rho u'' v''}$, and $\frac{1}{2} \tilde{\rho u'' u'' v''}$, respectively. The profiles are plotted at Pe_H shown with “*” in Figure 6.13(a)

wall boundary conditions, the peak of temperature occurs within the BL, which coincides with minimum density and maximum viscosity. In contrast, for adiabatic wall boundary conditions, the temperature is maximum at the wall. Generally, higher M_e leads to lower density and higher viscosity, but the wall temperature also has a crucial effect on both density and viscosity within the BL. In Figure 6.7(a), the dashed lines present the stress-weighted density expressed in Eq. (6.16). There is an inverse relation between edge Mach number and ρ_2 ; the higher M_e , the lower ρ_2 . In addition to the edge Mach number influence, higher wall temperature also decreases the stress-weighted density. This can be clearly observed by comparing D-5 and E-5, where ρ_2 is smaller for D-5 with higher T_w .

Normalized μ_2 and μ_H —reference viscosities in the AMI and MTEI equations—by the edge viscosity are shown in Figure 6.7(b) with dashed and dashed-dotted lines, respectively. According to the definition of μ_2 , Eq. (6.11), the value of it is not necessarily between μ_e and μ_w , and it depends on the streamwise location. In fact, μ_2 absorbs the effect of wall cooling and the temperature rise within the BL. The deviation between μ_2 and μ_H is smaller when the edge-wall temperature difference is weaker (strong wall-cooling). For example, for E-5, which represents the highest wall-cooling case,

the difference between μ_2 and μ_H is about 1%. Conversely, this deviation becomes more substantial for the cases with higher T_w , like in D-5.

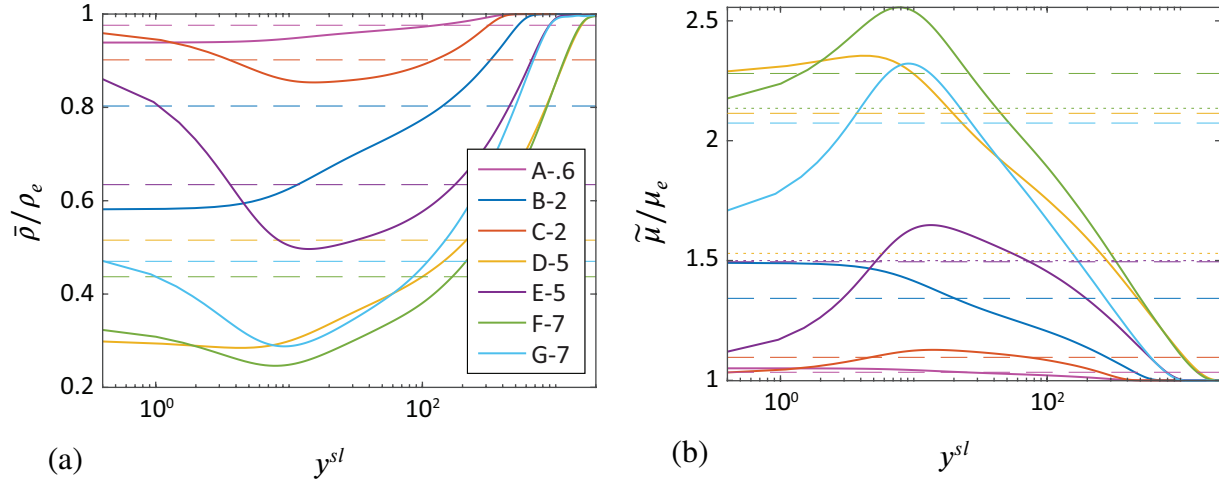


Figure 6.7: Normalized (a) average density by the edge density, and (b) Favre average viscosity by the edge viscosity. The dashed lines in (a) show ρ_2 , Eq. (6.16). Also, the dashed and dotted lines in (b) represent the value of μ_2 , Eq. (6.11), and μ_H , Eq. (6.28), respectively. The profiles are plotted at Re_2 shown with “*” in Figure 6.9(a), except for μ_H that is plotted at Pe_H shown with “*” in Figure 6.13(a)

As discussed in sections 6.1.1 (for AMI equation) and 6.1.2 (for MTEI equation), to isolate the ZPG laminar contribution, it’s necessary to determine the appropriate length scale ℓ . This requires solving the self-similar momentum and energy equations for compressible (or incompressible) BLs. The Blasius solution can simply be used to get ℓ according to an incompressible laminar BL. To obtain ℓ from a compressible laminar BL we use coefficients c_2 and c_H from Eqs. (6.41) and (6.43), respectively, for the AMI and MTEI equations. These coefficients yield the suitable linear relationship between ℓ and δ_2 (and δ_H) concerning the choice of the reference viscosity. The self-similar solver, Section 6.2.1, takes the required edge and wall flow parameters as inputs, provided in Table 6.1, then outputs the self-similar velocity and temperature profiles.

Angular momentum integral equation

This section exhibits the use of the AMI equation, Eq. (6.7), to analyze the DNS datasets summarized in Table 6.1. For demonstration purposes, the stress-weighted viscosity, μ_2 , is chosen as the reference viscosity, and the length scale is chosen proportional to the momentum thickness, $\ell \sim \delta_2$. The coefficient of proportionality is calculated from the ODE solution to the self-similar ZPG laminar BL equations described previously. Recall that the choice of μ_2 is motivated by the AMI equation, while the choice of δ_2 comes from its significance in the momentum integral equation, see Section 6.1.1. Thus, the following analysis interprets turbulent boundary layer physics relative to a baseline laminar boundary layer having the same edge Mach number (M_e), edge temperature (T_e), wall temperature (T_w), and the Reynolds number defined by $Re_2 = \rho_e U_e \delta_2 / \mu_2$.

With this choice, the AMI length scale is based on a compressible laminar solution is $\ell = \ell_{2,C}$, where the subscripts “2” and “C” denote the reference viscosity, μ_2 , and compressible laminar solution, respectively. Another related possibility, which is a useful foil, is to use an incompressible laminar boundary layer, i.e., a solution to the Blasius equation [12], as the baseline for AMI analysis. This laminar boundary layer is still chosen to match the Re_2 of the turbulent boundary layer to be analyzed, but the edge Mach number is zero, and no temperature variation is included, $T_w = T_e$. This choice is denoted $\ell = \ell_{IC}$ where “IC” signifies the option of an incompressible laminar BL.

Figure 6.8 presents each term in the AMI equation using Re_2 and $\ell_{2,C}$. Data from an incompressible (IC) turbulent BL simulation with heat transfer [176, 82] are also included. For the given data, the maximum (streamwise averaged) relative residual error of the AMI equation, Eq. (6.7), is less than or (approximately) equal to 5%. The residual error in closing the AMI equation from DNS data is primarily caused by statistical convergence error, which is amplified by the streamwise derivative needed to compute the term proportional to $d\delta_2^\ell/dx$. Thus, the error depends mainly on the length of time used for averaging each simulation and the error for the cases shown here was deemed sufficiently small for our present purposes.

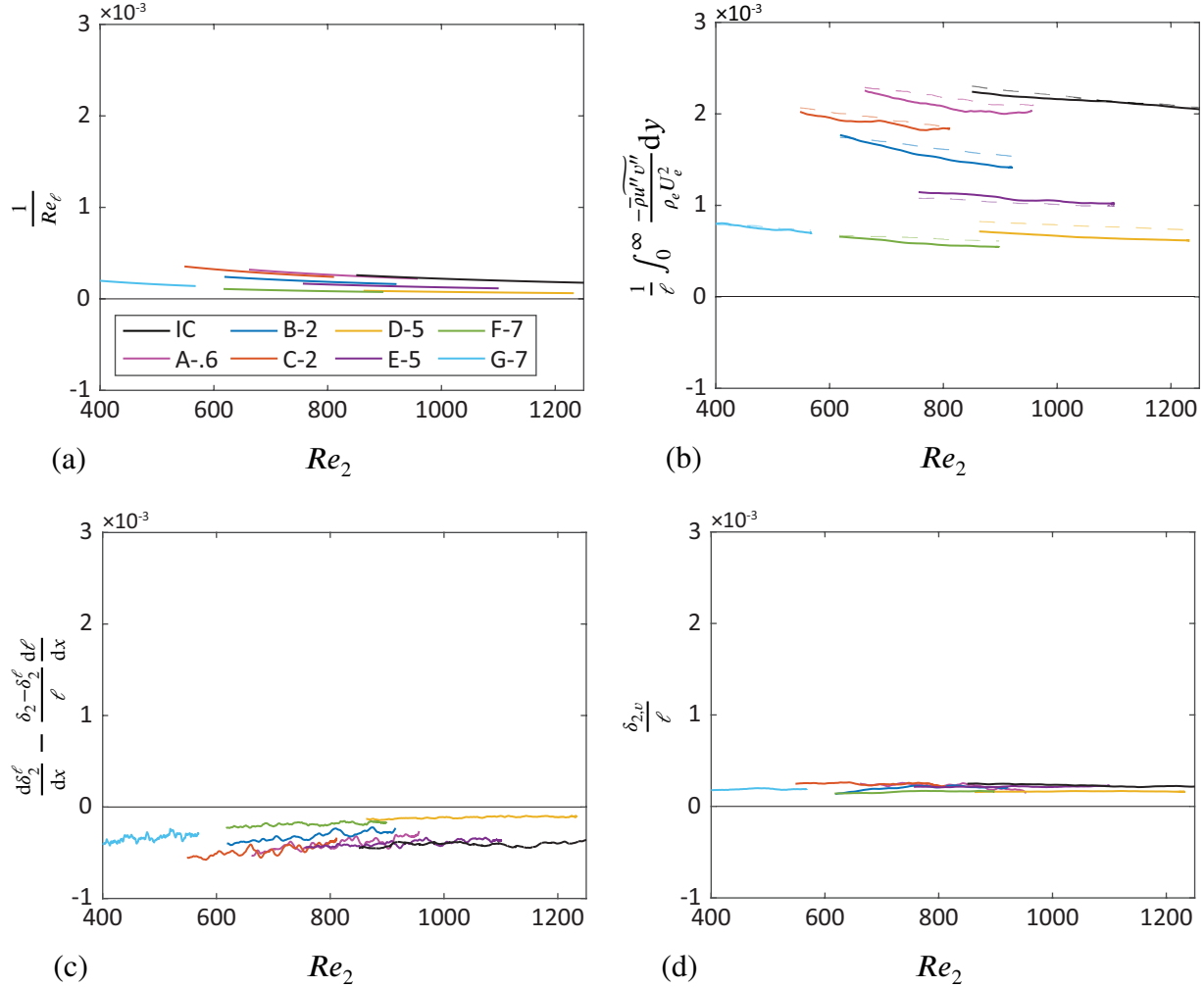


Figure 6.8: Evaluation of non-negligible terms in the AMI equation, Eq. (6.7), based on $\ell = \ell_{2,C}$ and $\mu_{\text{Ref}} = \mu_2$ for the cases in Table 6.1 within the fully turbulent regime: (a) baseline laminar skin friction, (b) the integral torque of the Reynolds shear stress –the dashed lines exhibit $C_f/2$ –, (c) the streamwise growth of the angular momentum thickness, and (d) the torque due to mean wall-normal velocity. Each term is shown as a function of Re_2 , Eq. (6.14). A part of the upstream data is truncated because of the effect of the turbulent recycling.

Figure 6.8(a) presents the $C_f/2$ of the equivalent compressible ZPG laminar BL at the same Reynolds number, Re_2 . The laminar skin friction is relatively small compared to the fully turbulent BL –about 15%– and diminishes slowly with the Reynolds number, $\sim Re_2^{-1}$. The reference laminar BL depends on M_e , T_e , and T_w of the turbulent BL case, so this term shows some variation as expected, though not significant compared with the *turbulent torque*, Fig. 6.8(b). The integral of the Reynolds shear stress is the primary contributor to enhancing $C_f/2$ compared with the other terms. It represents

the total torque due to Reynolds shear stress carrying high-momentum flow toward the wall. This behavior is consistent with the observation in Ref. [179] (for $M_e = 2.5$ and adiabatic wall, using edge viscosity for the reference Reynolds number). The *turbulent torque* gradually diminishes with Re_2 approximately at the same pace as $C_f/2$.

In Figure 6.8(c), the rate of the *streamwise growth* of the angular momentum thickness is shown for each case. This term has a negative contribution to skin friction, as the turbulent BL grows thicker than its laminar counterpart, absorbing a small part of the Reynolds shear stress torque into the growth of the angular momentum. According to Figure 6.8(c), the variation in this term is substantially less than that of the Reynolds shear stress integral in Figure 6.8(b). Nonetheless, a minor opposite trend can be observed.

The contribution of the *mean wall-normal torque* to $C_f/2$ is presented in Figure 6.8(d). For a fully turbulent regime, the *mean wall-normal torque* has a relatively weak influence and does not vary significantly with streamwise direction, consistent with previous observations of incompressible flows [38, 82]. It is worth mentioning the other terms on the right-hand side of the AMI equation, including *edge pressure gradient torque* and *negligible terms*, are at least an order of magnitude smaller than those shown here. Also, the *deviation* term vanishes when $\mu_{\text{Ref}} = \mu_2$ by definition. For completeness, these terms are shown in Appendix C.1.

The impact of the edge Mach number and wall temperature on the terms in the AMI equation is succinctly demonstrated in Fig. 6.8, showing a greater influence by the edge Mach number than the wall temperature. The viscous dissipation roughly scales with M_e^2 and generates high temperatures in the near-wall region. As the pressure remains approximately uniform across the BL, the density in the near-wall region decreases with increasing Mach number. The ability of correlated velocity fluctuations, $\widetilde{u''v''}$, to cause a net momentum flux is proportional to the mean density, $\bar{\rho}$. Therefore, the *turbulent torque* in the AMI equation generally decreases with increasing M_e . The *laminar* and *streamwise growth* terms similarly depend on the mean density and decrease in magnitude with increasing M_e . The variation in *turbulent torque* is clearly the dominant effect in Fig. 6.8

so that the skin friction decreases with increasing M_e . This is consistent with the well-known inverse relationship between the edge Mach number and the skin-friction coefficient for laminar and turbulent BLs [171, 172].

After the effect of the edge Mach number, the AMI equation is also sensitive to the wall temperature. Lower wall temperatures (stronger wall-cooling) are known to increase the laminar and turbulent skin frictions [172, 167]. Higher wall temperature enhances the turbulent wall-normal transport of the Reynolds shear stress away from the wall [3]. Thus, when the surface temperature is higher, lower skin friction drag is expected. Figure 6.8 shows that the enhancement of *turbulent torque* by lower T_w is significant. For example, comparing D-5 and E-5 with the same $M_e = 5$ but one with strong wall cooling (E-5) shows roughly 20% higher *turbulent torque* for E-5. A similar trend can also be seen for $M_e = 2$ by comparing B-2 and C-2. The difference in wall temperature for F-7 and G-7 ($T_w/T_{aw} = 0.3$ and 0.2 , respectively) is apparently not significant enough to cause a noticeable difference in the AMI terms. As with the Mach number, the increase of Reynold shear stress with decreasing wall temperature can be linked to an associated increase in the near-wall mean density. Generally, an increase in *turbulent torque* due to lower wall temperatures is slightly offset by a much weaker opposing trend in the *streamwise growth* of angular momentum.

Figure 6.9 directly considers the skin friction coefficient (the sum of terms shown in Fig. 6.8) and further investigates the impact of the edge Mach number and wall temperature on the *turbulent torque*. Figure 6.9(a) compares the skin friction with the sum of RHS terms in the AMI equation, verifying the calculations. Also shown is the *turbulent torque*, which is just one of the terms in the AMI equation. Evidently, the trend in turbulent torque closely matches the skin friction coefficient trend with M_e and T_w . To examine this in more detail, Fig. 6.9(b) compares the integrand of the *turbulent torque* term. Interestingly, the length scale $\ell_{2,C}$ is fairly effective in collapsing the wall-normal extent of the turbulent boundary layers across different Mach numbers and wall temperatures. The trend in skin friction coefficient, then, can be traced to the variation in the magnitude of the Reynolds shear stress, $-\overline{\rho u'v'}$. To quantify the extent to which the trends in Reynolds

shear stress magnitude may be explained by the trends in near-wall mean density discussed in the previous two paragraphs, the inset of Fig. 6.9(b) shows the Reynolds shear stress profiles divided by the mean density. The result is a significant increase in similarity amongst the cases, even if there is no complete collapse. Therefore, the effect of M_e and T_w on skin friction coefficient may be explained mainly by the influence of mean density, $\bar{\rho}$, in determining the efficiency with which correlated velocity fluctuations, $\widetilde{u''v''}$, transport momentum across the boundary layer. More specifically, at higher edge Mach number (and higher wall temperature), lower near-wall density reduces the momentum transport and, subsequently, skin friction.

Alternatively, the variation of the skin-friction coefficient with M_e and T_w may be tied to trends in the laminar compressible BL. Figure 6.9(c) shows the *turbulent torque* from the AMI equation when the baseline laminar BL is chosen at $M_e = 0$ rather than at the matching M_e of the turbulent case. In other words, $\ell = \ell_{IC}$ is the same for all cases, calculated using the solution to the Blasius equation. Interestingly, ℓ_{IC} leads to much closer collapse for the *turbulent torque* compared with the compressible length scale $\ell_{2,C}$ (matched M_e) in Figure 6.9(a). However, there is still some variation in Fig. 6.9(c) and the Reynolds shear stress profiles, i.e., the integrands of the *turbulent torque*, show substantial differences in Fig. 6.9(d). Both the width (y/ℓ axis) and peak are different for each case, showing a strong dependence on M_e and T_w , though the integrals of each curve are quite similar. According to Figure 6.9(b), as already seen for higher M_e , the peak of the profile of the normalized Reynolds shear stress is lower, yet the width related to ℓ_{IC} is larger. For example, the width of integrands for F-7 and G-7 extend beyond $y/\ell_{IC} = 6$. Also, colder wall temperature causes stronger maximum normalized Reynolds shear stress but over a smaller relative width. This can be seen by comparing the profiles of D-5 with E-5 or B-2 with C-2. Inset of Figure 6.9(d) shows the normalized Reynolds shear stress by the edge conditions multiplied by the ratio between the compressible and incompressible length scales, $\ell_{2,C}/\ell_{IC}$, plotted with respect to $y/\ell_{2,C}$ (consistent with Figure 6.9(b)). Although there is still a subtle edge Mach number influence, in the inset of Figure 6.9(d), there is a better collapse between the cases with the same T_w/T_{aw} ratio –representation of wall-cooling strength. For instance, comparing C-2 and D-5, $T_w/T_{aw} = 0.6$, we observe the peak values

are roughly the same (but slightly shifted). Therefore, the skin friction of a high-speed turbulent BL relative to a $M_e = 0$ turbulent BL may be quantitatively (but not perfectly) tied to the same relative comparison for laminar boundary layers, provided the comparisons are done at matched Re_2 as defined in Eq. (6.14).

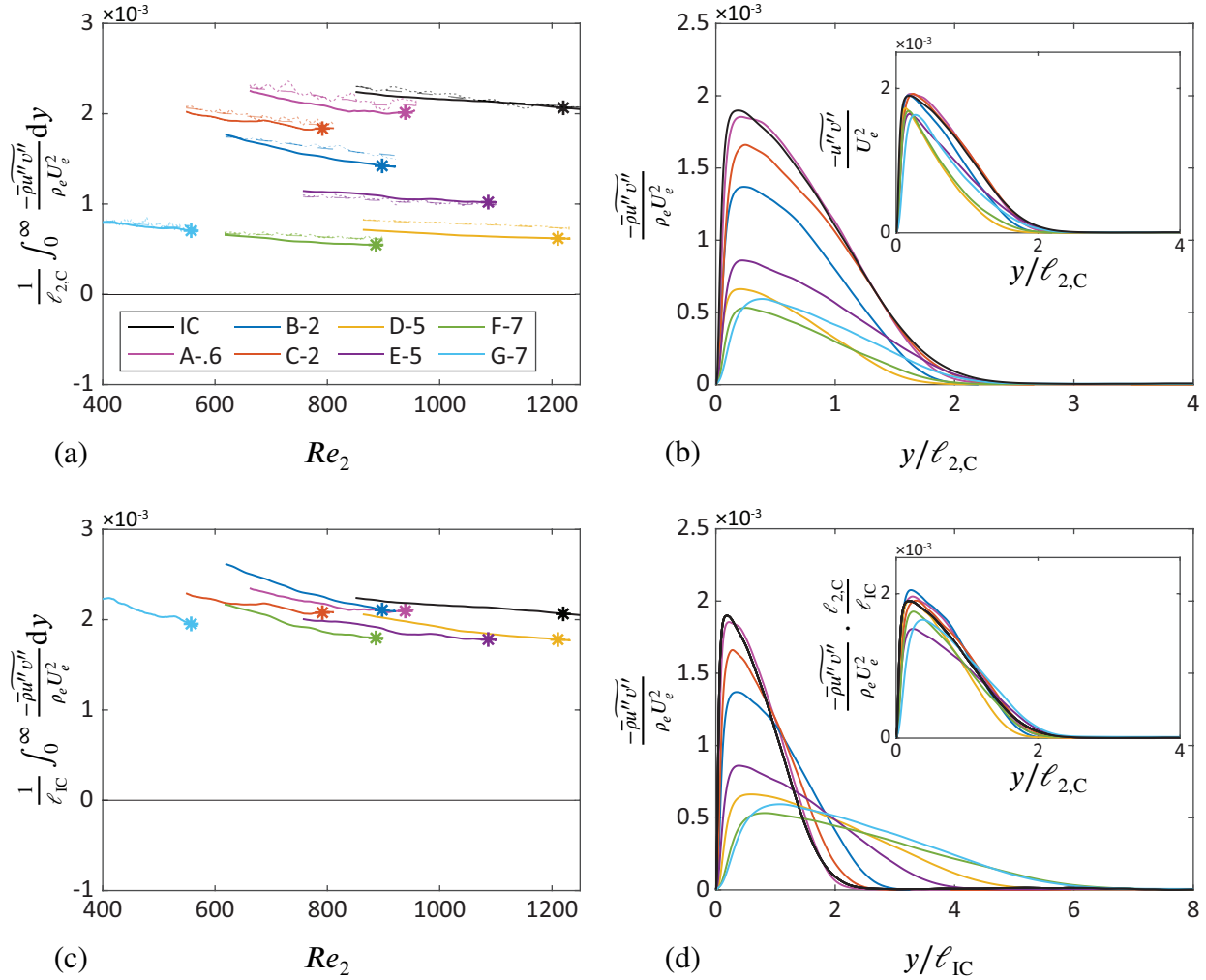


Figure 6.9: Contribution of the *turbulent torque* to $C_f/2$ and the profile of its integrand at “*”: (a) turbulent torque by choosing ℓ based on self-similar laminar compressible BLs, $\ell = \ell_{2,C}$, and (b) profile of the integrand of turbulent torque with respect to wall-normal distance normalized by $\ell_{2,C}$. In (a), the thinner dashed- and dotted lines show the $C_f/2$ and the right-hand side of the AMI equation. The Inset of (b) exhibits the integrand of turbulent torque by removing the effect of density variation within the BL. (c) The *turbulent torque* by choosing ℓ based on Blasius solution for IC BLs, $\ell = \ell_{IC}$, and (d) profile of the integrand of the *turbulent torque* with respect to the wall-normal distance normalized by ℓ_{IC} . Inset of (d) presents the integrand of the *turbulent torque* multiplied by the ratio of compressible and incompressible length scales, $\ell_{2,C} = \ell_{IC}$, with respect to $y/\ell_{2,C}$.

In the analysis of turbulent BLs, it is common to use the viscosity at the wall, μ_w , as the reference viscosity. This has proven particularly effective when the wall temperature is near the adiabatic wall temperature [131]. Figure 6.10 examines the comparison between choosing $\mu_{\text{Ref}} = \mu_2$ and $\mu_{\text{Ref}} = \mu_w$ on *turbulent torque* (white background), *laminar friction* (light gray background), and *streamwise growth* (dark gray background). In this figure, each term from the RHS of the AMI equation, Eq. (6.7), is normalized by $C_f/2$. Thus, this figure can be interpreted as showing the percent contribution of each term to the skin friction coefficient.

For $\mu_{\text{Ref}} = \mu_2$ in Figure 6.10(a), the normalized *turbulent torque* is almost equal to one for both cases, which is consistent with the dominant effect of turbulence on momentum transport and skin friction enhancement. This is simply another way to visualize the data from Fig. 6.9(a), where it was already shown that the *turbulent torque* term closely followed the skin friction coefficient for $\ell = \ell_{2,C}$. Choosing μ_2 as the reference viscosity leads to a closer collapse of the *turbulent torque* around one (1.0) for the given data compared with the result of choosing the wall viscosity as the reference, Figure 6.10(b). This can be clearly seen for E-5 (purple), which has the strongest wall cooling, and the normalized *turbulent torque* is roughly 50% larger. A similar effect is observed for the *laminar friction* and *streamwise growth* when $\mu_{\text{Ref}} = \mu_w$. In fact, taking E-5 as an example again, we observe almost 300% higher negative contribution by normalized *streamwise growth* if we pick μ_w as the reference viscosity. The effect of wall temperature is much weaker when choosing $\mu_{\text{Ref}} = \mu_2$. This comparison provides a further justification for the use of μ_2 –as the reference viscosity– in the above analysis, in addition to its physical interpretability as the stress-weighted average viscosity. This choice enables the identification of some of the above trends with mean density and laminar BL length scale.

The overall impact of the trends observed in Figs. 6.9 and 6.10 can be concisely summarized in terms of the overall impact on skin friction by using the trends to construct transformations between compressible and incompressible skin friction coefficient. Figure 6.11 shows the results of two such transformations, (i) based on stress-weighted density, ρ_2 , and (ii) laminar BL length scale, ℓ .

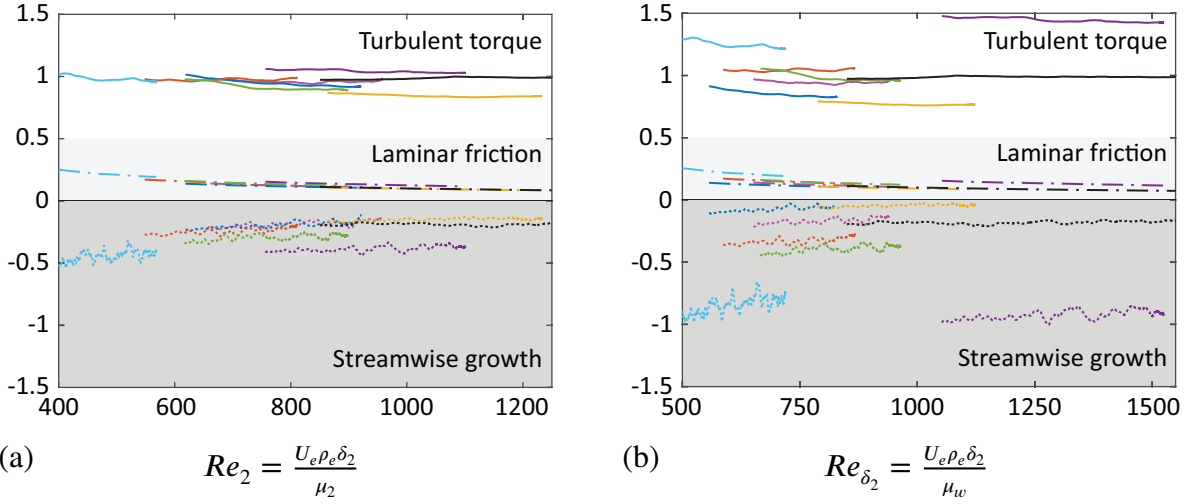


Figure 6.10: Normalized contribution of *turbulent torque* (white background), *laminar friction* (light gray background), and *streamwise growth* (dark gray background) by $C_f/2$: when the reference viscosity (a) $\mu_{\text{Ref}} = \mu_2$, and (b) $\mu_{\text{Ref}} = \mu_w$.

Figure 6.11(a) shows $C_f/2$ for the compressible and incompressible data without transformation. Assuming $C_f/2$ is roughly equal to the *turbulent torque*, combined with the role of mean density observed in Fig. 6.9(b), suggests multiplying $C_f/2$ with the ratio of ρ_e/ρ_2 . According to Figure 6.11(b), this transformation only partially compensates for different edge Mach numbers and wall temperature; it is not a strong enough correction to compensate for the entirety of the compressibility effect. Indeed, a closer inspection of Fig. 6.9(b) indicates that the peak of $\widetilde{u''v''}/U_e^2$ still varies noticeably for $M_e = 5$ and 7. Thus, the AMI equation provides a way to quantify the impact of lower mean density on the skin friction coefficient. The density ratio correction ρ_e/ρ_2 is too simple to explain the entire effect of compressibility but still explains a significant part of it. There are several explanations for this, including the effect of the imposed boundary conditions, e.g., viscosity variation, and internal regulation that becomes considerable for relatively high M_e [123, 107].

Another transformation approach is inspired by Figure 6.9(c) where Blasius solution was used to obtain the AMI length scale, $\ell = \ell_{\text{IC}}$, and a relatively suggestive collapse of *turbulent torques* was observed. Figure 6.9(d) further shows the ability of the length scale ratio between compressible and incompressible laminar flows, $\ell_{2,C}/\ell_{\text{IC}}$, in obtaining better similarity in the Reynolds shear

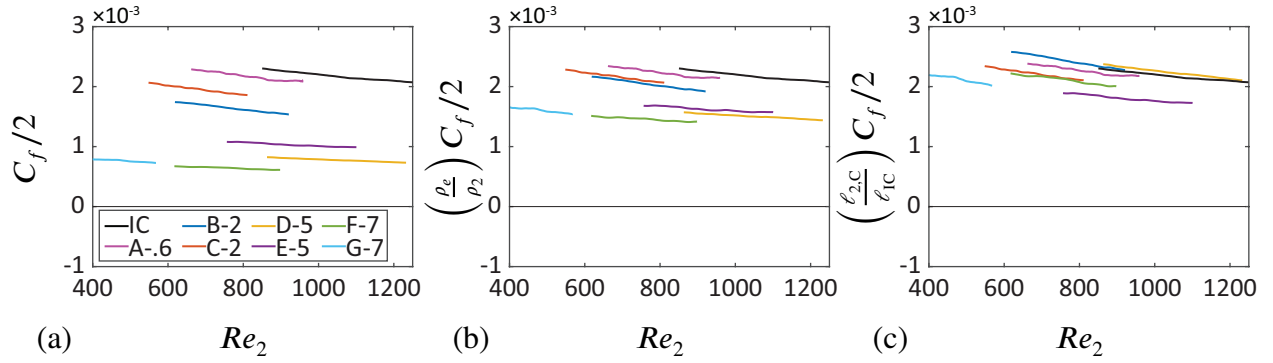


Figure 6.11: (a) Skin friction coefficients without transformation, (b) integral transformation based on stress-weighted density, and (c) integral transformation based on the ratio of the compressible and incompressible AMI length scales.

stress profiles. Because for a fully turbulent regime, the dominant source of skin friction is due to Reynolds shear stress, we apply this ratio directly to the skin friction in Figure 6.11(c). This transformation performs well for the adiabatic wall cases with about a maximum deviation of 4% from the incompressible $C_f/2$. However, strong wall cooling still creates noticeable deviation for $\left(\ell_{2,C}/\ell_{1C}\right) C_f/2$ from the incompressible $C_f/2$, up to roughly 20% for E-5. Thus, the self-similar laminar BL solutions appear useful in providing information about turbulent BL skin friction, at least when the stress-weighted average viscosity is used to define the Reynolds number, Re_2 , at which the relevant ratios are computed.

Moment of total enthalpy integral equation

At high Mach numbers, the surface heat transfer is often of more significant concern than the skin friction drag. Therefore, quantitative mapping of flow phenomena throughout the BL and how they alter the Stanton number is crucial. This section applies the MTEI analysis, discussed in section 6.1.2, to the DNS data with relatively high edge Mach numbers and non-zero surface heat flux. We limit our focus to the higher Mach number cases D-5, E-5, and F-7, for which the wall temperature is lower than the adiabatic wall temperature but higher than the edge wall temperature. G-7 is not included in the MTEI analysis as it is quite similar to F-7 –the same edge Mach number and

very close wall cooling effect— but with a lower Reynolds number range. This similar behavior was already observed in the AMI analysis, Section 6.2.2, especially in Figure 6.8(b) in which the turbulence skin friction enhancement of F-7 is approximately the continuation of G-7 at higher Reynolds number. The compressible data is compared with the incompressible, constant property turbulent BL with heat transfer [176]. For the incompressible BL data, the non-dimensional wall-edge temperature difference and Prandtl number are unity. Most of the discussion provided in section 6.2.2 for the AMI equation and momentum transport is analogous to the MTEI equation and energy transport but a bit more complex. The total enthalpy conservation is the basis of the MTEI equation, which consists of two energy transport mechanisms: kinetic energy and internal energy. Considering the Mach number as a dimensionless ratio of kinetic energy and internal energy, for incompressible flows, the kinetic is neglected, $M_e = 0$. Conversely, for high-speed flows, the kinetic energy is significant and even dominant.

Figure 6.12 shows the breakdown of the Stanton number using the MTEI equation for the four major flow phenomena with respect to the Peclet number $Pe_H = Re_H Pr_{Ref}$, where $Re_H = \rho_e \delta_H U_e / \mu_H$ is the Reynolds number based on the given reference viscosity; the full budget is provided in Appendix C.2. Recall that $Pr_{Ref} = 1$ is chosen here to make the St number based on the edge stagnation temperature rather than the adiabatic wall temperature. Here, the length scale $\ell = \ell_{H,C}$ is determined based on the reference viscosity $\mu_{Ref} = \mu_H$ and self-similar ZPG compressible laminar BL solution. Figure 6.12(a) shows the *laminar* Stanton number that gradually diminishes with the Peclet number, Pe_H , as we go further downstream. According to Figures 6.12(a,d), the *mean wall-normal* transport also weakly contributes to the surface heat flux and does not show a significant variation between the cases. Moreover, similar to its AMI counterpart, the *mean wall-normal* change with respect to Pe_H is negligible.

Figure 6.12(b) exhibits the direct contribution of turbulence on surface heat flux through wall-normal turbulent flux of total enthalpy, $-\overline{\rho H'' v''}$. The *turbulent flux* is larger in magnitude and shows more significant variation than the other three terms displayed in Fig. 6.12. Since both kinetic

and internal energies are embedded within the definition of total enthalpy, the contribution of the *turbulent flux* of total enthalpy to the Stanton number in the MTEI equation can be split; according to Figure 4.1(b), the turbulent transport of the mean kinetic energy, $\overline{\rho u u'' v''}$, is the primary contributor due to relatively high M_e (high edge kinetic energy). Turbulence via Reynolds shear stress carries this kinetic energy flow toward the wall, where it stagnates and generates a tremendous amount of heat flux toward the wall. Conversely, the turbulent flux of enthalpy, $c_p \overline{\rho T'' v''}$, partially removes high internal energy flows from the wall toward the edge ($T_w \geq T_e$). In other words, the balance of these two mechanisms is essentially the net contribution of *turbulent flux* to the Stanton number.

The *streamwise growth* of the first moment of total enthalpy thickness is the only negative term. In fact, *streamwise growth* helps cool the wall by absorbing some of the turbulent flux into downstream growth rather than wall heat flux. For instance, comparing D-5 and E-5, it is evident the flux by *streamwise growth* is more substantial for E-5 with more intense wall-cooling.

In Figure 4.2(a), the significant reduction of the near-wall mean density due to the rise of temperature within the BL was shown. This reduction, subsequently, decreases the turbulent momentum and total enthalpy flux. According to Figure 6.13(a), the ratio of *turbulent flux* and the Stanton number is roughly between 90% to over 130%. This number is closer to $\approx 90\%$ for D-5 (weakest wall-cooling). However, the *turbulent flux* becomes greater than the Stanton number for the cases with stronger wall-cooling, such as E-5. The enhancement of *turbulent flux* for the cases with strong wall-cooling is examined in Figure 6.13(b); here, we plot the profile of its integrand with respect to the wall-normal direction within the fully turbulent regime, at “*”. Evidently, there is no meaningful similarity in the profiles of the integrands. However, by removing the mean density variation across the BL, inset of Figure 6.13(b), the profiles become significantly more similar, even if they do not truly collapse. In other words, much of the variation in *turbulent flux* contributions to the enhanced surface heat flux can be attributed simply to the lower mean density in the near-wall region diminishing the effectiveness of turbulent fluctuations in transporting energy toward the wall. In fact, by removing the effect of density variation across the BL, the contribution of *turbulent flux* to

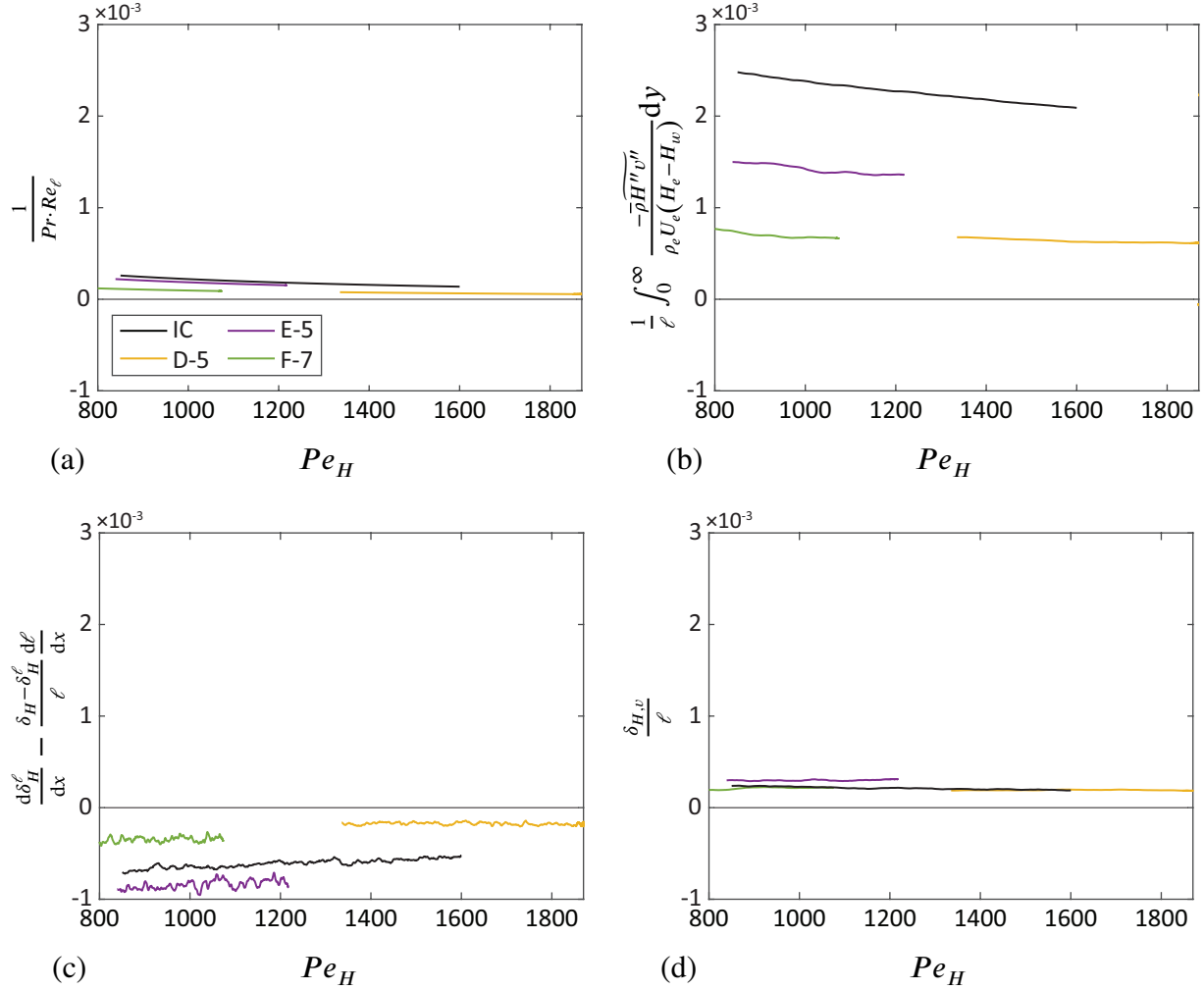


Figure 6.12: Budget of MTEI based on $\ell = \ell_{H,C}$ and $\mu_{\text{Ref}} = \mu_H$ within the fully turbulent regime: (a) laminar Stanton number, (b) contribution of turbulent flux to Stanton number, (c) streamwise growth of the first moment of total enthalpy thickness, and (d) contribution of mean wall-normal flux. The incompressible (IC) data is shown in black. A part of the upstream data is truncated because of the effect of the turbulent recycling.

St , for all cases, is significantly more similar to the incompressible case. This observation matches the results observed earlier in the inset of Figure 4.4(b) for the *turbulent torque* by the Reynolds shear stress.

In Figure 6.13, the turbulent flux of total enthalpy is consistently higher for the strongly cooled case E-5. To shed more light on this, Fig. 6.14 explores the decomposition of the total enthalpy flux, $\overline{\rho v'' H''}$, into two components: (i) the turbulent transport of mean kinetic energy, $\overline{\rho \tilde{u}'' v''}$, and (ii)

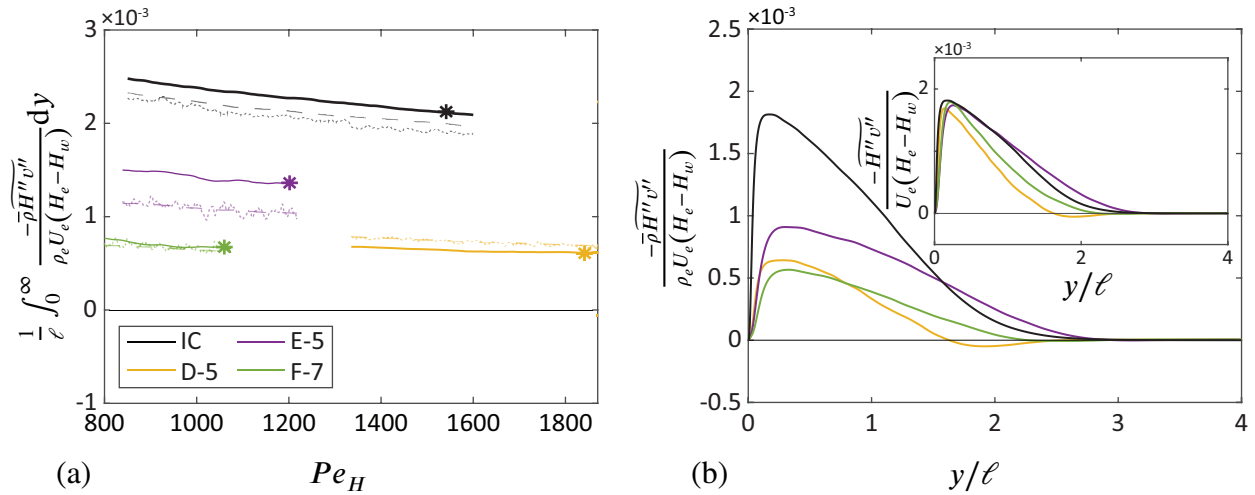


Figure 6.13: Contribution of *turbulent flux* to St and the profile of its integrand at “*”: (a) turbulent flux of total enthalpy based on $\ell = \ell_{H,C}$, and (b) profile of its integrand with respect to the wall-normal distance normalized by $\ell_{H,C}$. In (a), the dim, thin dashed- and dotted lines show the St and the right-hand side of the MTEI equation. The inset of (b) shows the integrand of *turbulent flux* by pulling out the influence of density variation within the BL.

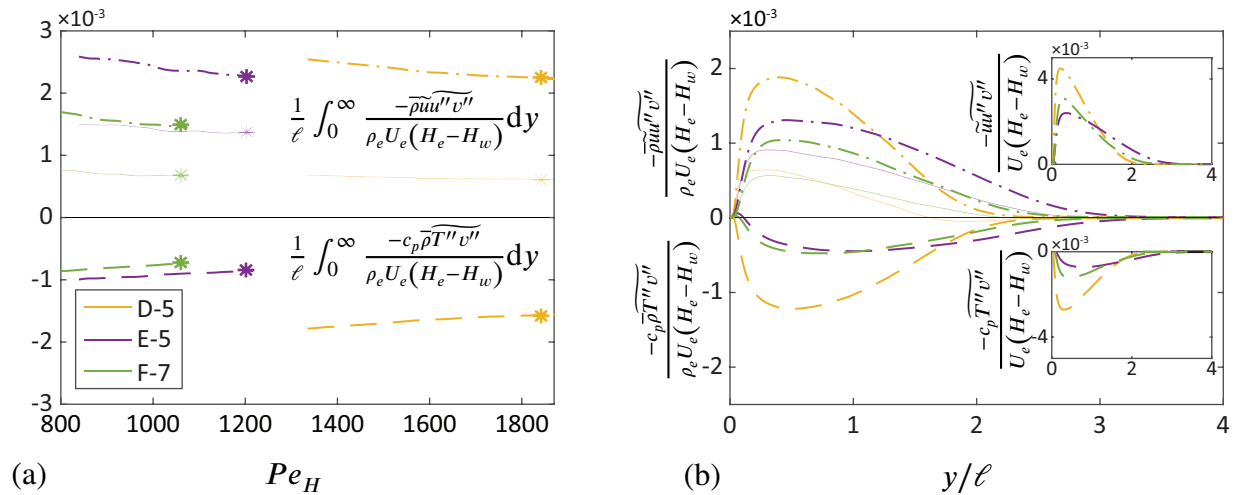


Figure 6.14: Decomposition of the *turbulent flux* of total enthalpy and the profile of its integrand at “*”: (a) direct contribution of turbulent transport of mean kinetic energy (dashed-dotted line) and turbulent enthalpy (heat) flux (dashed lines) to St with respect to the streamwise location, Pe_H , and (b) profile of their integrands with respect to wall-normal distance normalized by $\ell_{H,C}$. In (a,b), the dim, thin solid lines represent the net contribution of the turbulent flux of total enthalpy. Insets of (b) show the integrands by pulling out the effect of density variation within the BL.

the turbulent enthalpy flux, $c_p \bar{\rho} \widetilde{T'' v''}$. Figure 6.14(a) represents their direct contribution to St . The Reynolds shear stress increases St by bringing the mean kinetic energy toward the wall. On the

other hand, the turbulent enthalpy flux advects enthalpy away from the wall for most of the boundary layer (except below the temperature peak). The profiles of the integrands of turbulent transport of mean kinetic energy and turbulent enthalpy flux in Figure 6.14(b) confirms the aforementioned effect; the profile of turbulent enthalpy flux for F-7 is just slightly lower than E-5, yet there is a clear drop in the turbulent transport of mean kinetic energy for F-7 with a higher edge Mach number. In contrast to the influence of M_e , which was more effective on turbulent flux of mean kinetic energy, the impact of T_w is more substantial on turbulent enthalpy flux rather than turbulent transport of mean kinetic energy. According to Figure 6.14(a), a comparison between D-5 and E-5 reveals stronger wall-cooling in E-5 slightly (about 10%) reduces the turbulent transport of mean kinetic energy flux. On the other hand, the (absolute) effect of turbulent flux of enthalpy drops substantially for roughly 80%. The weaker effect of turbulent enthalpy flux in case E-5 may be conceptually associated with a smaller temperature difference, $T_w - T_e$, due to stronger wall-cooling.

Despite the relative similarity observed for the total enthalpy flux in the inset of 6.13(b) after removing the density effect, the two contributing fluxes (turbulent enthalpy flux and turbulent flux of the mean kinetic energy) individually do not show the same degree of similarity in Figure 6.14(b). Here, by removing the explicit influence of density variation on turbulent fluxes, the effect of edge Mach number is significantly reduced, so the profiles are then sorted primarily based on the imposed wall temperature from the highest, D-5, to the lowest, E-5; higher T_w leads to larger integrand magnitudes.

Taking D-5 as an example with the hottest wall in the given DNS data justifies the concept of heat conduction due to the edge-wall temperature difference and how turbulent enthalpy flux toward the edge resists the generated heat at the wall by stagnating edge kinetic energy. In fact, this mechanism explains the net negative $\overline{\rho v'' H''}$ values close to the edge of BL from $y/\ell \approx 1.7$ to $y/\ell \approx 2.3$, where turbulent enthalpy flux (negative contribution to net St) becomes greater than the turbulent transport of the mean kinetic energy (positive contribution to net St). In conclusion, the turbulent

transport of the total enthalpy via mean kinetic energy is slightly more localized near the wall. It attenuates lightly quicker away from the wall rather than the turbulent enthalpy flux.

In summary, this section shows the capability of the MTEI equation as a quantitative mapping between the flow phenomena above the wall and how they impact the net surface heat flux. The MTEI equation distinguishes the contribution of kinetic energy and internal energy on heat flux, and one can understand how and when they resist each other depending on the given edge and wall flow conditions.

6.3 Conclusion

In this chapter, an angular momentum integral (AMI) equation was introduced for compressible flow boundary layers (BL) with variable density and viscosity. The AMI equation provides a simple way to quantify how turbulence and other flow phenomena such as compressibility impact the BL skin friction coefficient relative to an equivalent zero pressure gradient (ZPG) laminar BL. Moreover, a moment of total enthalpy integral (MTEI) equation is developed for high-speed BLs with surface heat flux. Analogous to the AMI equation, the MTEI equation quantifies the enhancement of a BL's Stanton number by turbulent fluxes and other flow phenomena relative to the laminar BL case. The resulting AMI and MTEI equations are given in Eq. (6.7) and Eq. (6.23), respectively. A calorically perfect gas assumption is maintained in this work but can be relaxed to include high-enthalpy effects in future works.

The AMI equation is an integral conservation law for the first moment about $y = \ell(x)$ of velocity defect, normalized to be written in terms of the skin-friction coefficient. The length scale, ℓ , about which the moment is taken to be the center of action of the viscous force for a laminar BL sharing the same Reynolds number, such that the skin friction of an equivalent ZPG laminar BL is isolated into a single term as a function of the Reynolds number only. This choice allows the other terms in

the AMI equation to be straightforwardly interpreted as an enhancement (or attenuation) of the skin friction coefficient relative to the laminar baseline case. The length scale for the Reynolds number similarity can be tailored to suit the desired interpretation of the analysis.

Similarly, the MTEI equation is an integral conservation law for the first moment of total enthalpy defect, written in the dimensionless form in terms of the Stanton number. For the MTEI equation, the moment is centered about the center of action of the combined conductive heat flux and viscous kinetic energy flux for an equivalent ZPG laminar BL. This results in an equation that contains the laminar BL Stanton number in a single term as a function of the Reynolds (or Peclet) number, allowing a specific interpretation of the other terms in the MTEI equation as enhancements or attenuations of surface heat flux relative to the baseline laminar case.

For compressible BLs with variable viscosity, a reference viscosity must also be chosen. The form of the AMI equation itself suggests the choice of the shear stress weighted viscosity, μ_2 , as the representative viscosity of the BL. Moreover, a reference viscosity and conductivity, μ_H and k_H , respectively, emerge from the MTEI equation as natural choices for representative transport coefficients in high-speed BLs.

The compressible AMI equation was applied to the DNS data from turbulent BLs having a range of edge Mach numbers, M_e , and wall temperature boundary conditions, T_w . Relative to laminar BLs with the same M_e , T_w , and momentum thickness Reynolds number based on μ_2 (Re_2), the trend in skin friction for turbulent BLs closely followed the behavior in the Reynolds shear stress integral. It is demonstrated that choosing μ_2 shows a better collapse for compressible BLs compared with the choice of μ_w .

A closer inspection of the Reynolds shear stress integrand revealed that the lower skin friction for higher M_e , higher T_w cases is associated primarily with lower near-wall mean densities. The effect of compressibility on the skin friction coefficient may be summarized as follows. Fluid entrained into the BL from the edge is decelerated with tiny pressure variation across the BL, leading to

higher temperatures and lower densities in the near-wall region. Turbulent enhancement of wall shear stress relies primarily on the transport of momentum across the BL by the Reynolds shear stress, $-\overline{\rho u'' v''}$. Normalized by the edge velocity, U_e^2 , the covariance of streamwise and wall-normal velocities does not vary as strongly with M_e and T_w . However, the mean density drops significantly in the near-wall region for high M_e and T_w , considerably decreasing the turbulent momentum flux, leading to lower skin-friction coefficients.

An alternative description of skin friction coefficient trends in compressible BLs can be made using the incompressible laminar solution (i.e., Blasius). The ratio of length scales based on the incompressible and compressible laminar solutions is also shown to capture much of the variation in skin friction coefficient with M_e and T_w . This suggests that when BLs are compared with similarity based on $Re_2 = \rho_e U_e \delta_2 / \mu_2$, the effect of compressibility on laminar BLs somewhat closely matches its impacts on turbulent BLs, especially for adiabatic or weakly cooled walls.

Applying the MTEI equation to the DNS dataset with non-zero heat flux, an analogous compressibility effect was observed for the total enthalpy transport. Reduction in the Stanton number observed at higher edge Mach numbers and wall temperatures could be most explained by simply considering the impact of mean density on turbulent fluxes. However, another physical effect relating to wall-cooling, $T_w - T_e$ (edge-wall temperature difference), was observed. The lower the edge-wall temperature difference in the case of strongly cooled walls suppresses the turbulent enthalpy flux ($c_p \overline{\rho v'' T''}$) much more than the turbulent transport of the mean kinetic energy ($\overline{\rho u'' v''}$). In fact, this further explores how intense wall cooling breaks the analogy between the skin friction coefficient and the Stanton number.

In conclusion, the AMI and MTEI equations are shown to be a practical tool for using DNS (or experimental) data to elucidate essential physics in high-speed turbulent BLs. The present work demonstrates their use for fully turbulent BLs with a calorically perfect gas. One possible future approach is to further quantify the contribution of different turbulent length scales (turbulent structures) using the AMI and MTEI equations. This will be fruitful in comprehending the effect of

turbulent structures in compressible BLs on surface drag and heat transfer in comparison with incompressible BLs. It would also facilitate the exploration of how the integral approach pursued here may complement existing velocity profile transformations to elucidate high-speed effects on turbulent BL physics. Crucial applications to hypersonic aerothermodynamics can be addressed with extensions of AMI and MTEI to include high-enthalpy effects such as variable specific heats because of the vibrational excitation and changing chemical composition. The peak surface heat flux during transition to turbulence is often crucial, so the application of the MTEI equation to transitional BLs with various instability modes may prove quite fruitful, given the exceptional trends that have been observed using moment-integral equations for transitional incompressible BLs [38, 82]. Ultimately, this line of research can provide a robust, more quantitative understanding of the relationship between transitional and turbulent flow physics and the dangerously high surface heat fluxes on hypersonic vehicles.

Chapter 7

Application of the First-moment Integral Equations

Previous chapters focused on utilizing the first-moment integral equations, such as AMI and MTEI, as analysis tools for studying transitional and turbulent boundary layers. This chapter explores additional applications of the first-moment integral equations for boundary layers. Firstly, we introduce the application of the AMI equation to boundary layers with flow control. This involves extending the analysis to incorporate the effects of various flow control mechanisms, e.g., surface suction or blowing, on wall-bounded flows. Furthermore, we explore a turbulent modeling platform based on solving the integral form of the Navier-Stokes equations. This approach holds promise for developing computationally efficient models.

7.1 Flow Control in Wall-bounded Flows

Flow control is a central topic in fluid dynamics that is concerned with devising passive or active means of intervention with the flow structure and its underlying mechanisms in a manner that

causes desirable changes in the overall flow behavior. Through flow control, it is possible, in principle, to enable favorable outcomes such as, for example, delay of laminar-to-turbulent transition and reduction of skin-friction drag in wall-bounded flows [47]. These scenarios allow for substantial savings in fuel expenditure for air, sea, land vehicles, wind, and water turbines, long-range gas and liquid pipelines, and other similar applications. A flow control scheme can be either active or passive. The active methods require providing power to the control system, which might be time-dependent. Flow control by active means has been extensively investigated over the past few decades [169, 98, 74, 55, 2, 68]. Active control schemes require a source of power. For example, for the flight of X-21, there was a constant suction porous surface at the leading edge on a swept wing that caused a transition delay up to a chord Reynolds number 4.7×10^7 [47]. This achievement, however, came with a substantial power cost to run the control scheme, and sometimes, this power is higher than the power saved due to drag reduction. Moreover, other environmental obstructions could impact the efficiency of the control scheme, e.g., insects clogging the porous suction. Passive techniques, on the other hand, are desirable because of their simplicity and low cost, i.e., no active control devices, wires, ducts, slots, etc., are needed, and no electric power is required to drive the control process. Passive techniques widely explored in the literature include the use of riblets [166, 49], roughness [26, 44], or porous features [1] on the surface exposed to the flow, or coating the surface with a compliant material [92, 11, 16, 48, 18, 101, 27, 102, 39]. These passive techniques were shown to be practical for some cases. Yet, their robustness for engineering applications is challenging. For instance, using compliant coating was observed to be successful for (turbulent) drag reduction [91]; however, consistent and definitive proof is absent regarding the efficacy of compliant coatings in the stabilization of TS waves. Moreover, the utilization of such compliant surfaces was initially deemed suitable primarily for marine settings, mainly because the panels needed to be excessively flexible for aerospace applications [19]. This determination notably curtails the potential use of compliant surfaces for flow control within aeronautical contexts. The next section presents a modified form of the AMI equation that includes the explicit role of non-zero wall-normal velocity on the skin friction coefficient. Subsequently, a set of turbulent BL

over an airfoil with suction and blowing is examined by this form of AMI analysis.

7.1.1 Surface suction and blowing

The AMI equation, defined in 5.7, can be revised for BLs with a non-zero wall-normal velocity at the surface. If the wall-normal velocity at the wall is not zero, an extra term appears in the AMI equation as

$$\frac{C_f}{2} = \frac{1}{Re_\ell} + \frac{1}{\ell} \int_0^\infty \frac{-\overline{u'v'}}{U_{io}^2} dy + \frac{\delta_1^\ell}{U_{io}} \frac{dU_{io}}{dx} + \left(\frac{d\delta_2^\ell}{dx} + \frac{\delta_2^\ell - \delta_2}{\ell} \frac{d\ell}{dx} + \frac{2\delta_2^\ell}{U_{io}} \frac{dU_{io}}{dx} + \frac{\delta_{2,v}}{\ell} \right) - \frac{V_w}{U_{io}} + \mathcal{I}^\ell, \quad (7.1)$$

where V_w denotes the non-zero wall-normal velocity at the wall. The fifth term in Eq. 7.1 accounts directly for the surface penetration effect or the presence of non-zero wall-normal velocity at the wall. This term, known as *wall BC*, directly depends on $V_w(x)$ and illustrates how the imposed wall BCs influence the skin friction coefficient. It is naturally zero for flows with no-penetration BC. However, for BLs subject to flow control schemes such as surface suction or blowing, this term alters the budget of the AMI equation.

We apply Eq. 7.1 to a set of incompressible turbulent BLs over NACA-4412 airfoil at an angle of attack of 5° . Similar to section 5.2, the Reynolds number based on the chord length (c) is $Re_c = U_\infty c / \nu = 400,000$, where U_∞ denotes the free-stream velocity. Apart from the reference Wing case that was discussed in Chapter 5, two other BLs under the same flow configuration are studied, but with control schemes employing surface suction (Wing-suction) and blowing (Wing-blowing). The control surface extends from $\xi/c = 0.25$ to $\xi/c = 0.855$, with a constant control intensity set at $0.1\%U_\infty$ [5]. Figure 7.1 illustrates the budget of the AMI equation for turbulent BL over an airfoil under suction and blowing, compared with the reference Wing discussed earlier. For the convenience of the reader, the control surface is shaded in Fig. 7.1.

With surface suction (or blowing), *laminar friction* (not shown here) is marginally higher (or lower)

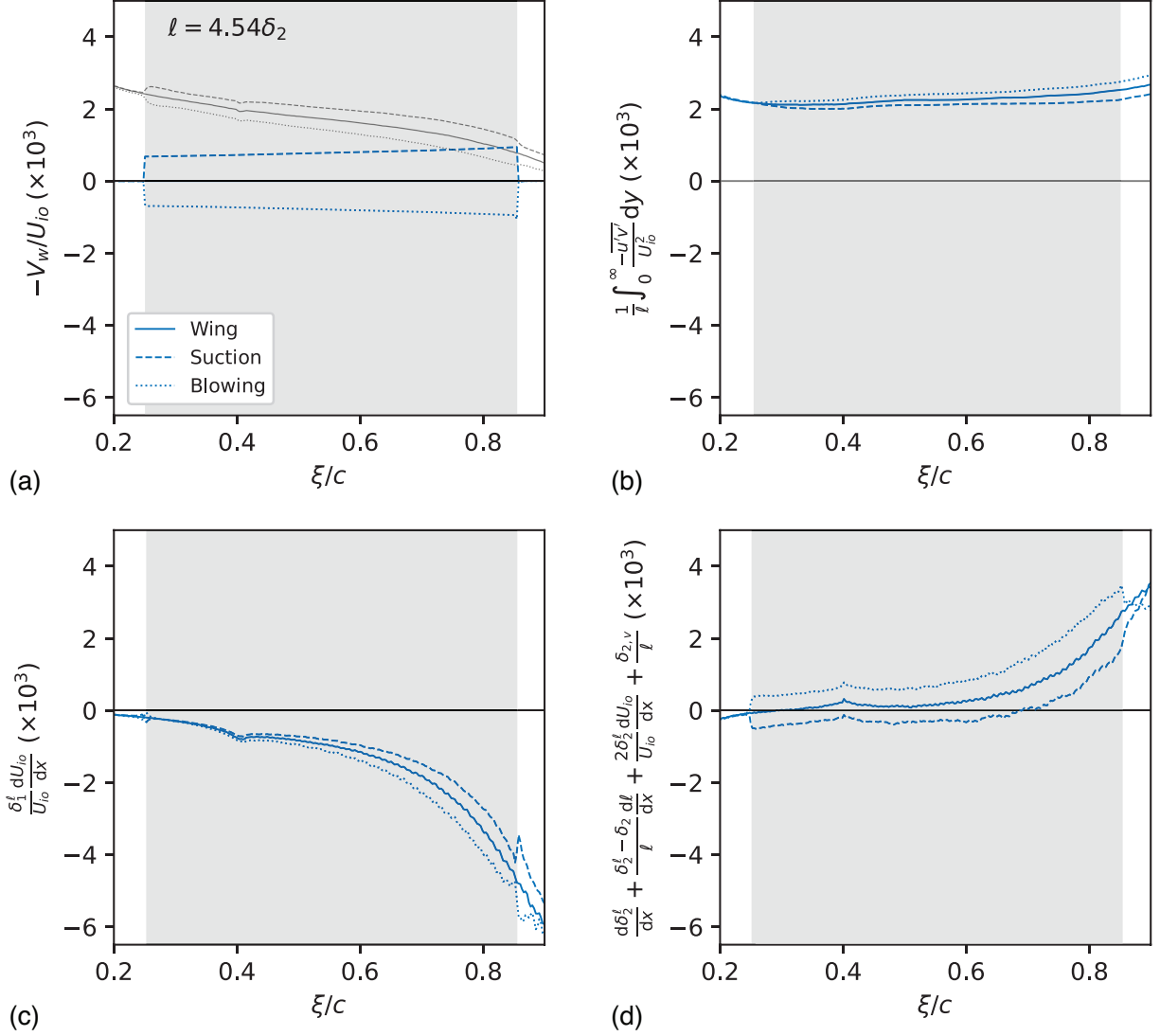


Figure 7.1: The AMI budget of the reference wing compared with the suction and blowing cases with respect to ξ/c for: (a) *turbulent torque*, (b) *pressure gradient*, (c) *mean flux*, and (d) *wall BC*. The shaded gray region denotes the streamwise position under suction (or blowing). In (a) shaded black lines exhibit $C_f/2$.

than the reference case as BL thickness reduces (or increases) downstream; thinning of δ_{99} is correlated with a reduction in δ_2 , and hence ℓ . Ignoring the contribution of *laminar friction*, which is not effectively impacted by either suction (or blowing), a major flow phenomenon is *wall BC*. In the AMI equation, the direct impact of suction and blowing (or any imposed wall BC) on $C_f/2$ is associated with *wall BC*. This flow phenomenon explicitly depends on the wall-normal velocity at the surface, V_w . Figure 7.1 (a) depicts *wall BC* along with $C_f/2$ (shown in shaded black lines).

In these plots, suction is represented by dashed lines, and the blowing case is illustrated by dotted lines, while the reference case without control is represented by solid lines. As expected, suction naturally increases the skin friction coefficient by enhancing the wall-edge velocity gradient and pulling higher momentum fluid toward the wall. On the other hand, surface blowing leads to about a 20% reduction of C_f with respect to the reference case by thickening the boundary layer. With regular no-slip and no-penetration wall BCs, *wall BC* is naturally zero, as shown for the reference wing. For instance, in the surface suction (or blowing) case, the relative contribution of *wall BC* reads from 24% (or -35%) at the leading edge to approximately 80% (or $\sim -200\%$) at the trailing edge of the control region. This monotonic increase of the relative contribution downstream is merely due to the reduction of $C_f/2$ because V_w is imposed to be a constant.

Despite the limited influence of suction (or blowing) on *laminar friction*, the control region changes the turbulence enhancement. As shown in figure 7.1 (b), the impact of suction (or blowing) on *turbulent torque* is opposite and less significant compared to its impact on C_f . For example, surface suction increases the skin-friction coefficient but diminishes *turbulent torque*. The AMI equation quantifies the maximum change of *turbulent torque* to be, respectively, -10% and 9% for suction and blowing. Moreover, suction (or blowing) seems to have a cumulative effect on *turbulent torque*; at the leading edge of the control region, the difference between *turbulent torques* is negligible, yet it increases downstream. Therefore, for the suction case, the lower downstream *turbulent torque* shows surface suction alleviates the impact of pressure gradient on the upstream-to-downstream variation of the turbulence enhancement; the difference of *turbulent torque* between $\xi/c = 0.2$ to $\xi/c = 0.9$ is less than 1%, while in the reference case, this number was reported to be 13%. These results suggest that surface suction must reduce the negative contribution of *pressure gradient* by pulling the flow towards the wall.

As presented in figure 7.1 (c), similar to the *turbulent torque* analysis, the impact of surface suction (or blowing) on *pressure gradient* appears to be cumulative too. Within $\xi/c \leq 0.4$, the effect of suction (or blowing) on *pressure gradient* is insignificant. However, the accumulated effect

becomes more pronounced downstream of $\xi/c = 0.4$, also slightly influencing the growth rate of *pressure gradient*. The AMI analysis quantifies the maximum impact of surface suction on *pressure gradient* to be approximately 14%, observed at the trailing edge of the control surface, compared with the reference wing. Surface blowing has a similar but opposite effect, enhancing the strength of *pressure gradient*.

Due to the natural cumulative effect of suction (or blowing) on *turbulent torque* and *pressure gradient*, *mean flux* is the only flow phenomenon partially resisting the immediate impact of *wall BC* on C_f . In other words, *mean flux* alleviates the non-equilibrium caused by both *pressure gradient* and *wall BC*. In the spatial range of $0.2 \leq \xi/c \leq 0.4$, where *pressure gradient* is relatively weak, the absolute contribution of *mean flux* to $C_f/2$ is small for the reference Wing. In the suction (or blowing) case, on the other hand, *mean flux* resists the immediate skin-friction enhancement (or reduction) caused by *wall BC*. The immediate response of *mean flux* to suction (or blowing) can be understood by looking into its sub-terms. As described in section 5.1, *mean flux* is the sum of the streamwise growth of the BL thickness and the mean wall-normal flux, first introduced in [38]. Suction (or blowing) only implicitly influences the streamwise growth of the BL. However, the mean wall-normal flux absorbs the immediate change of suction (or blowing). This term, demonstrated to enhance wall shear stress in fully turbulent flows [38, 82, 81], exhibits a weaker effect with suction but a stronger impact with blowing at the surface of the control region. This is a consequence of suction (or blowing) altering the mean wall-normal velocity profile, influencing the wall-normal transport of momentum, particularly near the surface. For example, suction induces a region with negative mean wall-normal velocity, leading to an inverse contribution of mean wall-normal flux. Therefore, *mean flux* compensates for approximately 70% of the *wall BC*'s friction enhancement, primarily by generating weaker (and sometimes negative) mean wall-normal flux. Interestingly, this observation parallels findings in transitional incompressible boundary layers ([82]), where a small region near the surface exhibited wall-normal deceleration and $\bar{v} \leq 0$, forcing the near-wall flow to accelerate in the streamwise direction due to the continuity constraint.

The authors contends that BLs with surface suction and transitional flows, which are characterized by the presence of negative near-surface wall-normal velocity, hold the potential to foster other flow control schemes.

7.2 Wall-normal Integral-based Turbulent Modelling

The development and application of integral-based methods for the analysis and modeling of wall-bounded flows began with the study of laminar boundary layer (BL) flows [165, 132, 153] and expanded to turbulent flows with the introduction of wall-normal integrals in the RANS equations [88]. While the advancements in numerical computation have facilitated the solution of fully three-dimensional partial differential equations, such as the Navier-Stokes equations, through high-fidelity platforms like DNS, the computational cost remains prohibitively high, particularly for applications involving higher Reynolds numbers [181]. Even less expensive numerical methods, like LES, are still computationally demanding at Reynolds numbers relevant to practical applications [181].

The significant impact of turbulent motions with streamwise extents comparable to the BL thickness, channel half-height, or pipe radius presents intriguing challenges and opportunities for modeling [70, 86, 63, 111]. These large-scale motions (LSMs) and superstructures –or very-large-scale motions (VLSMs)– exhibit substantial wall-normal extent (as illustrated in Fig. 1.6) and contribute significantly to turbulent kinetic energy and Reynolds stress across much of the boundary layer. The primary challenge in developing models for wall-bounded turbulence based on (V)LSMs lies in creating an efficient framework directly derived from conservation laws, e.g., the Navier-Stokes equations.

One approach to address this challenge, proposed by Ragan & Johnson [134], involves utilizing instantaneous wall-normal integrals of first principles. This approach can be interpreted as an LES

version of traditional RANS-based integral methods, inspired by the budget of the angular momentum integral equation for the turbulent enhancement. As shown in figures 5.10 more than 60% of the zeroth integral of (or total) Reynolds shear stress, known as *turbulent torque*, is accumulated within the outer region of the BL. This value reaches to more than 90% for the near-equilibrium BLs, e.g., zero-pressure-gradient BLs. These prior observations clearly show the importance of the outer region of the flow in capturing the dominant effect of Reynolds shear stress.

Applying the concept of zeroth and first moments to the DNS data from the Johns Hopkins Turbulence Databases for a turbulent channel flow with $Re_\tau = 1000$ [51] as a *priori* test, Ragan & Johnson [134] observed that the larger turbulent structures still exist in the two-dimensional field of instantaneous wall-normal integrated velocity (see Figure 7.2). Figure 7.2 (a) displays the inner-scaled

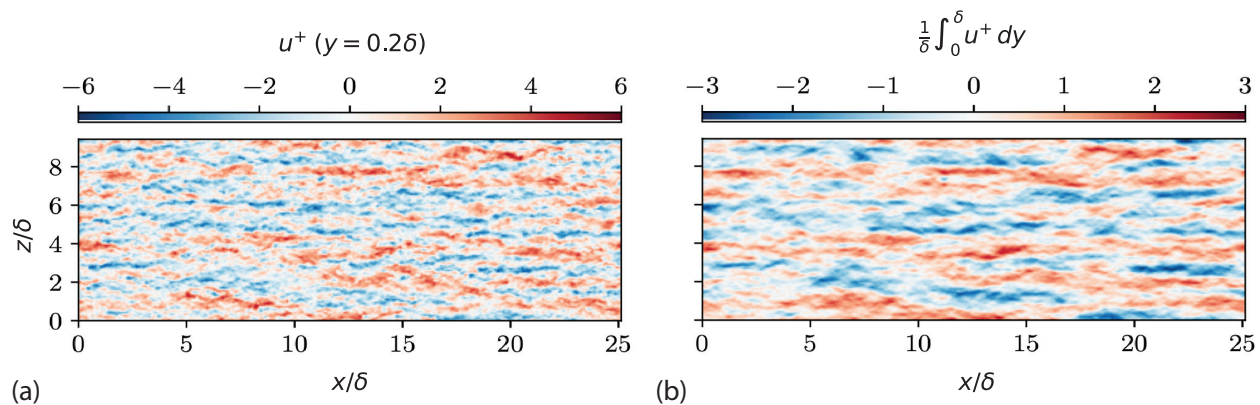


Figure 7.2: Comparison of the inner-scaled instantaneous streamwise velocity in $x - z$ plane: (a) at wall-normal distance $y/\delta = 0.2$, and (b) after applying the wall-normal integral operator. Results from Ragan & Johnson [134].

instantaneous streamwise velocity component in the $x - z$ plane away from the wall at $y/\delta = 0.2$) in which the large-scale streaky turbulent structures are evident. Upon applying the wall-normal integral operator –similar to a filter– to $\overline{u'}^+$, the large-scale streaks are preserved almost identically at similar locations within the $x - z$ plane (Figure 7.2 (b)). These findings suggest that the zeroth- and first-moment integral operators approximately retain a significant portion of the turbulent dynamics. These findings are in parallel with our previous analysis using the angular momentum integral equation in boundary layers, where we observed that up to 90% of the turbulent enhancement

is attributed to the outer region and (V)LSMs.

Chapter 8

Conclusion and Future Works

The focus of this thesis was developing the first-moment integral equations as an analysis tool to examine the surface friction and heat flux in boundary layer flows. The first-moment integral equations are derived from the first principles without any assumption. For instance, the angular momentum integral (AMI) equation, first introduced by Elnahhas & Johnson [38], is derived from the conservation of momentum and shows how different flow phenomena above the wall impact the skin friction coefficient. With a similar approach, the moment of (total) enthalpy integral (MTEI) equation is obtained from the energy conservation and yields a decomposition for the Stanton number.

8.1 Summary of Completed Works

A boundary layer, first hypothesized by Prandtl, is a thin layer of flow in the vicinity of a surface where the no-slip boundary condition is imposed, so the viscous effects are significant. This layer is known for generating friction drag and is responsible for heat transfer between the fluid state and surface. Although known as a canonical flow, the physics of boundary layer flows can be

complex. This complexity arises when the boundary layer transitions to turbulence. Furthermore, the geometry of the problem, like significant curvature effects, adds additional physical phenomena to the fluid flow. If the flow is in a high-speed regime, the density variation and compressibility effects make the physics of turbulent flows further intriguing. In the following text, I summarize how the first-moment integral equations in this work had been implemented to examine the impact of different flow phenomena on the skin friction coefficient and Stanton number.

- I extended the first-moment integral equation on the basis of the AMI equation to incompressible transitional and turbulent boundary layer flows with heat transfer. The moment of enthalpy integral (MEI) equation was introduced to decompose the Stanton number, quantifying how flow phenomena above the wall impact the surface heat flux relative to the reference laminar flow at the same Reynolds number. Furthermore, the peak skin friction and heat flux were examined during the transition. I implemented the AMI and MEI equation to demonstrate how *streamwise growth* and *mean wall-normal flux* resist the rapidly growing Reynolds shear stress enhancement of the skin friction coefficient and Stanton number during the transition. The growth of the Reynolds shear stress during the transition forces the near-wall flow to accelerate –an effect similar to the favorable pressure gradient. Due to the continuity constraint, the near-wall wall-normal velocity becomes negative in that region, carrying high-momentum flow toward the wall. The author believes this region can yield an optimized flow control outcome since the negative wall-normal velocity would further stimulate the control scheme.
- I re-arranged the AMI equation to tackle turbulent boundary layers encountering non-zero pressure gradients. The reformulated form of AMI is based on the inviscid velocity instead of the edge or free stream velocities, as the outer layer velocity scale. Such a choice improves the robustness of integral equations by alleviating the ambiguity in the definition of the boundary layer thickness. The modified AMI equation was applied to flows over a suction side of an airfoil and a two-dimensional Gaussian bump, where in both, the pressure gradient

is imposed by the geometry of the surface, i.e., curvature effects. I concluded the strength of the adverse pressure gradient does not significantly impact the explicit turbulent enhancement of skin friction, e.g., *turbulent torque*. This observation is aligned with the budget of the AMI equation for flows over a flat plate with an imposed adverse pressure gradient. In the bump flow, the AMI equation captured the re-laminarization process caused by (strong) favorable pressure gradients; during flow acceleration, *turbulent torque* reduced substantially, while *laminar* friction increased. Additionally, using the AMI analysis, I showed this so-called re-laminarization is truly attributed to frozen turbulence rather than suppressing the turbulence. I further implemented the AMI equation to examine the pressure gradient history effects on boundary layer turbulent statistics. The AMI equation offers a pressure gradient parameter, β_ℓ , (as a counterpart of the non-equilibrium Clauser parameter, β), which yields more robust similarity between two distinct boundary layers at matching β_ℓ than what β gives. Specifically, I observed a strong correlation between β_ℓ and the skin friction coefficient.

- I extended the AMI equation to high-speed boundary layers, including the compressibility effects. Furthermore, I introduced the MTEI equation on the basis of the AMI equation to study the surface heat flux in those flows. The AMI and MTEI equations were applied to a set of compressible direct numerical simulation datasets for a fully turbulent boundary layer over a flat plate with a wide range of edge Mach numbers from subsonic to supersonic flows. The integral equations suggest defining a reference viscosity (and thermal conductivity) over a common choice of wall quantities. Such a choice yields a more robust collapse of boundary layers with different edge and wall conditions. Using these reference quantities, I demonstrated the primary difference between the distribution of the normalized Reynolds shear stress (by the edge velocity) in the wall-normal direction for different boundary layers is due to the mean density profile. In other words, the profile of $-\overline{u''v''}/U_e^2$ is significantly similar for a wide range of edge Mach numbers and wall conditions. I also obtained a mapping between the skin friction coefficient of compressible and incompressible boundary layers using the ratio between the AMI length scale of compressible and incompressible flows. This

transformation yields an accurate prediction for adiabatic wall cases, while its accuracy diminishes as the wall-cooling gets stronger. A similar analysis was performed to examine the significant surface heat flux of supersonic datasets.

- Besides using the first-moment integral equation as a post-processing platform, they can be used to develop and optimize flow control schemes. Specifically, the AMI equation was modified to yield a term for the explicit contribution of non-zero wall-normal boundary conditions. Applying this to flow over an airfoil with surface suction and blowing exhibited a weak impact of the control scheme on the turbulent enhancement. The AMI equation can also be implemented to examine other control schemes. Furthermore, I discussed the potential for developing integral equations as a computationally efficient approach to turbulent modeling. One avenue involves solving the zeroth- and first-moments of the integral of Navier-Stokes equations, merely resolving the outer region of wall-bounded flows. My earlier observation supports this proposition that over 80% of the turbulent enhancement captured by the AMI equation is concentrated in the outer region.

8.2 Future Research Ideas

In light of the findings of this thesis, I propose the following subjects as potential paths for further investigation.

- Expanding the application of first-moment integral equations to boundary layer flows over rough surfaces presents a promising avenue for research. Surface roughness, typically characterized by roughness functions or empirical methods, appears as an extra term in the governing equations. By taking the first-moment integral, we can directly quantify the explicit impact of surface roughness on both surface friction and heat flux relative to base laminar flow. Furthermore, extending the integral equations to incorporate surface roughness enables

us to investigate how roughness alters turbulent enhancement compared to smooth surfaces. By systematically analyzing turbulent statistics and flow dynamics over rough surfaces, we can develop more robust models for flows with surface roughness.

- The application of the first-moment integral equations to boundary layer flows with significant curvature effects is a crucial avenue for future research. While this thesis primarily focused on flows where direct curvature impact was limited, such as bump flows, the influence of curvature can be substantial in cases involving flows around blunt bodies or certain airfoils. Therefore, it becomes imperative to extend the AMI analysis to include explicit curvature effects and assess their impact on turbulent enhancement. An initial step towards this analysis involves deriving the integral equations in a general curvilinear coordinate system. To the best of the author's knowledge, there is currently no systematic set of integral equations available for such a coordinate system. Thus, future research efforts should focus on formulating integral equations that account for the complex interplay between curvature effects and turbulent boundary layer dynamics. This will provide valuable insights into how curvature influences turbulence enhancement and aid in the development of more accurate turbulence models for curved boundary layer flows.
- Implementing the Angular Momentum Integral (AMI) equation for flows approaching separation or in separated flow regimes presents an intriguing avenue for further investigation. Since the AMI equation is derived from fundamental conservation equations without relying on the boundary layer approximation, it holds potential applicability to separated flows. Studying separated flows using the AMI equation requires access to reliable and sufficiently averaged turbulent datasets. By conducting such an analysis, we can gain deeper insights into how separated flow phenomena, such as separation bubbles, influence turbulence dynamics. This research endeavor can enhance our understanding of the intricate interactions between separated regions and turbulence structures, paving the way for more accurate modeling and prediction of separated flow behavior.

- Investigating the application of first-moment integral equations to transitional high-speed compressible boundary layers represents a compelling research direction. While this thesis concentrated on fully turbulent compressible flows, where turbulence was triggered by turbulent recycling, the intriguing findings regarding transitional incompressible boundary layers prompt exploration into compressible regimes. Applying the AMI analysis to transitional compressible boundary layers entails examining the first- and second-mode of transition and assessing how various flow phenomena in the AMI equation respond to these transitional states at different frequencies. By conducting such investigations, we can gain valuable insights into the transitional behavior of compressible boundary layers, facilitating a deeper understanding of the underlying physics and providing insights into developing robust control schemes. Additionally, the first-moment integral equations can be extended to transitional and turbulent high-speed flows considering the high-enthalpy effects. This requires deriving the equations for each species as well as including additional terms in the momentum and energy conservation. By doing so, one can examine how dissociation due to the high-enthalpy effect could impact the turbulent enhancement of the surface friction and heat flux.

Bibliography

- [1] N. Abderrahaman-Elena and R. García-Mayoral. Analysis of anisotropically permeable surfaces for turbulent drag reduction. *Physical Review Fluids*, 2:114609, 2017.
- [2] M. Amitay, B. A. Tuna, and H. Dell’Orso. Identification and mitigation of T-S waves using localized dynamic surface modification. *Physics of Fluids*, 28:064103, 2016.
- [3] G. Araya, C. J. Lagares, J. Santiago, and K. E. Jansen. Wall temperature effect on hypersonic turbulent boundary layers via dns. In *AIAA Scitech 2021 Forum*, page 1745, 2021.
- [4] K. Asada and S. Kawai. Large-eddy simulation of airfoil flow near stall condition at reynolds number 2.1×10^6 . *Physics of Fluids*, 30(8), 2018.
- [5] M. Atzori, F. Mallor, R. Pozuelo, K. Fukagata, R. Vinuesa, and P. Schlatter. A new perspective on skin-friction contributions in adverse-pressure-gradient turbulent boundary layers. *International Journal of Heat and Fluid Flow*, 101:109117, 2023.
- [6] M. Atzori, R. Vinuesa, A. Stroh, D. Gatti, B. Frohnappel, and P. Schlatter. Uniform blowing and suction applied to nonuniform adverse-pressure-gradient wing boundary layers. *Physical Review Fluids*, 6(11):113904, 2021.
- [7] R. Balin and K. E. Jansen. Direct numerical simulation of a turbulent boundary layer over a bump with strong pressure gradients. *Journal of Fluid Mechanics*, 918:A14, 2021.
- [8] A. Bannier, E. Garnier, and P. Sagaut. Riblet flow model based on an extended fik identity. *Flow, Turbulence and Combustion*, 95(2):351–376, 2015.
- [9] V. Baskaran, A. Smits, and P. Joubert. A turbulent flow over a curved hill part 1. growth of an internal boundary layer. *Journal of Fluid Mechanics*, 182:47–83, 1987.
- [10] V. Baskaran, A. Smits, and P. Joubert. A turbulent flow over a curved hill. part 2. effects of streamline curvature and streamwise pressure gradient. *Journal of Fluid Mechanics*, 232:377–402, 1991.
- [11] T. B. Benjamin. Effects of a flexible boundary on hydrodynamic instability. *Journal of Fluid Mechanics*, 9:513–532, 1960.
- [12] H. Blasius. *Grenzschichten in Flüssigkeiten mit kleiner Reibung*. Druck von BG Teubner, 1907.

- [13] A. Bobke, R. Örlü, and P. Schlatter. Simulations of turbulent asymptotic suction boundary layers. *Journal of Turbulence*, 17(2):157–180, 2016.
- [14] A. Bobke, R. Vinuesa, R. Örlü, and P. Schlatter. History effects and near equilibrium in adverse-pressure-gradient turbulent boundary layers. *Journal of Fluid Mechanics*, 820:667–692, 2017.
- [15] P. Bradshaw. The analogy between streamline curvature and buoyancy in turbulent shear flow. *Journal of Fluid Mechanics*, 36(1):177–191, 1969.
- [16] D. M. Bushnell, J. N. Hefner, and R. L. Ash. Effect of compliant wall motion on turbulent boundary layers. *Physics of Fluids*, 20(10):S31–S48, Oct. 1977.
- [17] G. V. Candler. Rate effects in hypersonic flows. *Annual Review of Fluid Mechanics*, 51(1):379–402, 2019.
- [18] P. W. Carpenter and A. D. Garrad. The hydrodynamic stability of flow over Kramer-type compliant surfaces. part 1. Tollmien-Schlichting instabilities. *Journal of Fluid Mechanics*, 155:465–510, 1985.
- [19] P. W. Carpenter, A. D. Lucey, and C. Davies. Progress on the use of compliant walls for laminar-flow control. *Journal of aircraft*, 38(3):504–512, 2001.
- [20] L. Castillo and W. K. George. Similarity analysis for turbulent boundary layer with pressure gradient: outer flow. *AIAA journal*, 39(1):41–47, 2001.
- [21] Y. Chang, S. S. Collis, and S. Ramakrishnan. Viscous effects in control of near-wall turbulence. *Physics of Fluids*, 14(11):4069–4080, 2002.
- [22] M. Chevalier, P. Schlatter, A. Lundbladh, and D. S. Henningson. *SIMSON: A pseudo-spectral solver for incompressible boundary layer flows*. 2007.
- [23] H. Choi, P. Moin, and J. Kim. Active turbulence control for drag reduction in wall-bounded flows. *Journal of Fluid Mechanics*, 262:75–110, 1994.
- [24] F. H. Clauser. Turbulent boundary layers in adverse pressure gradients. *Journal of the Aeronautical Sciences*, 21(2):91–108, 1954.
- [25] G. N. Coleman, C. L. Rumsey, and P. R. Spalart. Numerical study of turbulent separation bubbles with varying pressure gradient and reynolds number. *Journal of Fluid Mechanics*, 847:28–70, 2018.
- [26] C. Cossu and L. Brandt. Stabilization of Tollmien–Schlichting waves by finite amplitude optimal streaks in the blasius boundary layer. *Physics of Fluids*, 14:L57–L60, 2002.
- [27] C. Davies and P. W. Carpenter. Numerical simulation of the evolution of Tollmien-Schlichting waves over finite compliant panels. *Journal of Fluid Mechanics*, 335:361–392, 1997.

- [28] M. de Giovanetti, Y. Hwang, and H. Choi. Skin-friction generation by attached eddies in turbulent channel flow. *Journal of Fluid Mechanics*, 808:511–538, 2016.
- [29] D. B. DE GRAAFF and J. K. EATON. Reynolds-number scaling of the flat-plate turbulent boundary layer. *Journal of Fluid Mechanics*, 422:319–346, 2000.
- [30] S. Deck, N. Renard, R. Laraufie, and P. E. Weiss. Large-scale contribution to mean wall shear stress in high-reynolds-number flat-plate boundary layers up to $re\theta=13650$. *Journal of Fluid Mechanics*, 743:202–248, 2014.
- [31] J. C. Del Alamo and J. Jiménez. Spectra of the very large anisotropic scales in turbulent channels. *Physics of Fluids*, 15(6):L41–L44, 2003.
- [32] W. J. Devenport and K. T. Lowe. Equilibrium and non-equilibrium turbulent boundary layers. *Progress in Aerospace Sciences*, 131:100807, 2022.
- [33] M. Di Renzo, L. Fu, and J. Urzay. Htr solver: An open-source exascale-oriented task-based multi-gpu high-order code for hypersonic aerothermodynamics. *Computer Physics Communications*, 255:107262, 2020.
- [34] M. Di Renzo and J. Urzay. Direct numerical simulation of a hypersonic transitional boundary layer at suborbital enthalpies. *Journal of Fluid Mechanics*, 912:A29, 2021.
- [35] S. Dong, G. E. Karniadakis, and C. Chrysosostomidis. A robust and accurate outflow boundary condition for incompressible flow simulations on severely-truncated unbounded domains. *Journal of Computational Physics*, 261:83–105, 2014.
- [36] P. Durbin and S. Belcher. Scaling of adverse-pressure-gradient turbulent boundary layers. *journal of fluid mechanics*, 238:699–722, 1992.
- [37] G. Eitel-Amor, R. Örlü, and P. Schlatter. Simulation and validation of a spatially evolving turbulent boundary layer up to $re\theta= 8300$. *International Journal of Heat and Fluid Flow*, 47:57–69, 2014.
- [38] A. Elnahas and P. L. Johnson. On the enhancement of boundary layer skin friction by turbulence: an angular momentum approach. *Journal of Fluid Mechanics*, 940:A36, 2022.
- [39] A. Esteghamatian, J. Katz, and T. A. Zaki. Spatiotemporal characterization of turbulent channel flow with a hyperelastic compliant wall. *Journal of Fluid Mechanics*, 942:A35, 2022.
- [40] V. Falkneb and S. W. Skan. Lxxxv. solutions of the boundary-layer equations. *The London, Edinburgh, and Dublin Philosophical Magazine and Journal of Science*, 12(80):865–896, 1931.
- [41] Y. Fan, W. Li, M. Atzori, R. Pozuelo, P. Schlatter, R. Vinuesa, et al. Decomposition of the mean friction drag in adverse-pressure-gradient turbulent boundary layers. *Physical Review Fluids*, 5(11):114608, 2020.

- [42] A. Favre. Equations des gaz turbulents compressibles. *J. de Mecanique*, 4(3), 1965.
- [43] K. J. Franko and S. K. Lele. Breakdown mechanisms and heat transfer overshoot in hypersonic zero pressure gradient boundary layers. *Journal of Fluid Mechanics*, 730:491–532, 2013.
- [44] J. H. M. Fransson, L. Brandt, A. Talamelli, and C. Cossu. Experimental study of the stabilization of Tollmien–Schlichting waves by finite amplitude streaks. *Physics of Fluids*, 17:054110, 2005.
- [45] L. Fu, X. Y. Hu, and N. A. Adams. A family of high-order targeted eno schemes for compressible-fluid simulations. *Journal of Computational Physics*, 305:333–359, 2016.
- [46] K. Fukagata, K. Iwamoto, and N. Kasagi. Contribution of reynolds stress distribution to the skin friction in wall-bounded flows. *Physics of Fluids*, 14(11):L73–L76, 2002.
- [47] M. Gad-el Hak. *Flow control: passive, active, and reactive flow management*. Cambridge University Press, Cambridge, 2000.
- [48] M. Gad-El-Hak, R. F. Blackwelder, and J. J. Riley. On the interaction of compliant coatings with boundary-layer flows. *Journal of Fluid Mechanics*, 140:257–280, 1984.
- [49] R. García-Mayoral and J. Jiménez. Drag reduction by riblets. *Philosophical Transactions of the Royal Society A*, 369:1412–1427, 2011.
- [50] S. Gottlieb, C.-W. Shu, and E. Tadmor. Strong stability-preserving high-order time discretization methods. *SIAM Review*, 43(1):89–112, 2001.
- [51] J. Graham, K. Kanov, X. Yang, M. Lee, N. Malaya, C. Lalescu, R. Burns, G. Eyink, A. Szalay, R. Moser, et al. A web services accessible database of turbulent channel flow and its use for testing a new integral wall model for les. *Journal of Turbulence*, 17(2):181–215, 2016.
- [52] D. Greenblatt, K. B. Paschal, C.-S. Yao, J. Harris, N. W. Schaeffler, and A. E. Washburn. Experimental investigation of separation control part 1: baseline and steady suction. *AIAA journal*, 44(12):2820–2830, 2006.
- [53] K. P. Griffin, L. Fu, and P. Moin. General method for determining the boundary layer thickness in nonequilibrium flows. *Physical Review Fluids*, 6(2):024608, 2021.
- [54] K. P. Griffin, L. Fu, and P. Moin. Velocity transformation for compressible wall-bounded turbulent flows with and without heat transfer. *Proceedings of the National Academy of Sciences*, 118(34):e2111144118, 2021.
- [55] S. Grundmann and C. Tropea. Active cancellation of artificially introduced tollmien–schlichting waves using plasma actuators. *Experiments in Fluids*, 44:795–806, 2008.
- [56] M. Guala, S. Hommema, and R. Adrian. Large-scale and very-large-scale motions in turbulent pipe flow. *Journal of Fluid Mechanics*, 554:521–542, 2006.

- [57] J. M. Hamilton, J. Kim, and F. Waleffe. Regeneration mechanisms of near-wall turbulence structures. *Journal of Fluid Mechanics*, 287:317–348, 1995.
- [58] F. H. Harlow and J. E. Welch. Numerical calculation of time-dependent viscous incompressible flow of fluid with free surface. *The physics of fluids*, 8(12):2182–2189, 1965.
- [59] Z. Harun, J. P. Monty, R. Mathis, and I. Marusic. Pressure gradient effects on the large-scale structure of turbulent boundary layers. *Journal of Fluid Mechanics*, 715:477–498, 2013.
- [60] T. Herbert. Secondary instability of boundary layers. *Annual review of fluid mechanics*, 20(1):487–526, 1988.
- [61] S. Hoyas and J. Jiménez. Scaling of the velocity fluctuations in turbulent channels up to $Re\tau=2003$. *Physics of fluids*, 18(1), 2006.
- [62] P. Huang, G. N. Coleman, and P. Bradshaw. Compressible turbulent channel flows: Dns results and modelling. *Journal of Fluid Mechanics*, 305:185–218, 1995.
- [63] N. HUTCHINS and I. MARUSIC. Evidence of very long meandering features in the logarithmic region of turbulent boundary layers. *Journal of Fluid Mechanics*, 579:1–28, 2007.
- [64] N. Hutchins and I. Marusic. Large-scale influences in near-wall turbulence. *Philosophical Transactions of the Royal Society A: Mathematical, Physical and Engineering Sciences*, 365(1852):647–664, 2007.
- [65] Y. Hwang. Near-wall turbulent fluctuations in the absence of wide outer motions. *Journal of Fluid Mechanics*, 723:264–288, 2013.
- [66] Y. Hwang and Y. Bengana. Self-sustaining process of minimal attached eddies in turbulent channel flow. *Journal of Fluid Mechanics*, 795:708–738, 2016.
- [67] K. Iwamoto, K. Fukagata, N. Kasagi, and Y. Suzuki. Friction drag reduction achievable by near-wall turbulence manipulation at high reynolds numbers. *Physics of Fluids*, 17(1):011702–011702, 2005.
- [68] K. Jansen, M. Rasquin, J. Farnsworth, N. Rathay, M. Monastero, and M. Amitay. Interaction of a synthetic jet with separated flow over a vertical tail. *AIAA Journal*, 56:2653–2668, 2018.
- [69] K. E. Jansen, C. H. Whiting, and G. M. Hulbert. A generalized- α method for integrating the filtered navier–stokes equations with a stabilized finite element method. *Computer methods in applied mechanics and engineering*, 190(3-4):305–319, 2000.
- [70] J. Jiménez. The largest scales of turbulent wall flows. *CTR Annual Research Briefs*, 137:54, 1998.
- [71] J. JIMÉNEZ and A. PINELLI. The autonomous cycle of near-wall turbulence. *Journal of Fluid Mechanics*, 389:335–359, 1999.
- [72] J. Jiménez and P. Moin. The minimal flow unit in near-wall turbulence. *Journal of Fluid Mechanics*, 225:213–240, 1991.

- [73] P. Johnson. Toward evaluating contributions to skin friction enhancement by transition and turbulence in boundary layer flows. *Annual Research Briefs 2019, Center for Turbulence Research*, pages 223–235, 2019.
- [74] R. D. Joslin, R. A. Nicolaides, G. Erlebacher, M. Y. Hussaini, and M. D. Gunzburger. Active control of boundary-layer instabilities: Use of sensors and spectral controller. *AIAA Journal*, 33:1521–1523, 1995.
- [75] Y. Kametani, K. Fukagata, R. Örlü, and P. Schlatter. Effect of uniform blowing/suction in a turbulent boundary layer at moderate reynolds number. *International Journal of Heat and Fluid Flow*, 55:132–142, 2015.
- [76] T. V. Kármán. Über laminare und turbulente reibung. *ZAMM-Journal of Applied Mathematics and Mechanics/Zeitschrift für Angewandte Mathematik und Mechanik*, 1(4):233–252, 1921.
- [77] J. Kendall. Experiments on the generation of tollmien-schlichting waves in a flat plate boundary layer by weak freestream turbulence. *AIAA Paper*, (84-0011), 1984.
- [78] J. Kendall. Experiments on boundary-layer receptivity to freestream turbulence. In *36th AIAA Aerospace Sciences Meeting and Exhibit*, page 530, 1998.
- [79] A. Kianfar, M. Di Renzo, C. Williams, A. Elnahas, and P. Johnson. Angular momentum and moment of enthalpy integral equations for compressible boundary layers. *Bulletin of the American Physical Society*, 2022.
- [80] A. Kianfar, M. Di Renzo, C. Williams, A. Elnahas, and P. Johnson. An angular momentum integral equation for high-speed boundary layers. In *Proceedings of the Summer Program, Center for Turbulence Research, Stanford University*, pages 357–366, 2022.
- [81] A. Kianfar, M. Di Renzo, C. Williams, A. Elnahas, and P. L. Johnson. Angular momentum and moment of total enthalpy integral equations for high-speed boundary layers. *Physical Review Fluids*, 8(5):054603, 2023.
- [82] A. Kianfar, A. Elnahas, and P. L. Johnson. Quantifying how turbulence enhances boundary layer skin friction and surface heat transfer. *AIAA Journal*, pages 1–10, 2023.
- [83] J. Kim. Physics and control of wall turbulence for drag reduction. *Philosophical Transactions of the Royal Society A: Mathematical, Physical and Engineering Sciences*, 369(1940):1396–1411, 2011.
- [84] J. Kim and P. Moin. Application of a fractional-step method to incompressible navier-stokes equations. *Journal of computational physics*, 59(2):308–323, 1985.
- [85] J. Kim, P. Moin, and R. Moser. Turbulence statistics in fully developed channel flow at low reynolds number. *Journal of Fluid Mechanics*, 177:133–166, 1987.
- [86] K. C. Kim and R. J. Adrian. Very large-scale motion in the outer layer. *Physics of Fluids*, 11(2):417–422, 1999.

- [87] P. S. Klebanoff, K. D. Tidstrom, and L. M. Sargent. The three-dimensional nature of boundary-layer instability. *Journal of Fluid Mechanics*, 12(1):1–34, 1962.
- [88] S. J. Kline, M. V. Morkovin, G. Sovran, and D. J. Cockrell, editors. *Computation of Turbulent Boundary Layers – AFOSR-IFP-Stanford Conference Proceedings*, 1968.
- [89] S. J. Kline, W. C. Reynolds, F. A. Schraub, and P. W. Runstadler. The structure of turbulent boundary layers. *Journal of Fluid Mechanics*, 30(4):741–773, 1967.
- [90] V. Kosorygin, R. Radeztsky, and W. Saric. Laminar boundary-layer, sound receptivity and control. In *Laminar-Turbulent Transition: IUTAM Symposium, Sendai/Japan, September 5–9, 1994*, pages 517–524. Springer, 1995.
- [91] M. O. Kramer. Boundary-layer stabilization by distributed damping. *Journal of the Aerospace Sciences*, 27(1):69–69, 1960.
- [92] M. O. Kramer. Boundary layer stabilization by distributed damping. *Naval Engineers Journal*, 74(2):341–348, 1962.
- [93] P.-Å. Krogstad and P. E. Skåre. Influence of a strong adverse pressure gradient on the turbulent structure in a boundary layer. *Physics of Fluids*, 7(8):2014–2024, 1995.
- [94] J. Lee and T. Zaki. Signature of large-scale motions on turbulent/non-turbulent interface in boundary layers. *Journal of Fluid Mechanics*, 819:165–187, 05 2017.
- [95] J.-H. Lee and H. J. Sung. Structures in turbulent boundary layers subjected to adverse pressure gradients. *Journal of fluid mechanics*, 639:101–131, 2009.
- [96] J. H. Lee and H. J. Sung. Very-large-scale motions in a turbulent boundary layer. *Journal of Fluid Mechanics*, 673:80–120, 2011.
- [97] W. Li, Y. Fan, D. Modesti, and C. Cheng. Decomposition of the mean skin-friction drag in compressible turbulent channel flows. *Journal of Fluid Mechanics*, 875:101–123, 2019.
- [98] H. W. Liepmann and D. N. Nosenchuck. Active control of laminar-turbulent transition. *Journal of Fluid Mechanics*, 118:201–204, 1982.
- [99] R. K. Lobb, E. M. Winkler, and J. Persh. Nol hypersonic tunnel no. 4, results 7: experimental investigation of turbulent boundary layers in hypersonic flow. Technical report, NAVAL ORDNANCE LAB WHITE OAK MD, 1955.
- [100] A. Lozano-Durán, M. Hack, and P. Moin. Modeling boundary-layer transition in direct and large-eddy simulations using parabolized stability equations. *Physical review fluids*, 3(2):023901, 2018.
- [101] A. D. Lucey and P. W. Carpenter. Boundary layer instability over compliant walls: Comparison between theory and experiment. *Physics of Fluids*, 7:2355–2363, 1995.
- [102] M. Luhar, A. S. Sharma, and B. J. McKeon. A framework for studying the effect of compliant surfaces on wall turbulence. *Journal of Fluid Mechanics*, 768:415–441, 2015.

- [103] I. Marusic, R. Mathis, and N. Hutchins. Predictive model for wall-bounded turbulent flow. *Science*, 329(5988):193–196, 2010.
- [104] I. Marusic and J. P. Monty. Attached eddy model of wall turbulence. *Annual Review of Fluid Mechanics*, 51(1):49–74, 2019.
- [105] O. Marxen and T. A. Zaki. Turbulence in intermittent transitional boundary layers and in turbulence spots. *Journal of Fluid Mechanics*, 860:350–383, 2019.
- [106] R. Matai and P. Durbin. Large-eddy simulation of turbulent flow over a parametric set of bumps. *Journal of Fluid Mechanics*, 866:503–525, 2019.
- [107] K. Matsuno and S. K. Lele. Internal regulation in compressible turbulent shear layers. *Journal of Fluid Mechanics*, 907:R2, 2021.
- [108] F. Mehdi, T. G. Johansson, C. M. White, and J. W. Naughton. On determining wall shear stress in spatially developing two-dimensional wall-bounded flows. *Experiments in fluids*, 55:1–9, 2014.
- [109] F. Mehdi and C. M. White. Integral form of the skin friction coefficient suitable for experimental data. *Experiments in Fluids*, 50:43–51, 2011.
- [110] M. Metzger and J. Klewicki. A comparative study of near-wall turbulence in high and low reynolds number boundary layers. *Physics of Fluids*, 13(3):692–701, 2001.
- [111] J. Monty, N. Hutchins, H. Ng, I. Marusic, and M. Chong. A comparison of turbulent pipe, channel and boundary layer flows. *Journal of fluid mechanics*, 632:431–442, 2009.
- [112] J. P. Monty, Z. Harun, and I. Marusic. A parametric study of adverse pressure gradient turbulent boundary layers. *International Journal of Heat and Fluid Flow*, 32(3):575–585, 2011.
- [113] M. V. Morkovin. Effects of compressibility on turbulent flows. *Mécanique de la Turbulence*, 367(380):26, 1962.
- [114] M. V. Morkovin. On the many faces of transition. In *Viscous Drag Reduction: Proceedings of the Symposium on Viscous Drag Reduction held at the LTV Research Center, Dallas, Texas, September 24 and 25, 1968*, pages 1–31. Springer, 1969.
- [115] M. V. Morkovin. Bypass-transition research: issues and philosophy. In *Instabilities and Turbulence in Engineering Flows*, pages 3–30. Springer, 1993.
- [116] Y. Na and P. Moin. Direct numerical simulation of a separated turbulent boundary layer. *Journal of Fluid Mechanics*, 374:379–405, 1998.
- [117] R. Narasimha and K. Sreenivasan. Relaminarization in highly accelerated turbulent boundary layers. *Journal of Fluid Mechanics*, 61(3):417–447, 1973.
- [118] R. Narasimha and K. Sreenivasan. Relaminarization of fluid flows. *Advances in applied mechanics*, 19:221–309, 1979.

- [119] R. Narasimha and K. Sreenivasan. Relaminarization of fluid flows. *Advances in applied mechanics*, 19:221–309, 1979.
- [120] M. Nishioka, Y. Ichikawa, et al. An experimental investigation of the stability of plane poiseuille flow. *Journal of Fluid Mechanics*, 72(4):731–751, 1975.
- [121] K. Nobuhide, H. Yosuke, F. Koji, and I. Kaoru. Control of turbulent transport: Less friction and more heat transfer. *Journal of Heat Transfer*, 134(3), 01 2012.
- [122] P. Orlandi. *Fluid flow phenomena: a numerical toolkit*, volume 55. Springer Science & Business Media, 2000.
- [123] D. Papamoschou and A. Roshko. The compressible turbulent shear layer: an experimental study. *Journal of Fluid Mechanics*, 197:453–477, 1988.
- [124] D. Passiatore, L. Sciacovelli, P. Cinnella, and G. Pascazio. Finite-rate chemistry effects in turbulent hypersonic boundary layers: A direct numerical simulation study. *Phys. Rev. Fluids*, 6:054604, May 2021.
- [125] V. Patel. Calibration of the preston tube and limitations on its use in pressure gradients. *Journal of Fluid Mechanics*, 23(1):185–208, 1965.
- [126] V. C. Patel and M. R. Head. Reversion of turbulent to laminar flow. *Journal of Fluid Mechanics*, 34(2):371–392, 1968.
- [127] A. T. Patera. A spectral element method for fluid dynamics: laminar flow in a channel expansion. *Journal of computational Physics*, 54(3):468–488, 1984.
- [128] Y. Peet and P. Sagaut. Theoretical prediction of turbulent skin friction on geometrically complex surfaces. *Physics of Fluids*, 21(10):105105, 2009.
- [129] E. Perlman, R. Burns, Y. Li, and C. Meneveau. Data exploration of turbulence simulations using a database cluster. In *Proceedings of the 2007 ACM/IEEE Conference on Supercomputing*, pages 1–11, 2007.
- [130] S. Pirozzoli. Generalized conservative approximations of split convective derivative operators. *Journal of Computational Physics*, 229(19):7180–7190, 2010.
- [131] S. Pirozzoli and M. Bernardini. Turbulence in supersonic boundary layers at moderate reynolds number. *Journal of Fluid Mechanics*, 688:120–168, 2011.
- [132] K. Pohlhausen. Zur näherungsweise integration der differentialgleichung der laminaren grenzschicht. *ZAMM-Journal of Applied Mathematics and Mechanics/Zeitschrift für Angewandte Mathematik und Mechanik*, 1(4):252–290, 1921.
- [133] S. B. Pope. Turbulent flows. *Measurement Science and Technology*, 12(11):2020–2021, 2001.
- [134] T. Ragan and P. Johnson. On the statistics of instantaneous wall-normal integrals. *Bulletin of the American Physical Society*, 2023.

- [135] N. Renard and S. Deck. A theoretical decomposition of mean skin friction generation into physical phenomena across the boundary layer. *Journal of Fluid Mechanics*, 790:339–367, 2016.
- [136] E. Reshotko. Disturbances in a laminar boundary layer due to distributed surface roughness. *Turbulence and chaotic phenomena in fluids*, pages 39–46, 1984.
- [137] E. Reshotko. Boundary layer instability, transition and control. In *32nd Aerospace Sciences Meeting and Exhibit*, page 1, 1994.
- [138] E. Reshotko. Transient growth: A factor in bypass transition. *Physics of Fluids*, 13(5):1067–1075, 2001.
- [139] O. Reynolds. Xxix. an experimental investigation of the circumstances which determine whether the motion of water shall be direct or sinuous, and of the law of resistance in parallel channels. *Philosophical Transactions of the Royal Society of London*, 174:935–982, 1883.
- [140] W. S. Saric, H. L. Reed, and E. J. Kerschen. Boundary-layer receptivity to freestream disturbances. *Annual review of fluid mechanics*, 34(1):291–319, 2002.
- [141] P. Schlatter, S. Stolz, and L. Kleiser. Les of transitional flows using the approximate deconvolution model. *International journal of heat and fluid flow*, 25(3):549–558, 2004.
- [142] H. Schlichting and J. Kestin. *Boundary layer theory*, volume 121. Springer, 1961.
- [143] M. L. Shur, P. R. Spalart, M. K. Strelets, and A. K. Travin. Synthetic turbulence generators for rans-les interfaces in zonal simulations of aerodynamic and aeroacoustic problems. *Flow, turbulence and combustion*, 93:63–92, 2014.
- [144] R. L. Simpson. Turbulent boundary-layer separation. *Annual Review of Fluid Mechanics*, 21(1):205–232, 1989.
- [145] P. E. Skaare and P.-Å. Krogstad. A turbulent equilibrium boundary layer near separation. *Journal of Fluid Mechanics*, 272:319–348, 1994.
- [146] J. P. Slotnick. Integrated cfd validation experiments for prediction of turbulent separated flows for subsonic transport aircraft. In *NATO science and technology organization, meeting proceedings RDP, STO-MP-AVT-307*, 2019.
- [147] E. A. Spiegel and G. Veronis. On the boussinesq approximation for a compressible fluid. *Astrophysical Journal*, vol. 131, p. 442, 131:442, 1960.
- [148] E. F. Spina and A. J. Smits. Organized structures in a compressible, turbulent boundary layer. *Journal of Fluid Mechanics*, 182:85–109, 1987.
- [149] J. Sternberg. *The transition from a turbulent to a laminar boundary layer*. PhD thesis, Johns Hopkins university, 1955.
- [150] A. Stroh, B. Frohnäpfel, P. Schlatter, and Y. Hasegawa. A comparison of opposition control in turbulent boundary layer and turbulent channel flow. *Physics of fluids*, 27(7), 2015.

- [151] Y. Tamaki, Y. Fukushima, Y. Kuya, and S. Kawai. Physics and modeling of trailing-edge stall phenomena for wall-modeled large-eddy simulation. *Physical Review Fluids*, 5(7):074602, 2020.
- [152] H. Tennekes and J. L. Lumley. *A first course in turbulence*. MIT press, 1972.
- [153] B. Thwaites. Approximate calculation of the laminar boundary layer. *Aeronautical Quarterly*, 1(3):245–280, 1949.
- [154] A. Townsend. The properties of equilibrium boundary layers. *Journal of Fluid Mechanics*, 1(6):561–573, 1956.
- [155] A. Townsend. *The structure of turbulent shear flow*. Cambridge university press, 1976.
- [156] A. Trettel and J. Larsson. Mean velocity scaling for compressible wall turbulence with heat transfer. *Physics of Fluids*, 28(2):026102, 2016.
- [157] Y. Tsuji and Y. Morikawa. Turbulent boundary layer with pressure gradient alternating in sign. *Aeronautical Quarterly*, 27(1):15–28, 1976.
- [158] A. Uzun and M. R. Malik. Large-eddy simulation of flow over a wall-mounted hump with separation and reattachment. *AIAA Journal*, 56(2):715–730, 2018.
- [159] A. Uzun and M. R. Malik. Simulation of a turbulent flow subjected to favorable and adverse pressure gradients. *Theoretical and Computational Fluid Dynamics*, 35:293–329, 2021.
- [160] A. Uzun and M. R. Malik. High-fidelity simulation of turbulent flow past gaussian bump. *AIAA Journal*, 60(4):2130–2149, 2022.
- [161] E. R. Van Driest. Turbulent boundary layer in compressible fluids. *Journal of the Aeronautical Sciences*, 18(3):145–160, 1951.
- [162] R. Vinuesa, S. M. Hosseini, A. Hanifi, D. S. Henningson, and P. Schlatter. Pressure-gradient turbulent boundary layers developing around a wing section. *Flow, turbulence and combustion*, 99:613–641, 2017.
- [163] R. Vinuesa, P. S. Negi, M. Atzori, A. Hanifi, D. S. Henningson, and P. Schlatter. Turbulent boundary layers around wing sections up to $Re = 1,000,000$. *International Journal of Heat and Fluid Flow*, 72:86–99, 2018.
- [164] R. Vinuesa, P. H. Rozier, P. Schlatter, and H. M. Nagib. Experiments and computations of localized pressure gradients with different history effects. *AIAA journal*, 52(2):368–384, 2014.
- [165] T. von Kármán. Über laminare und turbulente reibung. *Z. Angew. Math. Mech.*, 1:233–252, 1921.
- [166] M. J. Walsh and L. M. Weinstein. Drag and heat transfer on surfaces with small longitudinal fins. In *11th Fluid and Plasma Dynamics Conference, Seattle, Washington, USA, July 11-12, 1978*.

- [167] R. D. Watson. Wall cooling effects on hypersonic transitional/turbulent boundary layers at high reynolds numbers. *AIAA Journal*, 15(10):1455–1461, 1977.
- [168] D. Webster, D. DeGraaff, and J. Eaton. Turbulence characteristics of a boundary layer over a two-dimensional bump. *Journal of Fluid Mechanics*, 320:53–69, 1996.
- [169] O. H. Wehrmann. Tollmien-Schlichting waves under the influence of a flexible wall. *Physics of Fluids*, 8:1389–1390, 1965.
- [170] C. Wenzel, T. Gibis, and M. Kloker. About the influences of compressibility, heat transfer and pressure gradients in compressible turbulent boundary layers. *Journal of Fluid Mechanics*, 930:A1, 2022.
- [171] F. White. *Viscous Fluid Flow*. McGraw-Hill international edition. McGraw-Hill, 2006.
- [172] F. M. White and G. H. Christoph. A simple theory for the two-dimensional compressible turbulent boundary layer. *Journal of Basic Engineering*, 94:636–642, 1972.
- [173] C. H. Whiting. *Stabilized finite element methods for fluid dynamics using a hierarchical basis*. Rensselaer Polytechnic Institute, 1999.
- [174] C. Williams, M. Di Renzo, P. Moin, and J. Urzay. Locally self-similar formulation for hypersonic laminar boundary layers in thermochemical nonequilibrium. *Annual Research Briefs, Center for Turbulence Research, Stanford University*, 2021.
- [175] O. Williams, M. Samuell, E. S. Sarwas, M. Robbins, and A. Ferrante. Experimental study of a cfd validation test case for turbulent separated flows. In *AIAA Scitech 2020 Forum*, page 0092, 2020.
- [176] X. Wu, P. Moin, J. M. Wallace, J. Skarda, A. Lozano-Durán, and J.-P. Hickey. Transitional–turbulent spots and turbulent–turbulent spots in boundary layers. *Proceedings of the National Academy of Sciences*, 114(27):E5292–E5299, 2017.
- [177] X. Wu and K. D. Squires. Numerical investigation of the turbulent boundary layer over a bump. *Journal of Fluid Mechanics*, 362:229–271, 1998.
- [178] Q.-J. Xia, W.-X. Huang, C.-X. Xu, and G.-X. Cui. Direct numerical simulation of spatially developing turbulent boundary layers with opposition control. *Fluid Dynamics Research*, 47(2):025503, 2015.
- [179] D. Xu, P. Ricco, and L. Duan. Decomposition of the skin-friction coefficient of compressible boundary layers. *Physics of Fluids*, 35(3):035107, 2023.
- [180] D. Xu, J. Wang, and S. Chen. Skin-friction and heat-transfer decompositions in hypersonic transitional and turbulent boundary layers. *Journal of Fluid Mechanics*, 941:A4, 2022.
- [181] X. I. Yang and K. P. Griffin. Grid-point and time-step requirements for direct numerical simulation and large-eddy simulation. *Physics of Fluids*, 33(1), 2021.

- [182] T. A. Zaki. From streaks to spots and on to turbulence: exploring the dynamics of boundary layer transition. *Flow, turbulence and combustion*, 91:451–473, 2013.
- [183] W. Zhang, H.-N. Zhang, J. Li, B. Yu, and F. Li. Comparison of turbulent drag reduction mechanisms of viscoelastic fluids based on the fukagata-iwamoto-kasagi identity and the renard-deck identity. *Physics of Fluids*, 32(1), 2020.
- [184] Y.-S. Zhang, W.-T. Bi, F. Hussain, X.-L. Li, and Z.-S. She. Mach-number-invariant mean-velocity profile of compressible turbulent boundary layers. *Physical Review Letters*, 109(5):054502, 2012.

Appendix A

Full budget of the AMI Equation for flows with Pressure Gradient

Wing dataset

This appendix provides the full budget of the AMI equation, including *negilible* terms, for the Wing dataset. Figure A.1 exhibits $C_f/2$ and the sum of the all terms in the right-hand side of Eq. 5.7, denoted as RHS , where a great match between the left and right-hand sides of the AMI budget is evident. Unsurprisingly, *negilible* remains insignificant even downstream under relatively higher adverse pressure gradient.

Bump dataset

This appendix presents the complete budget of the AMI equation, including negligible terms, for the Bump dataset. Figure A.2 illustrates $C_f/2$ and the sum of all terms on the right-hand side of Eq. 5.7, labeled as RHS . A good agreement is observed between the left and right-hand sides of the AMI equation, except in regions very close to separation (or separated flow). Additionally,

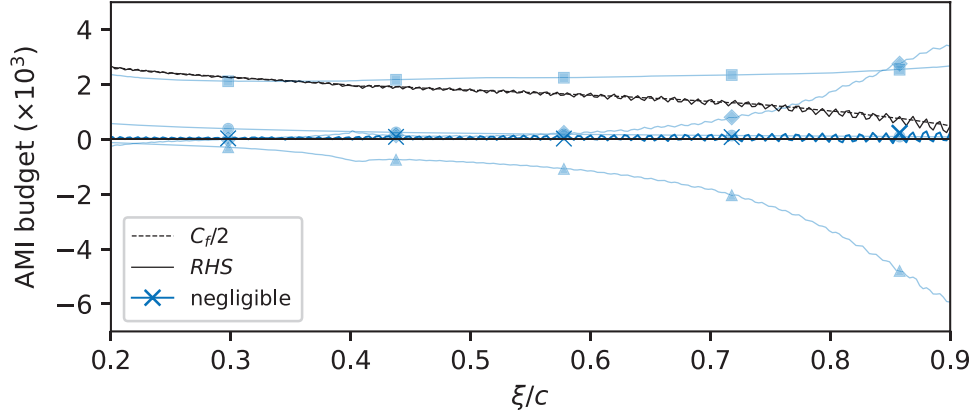


Figure A.1: The full budget of AMI equation for the Wing dataset. Here, $\ell = 4.54\delta_2$ obtained from Blasius solution. The shaded lines represent the flow phenomena already shown in Fig. 5.6.

downstream of the separation bubble, where flow reattachment occurs, the sum of the right-hand side of Eq. 5.7 fluctuates around $C_f/2$. This suggests that the AMI analysis captures the physics within this region, although insufficient averaging leads to oscillations.

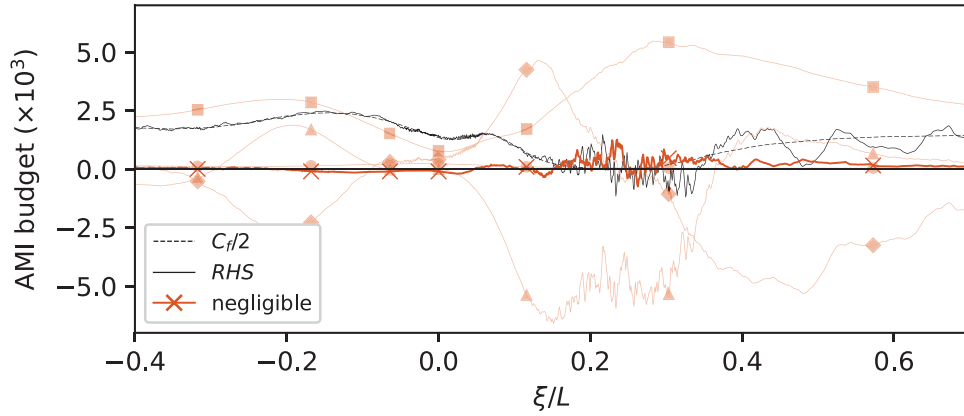


Figure A.2: The full budget of AMI equation for the Bump dataset. Here, $\ell = 4.54\delta_2$ obtained from Blasius solution. The shaded lines represent the flow phenomena already shown in Fig. 5.7.

As expected, *negligible* terms remain insignificant away from the separation region. However, near and within the separation bubble, the terms neglected by the boundary layer approximation and unsteady acceleration become significant. Furthermore, the (absolute) contribution of *negligible* terms slightly increases where the flow is accelerating within the favorable pressure gradient region. The authors attribute this marginal enhancement to an increase in the streamwise derivatives that

appear in Eq. 5.6. Specifically, the streamwise derivative of $\overline{u'u'}$ is higher than the other regions of the flow.

Comparison between edge and inviscid velocities

The comparison between the inviscid velocity at the surface and the edge velocity, both computed by implementing the local reconstruction method is showing in figure A.3 (a, b), respectively, for the Wing and Bump datasets. For the Wing case, the difference between U_{io} and U_e is small. Similarly,

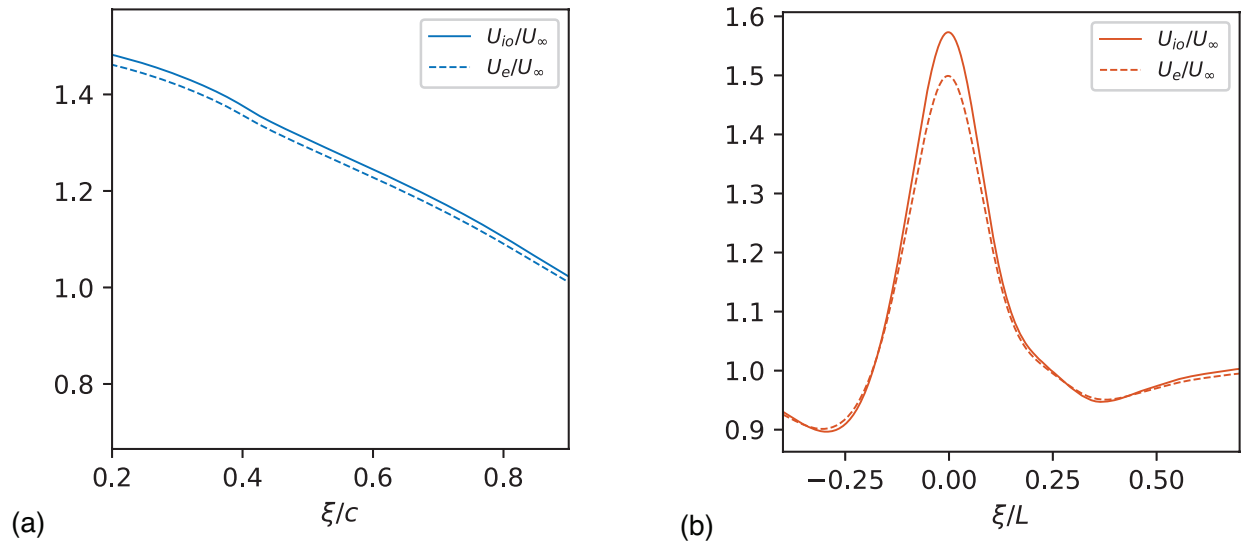


Figure A.3: Comparison between the normalized inviscid velocity at the wall and the edge velocity by U_∞ ; (a) for the Wing case, and (b) for the Bump flow.

for the bump flow, away from the bump's peak U_{io} and U_e match; however, near the bump's peak at $\xi/L = 0$, the difference between these two velocity scales increases. This is primarily attributed to the curvature effect that is stronger in the Bump case, especially near its peak. Note that comparing the budget of the AMI equation reveals that using U_{io} as the outer-scale velocity yields a more robust analysis with a smaller error.

Appendix B

Step-by-step Full Derivation of Angular Momentum Integral Equation

Here, the step-by-step derivation of the AMI equation is provided. Favre average Navier-Stokes equation for statistically two-dimensional compressible BLs reads

$$\frac{\partial \bar{\rho}}{\partial t} + \frac{\partial}{\partial x}(\bar{\rho}\tilde{u}) + \frac{\partial}{\partial y}(\bar{\rho}\tilde{v}) = 0, \quad (\text{B.1})$$

for continuity and

$$\frac{\partial}{\partial t}(\bar{\rho}\tilde{u}) + \frac{\partial}{\partial x}(\bar{\rho}\tilde{u}\tilde{u}) + \frac{\partial}{\partial y}(\bar{\rho}\tilde{u}\tilde{v}) = -\frac{d\bar{p}}{dx} + \frac{\partial}{\partial x}(\bar{\tau}_{xx} - \bar{\rho}\widetilde{u'u'}) + \frac{\partial}{\partial y}(\bar{\tau}_{xy} - \bar{\rho}\widetilde{u'v'}), \quad (\text{B.2})$$

for x -momentum, where we assumed the mean pressure is not changing in y -direction. We can further assume

$$\bar{\tau}_{xy} \approx \overline{\mu \frac{\partial u}{\partial y}}. \quad (\text{B.3})$$

The governing equation at the edge of the BL yields

$$\frac{\partial}{\partial t} (\rho_e U_e) + \rho_e U_e \frac{dU_e}{dx} = -\frac{dP_e}{dx}, \quad (\text{B.4})$$

presuming the edge conditions are independent of the wall-normal direction, y . Subtracting Eq. (B.2) from Eq. (B.4) gives the average x -momentum deficit equation as

$$\rho_e U_e \frac{dU_e}{dx} - \frac{\partial}{\partial x} (\overline{\rho u u}) - \frac{\partial}{\partial y} (\overline{\rho u v}) = -\frac{\partial}{\partial y} \left(\overline{\mu \frac{\partial u}{\partial y}} \right) + \frac{\partial}{\partial y} (\overline{\rho u'' v''}) - I_M, \quad (\text{B.5})$$

in which

$$I_M = \frac{\partial}{\partial t} (\rho_e U_e - \overline{\rho u}) + \frac{\partial}{\partial x} \left(-\overline{\rho} \left(\overline{u'' u''} \right) + \frac{\partial}{\partial x} (\overline{\tau_{xx}}) \right) - \left(\frac{dP_e}{dx} - \frac{d\overline{p}}{dx} \right) \quad (\text{B.6})$$

representing the negligible terms for statistically two-dimensional BLs. re-arranging the Eq. (B.5), and implementing continuity equation the x -momentum deficit can be re-written as

$$\begin{aligned} & \rho_e U_e \frac{dU_e}{dx} \left(\left(1 - \frac{\overline{\rho}}{\rho_e} \frac{\tilde{u}}{U_e} \right) + 2 \left(\frac{\overline{\rho}}{\rho_e} \frac{\tilde{u}}{U_e} \left(1 - \frac{\tilde{u}}{U_e} \right) \right) \right) + U_e^2 \frac{d\rho_e}{dx} \left(\frac{\overline{\rho}}{\rho_e} \frac{\tilde{u}}{U_e} \left(1 - \frac{\tilde{u}}{U_e} \right) \right) \\ & + \rho_e U_e^2 \frac{\partial}{\partial x} \left(\frac{\overline{\rho}}{\rho_e} \frac{\tilde{u}}{U_e} \left(1 - \frac{\tilde{u}}{U_e} \right) \right) + \rho_e U_e^2 \frac{\partial}{\partial y} \left(\frac{\overline{\rho}}{\rho_e} \frac{\tilde{v}}{U_e} \left(1 - \frac{\tilde{u}}{U_e} \right) \right) \\ & + \frac{\partial}{\partial y} \left(\overline{\mu \frac{\partial u}{\partial y}} \right) - \frac{\partial}{\partial y} (\overline{\rho u'' v''}) + I_M = 0. \end{aligned} \quad (\text{B.7})$$

To obtain the angular momentum (or the first moment of momentum) form, we multiply the whole Eq. (B.7) by $(y - \ell)$, where ℓ is the appropriate choice of length scale based on laminar skin friction discussed in 6.2.2. Then, we integrate the equation in the wall-normal direction, $\int_0^\infty (y - \ell(x)) \{ \cdot \} dy = 0$.

Integration of the first two terms in the left-hand side of Eq. (B.7) yields

$$\begin{aligned}
(1) &\rightarrow \rho_e U_e \frac{dU_e}{dx} \int_0^\infty (y - \ell) \left\{ \left(1 - \frac{\bar{\rho}}{\rho_e} \frac{\tilde{u}}{U_e} \right) + 2 \left(\frac{\bar{\rho}}{\rho_e} \frac{\tilde{u}}{U_e} \left(1 - \frac{\tilde{u}}{U_e} \right) \right) \right\} dy = \\
&\quad - \ell \rho_e U_e \frac{dU_e}{dx} \int_0^\infty \left(1 - \frac{y}{\ell} \right) \left\{ \left(1 - \frac{\bar{\rho}}{\rho_e} \frac{\tilde{u}}{U_e} \right) + 2 \left(\frac{\bar{\rho}}{\rho_e} \frac{\tilde{u}}{U_e} \left(1 - \frac{\tilde{u}}{U_e} \right) \right) \right\} dy = \\
&\quad - \ell \rho_e U_e \frac{dU_e}{dx} (\delta_1^\ell + 2\delta_2^\ell), \\
(2) &\rightarrow U_e^2 \frac{d\rho_e}{dx} \int_0^\infty (y - \ell) \left\{ \frac{\bar{\rho}}{\rho_e} \frac{\tilde{u}}{U_e} \left(1 - \frac{\tilde{u}}{U_e} \right) \right\} dy = \\
&\quad - \ell U_e^2 \frac{d\rho_e}{dx} \int_0^\infty \left(1 - \frac{y}{\ell} \right) \left\{ \frac{\bar{\rho}}{\rho_e} \frac{\tilde{u}}{U_e} \left(1 - \frac{\tilde{u}}{U_e} \right) \right\} dy = -U_e^2 \frac{d\rho_e}{dx} \delta_2^\ell.
\end{aligned}$$

These two terms originated from the edge pressure gradient due to the streamwise variation of edge velocity and density, respectively. The integration of the third term in the left-hand side of Eq. (B.7), which represents the streamwise variation of the streamwise flux of momentum deficit, gives

$$\begin{aligned}
(3) &\rightarrow \rho_e U_e^2 \int_0^\infty (y - \ell) \left\{ \frac{\partial}{\partial x} \left(\frac{\bar{\rho}}{\rho_e} \frac{\tilde{u}}{U_e} \left(1 - \frac{\tilde{u}}{U_e} \right) \right) \right\} dy = \\
&\quad - \ell \rho_e U_e^2 \left(\frac{\partial}{\partial x} \int_0^\infty \left(1 - \frac{y}{\ell} \right) \left\{ \frac{\bar{\rho}}{\rho_e} \frac{\tilde{u}}{U_e} \left(1 - \frac{\tilde{u}}{U_e} \right) \right\} dy + \right. \\
&\quad \left. \frac{1}{\ell} \frac{d\ell}{dx} \left(- \int_0^\infty \left(1 - \frac{y}{\ell} \right) \left\{ \frac{\bar{\rho}}{\rho_e} \frac{\tilde{u}}{U_e} \left(1 - \frac{\tilde{u}}{U_e} \right) \right\} dy + \int_0^\infty \frac{\bar{\rho}}{\rho_e} \frac{\tilde{u}}{U_e} \left(1 - \frac{\tilde{u}}{U_e} \right) dy \right) \right) = \\
&\quad - \ell \rho_e U_e^2 \left(\frac{d\delta_2^\ell}{dx} + \frac{\delta_2^\ell - \delta_2}{\ell} \frac{d\ell}{dx} \right).
\end{aligned}$$

The fourth term in Eq.(B.7) depends on the mean wall-normal flux of the streamwise momentum deficit. Integration of this term and applying no-penetration through the wall reads

$$\begin{aligned}
(4) &\rightarrow \rho_e U_e^2 \int_0^\infty (y - \ell) \frac{\partial}{\partial y} \left\{ \frac{\bar{\rho}}{\rho_e} \frac{\tilde{v}}{U_e} \left(1 - \frac{\tilde{u}}{U_e} \right) \right\} dy = \\
&\quad - \ell \rho_e U_e^2 \left(\left[\left(1 - \frac{y}{\ell} \right) \frac{\bar{\rho}}{\rho_e} \frac{\tilde{v}}{U_e} \left(1 - \frac{\tilde{u}}{U_e} \right) \right]_0^\infty + \frac{1}{\ell} \int_0^\infty \frac{\bar{\rho}}{\rho_e} \frac{\tilde{v}}{U_e} \left(1 - \frac{\tilde{u}}{U_e} \right) dy \right) = -\rho_e U_e^2 \delta_2^v.
\end{aligned}$$

The viscous effect and wall shear stress are embedded in the fifth term on the left-hand side of Eq.(B.7). Integrating this term across the wall-normal direction gives

$$(5) \rightarrow \int_0^\infty (y - \ell) \left\{ \frac{\partial}{\partial y} \left(\overline{\mu \frac{\partial u}{\partial y}} \right) \right\} dy = \left[(y - \ell) \left(\overline{\mu \frac{\partial u}{\partial y}} \right) \right]_0^\infty - \int_0^\infty \overline{\mu \frac{\partial u}{\partial y}} dy = \ell \tau_w - \int_0^\infty \overline{(\mu - \mu_{\text{Ref}}) \frac{\partial u}{\partial y}} dy - \mu_{\text{Ref}} U_e.$$

Integration of the sixth term yields

$$(6) \rightarrow \int_0^\infty (y - \ell) \left\{ -\frac{\partial}{\partial y} \left(\overline{\rho u'' v''} \right) \right\} dy = - \left[(y - \ell) \frac{\partial}{\partial y} \left(\overline{\rho u'' v''} \right) \right]_0^\infty + \int_0^\infty \overline{\rho u'' v''} dy = \int_0^\infty \overline{\rho u'' v''} dy,$$

where the contribution of Reynolds shear stress on skin friction is preserved. It's worth mentioning that the integral of the Reynolds shear stress –without using the first-moment method– vanishes because the turbulence doesn't naturally exist either at the wall or within the irrotational edge. Finally, the integral of the seventh term, which represents all the negligible flow phenomena for statistically two-dimensional BLs, is

$$(7) \rightarrow \int_0^\infty (y - \ell) \{ I_M \} dy = \ell \int_0^\infty \left(1 - \frac{y}{\ell} \right) \{ I_M \} dy.$$

Normalizing all the integrals determined above with the edge dynamic pressure, $\rho_e U_e/2$, yields the angular momentum integral (AMI) equation for skin-friction coefficient C_f

$$\begin{aligned} \frac{C_f}{2} &= \frac{1}{Re_\ell} + \frac{1}{\ell} \int_0^\infty \frac{-\overline{\rho u'' v''}}{\rho_e U_e^2} dy + \left\{ \frac{d\delta_2^\ell}{dx} - \frac{\delta_2 - \delta_2^\ell}{\ell} \frac{d\ell}{dx} \right\} + \frac{\delta_2^v}{\ell} + \frac{1}{\ell} \int_0^\infty \frac{\overline{(\mu - \mu_{\text{Ref}}) \frac{\partial u}{\partial y}}}{\rho_e U_e^2} dy \\ &+ \left\{ \frac{1}{U_e} \frac{dU_e}{dx} (\delta_1^\ell + 2\delta_2^\ell) + \frac{1}{\rho_e} \frac{d\rho_e}{dx} \delta_2^\ell \right\} + I_M^\ell. \end{aligned} \quad (\text{B.8})$$

In the above equation

$$\mathcal{I}_M^\ell = \frac{1}{\rho_e U_e^2} \int_0^\infty \left(1 - \frac{y}{\ell}\right) I_M dy \quad (\text{B.9})$$

is the contribution of all negligible terms to the skin friction coefficient.

Deriving the moment of total enthalpy integral (MTEI) equation, Eq.(6.23), takes similar steps elaborated above, but starting with the total enthalpy equation for compressible BLs.

Appendix C

Full Budget of the First-moment Integral Equations for High-speed Flows

C.1 Angular Momentum Integral Equation

In Figures 4.3(a,b,c,d), the four significant terms in AMI equation with choosing the shear stress weighted viscosity as the reference viscosity, $\mu_{\text{Ref}} = \mu_2$, and self-similar compressible laminar solution as the base for the AMI length scale, $\ell = \ell_{2,C}$, are shown. Here, the contributions of the other flow phenomena are provided to complete the budget of the AMI equation.

C.2 Moment of Total Enthalpy Integral Equation

To complete the budget of the MTEI equation, here, we provide the contribution of the other flow phenomena including the flux due to *deviation* from reference viscous transport, *edge pressure gradient flux*, *negligible terms*, and *wall temperature variation* flux to the surface heat transfer. Similar to Figure 4.6(a,b,c,d), the reference viscosity is μ_H , and the MTEI length scale is computed

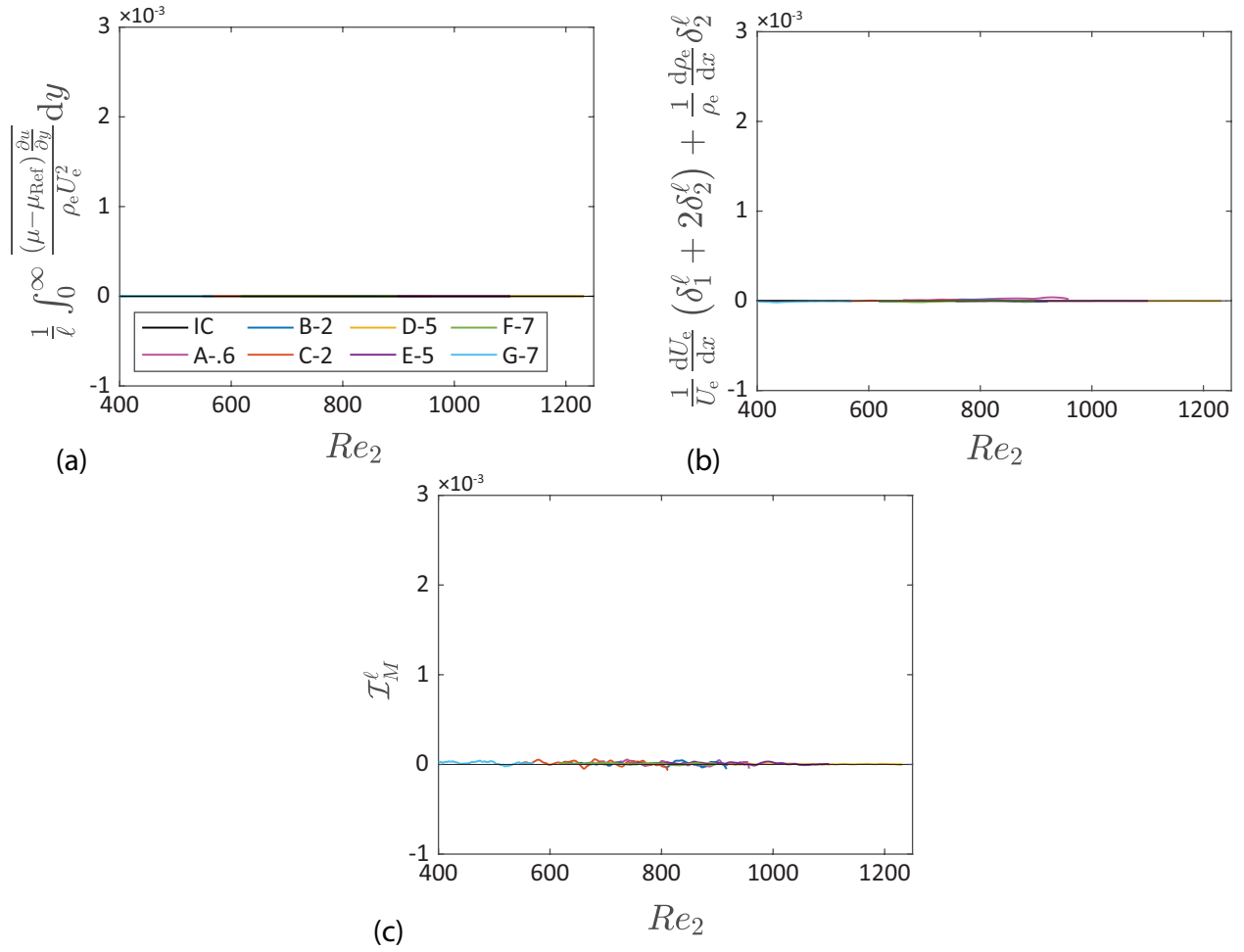


Figure C.1: Contribution of (a) viscous deviation from reference viscosity, (b) torque due to the edge pressure gradient, and (c) the negligible terms due to departure from the BL approximations to the AMI equation, Eq. (6.7), based on $\mu_{\text{Ref}} = \mu_2$ and $\ell = \ell_{2,C}$

from the self-similar compressible laminar solution, $\ell = \ell_{H,C}$.

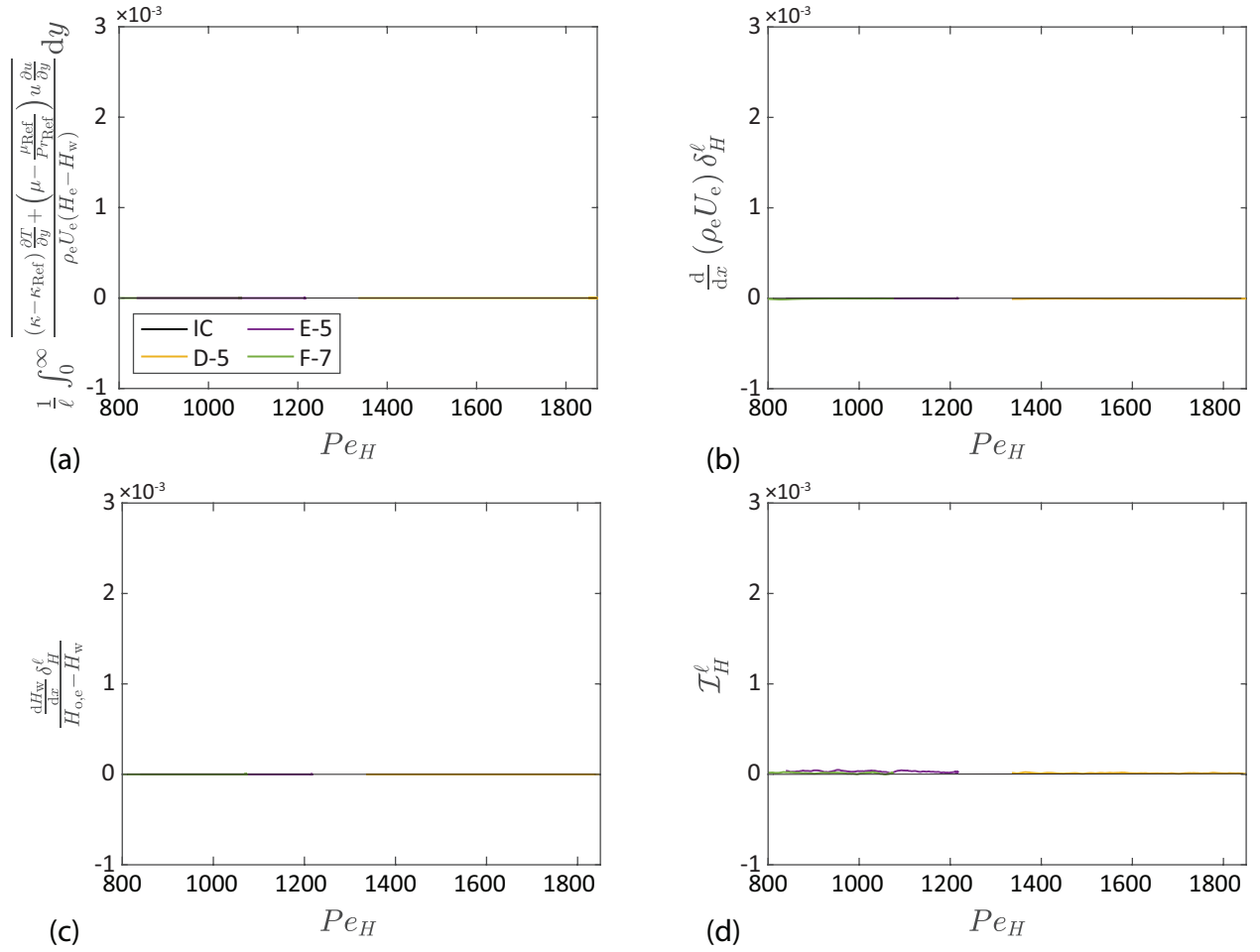


Figure C.2: Contribution of (a) deviation from reference viscous transport, (b) flux due to the edge pressure gradient, (c) non-isothermal wall temperature, and (d) the negligible terms due to departure from the BL approximations to the MTEI equation, Eq. (6.23), based on $\mu_{\text{Ref}} = \mu_H$ and $\ell = \ell_{H,C}$.